Forschungsbericht 2024-07

The role of methane for chemistry-climate interactions

Laura Marcella Stecher

Deutsches Zentrum für Luft- und Raumfahrt
Institut für Physik der Atmosphäre
Oberpfaffenhofen

Dissertation
an der Fakultät für Physik
der Ludwig-Maximilians-Universität
München

DLR Deutsches Zentrum für Luft- und Raumfahrt

Forschungsbericht 2024-07

The role of methane for chemistry-climate interactions

Laura Marcella Stecher

Deutsches Zentrum für Luft- und Raumfahrt
Institut für Physik der Atmosphäre
Oberpfaffenhofen

Dissertation
an der Fakultät für Physik
der Ludwig-Maximilians-Universität
München

194 Seiten
47 Bilder
17 Tabellen
159 Literaturstellen

DLR Deutsches Zentrum für Luft- und Raumfahrt

Herausgeber:

Deutsches Zentrum
für Luft- und Raumfahrt e. V.
Wissenschaftliche Information
Linder Höhe
D-51147 Köln

ISSN 1434-8454
ISRN DLR-FB-2024-07
Erscheinungsjahr 2024

DOI: 10.57676/3h5c-1853

Klimamodellierung, Klima-Chemie Wechselwirkungen, Methan, Strahlungsantrieb, Klimasensitivität, Ozon

(Veröffentlicht in Englisch)

Laura Marcella STECHER
DLR, Institut für Physik der Atmosphäre, Oberpfaffenhofen

Die Rolle von Methan für Klima-Chemie Wechselwirkungen
Dissertation, Ludwig-Maximilians-Universität, München

Methan (CH_4), das zweitwichtigste Treibhausgas, das direkt durch anthropogene Aktivitäten emittiert wird, wird in der Atmosphäre chemisch abgebaut. Die chemische Senke von CH_4 hängt von der Temperatur und von der Konzentration der Reaktionspartner ab, von denen das Hydroxyl Radikal (OH) der Wichtigste ist. Die atmosphärische Lebensdauer von CH_4 ist also nicht konstant und Änderungen der Lebensdauer wirken sich auf die Konzentration von CH_4 aus, was die Wirkung von CH_4 als Treibhausgas beeinflusst.

Im Rahmen dieser Dissertation wurde die Rückkopplung des atmosphärischen CH_4-Mischungsverhältnis auf Grund von Änderungen der chemischen Senke in einem sich erwärmenden Klima untersucht. Dafür wurden Simulationen mit einem Klima-Chemie-Modell durchgeführt. Die wesentliche Neuerung des Set-ups ist, dass CH_4-Emissionen anstelle von einem vorgeschriebenen CH_4-Mischungsverhältnis am Unterrand des Modells verwendet wurden. Das bedeutet, dass Änderungen der chemischen Senke auf das Mischungsverhältnis zurückwirken, und, dass sich auch sekundäre Rückkopplungen von, z.B. Ozon und OH, einstellen können.

climate modelling, chemistry-climate interactions, methane, radiative forcing, climate sensitivity, ozone

(Published in English)

Laura Marcella STECHER
German Aerospace Center (DLR), Institute of Atmospheric Physics, Oberpfaffenhofen

The role of methane for chemistry-climate interactions

Doctoral thesis, Ludwig-Maximilians-Universität, München

Methane (CH_4), the second most important greenhouse gas directly emitted by human activity, is removed from the atmosphere via chemical decomposition. The chemical sink of CH_4 depends on the temperature and on the abundance of its reaction partners, of which the hydroxyl radical (OH) is the most important. Thus, the atmospheric lifetime of CH_4 is not constant and changes of the latter feed back on the atmospheric CH_4 abundance, which has implications for its potential as a greenhouse gas.

In the present thesis, the response of the of the atmospheric CH_4 abundance caused by changes of its chemical sink in a warming climate is investigated. For this, simulations with a chemistry-climate model were conducted. The essential innovation of the simulation set-up is that CH_4 emission fluxes were used instead of prescribed CH_4 mixing ratios at the surface. This means that changes of the chemical sink can feed back on the CH_4 mixing ratios, and that also secondary feedbacks of, e.g. ozone and OH, can evolve.

The role of methane for chemistry-climate interactions

Laura Marcella Stecher

München 2023

The role of methane for chemistry-climate interactions

Laura Marcella Stecher

Dissertation
an der Fakultät für Physik
der Ludwig–Maximilians–Universität
München

vorgelegt von
Laura Marcella Stecher
aus München

München, 21. Dezember 2023

Erstgutachter: Prof. Dr. habil. Martin Dameris

Zweitgutachter: Prof. Dr. Bernhard Mayer

Tag der Abgabe: 21. Dezember 2023

Tag der mündlichen Prüfung: 14. März 2024

Zusammenfassung: Die Rolle von Methan für Klima-Chemie Wechselwirkungen

Methan (CH_4), das zweitwichtigste Treibhausgas, das direkt durch anthropogene Aktivitäten emittiert wird, wird in der Atmosphäre chemisch abgebaut. Die chemische Senke von CH_4 hängt von der Temperatur und von der Konzentration der Reaktionspartner ab, von denen das Hydroxyl Radikal (OH) der Wichtigste ist. Die atmosphärische Lebensdauer von CH_4 ist also nicht konstant und Änderungen der Lebensdauer wirken sich auf die Konzentration von CH_4 aus, was die Wirkung von CH_4 als Treibhausgas beeinflusst.

Aus diesem Grund untersucht die vorliegende Arbeit die Rückkopplung des atmosphärischen CH_4-Mischungsverhältnis auf Änderungen der chemischen Senke in einem sich erwärmenden Klima. Dafür werden Simulationen mit einem Klima-Chemie-Modell durchgeführt. Die wesentliche Neuerung des Set-ups ist, dass CH_4-Emissionen anstelle von einem vorgeschriebenem CH_4-Mischungsverhältnis am Unterrand des Modells verwendet werden. Das bedeutet, dass Änderungen der chemischen Senke auf das Mischungsverhältnis zurückwirken und, dass sich auch sekundäre Rückkopplungen einstellen können. Mit dieser Modellkonfiguration werden Sensitivitätssimulationen mit entweder erhöhtem Mischungsverhältnis von Kohlenstoffdioxid (CO_2) oder erhöhten CH_4-Emissionen durchgeführt.

Während die Erhöhung von CO_2 die chemische Zusammensetzung der Atmosphäre nur indirekt durch induzierte Temperaturänderungen beeinflusst, spielen chemische Wechselwirkungen eine wichtige Rolle bei der direkten Reaktion auf die CH_4-Störung. Die erhöhten CH_4-Emissionen reduzieren OH und verlängern damit die atmosphärische Lebensdauer von CH_4. Dadurch erhöht sich das CH_4-Mischungsverhältnis um einen größeren Faktor als die Emissionen. Darüber hinaus beeinflusst die chemische Senke von CH_4 die Konzentrationen von Ozon (O_3) und stratosphärischem Wasserdampf. Die damit verbundenen Strahlungseffekte sind wichtige Beiträge zum effektiven Strahlungsantrieb der CH_4-Störung.

Die Änderungen der chemischen Zusammensetzung, die allein durch die Erwärmung der Troposphäre verursacht werden, sind qualitativ gleich für die CO_2- und die CH_4-Störung. Die wärmere und feuchtere Troposphäre führt zu einer Verkürzung der Lebensdauer von CH_4 und damit zur Abnahme von atmosphärischem CH_4. Die Tatsache, dass sich das CH_4-Mischungsverhältnis tatsächlich je nach Änderung der chemischen Senke einstellt, ermöglicht sekundäre Rückkopplungen, von z.B. O_3 und OH. Die Klimaänderung von troposphärischem O_3 wird durch eine Vielzahl von Prozessen beeinflusst, deren quantitative Beiträge mit einer Attributionsmethode geschätzt werden. Die Klimaänderungen von CH_4 und O_3 führen zu negativen Strahlungseffekten, d.h. es wird erwartet, dass sie die Änderung der globalen Temperatur am Boden dämpfen. Schließlich deuten die Ergebnisse darauf hin, dass die CH_4-Störung die gleiche Änderung der globalen Temperatur am Boden pro vorgegebenem effektivem Strahlungsantrieb hervorruft wie die CO_2-Störung, was die Eignung des Konzept des effektiven Strahlungsantrieb für CH_4-Störungen bestätigt.

Abstract: The role of methane for chemistry-climate interactions

Methane (CH_4), the second most important greenhouse gas directly emitted by human activity, is removed from the atmosphere via chemical decomposition. The chemical sink of CH_4 depends on the temperature and on the abundance of its reaction partners, of which the hydroxyl radical (OH) is the most important. Thus, the atmospheric lifetime of CH_4 is not constant and changes of the latter feed back on the atmospheric CH_4 abundance, which has implications for its potential as a greenhouse gas.

Motivated by this, the present thesis investigates the response of the atmospheric CH_4 abundance, as a consequence to changes of its chemical sink, in a warming climate on the basis of chemistry-climate model simulations. The essential innovation of the simulation set-up is that CH_4 emission fluxes are used instead of prescribed CH_4 mixing ratios at the lower boundary. This means that changes of the chemical sink can feed back on the CH_4 mixing ratios, and that also secondary feedbacks can evolve without constraints. Using this model configuration, sensitivity simulations with, either increased atmospheric mixing ratios of carbon dioxide (CO_2), or increased emissions of CH_4 are performed.

While the CO_2 perturbation affects the chemical composition of the atmosphere only indirectly by induced temperature changes, chemical interactions play an important role for the direct response following the CH_4 perturbation. The increased CH_4 emissions reduce the abundance of OH, and thereby extend the atmospheric lifetime of CH_4. As a result of this process, the CH_4 mixing ratios increase by a larger factor than the emissions. In addition, the chemical decomposition of CH_4 affects the abundance of ozone (O_3) and stratospheric water vapour. The radiative effects of the corresponding composition changes are important contributions to the effective radiative forcing of the CH_4 perturbation.

The composition changes caused by the isolated effect of tropospheric warming induced by, either the CO_2, or the CH_4 perturbation, are qualitatively the same. Warming and moistening of the troposphere lead to a shortening of the CH_4 lifetime, and correspondingly to a reduction of CH_4 mixing ratios. The fact, that the CH_4 mixing ratios explicitly respond to changes of the chemical sink, enables secondary feedbacks of, e.g. O_3 and OH. The climate response of tropospheric O_3 is influenced by a variety of processes, the quantitative importance of which is estimated by an attribution method. The climate responses of CH_4 and O_3 induce negative radiative effects, which means that they are expected to dampen the resulting change of the global surface air temperature. Finally, the results suggest that the CH_4 perturbation induces the same response of the global surface air temperature per specified effective radiative forcing as the CO_2 perturbation, which confirms the usefulness of the effective radiative forcing framework for CH_4 perturbations.

Contents

Chapter 1

Introduction

1.1 Motivation

The latest report of the Intergovernmental Panel on Climate Change (IPCC) states clearly that "it is unequivocal that human influence has warmed the atmosphere, ocean and land since pre-industrial times." (Chapter 3 in IPCC, 2021; Eyring et al., 2021). The warming is a result of increasing anthropogenic emissions of greenhouse gases (GHGs), mainly carbon dioxide (CO_2), methane (CH_4) and nitrous oxide (N_2O, IPCC, 2021). Limiting global warming has beneficial consequences for humans and natural systems because climate-related risks such as the rise of the sea level, extreme events such as heatwaves and strong precipitation, drought and water availability, and food security depend on the amplitude of warming (IPCC, 2018). Therefore, the Paris Agreement (https://www.un.org/en/climatechange/paris-agreement, last accessed 2023-11-14), which is an international treaty to level the response of the global surface air temperature (GSAT) below 2°C, while aiming to keep it below 1.5°C, was adopted.

A fundamental concept in climate research relates the response of GSAT to the so-called radiative forcing (RF). RF specifies a perturbation of the Earth's energy budget induced by anthropogenic or natural activity. The parameter that relates RF and GSAT is the climate sensitivity parameter. It quantifies the response of GSAT per RF. Following this concept, RF being a predictor of the GSAT response can be used as a metric to assess policy driven mitigation options and the relative importance of individual perturbation agents (Ramaswamy et al., 2018). However, this relation is only meaningful if the RF is representative of the change of GSAT. This is the case if the processes that determine the climate sensitivity are known and if they are the same for different perturbation agents.

Different definitions of RF have evolved to better fulfil this requirement. In this thesis the definition of effective radiative forcing (ERF) is used. Following the ERF framework, the fast response and the climate response are assessed separately so that rapid radiative adjustments are part of the forcing and only climate feedbacks that are coupled to the GSAT response contribute to the climate sensitivity. More information about ERF, rapid radiative adjustments and climate feedbacks is given in Sect. 2.2. ERF is currently considered the most appropriate definition of RF (Chapter 7 in IPCC, 2021; Forster et al., 2021).

CH_4 is after CO_2 the second most important GHG directly emitted by human activity. In comparison with CO_2, CH_4 has a stronger global warming potential per molecule (Chapter 7 in IPCC, 2021; Forster et al., 2021) and a relative short atmospheric lifetime of about 10 years (e.g. Prather et al., 2012; Stevenson et al., 2020). Therefore, reducing atmospheric CH_4 mixing ratios is an effective option for mitigating short term climate change and is considered a crucial contribution to meet the goal of the Paris Agreement (Saunois et al., 2016; Collins et al., 2018; Ocko et al., 2021; UNEP-CCAC, 2021; Staniaszek et al., 2022). Thus, political action focusing especially on CH_4 reduction is carried out. For instance, more than 100 countries signed the Global Methane Pledge in 2021, which implies commitment to reduce global anthropogenic CH_4 emissions by at least 30 % below 2020 levels by the year 2030 (Global Methane Pledge, https://www.globalmethanepledge.org/, last accessed 2023-11-14).

The relative short atmospheric lifetime of CH_4 is a consequence of CH_4 being a chemically active species. The most important sink of atmospheric CH_4 is the oxidation with the hydroxyl radical (OH, e.g. Saunois et al. (2020)). Therefore, understanding the chemical mechanisms underlying the CH_4 oxidation is crucial when assessing its climate impact and possible mitigation options.

CH_4 oxidation leads to the production of water vapour (H_2O) and ozone (O_3), which contributes significantly to its ERF (Shindell et al., 2009; Stevenson et al., 2013; Winterstein et al., 2019; Thornhill et al., 2021b; O'Connor et al., 2022). About 40% of the total pre-industrial to present-day RF of O_3 can be attributed to changes of CH_4 (Thornhill et al., 2021b). In addition to its climate impact, tropospheric O_3 poses harmful effects on human health (Nuvolone et al., 2018) and on vegetation (Ashmore, 2005). Therefore, mitigation options involving CH_4 emission reduction have beneficial effects on air quality (Shindell et al., 2012; Staniaszek et al., 2022) and plant productivity (Sitch et al., 2007). These co-benefits of air quality improvement and climate change mitigation are especially

desirable as air quality control involving the reduction of, for example, aerosols amplifies global warming (e.g., Shindell et al., 2012; Stohl et al., 2015; Allen et al., 2021). Furthermore, enhanced plant primary productivity by O_3 reduction feeds back on the efficiency of the land-carbon sink (Sitch et al., 2007). In addition to the effects of O_3 and H_2O production, the CH_4 oxidation reduces OH, which feeds back onto its own atmospheric lifetime (Winterstein et al., 2019) and affects the rate of formation of secondary aerosols leading to a shift in the aerosol-size distribution. The latter in turn influences aerosol-radiation interactions and aerosol-cloud interactions, and might be another important indirect contribution to the ERF of CH_4 (Kurtén et al., 2011; O'Connor et al., 2022).

Next to its importance for indirect contributions to the ERF, the CH_4 oxidation largely constrains the atmospheric lifetime of CH_4 and, thus, together with the magnitude of the emissions, its direct climate effect. The atmospheric lifetime of CH_4 is not constant, but depends on temperature and on the chemical background, which determines the abundance of its sink reactants, especially OH. OH is influenced by a magnitude of factors (e.g. Voulgarakis et al., 2013; Frank, 2018, see also Sect. 2.4). For instance, the studies of Stevenson et al. (2022) and Skeie et al. (2023) suggest that the strong decrease of emissions of nitrogen oxides NO and NO_2 (NO_x) caused by COVID-19 restrictions led to an extension of the CH_4 lifetime that can partly explain the strong increase of CH_4 mixing ratios during the year 2020 (e.g. Lan et al., 2023). Further, OH is influenced by meteorological factors such as humidity and temperature (e.g. Voulgarakis et al., 2013). Hence, climate feedbacks influencing the chemical sink of CH_4 and thereby its lifetime are expected. More precisely, the CH_4 lifetime is projected to shorten as a result of tropospheric warming (Voulgarakis et al., 2013; Frank, 2018; Stecher et al., 2021). Up to date, only a limited number of studies have assessed the corresponding response of CH_4 mixing ratios directly (Heimann et al., 2020). In contrast, the resulting reduction of CH_4 mixing ratios and the corresponding radiative effect are usually estimated from the response of its atmospheric lifetime (Dietmüller et al., 2014; Heinze et al., 2019; Thornhill et al., 2021a) as CH_4 mixing ratios are normally prescribed at the lower boundary in chemistry-climate models (CCMs).

This method, however, restricts indirect feedbacks induced by the CH_4 response. On the one hand, the resulting CH_4 response would in turn alter the atmospheric CH_4 lifetime, which would lead to subsequent adaptions of the CH_4 mixing ratios. The derivation of the CH_4 response from the lifetime change usually accounts for this effect by including a constant feedback factor (f) (Heinze et al., 2019; Thornhill et al., 2021a). Estimates of f based on CCM simulations with perturbed CH_4 mixing ratios suggest a value between

1.2–1.4 (Fiore et al., 2009; Voulgarakis et al., 2013; Stevenson et al., 2013; Thornhill et al., 2021b; Stevenson et al., 2020). This means that any change of CH_4 production or loss would be amplified by a factor of 1.2–1.4. Holmes (2018) finds that f can vary geographically and seasonally, and that it strengthens for increasing CH_4 burden. On the other hand, the subsequent CH_4 response would affect other chemical constituents such as O_3. This effect is also sometimes parameterized by scaling the sensitivity of O_3 towards CH_4 perturbations with the expected CH_4 response (Fiore et al., 2009; Thornhill et al., 2021b), but is lacking in estimates of the effect of O_3 on climate sensitivity (Dietmüller et al., 2014; Nowack et al., 2015; Marsh et al., 2016; Li and Newman, 2023).

This thesis aims at quantifying the radiative feedback of atmospheric CH_4 and its impact on the model's climate sensitivity by explicitly simulating the climate response of CH_4. This is realized by using CH_4 surface emission fluxes instead of prescribed surface mixing ratios in the used CCM set-up. Thereby, the CH_4 mixing ratios adjust to changes in its chemical sink without constraints, and secondary feedbacks are free to evolve explicitly. This thesis gives, to my knowledge, the first estimate of the role of interactive gas-phase chemistry on the climate sensitivity with explicit accounting for of the CH_4 feedback. Further, as the analysis follows the ERF framework, the role of chemical rapid radiative adjustments and slow climate feedbacks is analysed separately.

1.2 Research questions and outline

The present thesis investigates the research question:

> What is the role of CH_4 for chemistry-climate interactions?

Thereby, this thesis aims at improving the understanding of processes that affect the atmospheric composition and its interaction with climate change. Both, the effects of CO_2 and of CH_4 perturbations are assessed because of their different effects on atmospheric chemistry. CH_4 directly affects the chemical composition through products of its chemical sink, whereas CO_2 has only indirect impacts through, e.g. the temperature change. Therefore, following the ERF framework, the fast response and the GSAT-mediated climate response are assessed separately. In addition, this thesis investigates how the composition changes translate into radiative perturbations that may affect the ERF and the climate sensitivity. Finally, this thesis assesses whether the climate sensitivity parameter for CH_4 perturbations can be assumed to be the same as for CO_2 perturbations.

Thus, the generalized research question is separated into the following five detailed research questions:

1. How does the chemical sink of atmospheric CH_4 respond in the fast and in the climate response if perturbed by either increased CO_2 mixing ratios or increased CH_4 emissions? How do these changes of the chemical sink feed back on atmospheric CH_4 mixing ratios?

2. Which processes play a role in the fast and in the climate response of O_3 if perturbed by either CO_2 or CH_4 increase? Is the climate response of O_3 affected by the explicit accounting for of the CH_4 feedback?

3. What is the effect of interactive chemistry on the temperature response and on the response of H_2O mixing ratios?

4. How large are the contributions of chemical rapid radiative adjustments and slow climate feedbacks on the ERF and on the climate sensitivity?

5. Is the climate sensitivity parameter different for the CH_4-perturbation compared to the CO_2-perturbation if chemical feedbacks are accounted for in the simulation set-up?

This thesis is structured as follows: First, information about the scientific background is summarized in Chapter 2, which covers information about the greenhouse effect, the framework of radiative forcing and the climate sensitivity, sources and sinks of atmospheric CH_4, and interactions of atmospheric chemistry.

Chapter 3 introduces the used methods. To target the research questions a number of numerical simulations are performed with the CCM ECHAM/MESSy Atmospheric Chemistry (EMAC). A CCM allows to investigate the two-way coupling between chemical composition changes and the climate state, e.g. temperature, circulation or precipitation, under imposed perturbations. Sect. 3.1 describes the used model system, and Sect. 3.2 gives an overview of the performed simulations and their set-up. To assess the fourth detailed research question, the radiative effects of individual processes are quantified using two different methods, which are explained in Sect. 3.3.

The results of the CO_2 perturbation experiments are presented in Chapter 4. More precisely, this chapter assesses the response of CH_4 and O_3 mixing ratios (Sect. 4.1), as well as the change of the temperature and H_2O mixing ratios (Sect. 4.2). In addition, Sect. 4.3 assesses the contribution of individual processes to the corresponding RF and the climate sensitivity. Chapter 5 presents the results of the CH_4 perturbation experiments and is structured in the same way as the previous chapter. The results presented in both chapters are discussed in Chapter 6. Chapter 7 answers the research questions and concludes with an outlook. The appendices at the end of this thesis provide further technical details, as well as supporting information for the scientific results presented in this study.

Chapter 2

Scientific Background

This chapter summarizes the scientific background important for this thesis. First, it explains the greenhouse effect and the underlying physical principles (Sect. 2.1). Secondly, it introduces the framework of radiative forcing and climate sensitivity (Sect. 2.2). Afterwards, it gives information about sources and sinks of CH_4 (Sect. 2.3) followed by an introduction into atmospheric chemistry (Sect. 2.4).

2.1 The greenhouse effect

This section introduces basic principles of atmospheric radiative transfer as these are the basis of the greenhouse effect of atmospheric trace gases, such as H_2O, CO_2, O_3, CH_4, N_2O and others. Further, it recaps estimates of global mean radiation fluxes of the Earth-atmosphere energy budget.

2.1.1 Solar and terrestrial emission spectra

For atmospheric radiative transfer the radiation spectrum is usually divided into the solar shortwave (SW; 0.1 to 4 μm) and the terrestrial longwave (LW; 4 to 100 μm) range. These wavelength ranges account for over 99% of the radiative energy emitted by the Sun and the Earth, respectively (Petty, 2006). The intensity of radiation at one specific wavelength, B_λ, is temperature dependent. For a blackbody (a perfect emitter) it is given by the Planck's function

$$B_\lambda(T) = \frac{2hc^2}{\lambda^5(e^{hc/(k_B\lambda T)} - 1)}, \tag{2.1}$$

where c = 2.99792458 $\times$ 10^8 m s^{-1} is the speed of light, h = 6.62607015 $\times$ 10^{-34} J s is Planck's constant, and k_B = 1.380649 $\times$ 10^{-23} J K^{-1} is Boltzmann's constant. B_λ has units of W m^{-2} μm^{-2} sr^{-1}. Planck's function gives an upper bound of the intensity emitted at one specific wavelength and temperature. The emission spectra for blackbodies at temperatures of 6000 K (typical for the Sun) and 250 and 300 K (typical for the Earth) are shown in Fig. 2.1 (a). The normalized emission spectra (Fig. 2.1 b)) illustrate the separation of SW and LW spectra at approximately 4 μm.

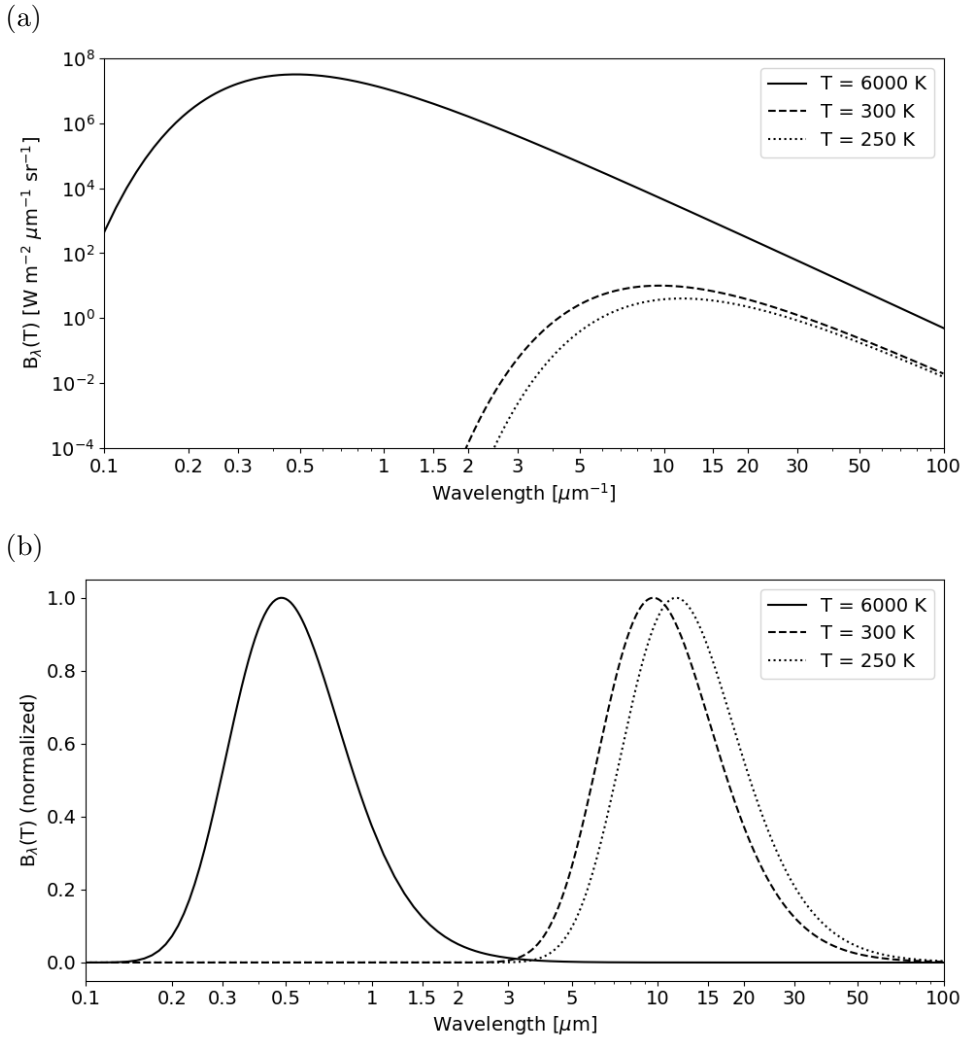

Figure 2.1: Blackbody emission curves at temperatures of 6000 K (typical for the Sun), and 250 and 300 K (typical for the Earth). (a) Actual value of the Planck's function in [W m^{-2} μm^{-2} sr^{-1}], plotted on a logarithmic vertical and horizontal axis. (b) The value of the Planck's function normalized by the respective maximum. The illustration is based on Fig. 6.2 by Petty (2006).

The broadband flux (density) is the intensity emitted by the full wavelength range and into one hemisphere. It can be derived by integrating Eq. 2.1 over all wavelengths and over the 2π steradians of the solid angle of one hemisphere. In spherical polar coordinates this gives

$$F(T) = \int_0^{\infty} \int_0^{2\pi} \int_0^{\pi/2} cos(\theta)\ sin(\theta)\ B_\lambda(T)\ d\lambda\ d\phi\ d\theta \tag{2.2}$$

$$= \pi \int_0^{\infty} B_\lambda(T)\ d\lambda. \tag{2.3}$$

The integration over the solid angle reduces to multiplication with a factor of π as B_λ of a blackbody is isotropic and therefore does not dependent on ϕ and θ. Solving the integral over the wavelength gives the Stefan-Boltzmann law

$$F(T) = \sigma T^4, \tag{2.4}$$

where $\sigma = \frac{2\pi^5 k_B^4}{15c^2h^3}$ is the Stefan-Boltzmann constant in units of W m^{-2} K^{-4}.

2.1.2 Absorption and emission by atmospheric gases

This section explains the interaction of atmospheric gases with radiation. Unless otherwise mentioned it follows Chapter 9 in Petty (2006). Molecules can absorb and emit photons. The absorption (emission) of one photon increases (decreases) the energy E of the molecule by the energy of the photon

$$E = \frac{hc}{\lambda}. \tag{2.5}$$

The increase or decrease in the molecule's internal energy can contribute to changes in

- translational kinetic energy of molecules (i.e. temperature),
- rotational kinetic energy of polyatomic molecules ($\lambda > 20\ \mu$m),
- vibrational kinetic energy of polyatomic molecules ($1\ \mu\text{m} < \lambda < 20\ \mu$m) or
- electronic transitions ($\lambda < 1\ \mu$m).

The energy of different rotational, vibrational and electronic states is quantized. This means that a photon can be absorbed by a molecule only if its energy corresponds to the energy required for the transition from the molecule's original state to one of its allowed

states. The allowed energy states are specific to the structure of each molecule. The magnitude of required energy is different for the different modes of transitions, i.e. rotational, vibrational or electronic. Therefore, different wavelength ranges can be associated with different modes of transitions. Rotational transitions require relatively low energy so that radiation with $\lambda > 20$ μm is associated with it. Vibrational transitions can be triggered by radiation in the near and thermal infrared (1 μm $< \lambda <$ 20 μm). Combined rotational-vibrational transitions are possible, during which the state of the vibrational and the rotational mode is changed simultaneously. This leads to a split of the vibrational absorption line into multiple absorption lines in the absorption spectrum. For electronic transitions radiation in the SW range ($\lambda < 1$ μm) is required. In addition to the transitions described above, photodissociation and photoionization can occur. Photodissociation, also called photolysis, describes the split of a molecule caused by absorption of a photon with enough energy to overcome the chemical binding energy of the molecule. This process has no upper energy bound as the remaining energy is used as unquantized kinetic energy. Similarly, photoionization occurs if an atom absorbs a photon with enough energy to free one electron.

As mentioned above, the allowed transitions between states are determined by the specific structure of the molecule. The H_2O molecule is non-linear and has a permanent electric dipole moment. This leads to a wide range of possible rotational transitions. For wavelengths longer than 25 μm there is strong absorption by H_2O due to pure rotational transitions. Between 8 to 12 μm the absorption by H_2O is weak and the atmosphere relatively transparent. Therefore, this wavelength range is called the atmospheric window. Rotation-vibration bands are centred around 6.3 and 2.7 μm and additional higher order vibrational transition bands are in the SW range.

CO_2 has two strong rotation-vibration bands at 4.2 and 15 μm. Especially the 15 μm band is important as it is positioned near the peak of the LW spectrum (see Fig. 2.1). The 4.2 μm plays a minor role as it is neither positioned near the peak of the SW nor the LW range.

Similar as for H_2O, the structure of O_3 is non-linear and it has therefore a strong rotational spectrum. Its main vibrational bands are at 9.066, 14.27 and 9.597 μm. The GHG effect of the 14.27 μm band is suppressed by the abundance of CO_2. The other two bands are positioned in the atmospheric window region and are usually considered combined. There is another band at 4.7 μm, which plays a minor role as it is positioned at the edge of both, the SW and LW range (similar as the 4.2 μm CO_2 band). Additionally,

O_3 strongly absorbs in the SW range below 0.28 μm due to electronic excitation. This is important for life on Earth as stratospheric O_3 thereby serves as a protection layer against damaging solar ultraviolet radiation.

CH_4 has important vibrational bands at 1.7, 2.3, 3.3 and 7.6 μm (Byrom and Shine, 2022). Especially, the 7.6 μm band is important as it is positioned close to the atmospheric window region, in which the atmosphere is relatively transparent, especially at low H_2O abundance (Petty, 2006). The 7.6 μm band of CH_4 overlaps with the 7.8 μm band of N_2O. The other bands fall in the SW range and are not treated in all radiative transfer models used in General Circulation models (GCMs). Accounting for the effect of CH_4 SW absorption enhances the net radiative effect of CH_4 (Etminan et al., 2016; Byrom and Shine, 2022).

2.1.3 Earth-atmosphere energy budget

At the top of the atmosphere (TOA), Earth's energy balance is controlled by the amount of incoming and outgoing radiation. The total solar irradiance (TSI) specifies the solar irradiance that reaches TOA integrated over all wavelengths. It is not constant over time, but varies on different time scales, most prominently with the 11-year solar cycle (e.g. Matthes et al., 2017). An average value for TSI representing present-day is 1361 Watt per square meter (W m^{-2}) (Matthes et al., 2017). The area TSI refers to is the Earth's cross-section, i.e approximately a circular area with the Earth's radius. To get an estimate of the global mean radiation flux it must be redistributed over the Earth's surface, which results in an energy flux of about 340 W m^{-2} incoming solar radiation at TOA. This number and all other estimates of globally averaged radiation fluxes cited in the following, as well as their respective 95% uncertainty ranges, are from Chapter 7 in IPCC, 2021 (Forster et al., 2021, based on Wild et al. (2015, 2019)).

Part of the incoming solar radiation, 100^{+0}_{-3} W m^{-2}, is reflected by clouds, atmospheric molecules, aerosols, or the Earth's surface. The remaining part is absorbed by the atmosphere (80^{+9}_{-5} W m^{-2}) and at the surface (160^{+5}_{-5} W m^{-2}). The radiation absorbed at the surface is transformed into sensible heat consequently heating Earth's surface. The surface re-emits radiation in the LW spectral range depending on its temperature (see Sect. 2.1.1). The radiation flux emitted by the surface is not directly re-emitted into space, but partly absorbed or reflected by the atmosphere. The downward back radiation is further absorbed by Earth's surface heating it accordingly. The resulting thermal emission flux by Earth's surface is 398^{+2}_{-3} W m^{-2}, which is larger than the thermal outgoing radiation flux at TOA

(239^{+3}_{-2} W m^{-2}).

This effect is called the natural greenhouse effect and leads to an average temperature of Earth's surface of about 15 °C instead of -18 °C (e.g. Seinfeld and Pandis, 2016). Increasing levels of GHGs lead to enhanced absorption and downwelling of radiation, and consequently to enhanced warming of Earth's surface until a new equilibrium is reached. The mathematical framework that describes how the global mean surface temperature responds to a perturbation of Earth's energy balance is introduced in the following section.

2.2 Theoretical framework for radiative forcing and climate sensitivity

2.2.1 Radiative forcing and climate sensitivity

The fundamental principle behind the formulation of radiative forcing (RF) is that a perturbation of Earth's energy balance eventually leads to a change of the global surface air temperature (GSAT) to restore equilibrium. A positive RF, i.e. a net energy gain, requires an increase of outgoing thermal radiation into space, and is therefore associated with heating of the surface. Similarly, a negative RF, i.e. a net energy deficit, is associated with cooling of the surface to reduce the outgoing thermal radiation. Mathematically formulated, the change of GSAT, ΔT, is assumed to be linearly linked to RF (e.g. Ramaswamy et al., 2018):

$$\Delta T = \lambda \cdot RF, \tag{2.6}$$

with ΔT in K, RF in W m^{-2} and the proportionality constant λ in K / (W m^{-2}). λ is called the climate sensitivity parameter and reflects the magnitude of GSAT response per specified RF. RF may be regarded as a good predictor of GSAT if the climate sensitivity parameter is independent of the model used for its derivation and invariant for different types of perturbations (e.g. Ramaswamy et al., 2018). To compare the climate sensitivity parameters associated with different types of perturbations the efficacy was introduced (Hansen et al., 2005). It is defined as the climate sensitivity parameter of the considered perturbation λ_{pert} normalized by the climate sensitivity parameter of CO_2 λ_{CO_2}

$$r_{\text{pert}} = \frac{\lambda_{\text{pert}}}{\lambda_{CO_2}}. \tag{2.7}$$

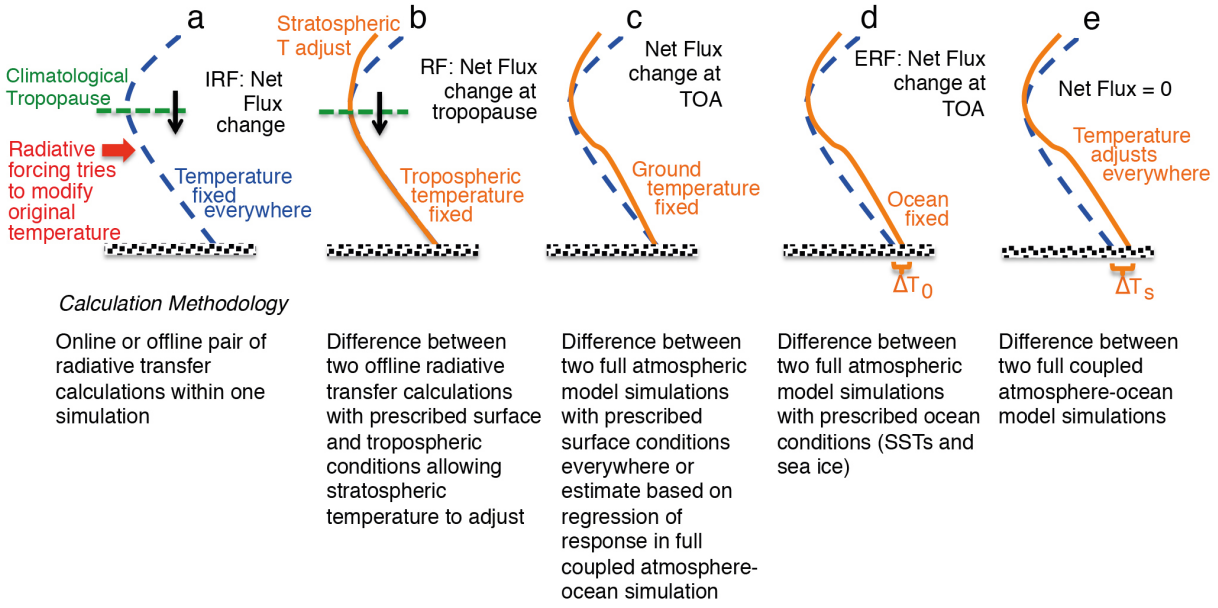

Figure 2.2: Illustration of different definitions of RF (Fig. 8.1 of IPCC, 2013). Panel a illustrates instantaneous RF (RF_{inst}) and panel b stratospheric adjusted RF (RF_{adj}). Panels c and d illustrate two methods to derive effective RF (ERF). Panel e represents the new equilibrium after sea surface temperatures adjust to the perturbation.

Different definitions of RF have evolved, aiming at better fulfilling the prerequisite of an efficacy of unity for different perturbation types. These definitions differ as to which degree the atmosphere is allowed to adjust to the imposed perturbation. Fig. 2.2 illustrates the different definitions as given by IPCC, 2013.

The first application of RF by Ramanathan (1975) used instantaneous radiative forcing (RF_{inst}), which is defined as the net radiative flux change at either TOA or at the tropopause excluding any adjustment (see panel a of Fig. 2.2). Shortly after, stratospheric adjusted radiative forcing (RF_{adj}) came up (Ramanathan and Dickinson, 1979) as it was realized that radiative equilibrium in the stratosphere is restored much faster than the typical time-scale of GSAT changes. RF_{adj} is defined as the net radiative flux change after stratospheric temperatures adjust to a new equilibrium without allowing any changes in tropospheric variables and stratospheric dynamics (see panel b of Fig. 2.2). This method is also called fixed dynamical heating (FDH) concept (Fels et al., 1980)). The net global RF_{adj} is identical whether evaluated at TOA or at the tropopause as the application of stratospheric temperature adjustment sets the region above the tropopause to radiative equilibrium.

Later, the effective radiative forcing (ERF) framework was introduced (Shine et al., 2003; Hansen et al., 2005). ERF conceptionally distinguishes between so called rapid radiative adjustments and (slow) climate feedbacks. Rapid radiative adjustments are responses to the perturbation that cause a change in the net TOA energy balance, but are uncoupled to the response of GSAT. Therefore, they are accounted as part of the forcing. There is no strictly defined time scale that separates rapid radiative adjustments and climate feedbacks. The naming "rapid" and "slow" originates from the fact that the response of GSAT is coupled to the response of sea surface temperatures (SSTs), which is delayed by the large heat capacity of the ocean. It is worth noting that the adjustment of stratospheric temperatures is considered as one rapid radiative adjustment in the ERF framework. However contrary to $\mathrm{RF_{adj}}$, the adjustment of stratospheric temperatures in this context is not only directly induced by the perturbation, but can be also induced by other processes, for instance through composition changes. The conceptional advantage of ERF is that perturbation-specific adjustments are included in the forcing. Therefore, the climate sensitivity parameter is expected to be less dependent of the type of perturbation (e.g. Sherwood et al., 2015). Results from climate model studies suggest that this is indeed the case (Shine et al., 2003; Richardson et al., 2019).

Different practical realizations to determine ERF exist depending on the method to derive it (Forster et al., 2016). These are illustrated in panels c and d of Fig. 2.2. The definition in panel c separates ERF from any change in surface temperature. This is implemented by regressing the net TOA energy imbalance against the response of GSAT, ΔT, of a coupled atmosphere-ocean simulation. ERF is defined as the intercept of the regression line with ΔT=0 (Gregory et al., 2004). The advantage of this method is the clear separation between forcing and response at ΔT=0. However, a disadvantage is a large uncertainty in the derived ERF (Forster et al., 2016). As prescribing land surface temperatures in climate models is difficult to implement, another established method is using prescribed SSTs and sea ice concentrations (SICs) (Shine et al., 2003; Forster et al., 2016). Prescribing SSTs and SICs prevents most of the response of GSAT. There is, however, a response of land surfaces that can affect the rapid radiative adjustments of water vapour, the tropospheric air temperature and the lapse rate, the surface albedo, e.g. through snow cover, and clouds (Andrews et al., 2021). There exist several methods to correct ERF for the effect of land surface temperature response (Hansen et al., 2005; Tang et al., 2019). For instance, the radiative effect can be estimated as the response of land temperatures divided by the climate sensitivity ($\Delta \mathrm{T_{land}}/\lambda$), or by removing the (separately calculated)

rapid radiative adjustments associated with the land surface temperature change from ERF. This thesis adopts the ERF definition with ERF derived from simulations with prescribed SST and SIC, because it ensures a higher signal-to-noise ratio of forcings, rapid radiative adjustments and climate feedbacks than the regression method.

2.2.2 Adjustments and feedbacks

The analysis of individual rapid radiative adjustments and climate feedbacks can help to understand the underlying processes that lead to differences of the ERF and the climate sensitivity between different models (e.g. Bony et al., 2006; Smith et al., 2018; Zelinka et al., 2020) or different perturbation types (e.g. Yoshimori and Broccoli, 2008; Rieger et al., 2017; Bickel et al., 2020). This section introduces the formulations that relate different definitions of RF, rapid radiative adjustments and climate feedbacks, and presents the individual processes that are investigated in this thesis.

Adjustments

As explained in Sect. 2.2.1, $\mathrm{RF}_{\mathrm{inst}}$ and the sum of all rapid radiative adjustments yield ERF. This can be formulated as

$$ERF = RF_{inst} + \sum_i RA_i, \tag{2.8}$$

whereby

$$\sum_i RA_i = RA_{strat.\ temp.} + RA_{Planck} + RA_{LR} + RA_{H_2O} + RA_{albedo} + RA_{clouds} + RA_{chem}. \tag{2.9}$$

$RA_{strat.\ temp.}$ is the stratospheric temperature adjustment that can be directly induced by the perturbation or indirectly by changes of other processes. The direct effect of the perturbation is included in $\mathrm{RF}_{\mathrm{adj}}$. Stratospheric cooling (warming) leads to a weaker (stronger) emission of LW radiation into space and therefore enhances (decreases) the TOA energy imbalance, and is thus a positive (negative) contribution to the forcing. Depending on the perturbation type $RA_{strat.\ temp.}$ can be positive or negative (e.g. Smith et al., 2018).

The adjustment of tropospheric temperatures can be split in RA_{Planck}, the adjustment of surface temperatures, and RA_{LR}, the adjustment of the tropospheric temperature profile. From the definition of ERF it follows that RA_{Planck} is supposed to be small. However,

depending on the derivation method of ERF (see Sect. 2.2.1) RA_{Planck} can include a non-zero adjustment of land surface temperatures. The lapse rate describes the temperature change per height, which is on average a temperature decrease in the troposphere. A stronger (weaker) temperature decrease with height leads to less (more) outgoing LW radiation making RA_{LR} a positive (negative) contribution to the forcing.

RA_{H_2O} is the adjustment due to changes in H_2O. It is anti-correlated to RA_{LR} as the H_2O mixing ratios in the troposphere are strongly dependent on the temperature (Smith et al., 2018; Colman and Soden, 2021). This is because the partial pressure of H_2O in air is limited by the Clausius-Clapeyron relationship.

RA_{cloud} is the adjustment due to cloud cover and cloud microphysical properties. For instance, adjustments in the tropospheric lapse rate can affect cloud cover (Sherwood et al., 2015) resulting in radiative flux differences.

RA_{albedo} is the adjustment caused by changes in the surface albedo. In simulations with prescribed SICs RA_{albedo} is expected to be small. Nevertheless, the surface albedo can be affected by changes in snow cover caused by the response of land surface temperatures or changes in vegetation, soil texture, and ocean roughness.

In addition to the physical rapid radiative adjustments, chemical interactions can exhibit influence on radiatively active gases, whose responses lead to an associated change of the radiative flux at TOA. These chemically induced contributions to the ERF are denoted RA_{chem} in Eq. 2.9. In this thesis chemical rapid radiative adjustments of O_3 and CH_4 are considered. In addition, chemical interactions can also affect H_2O. For instance, chemically produced stratospheric H_2O contributes to the ERF of CH_4 perturbations (Shindell et al., 2009; Winterstein et al., 2019; Thornhill et al., 2021b; O'Connor et al., 2022). This effect is included in RA_{H_2O}.

Feedbacks

The change of GSAT affects other radiatively active parameters in the Earth system. These responses can cause radiative flux changes that feed back on the resulting equilibrium response of GSAT and are called climate feedbacks. Thus, climate feedbacks determine the climate sensitivity, the magnitude of GSAT response per specified RF.

Eq. 2.6 relates the equilibrium change in GSAT to the RF. However, more generally the radiative flux imbalance at TOA, denoted as R, can be described as a function of ERF

and the current response in GSAT dT (Chapter 7 in IPCC, 2021; Forster et al., 2021):

$$dR = ERF + \alpha \cdot dT. \tag{2.10}$$

In Eq. 2.10, ERF is used to emphasize that α includes only temperature-driven climate feedbacks. Previous studies analysed the full response in simulations with coupled ocean to represent the climate response (e.g. Dietmüller et al., 2014; Rieger et al., 2017). However, if strictly following the ERF approach, the difference between the full and the fast response should be analysed as climate response. If a new equilibrium is reached (dR = 0 in Eq. 2.10), it follows that ERF = - $\alpha \cdot \Delta$T. Thus, the feedback parameter α is the negative inverse of the climate sensitivity parameter λ ($\alpha = -\frac{1}{\lambda}$) in units Watt per square meter per K (W m^{-2} K^{-1}). The feedback parameter quantifies the change of net radiative flux at TOA for a given change in GSAT. Under the assumption of linearity it can be separated into radiative contributions from individual processes affected by the change in GSAT, i.e. the individual feedback parameters α_i, so that:

$$\alpha = \frac{\partial R}{\partial T} + \sum_i \frac{\partial R}{\partial X_i} \cdot \frac{\partial X_i}{\partial T} = \frac{\partial R}{\partial T} + \sum_i \alpha_i. \tag{2.11}$$

The first part of Eq. 2.11, $\frac{\partial R}{\partial T}$, is the "Planck response". It is the change in radiative flux directly caused by the GSAT response. Therefore, it is strictly speaking not a feedback (Sherwood et al., 2015). For a positive ERF $\frac{\partial R}{\partial T}$ is always negative as the GSAT response counteracts the imposed ERF. The system is stable if $|\frac{\partial R}{\partial T}| > |\sum_i \alpha_i|$. An individual climate feedback is positive (negative) if its response to a temperature increase causes a positive (negative) radiative flux change and an associated amplification (dampening) of the temperature increase.

The processes in addition to the "Planck response" that are considered for climate feedbacks in this thesis are the same as for the rapid radiative adjustments (Eq. 2.9):

$$\sum_i \alpha_i = \alpha_{strat.\ temp.} + \alpha_{LR} + \alpha_{H_2O} + \alpha_{albedo} + \alpha_{clouds} + \alpha_{chem} \tag{2.12}$$

$\alpha_{strat.\ temp.}$ represents the radiative flux change caused by the stratospheric temperature response resulting from the GSAT response. In addition to the direct effect of the GSAT response, it can include also stratospheric temperature adjustments from the climate response of radiatively active gases such as H_2O or O_3.

The climate feedback of tropospheric H_2O, α_{H_2O}, is expected to be positive. In a warming troposphere the abundance of H_2O rises. As H_2O itself is a GHG, an increased abundance of H_2O leads to enhanced atmospheric absorption and less emission of LW radiation into space. In addition to the feedback of α_{H_2O} in the troposphere, the stratosphere is expected to moisten under climate change. This leads to a positive climate feedback of stratospheric H_2O (Banerjee et al., 2019).

As noted for the rapid radiative adjustments, the lapse rate climate feedback, α_{LR}, is anti-correlated to the tropospheric H_2O feedback α_{H_2O} (Colman and Soden, 2021). The global lapse rate feedback is expected to be dominated by the lapse rate change in the tropics. In the tropics, the upper troposphere warms more strongly than the lower troposphere leading to a less steep temperature profile and enhanced emission of LW radiation into space, and is thus a negative feedback (Chapter 7 in IPCC, 2021; Forster et al., 2021).

The surface albedo feedback, α_{albedo}, is primarily determined by changes in the extent of sea ice and snow cover. Warming leads to the decline of sea ice and snow cover, resulting generally in a reduction of the surface albedo. This means less reflection of SW radiation, which makes α_{albedo} a positive feedback. The condition of snow, e.g. influences by its age, changed vegetation and soil parameters, or ocean roughness can also contribute to surface albedo changes (Chapter 7 in IPCC, 2021; Forster et al., 2021).

Clouds affect the TOA energy budget in the LW and in the SW spectrum. As clouds have a high albedo, incoming solar radiation is reflected, which has a cooling effect on the climate system. However, clouds also absorb outgoing LW radiation, enhancing the greenhouse effect, which leads to stronger surface warming. The strength of the greenhouse effect increases with height as tropospheric temperatures decrease with height. The net climate feedback of clouds is expected to be positive (Chapter 7 in IPCC, 2021; Forster et al., 2021).

In addition to the discussed physical climate feedbacks, additional processes are affected by the change of GSAT, which subsequently perturb the radiation balance. These processes can be related to vegetation, ocean, biogeochemistry, aerosols, and gas-phase chemistry (Heinze et al., 2019). This thesis focuses on climate feedbacks from chemistry-climate interactions. O_3 and CH_4 are both reactive trace gases so that they are affected by changes in atmospheric chemistry. Also H_2O is affected by chemical interactions. As for the rapid radiative adjustments both, physically and chemically, induced changes of H_2O contribute to α_{H_2O}. Possible chemistry-climate interactions are presented in Sect. 2.4.3.

2.3 Budget of atmospheric CH_4

The atmospheric abundance of CH_4 is determined by its sources and its sinks. This section summarizes present-day emission sources of CH_4, as well as its sinks. The sink of atmospheric CH_4 is mostly via chemical degradation. The corresponding sink reactions are presented in this section. Subsequent chemical reactions and their effect on other chemical trace gases are presented in Sect. 2.4.

2.3.1 CH_4 sources

CH_4 is emitted by different processes, which can be of natural or anthropogenic origin. For the period 2008 - 2017, the total CH_4 emissions are estimated at 576 [550–594] $\times$ 10^{12} g CH_4 per year ($Tg(CH_4)$ a^{-1}) by top-down and at 737 [594–881] $Tg(CH_4)$ a^{-1} by bottom-up approaches (Saunois et al., 2020). With the top-down approach, CH_4 emissions are determined inversely from atmospheric mixing ratio measurements, whereas for bottom-up estimates individual emission contributions are summed to the global scale. Bottom-up approaches suggest that approximately half of the emissions are natural and the other half anthropogenic, whereas top-down methods estimate the anthropogenic contribution at about 60 % (Saunois et al., 2020).

Depending on the production process, the emissions are categorised into biogenic, thermogenic and pyrogenic sources. Biogenic CH_4 is produced via the decomposition of organic matter under anaerobic conditions. Natural biogenic emissions are emissions from wetlands, freshwater systems, wild animals and termites. Anthropogenic biogenic emissions come from ruminant farming, landfills and rice agriculture. The agriculture and waste sector contributes about 60 % of the total anthropogenic emissions (Saunois et al., 2020).

Thermogenic CH_4 is formed by the transformation of organic matter into fossil fuels on geological time scales. Thermogenic CH_4 is released to the atmosphere by natural leaks and by the anthropogenic exploitation of fossil fuels. The fossil fuel sector contributes about 30 % to the total anthropogenic emissions (Saunois et al., 2020).

Pyrogenic CH_4 originates from the incomplete combustion of biomass. Emissions from burning of biomass and biofuel belong to this category. The fires can be of natural origin, for instance by lightning strikes, or anthropogenically caused. Biomass and biofuel burning contribute about 10 % of the total anthropogenic CH_4 emissions (Saunois et al., 2020).

2.3.2 CH_4 sinks and lifetime

The following reactions describe the chemical decomposition of methane:

$$CH_4 + OH \longrightarrow CH_3 + H_2O \quad \text{(R 2.1)}$$

$$CH_4 + O(^1D) \longrightarrow OH + CH_3 \quad \text{(R 2.2)}$$

$$CH_4 + Cl \longrightarrow CH_3 + HCl \quad \text{(R 2.3)}$$

Additionally, CH_4 can be decomposed by photolysis

$$CH_4 + h\nu \longrightarrow \text{products} \cdot \quad \text{(R 2.4)}$$

Reactions R 2.1 to R 2.3 are from Seinfeld and Pandis (2016) and Reaction R 2.4 is from Sander et al. (2014).

The oxidation with OH (Reaction R 2.1) in the troposphere accounts for about 90 % of the total CH_4 sink (e.g. Saunois et al., 2020). Additional tropospheric sinks are the decomposition by the reaction with chlorine (Cl) (Reaction R 2.3) and soil uptake. The tropospheric reaction with Cl is estimated to account for less than 5 % of the total sink. The estimate is, however, uncertain (Gromov et al., 2018; Hossaini et al., 2016; Saunois et al., 2020). Soil uptake is caused by methanoptrophic bacteria in the soils which consume CH_4 as energy source. It is estimated to contribute about 5 % to the total sink (Saunois et al., 2020, and references therein). Chemical loss in the stratosphere accounts for another 5 % of the total sink. This represents the combined effect of the reactions with OH, Cl and excited oxygen ($O(^1D)$). The partition among individual sink partners is uncertain (Saunois et al., 2020, and references therein). Photolysis of CH_4 becomes more important above the stratosphere (Saunois et al., 2020).

The multi-model means of CCM intercomparisons suggest a tropospheric lifetime of CH_4 with respect to the oxidation with OH of about 9 years for present-day conditions. Individual models lie in the range of 7.1 - 10.6 years (Voulgarakis et al., 2013; Saunois et al., 2020). Neither the CH_4 lifetime, nor the abundance of OH can be observed directly. Therefore, estimates of the CH_4 lifetime are derived from observations of species with known emissions, whose main sink is the oxidation with OH, such as methylchloroform (CH_3CCl_3). Observational estimates of CH_3CCl_3 indicate a CH_4 lifetime of 10.2 (+0.9 \ -0.7) years (Prinn et al., 2005) and 9.1 $\pm$ 0.9 years (Prather et al., 2012). Estimates of the whole-atmosphere lifetime of CH_4 from CCM intercomparisons are 8.2 years (Voulgarakis et al.,

2013), 7.8 years (Saunois et al., 2020) and 8.4 years (Stevenson et al., 2020), whereby the latter does not account for the soil sink.

In this thesis, the CH_4 lifetime with respect to the oxidation with OH is calculated following Jöckel et al. (2016) and Frank (2018) as

$$\tau_{CH_4}(t) = \frac{\sum_{b \in B} M_{CH_4}(b,t)}{\sum_{b \in B} k_{CH_4+OH}(T(b,t)) \cdot c_{air}(T(b,t), p(b,t), q(b,t)) \cdot OH(b,t) \cdot M_{CH_4}(b,t)}, \tag{2.13}$$

where M_{CH_4} is the mass of CH_4, k_{CH_4+OH} is the reaction rate coefficient of Reaction R 2.1, c_{air} is the concentration of air and OH is the mole mixing ratio of OH in the grid box $b \in B$. B is the region, for which the lifetime should be calculated, e.g. all grid boxes below the tropopause for the mean tropospheric lifetime. Following Atkinson (2003), the reaction rate coefficient at temperature T is calculated as

$$k_{CH_4+OH}(T) = 1.85 \times 10^{-20} \cdot T^{2.82} \cdot \exp\left(-\frac{987}{T}\right). \tag{2.14}$$

2.4 Atmospheric chemistry

The troposphere and the stratosphere are different chemical regimes. Tropospheric chemistry is for instance influenced by a higher abundance of H_2O, and by anthropogenic and biogenic surface emissions. Stratospheric chemistry, on the other hand, is influenced by solar ultraviolet radiation playing a crucial role for O_3 formation. This section gives an overview of the governing gas-phase chemistry in both regimes with a focus on how the sink reactions of CH_4 affect and are affected by the chemical composition and the climate state. The chemical reactions are from Seinfeld and Pandis (2016) unless otherwise indicated.

2.4.1 Tropospheric chemistry of CH_4, OH and O_3

Basic photochemical cycle of NO_2, NO and O_3

In the troposphere, the photolysis of nitrogen dioxide (NO_2) at wavelengths < 424 nm generates free oxygen atoms, which lead to the formation of O_3:

$$NO_2 + h\nu \longrightarrow NO + O \quad \text{(R 2.5)}$$

$$O + O_2 \longrightarrow O_3 + M \quad \text{(R 2.6)}$$

O_3 has no direct emission source and Reaction R 2.6 is the only significant source of O_3 in the troposphere (Seinfeld and Pandis, 2016). O_3 reacts with nitrogen oxide (NO) to regenerate NO_2:

$$O_3 + NO \longrightarrow NO_2 + O_2 \quad \text{(R 2.7)}$$

The steady-state O_3 concentration depends on the ratio of NO_2 to NO concentration (NO_2/NO). The presented photochemical cycle is influenced by CH_4 oxidation as its products can lead to the conversion of NO into NO_2 and consequently to a higher steady-state O_3 concentration. The corresponding chemical reaction chain is explained in the following paragraph.

Products of CH_4 oxidation and effect on O_3 formation

The oxidation of CH_4 with OH (Reaction R 2.1: $CH_4 + OH \longrightarrow CH_3 + H_2O$) produces one methyl ($CH_3$) molecule, which reacts with molecular oxygen (O_2) to form methyldioxide (CH_3O_2)

$$CH_3 + O_2 + M \longrightarrow CH_3O_2 + M\,. \quad \text{(R 2.8)}$$

The formed CH_3O_2 reacts mainly with NO and hydroperoxyl (HO_2) in the troposphere. Its reaction with NO is a source of NO_2 and of the methoxy radical (CH_3O). CH_3O reacts rapidly with O_2

$$CH_3O_2 + NO \longrightarrow CH_3O + NO_2 \quad \text{(R 2.9)}$$

$$CH_3O + O_2 \longrightarrow HCHO + HO_2. \quad \text{(R 2.10)}$$

If otherwise CH_3O_2 reacts with HO_2, methylhydroperoxide (CH_3OOH) is formed. CH_3OOH is a temporary sink for the HO_x family (OH and HO_2), but HO_x can be regenerated by photolysis (Reaction R 2.12) or pathway R 2.13 b of the reaction with OH:

$$\begin{aligned}
CH_3O_2 + HO_2 &\longrightarrow CH_3OOH + O_2 && \text{(R 2.11)}\\
CH_3OOH + h\nu &\longrightarrow CH_3O + OH && \text{(R 2.12)}\\
CH_3OOH + OH &\longrightarrow H_2O + CH_3O_2 && \text{(R 2.13 a)}\\
&\longrightarrow H_2O + CH_2OOH && \text{(R 2.13 b)}\\
&\qquad\qquad \downarrow \text{fast}\\
&\qquad\qquad HCHO + OH.
\end{aligned}$$

Reactions R 2.10 and R 2.13 b both produce formaldehyde (HCHO). The two main reactions of HCHO are photolysis or the reaction with OH, which can both produce carbon monoxide (CO) and HO_2:

$$\begin{aligned}
HCHO + h\nu &\xrightarrow{O_2} 2\,HO_2 + CO && \text{(R 2.14 a)}\\
&\longrightarrow H_2 + CO && \text{(R 2.14 b)}\\
HCHO + OH &\xrightarrow{O_2} HO_2 + CO + H_2O. && \text{(R 2.15)}
\end{aligned}$$

The oxidation of CO with OH ($CO + OH \longrightarrow CO_2 + HO_2$) produces additional HO_2.

The formation of HO_2 influences the basic photochemical cycle presented in the previous paragraph as HO_2 can react with NO to form NO_2

$$HO_2 + NO \longrightarrow NO_2 + OH\ . \qquad \text{(R 2.16)}$$

This reaction produces NO_2 and leads to O_3 formation via NO_2 photolysis (Reaction R 2.5). However, for low NO concentration HO_2 favours the reaction with O_3

$$HO_2 + O_3 \longrightarrow OH + 2\,O_2\,, \qquad \text{(R 2.17)}$$

which leads to effective O_3 loss.

Theoretical maximum yield of O_3 formation from CH_4 oxidation

The maximum O_3 yield from CH_4 oxidation is obtained if Reactions R 2.9, R 2.14 a, and R 2.16 are passed trough. This pathway produces four NO_2 molecules per oxidized CH_4 molecule, thus consequently four O_3 molecules:

$$\begin{aligned}
&\text{R 2.1 :} && \mathrm{CH_4 + OH \xrightarrow{O_2} CH_3O_2 + H_2O}\\
&\text{R 2.9 :} && \mathrm{CH_3O_2 + NO \xrightarrow{O_2} HCHO + HO_2 + NO_2}\\
&\text{R 2.14 a :} && \mathrm{HCHO + h\nu \xrightarrow{O_2} CO + 2\,HO_2}\\
&\text{R 2.16 :} && \mathrm{3\,(HO_2 + NO \longrightarrow NO_2 + OH)}\\
&\text{R 2.5 :} && \mathrm{4\,(NO_2 + h\nu \xrightarrow{O_2} NO + O_3)}\\
&\text{Net:} && \mathrm{CH_4 + 8\,O_2 \longrightarrow CO + H_2O + 2\,OH + 4\,O_3}
\end{aligned}$$

In addition, the CO oxidation can contribute at most one O_3 molecule. The absolute maximum yield is, therefore, five O_3 molecules per oxidized CH_4 molecule

$$\mathrm{CH_4 + 10\,O_2 \longrightarrow CO_2 + H_2O + 2\,OH + 5\,O_3}.$$

The maximum yield is, however, not achieved in the atmosphere as there are competing reactions, e.g. for the fate of CH_3O_2 and HO_2. The partition of CH_3O_2 and HO_2 reacting with NO depends on the NO concentration.

Drivers of the hydroxyl radical (OH)

The oxidation with OH largely constrains the sink of atmospheric CH_4 (see Sect. 2.3.2). Therefore, changes of OH have an important effect on the abundance of CH_4. OH is strongly reactive and therefore short-lived. This paragraph gives information about chemical processes that influence the abundance of OH. The main source of OH is

$$\mathrm{O(^1D) + H_2O \longrightarrow 2\,OH}. \qquad \text{(R 2.18)}$$

The $O(^1D)$ originates from the photolysis of O_3 at wavelengths < 319 nm

$$O_3 + h\nu \longrightarrow O_2 + O \quad \text{(R 2.19 a)}$$
$$\longrightarrow O_2 + O(^1D). \quad \text{(R 2.19 b)}$$

Reactions R 2.18 and R 2.19 b show that H_2O, O_3 and its photolysis rate directly affect OH formation. Furthermore, processes that influence the latter also affect OH indirectly. For instance, the photolysis rate is affected by cloud cover and by stratospheric O_3 concentrations as these constrain the amount of solar ultraviolet radiation reaching the troposphere (e.g. Voulgarakis et al., 2013). Moreover, high levels of NO_x increase OH through favoured O_3 production (see previous paragraph). In addition, the abundance of H_2O in the troposphere depends on the temperature.

The temperature also affects the OH sink as the reaction rate coefficient of the CH_4 oxidation is temperature dependent (see Eq. 2.14). CH_4 oxidation consumes OH making CH_4 to an important driver of the OH abundance (Voulgarakis et al., 2013; Winterstein et al., 2019; Stevenson et al., 2020). Apart from CH_4, OH reacts with a variety of atmospheric trace gases, such as CO and non-methane hydrocarbons (NMHCs), whose atmospheric abundances feed back on OH as well (e.g. Voulgarakis et al., 2013; Gaubert et al., 2017).

2.4.2 Stratospheric chemistry of O_3

About 90 % of the total O_3 burden is in the stratosphere, in the so called O_3 layer (Seinfeld and Pandis, 2016). O_3 formation in the stratosphere starts with the photolysis of O_2 at wavelengths < 242 nm. The thereby formed oxygens atoms react with O_2 to form O_3. The photolysis of O_3 produces oxygen atoms, which rapidly regenerate O_3. Therefore, only reaction R 2.22 removes O_3 finally from the atmosphere.

$$O_2 + h\nu \longrightarrow O + O \quad \text{(R 2.20)}$$
$$O + O_2 + M \longrightarrow O_3 + M \quad \text{(R 2.21)}$$
$$O_3 + h\nu \xrightarrow{\text{R 2.19 a}} O_2 + O$$
$$\xrightarrow{\text{R 2.19 b}} O_2 + O(^1D)$$
$$O_3 + O \longrightarrow O_2 + O_2. \quad \text{(R 2.22)}$$

The photochemical cycle of O_3 formation and destruction was introduced by Chapman (1930). However, this cycle alone predicts too high stratospheric O_3 concentrations compared to observations (Seinfeld and Pandis, 2016). In addition to the Chapman cycle, catalytic cycles of radicals from the families HO_x (OH, HO_2), NO_x (NO, NO_2), ClO_x (Cl, ClO) and BrO_x (Br, BrO) contribute to stratospheric O_3 depletion.

The catalytic O_3 depletion cycles are influenced by the CH_4 abundance in the stratosphere. Firstly, CH_4 is a source of HO_x as OH is formed by Reactions R 2.2 ($CH_4 + O(^1D) \longrightarrow OH + CH_3$) and R 2.18 ($O(^1D) + H_2O \longrightarrow 2\,OH$). The oxidation of CH_4 with OH (Reaction R 2.1) is an important source of stratospheric H_2O and contributes thereby also to HO_x production. About 10 % of the OH production between 20 and 50 km is with Reaction R 2.2 and about 90 % with Reaction R 2.18 (Seinfeld and Pandis, 2016). Secondly, Reaction R 2.3 ($CH_4 + Cl \longrightarrow CH_3 + HCl$) can interrupt the ClO_x cycle as it bounds Cl in the metastable reservoir species hydrogen chloride (HCl).

2.4.3 Chemistry-climate interactions

Global warming can affect chemical interactions by different processes. Important drivers are changes of temperature, humidity, atmospheric transport and circulation, and natural emissions.

Higher temperatures directly affect chemical conversions as many reaction rate coefficients are temperature dependent. As already mentioned, the oxidation of CH_4 with OH is temperature dependent and is expected to happen faster at higher temperatures (e.g. Frank, 2018). Furthermore, the depletion of stratospheric O_3 depends on temperature as Reaction R 2.22 ($O_3 + O \longrightarrow O_2 + O_2$) is slower at lower temperatures (Rosenfield et al., 2002; Portmann and Solomon, 2007).

Warming increases the abundance of H_2O in the troposphere, which affects chemical reactions with H_2O as reaction partner. For instance, the reaction of $O(^1D)$ with H_2O (Reaction R 2.18) is expected to be more effective. This leads on the one hand side to increased production of OH (e.g. Voulgarakis et al., 2013), and is on the other hand side an enhanced sink of O_3 (e.g. Stevenson et al., 2006). Also the abundance of stratospheric H_2O is expected to increase in a warming climate (Smalley et al., 2017; Banerjee et al., 2019). The amount of H_2O that enters the stratosphere is largely determined by the cold point temperatures (Randel and Park, 2019), which are expected to increase. Larger H_2O mixing ratios in the stratosphere affect the chemical composition by enhanced production of HO_x leading to enhanced depletion of O_3.

The spatial distribution of trace gases is also influenced by transport. The stratospheric residual mean circulation transports tropospheric air upward in the tropics, then poleward and downward in middle and high latitudes. This large scale circulation is called the Brewer-Dobson circulation (Dobson et al., 1929; Brewer, 1949). Results from CCM and GCM simulations suggest that the circulation will accelerate under global warming (Butchart, 2014). A strengthening of the upward transport in the tropics, also know as tropical upwelling, transports tropospheric airmasses into the stratosphere more effectively. This has important implications for the stratospheric composition. For instance, lower stratospheric O_3 mixing ratios decrease as more O_3 depleted air from the troposphere is transported upwards. Additionally, the redistribution of trace gases within the stratosphere is affected (Butchart, 2014). Furthermore, the transport from the stratosphere into the troposphere is expected to strengthen, which will lead to enhanced transport of stratospheric O_3 into the troposphere (Abalos et al., 2020).

Additionally, natural emissions of O_3 precursor species and CH_4 depend on the climate state. Lightning NO_x emissions depend on convection and CCM simulations suggest an increase in a warming climate (Voulgarakis et al., 2013; Griffiths et al., 2021). Also biogenic emissions of NO_x and NMHCs are expected to increase (Jöckel et al., 2016). Changes of O_3 precursor emissions affect the abundance of OH and thereby the oxidation capacity of the atmosphere. Natural CH_4 emission from wetlands, marine and freshwaters, permafrost and hydrates have the potential to increase in a warming climate (O'Connor et al., 2010; Dean et al., 2018).

Chapter 3

Methods

This chapter describes the used model system (Sect. 3.1) and introduces the simulation strategy (Sect. 3.2). Further, it explains the two different methods that are used to estimate the radiative effects of individual processes (Sect. 3.3).

3.1 Model Description

In this thesis the ECHAM/MESSy Atmospheric Chemistry (EMAC; Jöckel et al. (2016)) model is used, which is a global CCM within the Modular Earth Submodel System (MESSy) framework (Jöckel et al., 2010). This section provides general information about MESSy and EMAC (Sect. 3.1.1) and it describes MESSy submodels that are important for this study in more detail (Sect. 3.1.2 - 3.1.6). In the course of this thesis, I was involved in the developments of some MESSy submodels, which are summarized in the respective sections below.

3.1.1 The Modular Earth Submodel System and the chemistry-climate model EMAC

MESSy (Jöckel et al., 2005, 2010) provides a framework to flexibly couple different components of Earth System models (ESMs). Its approach is to modularize individual processes in so-called submodels.

The submodels are connected to each other and to a basemodel via the MESSy infrastructure that consists of four conceptional software layers: the Base Model Layer (BML), the Base Model Interface Layer (BMIL), the Submodel Interface Layer (SMIL) and the

Submodel Core Layer (SMCL) (Jöckel et al., 2010). At the final developing stage, the BML should only comprise a central clock for the time integration loop and a run control for the involved processes (Jöckel et al., 2005). As an intermediate step, usually a GCM or an idealized model is used as basemodel. The BMIL is based on generic infrastructure submodels that are responsible for, e.g. data and output management (CHANNEL, TRACER), grid definition (GRID), data import (IMPORT), time management (TIMER, QTIMER), switching on/off and control of submodels (SWITCH, CONTROL), and handling of tendencies of prognostic variables (TENDENCY). The SMIL connects the specific submodels to the BMIL. Finally, the SMCL consists of the basemodel independent implementation of each specific submodel. MESSy comprises currently about 111 submodels (MESSy Consortium, 2023), which can be categorised as infrastructure submodels, atmospheric chemistry submodels, physics submodels, and diagnostic submodels.

The separation of processes allows for set-ups with variable levels of complexity by switching on and off different components of the Earth system. For instance, MESSy can be used as a CCM by switching on the chemistry-related submodels or as an Atmosphere Ocean General Circulation model (AOGCM) by coupling an ocean submodel. Further, process studies with idealized or specialized basemodels are possible. For instance, in this thesis the MESSy basemodel RAD (MBM RAD), is used for calculating the radiative transfer offline (see Sect. 3.1.5).

The EMAC model is a CCM within MESSy, which uses the 5th generation European Centre Hamburg General Circulation model (ECHAM5, Roeckner et al. (2006)) as core atmospheric model. The physics routines of ECHAM5 have been modularized and reimplemented as MESSy submodels, and further developed since (Jöckel et al., 2016). Only the spectral dynamical core, the large scale advection scheme, and the nudging routines for Newtonian relaxation are remaining in the original form of ECHAM5 (MESSy Consortium, 2023).

EMAC represents processes in the troposphere and middle stratosphere, and their interaction with ocean, land and anthropogenic influences (Jöckel et al., 2010). It can be operated at different levels of complexity using the flexible MESSy infrastructure as described above. The two basic modes are the GCM mode without interactive chemistry and the complex CCM mode using among others the Module Efficiently Calculating the Chemistry of the Atmosphere (MECCA).

In the following, the MESSy submodels related to atmospheric chemistry (MECCA, JVAL, MSBM, SCAV and CH4 for a simplified CH_4 chemistry), the mixed layer ocean

(MLO) submodel (MLOCEAN), the submodels responsible for the radiative transfer (RAD, ALBEDO, AEROPT and CLOUDOPT) and the diagnostic submodel TAGGING are described in more detail because of their particular relevance for this thesis. A table with all used submodels is provided in Appendix B.

3.1.2 Chemical processes in EMAC

The Module Efficiently Calculating the Chemistry of the Atmosphere (MECCA; Sander et al. (2019)) defines the chemical reaction mechanism used in EMAC. MECCA is a comprehensive atmospheric chemistry module for both, the troposphere and the stratosphere. It uses the kinetic preprocessor (KPP; Sandu and Sander (2006)) software for the numerical integration of the chemical kinetic system. KPP translates the chemical reactions and their reaction rate coefficients into source code for solving the set of ordinary differential equations and provides multiple solvers for the numerical integration (Sandu and Sander, 2006).

In combination with MECCA additional submodels contribute to the representation of atmospheric chemistry. JVAL (Sander et al., 2014) calculates the photolysis rate coefficients, the so-called J-values. The Multiphase Stratospheric Box Model (MSBM; Jöckel et al. (2010)) accounts for the heterogeneous chemistry on polar stratospheric clouds (PSCs) based on Kirner et al. (2011) and on stratospheric background aerosol. The submodel SCAV (Tost et al., 2006) calculates atmospheric chemistry in the aqueous phase consistently to the chemical mechanism used in MECCA. Further, it parameterizes scavenging, the removal of trace gases and aerosol particles by clouds and precipitation. The submodel DDEP (Kerkweg et al., 2006a) calculates the dry deposition of trace gases and aerosol particles in the lowermost layer.

The chemical mechanism can be compiled depending on the need of complexity. The most detailed chemical mechanism available in MECCA and SCAV is the Master Chemical Mechanism (MCM; Jenkin et al. (1997)). For global climate simulations usually a sub-set of the available chemical reactions is used.

3.1.3 Simplified CH_4 chemistry (CH4)

With the MESSy submodel CH4 (Winterstein and Jöckel, 2021) a simplified version of the CH_4 chemistry can be included in otherwise purely dynamical (GCM) set-ups. The CH4 submodel comprises a chemical mechanism that includes the sink reactions of CH_4 with

OH, O(^{1}D), and Cl, as well as the photolysis rate (see Sect. 2.3 for the sink reactions). The reactants are provided as predefined fields. Further, the production of H_2O from the CH_4 oxidation can be fed back onto the specific humidity assuming a yield of two H_2O molecules per one CH_4 molecule. Accounting for this feedback is especially important for the budget of stratospheric H_2O (e.g. Frank et al., 2018). The submodel CH4 offers additional features like the simulation of CH_4 isotopologues and the consideration of CH_4 age and emission classes as diagnostics, which are not analysed here.

3.1.4 Mixed layer ocean (MLOCEAN)

The MESSy submodel MLOCEAN (Kunze et al. (2014); original ECHAM5 code by Roeckner et al. (1995), described in the ECHAM5 documentation (Chap. 6.3 – 6.5 in Roeckner et al., 2003)) represents the ocean heat uptake with a simple mixed layer (slab) ocean model assuming a constant depth of the mixed layer (usually 50 m). Coupling a MLO model is computationally less expensive than coupling an AOGCM. However, the MLO can be used only in equilibrium time slice simulations, in which the boundary conditions are repeated cyclically each year, as the oceanic heat uptake is represented on unrealistic time scales. Using the MLO, the coupling between atmosphere and ocean is confined to the exchange of heat.

MLOCEAN calculates the SST, the ice thickness and the ice temperature for ocean grid points. It derives the temperature of the oceanic mixed layer from the net surface heat flux, which is the local sum of the SW and LW radiation fluxes, the sensible heat flux, and the latent heat flux. A flux correction, or so-called q-flux, is added to the model's current surface heat flux. The flux correction is necessary to simulate a realistic control climate as it accounts for the vertical and horizontal heat transport of the ocean (Roeckner et al., 1995). The flux correction is calculated from a monthly resolved climatology of the net surface heat flux taken from a previous simulation with prescribed (realistic) SSTs and SICs. The net TOA radiation imbalance of this simulation should be below 1 W m^{-2}.

The ice temperature is calculated similarly to the ocean temperature assuming an ice slab of 0.1 m. In the Southern Hemisphere (SH), an additional flux of 20 W m^{-2} is added to the surface heat flux to avoid massive formation of sea ice (Roeckner et al., 2003).

3.1.5 Radiative transfer in EMAC

The radiative transfer scheme determines the quantification of RF and plays therefore a crucial role for this thesis. In this section an overview of the radiation infrastructure, the used radiative transfer scheme, MESSy specific features, and the MESSy basemodel RAD (MBM RAD) are presented.

The core of the radiative transfer calculation in MESSy is the RAD submodel (Dietmüller et al., 2016; Nützel et al., 2023). For the calculation of LW and SW radiative fluxes it uses input from other MESSy submodels:

- AEROPT (Dietmüller et al., 2016; Nützel et al., 2023) prepares the aerosol optical properties (LW and SW: aerosol optical thickness; SW: single scattering albedo and asymmetry factor), which are wavelength dependent. Depending on the set-up, the aerosol optical properties are either calculated using input from the interactive aerosol scheme or are derived from imported climatologies.

- CLOUDOPT (Dietmüller et al., 2016; Nützel et al., 2023) calculates the cloud-cover, clear-sky index, and the cloud optical properties (LW and SW: optical depth; SW: asymmetry factor and single scattering albedo of cloud particles), which are wavelength dependent.

- ALBEDO (Nützel et al., 2023) calculates the surface albedo. The submodel includes the ECHAM5 based routines for the calculation of the surface albedo and a solar zenith angle dependent parameterization.

- ORBIT (Dietmüller et al., 2016) provides the orbital parameters, i.e. the solar zenith angle, the distance between the Earth and the Sun, and the relative day length.

In addition, the specific humidity, prognostic variables from the base model such as temperature and pressure, and radiatively active trace gases (CO_2, CH_4, O_3, N_2O, CFC-11 and CFC-12) are required as input for RAD. For CFC-11 a bulk tracer can be used representing the radiative impact of CFC-11 and additional hydrochlorofluorocarbons (HCFCs) that are not explicitly accounted for in the radiative transfer scheme following the method recommended by Meinshausen et al. (2017).

In RAD the routines of two radiative transfer schemes are available. To date the default scheme is a modularized version of the radiative transfer scheme of ECHAM5, called E5rad in this thesis (see Dietmüller et al. (2016) for details). In the LW a version of RRTMG (Rapid Radiative Transfer Model; Mlawer et al. (1997); Iacono et al. (2008)) is used. It

subdivides the wavelength range from 3.33 to 1000 μm into 16 bands. The SW scheme is based on the four band scheme of Fouquart and Bonnel (1980) and covers the wavelength range from 0.25 to 4 μm. CH_4 absorption is accounted for in two LW bands (band 9: 7.19 - 8.47 μm; and band 16: 3.33 - 3.85 μm) and is not accounted for in the SW range. To improve the spectral resolution in the SW range in the stratosphere and mesosphere FUBRAD (Nissen et al., 2007; Kunze et al., 2014) is available. If activated, the radiative fluxes of the first band (0.25 - 0.69 μm, UV-vis) of the Fouquart and Bonnel (1980) scheme are replaced by FUBRAD above 70 hPa. FUBRAD additionally accounts for SW heating from the absorption by O_2 and O_3 at wavelengths shorter than 0.25 μm (Dietmüller et al., 2016).

E5rad underestimates the direct RF of CH_4 (Winterstein et al., 2019; Nützel et al., 2023), which is one reason for which an additional radiative transfer scheme, PSrad (Pincus and Stevens, 2013) was implemented into the MESSy system. In the framework of this thesis I contributed to the implementation (mainly to the submodels AEROPT and ALBEDO) and performed simulations for the tuning and evaluation of the GCM set-up with PSrad. Details about the implementation, tuning and evaluation of PSrad in EMAC are summarized by Nützel et al. (2023). PSrad is based on RRTMG in the LW, as well as in the SW range. In the LW it covers the wavelength range from 3.08 to 1000 μm in 16 bands, and in the SW the wavelength range from 0.2 to 12.2 μm in 14 bands. CH_4 absorption is accounted for in two LW bands (band 9: 7.19 - 8.47 μm; and band 16: 3.08 - 3.85 μm) and two SW bands (band 1: 3.08 - 3.85 μm; and band 3: 2.15 - 2.50 μm). With PSrad the representation of the direct RF of CH_4 is improved (Nützel et al., 2023).

The available radiative transfer schemes make use of some simplifications so that they can be used in GCM simulations. In the LW spectrum scattering is neglected (Roeckner et al., 2003; Pincus and Stevens, 2013). In addition, RRTMG uses the correlated k-approach (Mlawer et al., 1997), which is a method to reduce the computational costs while keeping sufficient accuracy. The spectral absorption coefficient $k(\lambda)$ varies irregularly with wavelength. Therefore, using a simple average of the absorption coefficient k for a broad wavelength band would introduce errors. Following Mlawer et al. (1997) the principle of the correlated k-approach is to rearrange the absorption coefficient k in ascending order, which gives a smoothly varying function of k. More precisely, one specific k is mapped to the fraction of the absorption coefficients in the wavelength band smaller than k, which is usually referred to as g, so that $g(k)$ can be interpreted as the cumulated probability function. The function $k(g)$ can be split into subintervals, usually called g-points, with a

representative constant value of the absorption coefficient, which is used for the radiative transfer in the subinterval. The resulting spectral intensities for each g-point weighted with the sizes of their subintervals are summed up to give an representative intensity for the whole wavelength band. "Correlated" in this context refers to the fact that the mapping from wavelength space to g space is the same for all atmospheric layers (Mlawer et al., 1997). Furthermore, to infer broadband radiation fluxes, the intensities would have to be integrated over the solid angle of one hemisphere (see also Sect. 2.1). For the LW and the diffuse part of the SW spectrum, i.e. the part not directly coming from the Sun, the diffusivity approximation is used for E5rad (Roeckner et al., 2003). This means that the dependence of the intensity on the zenith angle is approximated by the multiplication of the optical thickness by a factor of 1.66, which corresponds to a representative zenith angle of 53° ($1.66 = \frac{1}{cos(53°)}$, Mlawer et al., 1997). For the LW part of PSrad a similar approach is used. The diffusivity factor, however, varies between 1.5 and 1.8, depending on the wavelength band and on the total column water to improve accuracy (see RRTMG website; RRTMG (2023)).

From the divergence of radiative fluxes, the radiative temperature tendencies are calculated, which are fed back to the basemodel. In addition to the prognostic calculation of the radiative temperature tendency, RAD offers the option for diagnostic radiation calls (Dietmüller et al., 2016). This option can be used to quantify the radiative effects of the perturbations of individual parameters, e.g. the mixing ratios of radiatively active trace gases, in the same simulation. Furthermore, the diagnostic radiation calls can be used with the option of stratospheric temperature adjustment, which is explained in the next paragraph.

Stratospheric temperature adjustment in MESSy

MESSy offers the option to include stratospheric temperature adjustment in diagnostic radiation calls (Stuber et al., 2001). This means that RF_{adj} (see Sect. 2.2) can be calculated directly for all diagnostic radiation calls.

The technical implementation is explained by Stuber et al. (2001). Following an imposed perturbation, the temperatures in the stratosphere adjust quickly so that a new radiative equilibrium is formed. Temperatures in the troposphere remain thereby unchanged. This can be formulated as

$$\frac{dT^\star}{dt} = \left.\frac{dT^\star}{dt}\right|_{dyn} + \left.\frac{dT^\star}{dt}\right|_{rad} = 0 \text{ (stratosphere)} \tag{3.1}$$

$$T^\star = T \text{ (troposphere)}, \tag{3.2}$$

whereby the temperature $T^\star$ describes the state after stratospheric temperatures have adjusted to a new radiative equilibrium and tropospheric temperatures equal the unperturbed temperature T. The temperature tendency can be divided into a radiatively and a dynamically driven part. Following the fixed dynamical heating concept (Fels et al., 1980) the dynamic heating rates are assumed to remain unchanged, therefore

$$\left.\frac{dT^\star}{dt}\right|_{dyn} = \left.\frac{dT}{dt}\right|_{dyn}. \tag{3.3}$$

Eq. 3.3 can be substituted into Eq. 3.1

$$\frac{dT^\star}{dt} = \left.\frac{dT}{dt}\right|_{dyn} + \left.\frac{dT^\star}{dt}\right|_{rad}, \tag{3.4}$$

whereby the dynamic heating rates are calculated from the total temperature tendency and the radiative heating of the unperturbed radiation call

$$\left.\frac{dT}{dt}\right|_{dyn} = \frac{dT}{dt} - \left.\frac{dT}{dt}\right|_{rad}. \tag{3.5}$$

Eq. 3.4 does not assume a stationary equilibrium state, but a quasi-stationary evolving state of stratospheric temperatures, meaning that the adjusted stratospheric temperatures develop in accordance to the seasonal cycle and to the evolution of the perturbation (Stuber et al., 2001). As the stratospheric temperatures adjust to the quasi-stationary equilibrium iteratively, a spin-up might be required. The method requires the use of a tropopause definition, which is constant in time, as otherwise the domain, in which the stratospheric temperature adjustment is applied, changes (Stuber et al., 2001).

MESSy basemodel RAD (MBM RAD)

MBM RAD offers the possibility to calculate the MESSy radiation offline. The radiative transfer calculation is fully consistent with the scheme that is used in online simulations, i.e.

coupled to a dynamical core. Moreover, MBM RAD can be operated with both radiative transfer schemes that are currently implemented in MESSy, namely the default ECHAM5 scheme E5rad and PSrad. The infrastucture of MBM RAD was extended in the course of this thesis to be compatible with PSrad.

MBM RAD makes use of the submodels AEROPT, ALBEDO, CLOUDOPT, ORBIT and RAD. The use of the submodels AEROPT, ALBEDO and CLOUDOPT is optional as they are not required if either the aerosol optical properties, the surface albedos, or the cloud optical properties, respectively, of a previous EMAC simulation are used directly as import for the radiation calculation. All prognostic model variables that are necessary for the radiation calculation, such as e.g. the temperature, have to be provided as input for MBM RAD (see Tab. A.1 in the Appendix for an overview).

MBM RAD can be operated in two-dimensional mode using zonal means or in three-dimensional mode. In the three-dimensional case the horizontal grid equals the ECHAM5 grid, i.e. a quadratic Gaussian grid. In the vertical, the ECHAM5 hybrid vertical coordinate system or constant pressure levels can be used. Appendix A.2 shows how the grid of MBM RAD can be defined.

If the correct variables from a previous EMAC simulation are imported in double precision, and if the native EMAC model grid is used, MBM RAD reproduces the radiative fluxes of a previous EMAC simulation, regardless of which radiation scheme is used. This holds whether the cloud and aerosol optical properties are calculated online with CLOUDOPT and AEROPT, or whether they are provided as input from the EMAC simulation.

However, for the calculation of feedbacks of a multi-year EMAC simulation, it is not feasible to provide the output of the data required for each radiation time step of the EMAC simulation as the radiation is usually calculated every 36 minutes. Instead, a frequency of one radiation call every 5 to 10 hours is used for the calculation of feedbacks (Rieger et al., 2017). To analyse this potential sampling error, test simulations of 1 year were performed with EMAC, in which in the radiation was called every 36 minutes, for both radiative transfer schemes, E5rad and PSrad. Subsequently, the radiation was recalculated with MBM RAD with a frequency of one radiation calculation every 5 or 10 hours. The mean difference of the net TOA radiation budget between EMAC and MBM RAD is 0.002 W m^{-2} and -0.011 W m^{-2} for frequencies of the radiation calculation of 5 and 10 hours, respectively, with E5rad, and 0.083 W m^{-2} and 0.069 W m^{-2} with PSrad. The corresponding TOA radiative fluxes and a more detailed discussion are provided in Appendix A.3.

3.1.6 O_3 contributions (TAGGING)

The TAGGING method (Grewe et al., 2017; Rieger et al., 2018) quantifies the contributions of individual source categories to the mixing ratios of tagged tracers. Tagged tracers are O_3, CO, reactive nitrogen compounds (NO_y), peroxyacyl nitrate (PAN), NMHCs, OH, and HO_2. For these species or families of species the individual contributions of emission categories or source processes are calculated. Usually, the following 10 categories are considered: emissions from road traffic, shipping, aviation, anthropogenic non-traffic emissions (from e.g. industry), biogenic emissions, emissions of lightning NO_x, products of the chemical decomposition of N_2O, products of the chemical decomposition of CH_4, and stratospheric O_3 production by photolysis of O_2.

The tagged tracers (i.e. the individual contributions) undergo the same processes as the corresponding total species. These are transport, emissions, dry and wet deposition, and chemical production and loss (see Grewe et al. (2017) for details). For the short-lived species OH and HO_2 a steady-state between chemical production and loss is assumed (Rieger et al., 2017). The chemical reaction rates are derived from MECCA. Effective production and loss is taken into account for O_3, meaning that production and loss terms from a family, which includes all fast exchanges between O_3 and other chemical species, are considered. The tool *ProdLoss* (Grewe et al., 2017) is used to identify all reactions that contribute to effective O_3 production and loss in the applied chemical mechanism.

The reaction rates of effective O_3 production and loss are manually grouped into O_3 production and loss rates, depending on which tagged species contributes to O_3 production or loss. For a more complete assignment of the O_3 production rates of the chemical mechanism used for the EMAC simulations performed for phase 2 of the Chemistry Climate Model Initiative (CCMI, CCMI, 2023), additional O_3 production rates were introduced in the course of this thesis (see Tab. 3.1[1]). Using this definition, it is possible to assign all O_3 producing reactions, except 8, which are summarized in Tab. 3.2. These 8 reactions are grouped into *o3prod_untagged* for diagnostic output and are not directly included in the TAGGING. However, it is ensured that the sum of all O_3 categories equals the total O_3 tracer from MECCA. This means that the O_3 production through the latter 8 reactions is distributed over all categories. As a result of the modified grouping, O_3 production (Eq.

[1]The grouping is done in the diagtrac file *CCMI2-base-01-tagHOxstrato.tex*, which is available as part of the MESSy distribution.

13 by Grewe et al. (2017)) is now calculated as

$$\begin{aligned} P\_O_3 \;=\;& o3prod\_ho2 \cdot \frac{HO_2^{tag}}{HO_2} \\ &+ o3prod\_oh \cdot \frac{OH^{tag}}{OH} \\ &+ o3prod\_noy \cdot \frac{NO_y^{tag}}{NO_y} \\ &+ \frac{1}{2} \cdot o3prod\_ho2noy \cdot (\frac{HO_2^{tag}}{HO_2} + \frac{NO_y^{tag}}{NO_y}) \\ &+ \frac{1}{2} \cdot o3prod\_ohnoy \cdot (\frac{OH^{tag}}{OH} + \frac{NO_y^{tag}}{NO_y}) \\ &+ \frac{1}{2} \cdot o3prod\_ho2nmhc \cdot (\frac{HO_2^{tag}}{HO_2} + \frac{NMHC^{tag}}{NMHC}) \\ &+ \frac{1}{2} \cdot o3prod\_ro2 \cdot (\frac{NMHC^{tag}}{NMHC} + \frac{NO_y^{tag}}{NO_y}). \end{aligned} \tag{3.6}$$

The calculation of O_3 loss remains unchanged (Eq. 14 by Grewe et al. (2017)) as

$$\begin{aligned} D\_O_3 \;=\;& \frac{1}{2} \cdot o3loss\_oh \cdot (\frac{OH^{tag}}{OH} + \frac{O_3^{tag}}{O_3}) \\ &+ \frac{1}{2} \cdot o3loss\_ho2 \cdot (\frac{HO_2^{tag}}{HO_2} + \frac{O_3^{tag}}{O_3}) \\ &+ \frac{1}{2} \cdot o3loss\_no \cdot (\frac{NO_y^{tag}}{NO_y} + \frac{O_3^{tag}}{O_3}) \\ &+ \frac{1}{2} \cdot o3loss\_ro \cdot (\frac{NMHC^{tag}}{NMHC} + \frac{O_3^{tag}}{O_3}) \\ &+ o3loss\_xo \cdot \frac{O_3^{tag}}{O_3}. \end{aligned} \tag{3.7}$$

A second modification is the inclusion of the species ethyne (C_2H_2) to the NMHC family for the TAGGING if C_2H_2 is present in the used chemical mechanism. C_2H_2 was added to the chemical mechanism for phase 2 of CCMI and is emitted by the sectors biomass burning, anthropogenic non-traffic, shipping, and road traffic. The TAGGING of OH and HO_2 (Rieger et al., 2018) remains unchanged.

Table 3.1: Overview of grouping of chemical reactions into O_3 production and loss rates. Multiple chemical reactions can be combined into one production or loss rate because tracer families are considered for O_3, NO_y and NMHCs.

O_3 loss rates	Species contributing to O_3 loss
o3loss_oh	OH + O_3 combination
o3loss_ho2	HO_2 + O_3 combination
o3loss_no	NO_y + O_3 combination
o3loss_ro	NMHC + O_3 combination
o3loss_xo	O_3 (+ untagged species)
O_3 production rates	**Species contributing to O_3 production**
o3prod_o2	O_2 photolysis
o3prod_ho2[1]	HO_2
o3prod_oh[2]	OH
o3prod_noy[2]	NO_y
o3prod_ho2noy[2]	HO_2 and NO_y combination
o3prod_ohnoy[2]	OH and NO_y combination
o3prod_ho2nmhc[2]	HO_2 and NMHC combination
o3prod_ro2	NMHC and NO_y combination
o3prod_untagged	untagged species (all remaining reactions causing O_3 production)

[1] Former definition of *o3prod_ho2*: O_3 production from HO_2/OH and NO_y combination.

[2] Added O_3 production rate to TAGGING mechanism.

Table 3.2: Overview of chemical reactions that lead to effective O_3 production, but are not grouped into O_3 production rates with tagged species. O_3 production through these reactions is summarized in *o3prod_untagged* for diagnostic information (see Tab. 3.1).

MECCA reaction number	Reaction
G9600	$DMS + Cl \longrightarrow CH_3SO_2 + HCl + HCHO$
G9700	$DMS + Br \longrightarrow CH_3SO_2 + HBr + HCHO$
J4102	$CO_2 + h\nu \longrightarrow CO + O_3P$
J6101	$OClO + h\nu \longrightarrow ClO + O_3P$
J6300	$ClNO_2 + h\nu \longrightarrow Cl + NO_2$
J7300	$BrNO_2 + h\nu \longrightarrow Br + NO_2$
G9100	$SO + O_2 \longrightarrow SO_2 + O_3P$
G9102	$S + O_2 \longrightarrow SO + O_3P$

3.2 Simulation strategy

This thesis investigates the role of chemical-climate feedbacks caused by the sink of atmospheric CH_4 in CCM simulations perturbed by either CO_2 or CH_4 increase. To separate the effect of rapid radiative adjustments from slow climate feedbacks, two different types of CCM simulations are performed, either with predefined fixed SSTs, or with variable SSTs adapting to the climate change (suffix SSTfix or SSTvar, respectively). In addition, simulations with prescribed chemical tracer distributions are performed to isolate the effect of interactive chemistry on the climate sensitivity (suffix nochem). This section provides an overview of the performed simulations and the used boundary condition data for CH_4 and other species.

3.2.1 Outline of simulations

All simulations are conducted with EMAC (MESSy version d2.55.2[2]) at a resolution of T42L90MA, corresponding to a quadratic Gaussian grid of approximately 2.8° × 2.8° resolution in latitude and longitude, and 90 vertical levels with the uppermost level centred around 0.01 hPa. Further, all simulations are time slices, meaning that the boundary conditions and emission fluxes are repeated cyclically each year to obtain a statistical distribution of the climate state. The quasi-biennial oscillation (QBO) is nudged following the method of Giorgetta and Bengtsson (1999) as described by Jöckel et al. (2016), which introduces some interannual variability. An equilibrium period of 20 years is used for the analysis.

Table 3.3 lists all simulations that are analysed in the present study. The three simulations $REF^{SSTfix}{}_{chem}$, $REF^{SSTvar}{}_{chem}$ and $REF^{SSTvar}{}_{nochem}$ serve as references for the experiment simulations and represent present-day (year 2010) conditions. The reference set-up is based on Winterstein et al. (2019) and Stecher et al. (2021) with the important difference that surface emissions of CH_4 instead of prescribed mixing ratios are used. More information about the used boundary conditions for CH_4 and O_3 precursors is given below. The experiment simulations are perturbed by either increased CO_2 mixing ratios or increased CH_4 surface emissions. For both perturbation agents the following three different types of experiment simulations exist:

1. $ERFCO_2{}^{SSTfix}{}_{chem}$ and $ERFCH_4{}^{SSTfix}{}_{chem}$ are performed with prescribed SSTs and SICs to quantify the ERF and the rapid radiative adjustments following the fixed

[2]Git commit: e53681a26278955ce1071652c2921080a0b4df40

SST method (e.g. Forster et al., 2016). The prescribed multi-year monthly mean climatology of SSTs is an observational estimate of the years 2000 to 2009 from the Met Office Hadley Center (Rayner et al., 2003). The same climatology was used by Winterstein et al. (2019).

The perturbations of CO_2 and CH_4 are scaled to result in ERFs of similar magnitude. To assess the climate sensitivity of different perturbation agents, the respective forcings need to be at the same order of magnitude as the climate sensitivity can be dependent on the magnitude of the forcing (e.g. Dietmüller et al., 2014). The targeted ERF is at around 1.5 W m^{-2}, which should be large enough to cause significant and interpretable feedbacks (Forster et al., 2016), and small enough to be reached with realistically large perturbations of CO_2 and CH_4 (Dietmüller et al., 2014; Winterstein et al., 2019). Perturbations of 1.35×CO_2 mixing ratios and 2.75×CH_4 surface emissions result in ERFs of 1.609±0.154 W m^{-2} and 1.722±0.173 W m^{-2}, respectively (see Tab. 3.3). The scaling of 1.35×CO_2 mixing ratios or 2.75×CH_4 surface emissions are applied to all CO_2 and CH_4 perturbation experiments, respectively.

2. ECCC$CO_2$$^{\mathrm{SSTvar}}_{\mathrm{chem}}$ and ECCC$CH_4$$^{\mathrm{SSTvar}}_{\mathrm{chem}}$ are so-called equilibrium climate change simulations. In these simulations the MLO model (MESSy submodel MLOCEAN, see Sect. 3.1.4) accounts for the response of SSTs and SICs. From these simulations the climate sensitivity and the slow climate feedbacks can be assessed.

   The first two sets of simulations are performed with interactive chemistry using the MESSy submodel MECCA (denoted by suffix chem; see Sect. 3.1.2 for more information). The chemical mechanism used for for this study follows the MIM1 mechanism as used in the ESCiMo project (Jöckel et al., 2016). It covers the basic chemistry of O_3, CH_4, OH, HO_2, nitrogen oxides, alkanes and alkenes up to four C-atoms, and isoprene (C_5H_8). Further, halogen chemistry of bromine and chlorine species is included. Alkynes, aromatics and mercury are not considered. In total, the used mechanism covers 265 gas-phase, 82 photolysis and 12 heterogeneous reactions for 160 species.[3] In addition, the submodel SCAV (see Sect. 3.1.2) simulates the exchange between the gas and aqueous phase in clouds, aqueous phase chemistry, and subsequent wet deposition. Interactive chemistry-aerosol coupling is not included in this set-up. Prescribed aerosol surface concentrations are used for the calculation of heterogeneous chemical reactions as explained by Jöckel et al. (2016). Similarly,

[3]The chemical mechanism is created using the batch file CCMI2-base-01-tag.bat. It is the same chemical mechanism as CCMI2-base-01.bat with additional diagnostics for the TAGGING method.

climatologies of aerosol optical properties are prescribed for the radiation calculation. A combination of the tropospheric Tanre et al. (1984) climatology and stratospheric aerosol data from CCMI are used following Jöckel et al. (2016).

3. $ECCCO_2{}^{SSTvar}{}_{nochem}$ and $ECCCH_4{}^{SSTvar}{}_{nochem}$ are performed with the MLO model to account for tropospheric warming, but without interactive chemistry. In these simulations monthly climatologies of CH_4, CO_2, O_3, N_2O and the chlorofluorocarbons (CFCs) from $ERFCO_2{}^{SSTfix}{}_{chem}$ and $ERFCH_4{}^{SSTfix}{}_{chem}$, respectively, are prescribed. In these simulations physical climate feedbacks can evolve, whereas chemical climate feedbacks are suppressed. However, the effect of CH_4 oxidation on H_2O is accounted for via the MESSy submodel CH4 (see Sect. 3.1.3) to have a realistic distribution of stratospheric H_2O. Therefore, a climate feedback via the temperature dependent reaction rate coefficient of the CH_4 oxidation on stratospheric H_2O is possible. However, the isolated effect of the temperature response on H_2O production has been found to be negligible.

   As the chemical tracer distributions from the respective ERF experiments (and not from the reference) are prescribed, the effect of chemical rapid radiative adjustments is included in these simulations. Therefore, the comparison of $ECCCO_2{}^{SSTvar}{}_{chem}$ with $ECCCO_2{}^{SSTvar}{}_{nochem}$ and $ECCCH_4{}^{SSTvar}{}_{chem}$ with $ECCCH_4{}^{SSTvar}{}_{nochem}$ isolates the climate effect of interactive chemistry.

$REF^{SSTfix}{}_{chem}$ provides the flux correction for all MLO simulations (see Sect. 3.1.4 for an explanation of the method). The TOA imbalance in this simulation is -0.16 W m^{-2} (see Tab. 3.4) and thus sufficiently low.[4]

An essential feature of the simulation set-up is the use of CH_4 emission fluxes instead of prescribed CH_4 mixing ratios at the lower boundary for the simulations with interactive chemistry. This means that changes in the chemical sink can feed back onto the atmospheric CH_4 mixing ratios without constraints. The following section (Sect. 3.2.2) provides more information on the used CH_4 surface emission fluxes. As additional diagnostic, the submodel TAGGING (see Sect. 3.1.6) is used in the simulations with interactive chemistry to attribute O_3 changes to individual processes.

[4]For tuning the TOA radiation balance a time filter correction was re-introduced to the CLOUD submodel, which means that the temperature, specific humidity, cloud water and cloud ice from the current model time step are used, instead of from the time step before. This option was also active for the EMAC simulations performed for phase 1 of CCMI (Jöckel et al., 2016) and for the simulations analysed by Winterstein et al. (2019) and Stecher et al. (2021).

Table 3.3: Overview of performed simulations. REF indicates that the respective reference is used, which is 388.4 ppmv for the global mean surface mixing ratio of CO_2, and 625.3 Tg(CH_4) a^{-1} for the CH_4 surface emissions. For the ERF estimates the 95% uncertainty range is given as 2× the standard error based on 20 annual mean values.

simulation name	SST + SIC	chemical set-up	CO_2 VMR	CH_4 emissions	ERF [W m^{-2}]
$REF^{SSTfix}{}_{chem}$	prescribed	MECCA	REF	REF	-
$REF^{SSTvar}{}_{chem}$	MLO	MECCA	REF	REF	-
$REF^{SSTvar}{}_{nochem}$	MLO	prescribed from $REF^{SSTfix}{}_{chem}$	REF	REF	-
$ERFCO_2{}^{SSTfix}{}_{chem}$	prescribed	MECCA	×1.35	REF	1.609±0.154
$ECCCO_2{}^{SSTvar}{}_{chem}$	MLO	MECCA	×1.35	REF	-
$ECCCO_2{}^{SSTvar}{}_{nochem}$	MLO	prescribed from $ERFCO_2{}^{SSTfix}{}_{chem}$	×1.35	REF	-
$ERFCH_4{}^{SSTfix}{}_{chem}$	prescribed	MECCA	REF	×2.75	1.722±0.173
$ECCCH_4{}^{SSTvar}{}_{chem}$	MLO	MECCA	REF	×2.75	-
$ECCCH_4{}^{SSTvar}{}_{nochem}$	MLO	prescribed from $ERFCH_4{}^{SSTfix}{}_{chem}$	REF	×2.75	-

In addition to the online EMAC simulations, offline radiation calculations with MBM RAD (see Sect. 3.1.5) and additional EMAC atmosphere-only simulations are performed to quantify individual rapid radiative adjustments and slow climate feedbacks (see Sect. 3.3 for an explanation of the methods).

3.2.2 Boundary conditions of CH_4

The simulations with interactive chemistry use CH_4 surface emission fluxes instead of prescribed CH_4 surface mixing ratios. This section provides information about the background, the spatial distribution and magnitude of the used CH_4 emission fluxes, as well as the treatment of the CH_4 sink.

In a simulation set-up with CH_4 emissions, the CH_4 mixing ratios adjust depending on the one hand on the magnitude of the emissions, and on the other hand on the atmospheric lifetime of CH_4. The atmospheric lifetime of CH_4 is sensitive to many factors, e.g. the cloud parameterization scheme (hydrological cycle), the production of NO_x from lightning,

Table 3.4: Overview of global mean parameters of the three reference simulations: TOA net radiation imbalance, 2m air temperature, tropospheric CH_4 lifetime corresponding to the oxidation with OH, CH_4 volume mixing ratio in the lowermost layer, as well as online calculated emissions of lighting NO_x and biogenic NO_x and C_5H_8. The corresponding interannual standard deviation based on 20 annual mean values is given to estimate the year to year variability.

		$REF^{SSTfix}{}_{chem}$	$REF^{SSTvar}{}_{chem}$	$REF^{SSTvar}{}_{nochem}$
TOA rad. imbalance	[W m^{-2}]	-0.16 ± 0.26	-0.33 ± 0.25	-0.47 ± 0.28
2 m air temperature	[K]	288.02 ± 0.03	288.21 ± 0.06	287.63 ± 0.06
Trop. CH_4 lifetime	[a]	7.59 ± 0.03	7.58 ± 0.03	-
CH_4 surface VMR	[ppmv]	1.82 ± 0.00	1.82 ± 0.00	1.82
Lightning NO_x	[Tg(N) a^{-1}]	5.24 ± 0.12	5.25 ± 0.08	-
Biogenic NO_x	[Tg(N) a^{-1}]	5.99 ± 0.02	5.99 ± 0.03	-
Biogenic C_5H_8	[Tg(C) a^{-1}]	512.4 ± 5.3	510.4 ± 6.6	-

and temperature, and is therefore dependent on the configuration of the used CCM set-up (Frank, 2018; Voulgarakis et al., 2013). If the CH_4 emission inventory is not consistent with the CH_4 lifetime, the mixing ratios might not be realistic. To overcome this problem Frank (2018) provides an inverse optimized CH_4 emission inventory using a fixed-lag Kalman Filter that is consistent with the EMAC model. This so-called a posteriori CH_4 surface emission inventory is used in this study.

For the used set-up, the CH_4 emissions of the year 2010 are cyclically repeated each year and globally scaled by a factor of 1.08 corresponding to total CH_4 emissions of 625.3 Tg(CH_4) a^{-1}. The scaling was applied to bring the simulated CH_4 surface mixing ratios closer to observations. As the tropospheric mean CH_4 lifetime is about 10 years (e.g. Prather et al., 2012; Stevenson et al., 2022), the CH_4 mixing ratios of the year 2010 result not only from CH_4 emissions of the year 2010, but also from emissions of the years before. Therefore, it is not expected that the cyclic repetition of CH_4 emissions of the year 2010 will result in CH_4 mixing ratios that represent the year 2010 exactly. Applying the scaling, the resulting global mean CH_4 surface mixing ratio is 1.82 parts per million volume (ppmv) for all reference simulations (see Tab. 3.4). This is in close agreement with observational estimates for the years 2010 and 2012 of 1.80 and 1.81 ppmv by NOAA/ESRL (Lan et al., 2023), and 1.81 and 1.82 ppmv by the WMO World Data Centre for Greenhouse Gases (WMO, 2022). The estimates of NOAA/ESRL tend to be lower as only unpolluted marine surface sites contribute to the global estimate.

The total emissions of 625.3 Tg(CH_4) a^{-1} correspond well with bottom-up estimates for

Table 3.5: Global CH_4 emissions as prescribed in the reference simulations in [Tg(CH_4) a^{-1}].

Natural sources		Anthropogenic sources		Total sources	
wetlands	169.5	other	340.0		
other	44.2	rice	45.6		
wild animals	5.7	biomass burning	26.0		
	27.2				
volcanoes	3.2				
ocean	8.1				
Total natural	213.6	Total anthropogenic	411.6	Total	625.3

the period 2000–2017, but are larger than the corresponding top-down estimates (Saunois et al., 2020, see also Sect. 2.3). About 66% of the emissions are of anthropogenic origin (including biomass burning) and about 34% are of natural origin (see Tab. 3.5). Figure 3.1 shows the spatial distribution of the used CH_4 emission fluxes. The CH_4 emission fluxes remain unchanged in the course of the simulation. In particular, this set-up does not allow for climate feedbacks of natural CH_4 emission fluxes of e.g. wetlands or permafrost.

The chemical sink reactions of CH_4 with OH, $O(^1D)$ and Cl, and CH_4 photolysis are interactively accounted for by the submodel MECCA (see Sect. 3.1.2). In addition, the soil sink of CH_4 is included by the submodel DDEP, which uses a prescribed deposition rate (Spahni et al., 2011; Curry, 2007) that is scaled to the current CH_4 mixing ratios in the corresponding grid box. On average, the global soil sink is 27.65 Tg(CH_4) a^{-1} in the reference simulation $REF^{SSTfix}{}_{chem}$.

For the CH_4 perturbation experiments the surface emissions are scaled by a global mean factor of 2.75. The perturbation experiment $ERFCH_4{}^{SSTfix}{}_{chem}$ is initialized with the CH_4 mixing ratios of $REF^{SSTfix}{}_{chem}$ scaled by a factor of 2.75 to save computational resources. Subsequently, the CH_4 mixing ratios adjust in correspondence with the CH_4 lifetime. A discussion about the spin-up of the mass of CH_4 in $ERFCH_4{}^{SSTfix}{}_{chem}$ is given in Appendix D.

3.2.3 Boundary conditions of O_3 precursors

Precursor emissions of O_3, in particular NO_x, NMHCs and CO, have an important effect on OH and the CH_4 lifetime (e.g. Stevenson et al., 2013, 2020; Acquah, 2023). In the sim-

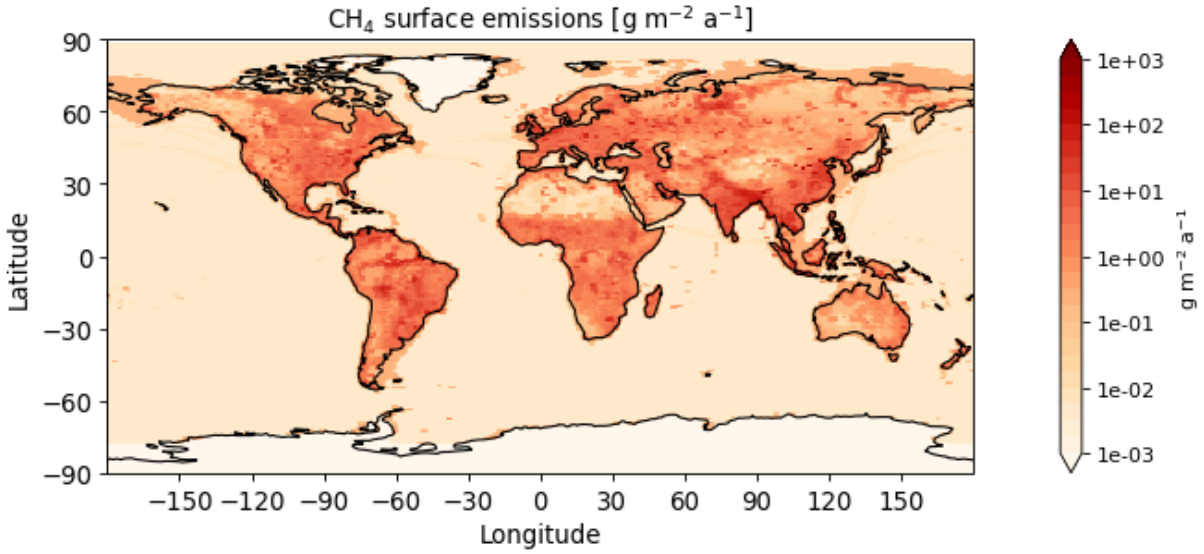

Figure 3.1: Spatial distributions of annual mean CH_4 emissions in [g m^{-2} a^{-1}] as used for the reference simulations. The CH_4 emissions are based on the inverse optimized emission inventory provided by Frank (2018). The colour levels are logarithmically spaced.

ulations with interactive chemistry O_3 precursor emissions are included similarly as in the EMAC simulations performed for the first phase of CCMI (Jöckel et al., 2016). Anthropogenic emissions of the MACCity inventory (Lamarque et al., 2010; Granier et al., 2011; Diehl et al., 2012) are prescribed, whereby the emissions of the year 2010 are repeated cyclically. In addition, a climatology of biogenic emissions of NMHCs and CO are prescribed from the Global Emissions InitiAtive (GEIA) as described by Jöckel et al. (2016).

Natural emissions of NO_x from lightning, NO_x and C_5H_8 from biogenic sources, as well as the exchange of chemical species between atmosphere and ocean are parameterized. For lightning NO_x the parameterization of Grewe et al. (2001) is used in the submodel LNOX (Tost et al., 2007). The total emissions from lightning NO_x are approximately 5.2 Tg(N) a^{-1} for both reference simulations with interactive chemistry (see Tab. 3.4). Interactive biogenic emissions of soil NO_x and C_5H_8 are calculated by the submodel ONEMIS (Kerkweg et al., 2006b). On average, biogenic NO_x emissions are approximately 6 Tg(N) a^{-1} and biogenic C_5H_8 emissions are 510 Tg(C) a^{-1} for both reference simulations (see Tab. 3.4). The atmosphere-ocean exchange of the chemical species C_5H_8, dimethyl sulfide (DMS) and methanol (CH_3OH) is parameterized using the submodel AIRSEA (Pozzer et al., 2006).

3.3 Adjustment and feedback analysis

An important part of this study is the quantification of individual radiative contributions to assess their importance for the ERF and the climate sensitivity. Two different methods are applied, which are introduced in this section. The first one is the Partial Radiative Perturbation (PRP) method (e.g. Colman and McAvaney, 1997; Rieger et al., 2017) and the second uses multiple diagnostic radiation calls in atmosphere-only EMAC simulations with the option to calculate stratospheric temperature adjustment (e.g. Dietmüller et al., 2016; Winterstein et al., 2019; Stecher et al., 2021). Both methods rely on the assumption that individual contributions to the ERF and the feedback parameter are separable (see Sect. 2.2). Another method for calculating individual radiative contributions would be by using radiative kernels (e.g. Soden et al., 2008), which is, however, not used here.

3.3.1 Partial Radiative Perturbation method

The PRP method can be used to estimate the radiative contribution of individual adjustment and feedback processes from the output of pairs of global climate model simulations. These pairs consist of a reference simulation and a perturbed experiment simulation, either with prescribed SSTs and SICs to assess rapid radiative adjustments, or with interactive ocean to assess the full response. The corresponding climate feedbacks are defined as the difference between the full response and the rapid radiative adjustments. The principle of the PRP method is to re-calculate a subset of the radiation calls of the online simulations perturbed by individual parameters offline. Therefore, all model variables that are necessary for the re-calculation of the radiation need to be stored as instantaneous output on the native model grid with an output frequency corresponding to the targeted radiation calculation frequency of the PRP method (see Appendix A for a list of required variables for the MESSy radiation). Only a subset of the radiation calls of the online simulations can be re-calculated due to computational and data storage constraints. In this study, the offline radiative transfer calculations for the PRP method are calculated every 10 hours.

The radiative contribution of the response of an individual process i, ΔR_i, is assessed by combining so-called "forward" and "backward" calculations. The combination of forward and backward is necessary to guarantee the separability of individual adjustment and feedback processes as it reduces correlations between them (Klocke et al., 2013; Rieger et al., 2017). The forward radiative contribution $\Delta R_i^{\text{forward}}$ is defined as the difference between the net radiative flux at TOA of a radiation call, for which all parameters are taken

from the reference simulation, except for the parameter of interest (x_i), which is taken from the experiment simulation, and an unperturbed radiation call with all parameters from the reference simulation

$$\Delta R_i^{\text{forward}} = R(x_i^{\text{exp}}, x_j^{\text{ref}}) - R(x_i^{\text{ref}}, x_j^{\text{ref}}). \tag{3.8}$$

Hereby, the unperturbed radiation call represents the radiative fluxes at one specific time step of the online reference simulation exactly and the perturbed radiation call represents the instantaneous effect of the perturbation at this specific time step. Therefore, the PRP method has the advantage that it can be applied to temporally highly variable processes, such as clouds (Rieger et al., 2017; Bickel et al., 2020). The backward radiative contribution $\Delta R_i^{\text{backward}}$ is calculated analogously as the difference between the net radiative flux at TOA of a radiation call, for which all parameters are taken from the experiment simulation, except for the parameter of interest, which is taken from the reference simulation, and a radiation call with all parameters from the experiment simulation

$$\Delta R_i^{\text{backward}} = -[R(x_i^{\text{ref}}, x_j^{\text{exp}}) - R(x_i^{\text{exp}}, x_j^{\text{exp}})]. \tag{3.9}$$

The centred radiative contribution is the average of the forward and backward calculation

$$\Delta R_i^{\text{centred}} = \frac{1}{2}(\Delta R_i^{\text{forward}} + \Delta R_i^{\text{backward}}). \tag{3.10}$$

Following the assumption of separability and linearity, the sum of all individual rapid radiative adjustments plus RF_{inst} should give the ERF as determined from the online simulations (see Eq. 2.8). Similarly, the sum of all individual climate feedback parameters (in W m^{-2} K^{-1}) should result in the total feedback parameter α (see Eq. 2.11), which can be expressed as $\alpha = -\frac{RF_{inst}}{\Delta T}$ (see Eq. 2.6). However, the PRP method is usually not completely closed, which is why residuum terms for the fast and the full response, RES_{RA} and RES_α, are introduced (Rieger et al., 2017; Bickel et al., 2020)

$$RES_{RA} = ERF - (RF_{inst} + \sum_i RA_i), \tag{3.11}$$

$$RES_\alpha = RF_{inst} + \sum_i \alpha_i \cdot \Delta T. \tag{3.12}$$

This study considers adjustments and feedbacks of the surface albedo, clouds, H_2O (separately for troposphere and stratosphere), O_3 (separately for troposphere and stra-

tosphere), CH_4 for the CO_2 perturbed online simulations (separately for troposphere and stratosphere), as well as the temperature related adjustments and feedbacks of the tropospheric lapse rate, surface temperatures (i.e. the Planck adjustment or feedback), and stratospheric temperatures (see Sect. 2.2 for more information on these processes). For quantification of the latter three, modified temperature fields combined from data of the reference and experiment simulations are used in the radiation calculation. The temperature field used for the lapse rate adjustment and feedback T^{LR} is set to reference conditions at the surface and in the stratosphere. For tropospheric grid boxes it is calculated as the difference between experiment conditions and the temperature difference at the surface of the corresponding atmospheric column $\Delta T_{\mathrm{surface}} = T^{\mathrm{exp}}_{\mathrm{surface}} - T^{\mathrm{ref}}_{\mathrm{surface}}$. Thus, for the forward radiation call it is calculated as

$$\begin{aligned} T^{\mathrm{LR}}_{\mathrm{surface}} &= T^{\mathrm{ref}}_{\mathrm{surface}} \\ T^{\mathrm{LR}}_{\mathrm{troposphere}} &= T^{\mathrm{exp}}_{\mathrm{troposphere}} - \Delta T_{\mathrm{surface}} \\ T^{\mathrm{LR}}_{\mathrm{stratosphere}} &= T^{\mathrm{ref}}_{\mathrm{stratosphere}}. \end{aligned} \tag{3.13}$$

The temperature field used for the Planck adjustment and feedback is set to experiment conditions at the surface and reference conditions in the stratosphere. For tropospheric grid boxes the surface temperature difference $\Delta T_{\mathrm{surface}}$ is added to the temperature of the reference simulation

$$\begin{aligned} T^{\mathrm{Planck}}_{\mathrm{surface}} &= T^{\mathrm{exp}}_{\mathrm{surface}} \\ T^{\mathrm{Planck}}_{\mathrm{troposphere}} &= T^{\mathrm{ref}}_{\mathrm{troposphere}} + \Delta T_{\mathrm{surface}} \\ T^{\mathrm{Planck}}_{\mathrm{stratosphere}} &= T^{\mathrm{ref}}_{\mathrm{stratosphere}}. \end{aligned} \tag{3.14}$$

For the stratospheric temperature adjustment and feedback a combination of stratospheric temperatures from the experiment and tropospheric and surface temperatures from the reference is used

$$\begin{aligned} T^{\mathrm{strat.\ temp.}}_{\mathrm{surface}} &= T^{\mathrm{ref}}_{\mathrm{surface}} \\ T^{\mathrm{strat.\ temp.}}_{\mathrm{troposphere}} &= T^{\mathrm{ref}}_{\mathrm{troposphere}} \\ T^{\mathrm{strat.\ temp.}}_{\mathrm{stratosphere}} &= T^{\mathrm{exp}}_{\mathrm{stratosphere}}. \end{aligned} \tag{3.15}$$

Hereby, the tropopause that separates tropospheric and stratospheric grid boxes is the

climatological tropopause calculated as tp_{clim} = 300 hPa–215 hPa $cos^2(\phi)$, with ϕ being the geographical latitude. In addition to the mentioned adjustment and feedback processes, RF_{inst} is calculated by exchanging only the perturbation agent of the online simulations (in the case of this thesis either CO_2 or CH_4) in an additional diagnostic radiation call. This implies that RF_{inst} is analogously calculated as a combination of a forward and a backward calculation in this study, which means a slight deviation from the usual procedure but keeps the residuum as low as possible (Rieger et al., 2017).

The technical implementation of the calculation of radiative fluxes is similar as done by Rieger et al. (2017) and Bickel et al. (2020). However, in this study MBM RAD (see Sect. 3.1.5) instead of a duplicate of the radiation code is used, which has the advantages that the same source code is used for the online simulations and for the adjustment and feedback analysis, and that updates of the MESSy radiation infrastructure, e.g. the implementation of PSrad (see Sect. 3.1.5 and Nützel et al. (2023)), are automatically available and can be made easily functional for the feedback tool as well. The radiative contributions of changes in the surface albedo, clouds, H_2O, O_3, CH_4 and CO_2 are calculated in one MBM RAD simulation using the MESSy option for multiple diagnostic radiation calls (Dietmüller et al., 2016; Nützel et al., 2023). An option to also exchange the surface albedo in individual radiation calls was implemented when the surface albedo calculation was moved to the MESSy submodel ALBEDO (Nützel et al., 2023). For the temperature related adjustments and feedbacks separate MBM RAD simulations are necessary as it is currently not possible to use different temperature fields in individual radiation calls.

The individual radiation calls are instantaneous, i.e. without the inclusion of the corresponding adjustment of stratospheric temperatures (see Sect. 3.1.5). In the course of this thesis, it was tested whether the option of stratospheric temperature adjustment could be used for the PRP method with MBM RAD. This would give the opportunity to estimate the stratospheric adjusted radiative impact of individual adjustment and feedback processes. However, as the method for calculating the adjustment of stratospheric temperatures works iteratively, it became obvious that a frequency of a radiation call every 10 hours is too low to apply the stratospheric temperature adjustment. In particular, for temporally variable perturbations, such as clouds and tropospheric humidity, the difference between the perturbed and unperturbed radiative temperature tendencies ($\frac{dT^\star}{dt}\big|_{rad}$ and $\frac{dT}{dt}\big|_{rad}$ in Eqs. 3.4 and 3.5) becomes too large. It could work for well-mixed trace gases, but further testing is required to use this option with confidence. Accounting for the induced stratospheric temperature adjustment is, however, important for certain per-

turbations, e.g. O_3 (Stuber et al., 2001). Therefore, an additional method (Dietmüller et al., 2014; Winterstein et al., 2019; Stecher et al., 2021) is used to estimate the stratospheric adjusted radiative contributions of H_2O, O_3, CH_4 and CO_2, which is explained in the next section.

3.3.2 Calculation of stratospheric adjusted radiative effects

Stratospheric adjusted estimates of radiative impacts of adjustments and feedbacks of H_2O, O_3, CH_4 and CO_2 are assessed in additional atmosphere-only EMAC simulations using the MESSy option for multiple diagnostic radiation calls (Dietmüller et al., 2016; Nützel et al., 2023) following the method used by, e.g. Winterstein et al. (2019) and Stecher et al. (2021). The atmosphere-only simulations are performed for 2 years (plus 1 year spin-up). The set-up is the same as for $\mathrm{REF^{SSTvar}}_{\mathrm{nochem}}$ (see Sect. 3.2), except that SSTs and SICs are prescribed using the same observational based climatology as used for $\mathrm{REF^{SSTfix}}_{\mathrm{chem}}$ (Rayner et al., 2003) to reduce inter-annual variability. The radiatively active trace gases CH_4, CO_2, O_3, N_2O and the CFCs are prescribed as monthly climatologies from the simulations $\mathrm{REF^{SSTfix}}_{\mathrm{chem}}$ or $\mathrm{REF^{SSTvar}}_{\mathrm{chem}}$. Thus, the background climate in the simulations represents reference conditions and the radiative contributions can therefore be interpreted as forward estimates.

In these simulations the first radiation call is used for providing the radiative heating rates that drive the base model, whereas the other radiation calls are purely diagnostic. For the CO_2 perturbed simulations with interactive chemistry, in total 16 diagnostic radiation calls are performed. Two are reference calls, which receive identical input as the prognostic radiation call, except for the specific humidity, for which a monthly mean climatology from the respective reference simulation is used instead of the prognostic specific humidity from the base model. One of the calls is calculated instantaneously, i.e. without accounting for the corresponding stratospheric temperature adjustment, to serve as reference for the instantaneous perturbations. The other call accounts for the stratospheric temperature adjustment induced by the difference between the prognostic and climatological specific humidity and serves as reference for the stratospheric adjusted perturbations.

In addition, radiation calls are performed, for which either CO_2 (for quantification of $\mathrm{RF_{inst}}$ and $\mathrm{RF_{adj}}$), tropospheric or stratospheric H_2O, tropospheric or stratospheric O_3, or tropospheric or stratospheric CH_4, are perturbed. The perturbed fields are monthly mean climatologies from the respective experiment simulation. For each perturbation, the instantaneous and the stratospheric adjusted radiative impact is quantified. The determined

instantaneous radiative impacts can be compared to the results of the PRP method (see previous section) to get an estimate of the error that results from using monthly mean fields for the perturbations and a slightly different background climate. For the non-H_2O perturbations the climatological specific humidity is used to be consistent with the reference calls.

Analogously, for the CH_4 perturbed simulations with interactive chemistry, in total 14 diagnostic radiation calls are necessary as perturbations of CH_4 (for RF_{inst} and RF_{adj}), tropospheric and stratospheric H_2O, and tropospheric and stratospheric O_3 are calculated. For the simulations without interactive chemistry, in total 8 radiation calls are necessary as perturbations for CO_2 or CH_4 (for RF_{inst} and RF_{adj}), and tropospheric and stratospheric H_2O are performed.

There is one methodological difference compared to Winterstein et al. (2019) and Stecher et al. (2021). They used the climatological specified humidity directly in the first prognostic radiation call, which then served as reference for the perturbed calls. However, here it was decided to use the prognostic specific humidity in the first radiation call as it is consistent with the model's background meteorology, e.g. the cloud cover. The influence on the calculated radiative impacts was tested and found to be up to 1.02% (or 0.004 W m^{-2}) with the maximum deviation for the H_2O perturbations, which is negligible in comparison to other uncertainties.

Chapter 4

CO_2 perturbation

This chapter presents the response of chemically active species and physical parameters to the increase of present-day CO_2 mixing ratios by a factor of 1.35. For each parameter the fast, the full, and the climate response, calculated as the difference of the full minus the fast response, are shown. This presentation allows to attribute processes either to the direct effect of the CO_2 perturbation, or to the effect of tropospheric warming, which is expected to be less dependent on the type of perturbation (e.g Sherwood et al., 2015). The response of the chemically active species CH_4 and O_3 is shown in Sect. 4.1. Subsequently, the response of temperature and humidity in the simulations with interactive chemistry, as well as the respective difference to the simulation without interactive chemistry is assessed in Sect. 4.2. Finally, individual radiative contributions to the ERF and the climate sensitivity are presented in Sect. 4.3.

4.1 Atmospheric response of chemically active species

4.1.1 Response of CH_4

Fig. 4.1 shows the annual zonal mean responses of CH_4 in the simulations ERF$CO_2{}^{\mathrm{SSTfix}}{}_{\mathrm{chem}}$ (fast response) and ECCC$O_2{}^{\mathrm{SSTvar}}{}_{\mathrm{chem}}$ (full response), and their difference, which is interpreted as the climate response. The fast response of CH_4 is dominated by increasing CH_4 mixing ratios in the upper stratosphere and mesosphere. In this region, stratospheric cooling (see Fig. 4.6 for the temperature response) leads to the prolongation of the CH_4 lifetime. A similar effect has been noted by Dietmüller et al. (2014). In addition, the reaction partners of CH_4 (OH, $O(^1D)$ and Cl) show decreases in the extratropics at pressure

levels of approximately 50 to 1 hPa (10 to 1 hPa for Cl). In the fast response, tropospheric CH_4 shows a slight increase below 2%.

In contrast to the fast response, the full response shows a significant decrease of CH_4 mixing ratios in the troposphere and lower stratosphere. Recall that CH_4 emissions are prescribed in the simulation set-up and cannot respond to changes in meteorology or composition. Thus, any climate feedback of natural CH_4 emissions (e.g. Dean et al., 2018) is suppressed. Therefore, the decrease of CH_4 mixing ratios results from enhanced chemical degradation of CH_4, mainly by the oxidation with OH. The tropospheric CH_4 lifetime with respect to the oxidation with OH shortens by about 7 months (0.56 a or 7.4 %, see Tab. 4.1). This shortening is a combined result of the direct influence of the temperature on the reaction rate coefficient and of increased OH mixing ratios. Fig. 4.2 shows the OH response. Tropospheric warming increases OH mixing ratios throughout the troposphere with the maximum increase in the tropics. The OH response is largely driven by the increase of tropospheric humidity associated with higher temperatures (see Fig. 4.9 for the response of H_2O). Additionally, $O(^1D)$, the other precursor of OH, increases in the upper tropical troposphere by up to 4 % (not shown).

In addition to the decrease in the troposphere, the CH_4 mixing ratios decrease also in the lower stratosphere as part of the full response. As the reaction partners of CH_4 do not show any significant response in the lower stratosphere, the decrease is likely a transport effect. Tropospheric air masses with reduced CH_4 mixing ratios compared to the reference simulation enter the stratosphere. Dietmüller et al. (2014) noted an increase of CH_4 mixing ratios throughout the stratosphere as a result of $2\times CO_2$ in their set-up, which suppressed the tropospheric feedback of CH_4 as CH_4 mixing ratios were prescribed at the surface. This supports the conclusion that the decrease of CH_4 in the stratosphere is a consequence of the decrease of CH_4 in the troposphere.

Previous studies also found that tropospheric warming leads to increasing OH mixing ratios and correspondingly to the shortening of the CH_4 lifetime (Voulgarakis et al., 2013; Dietmüller et al., 2014; Frank, 2018; Heimann et al., 2020; Stecher et al., 2021; Thornhill et al., 2021a). In the present CO_2 perturbation experiment, the CH_4 lifetime change per unit change of GSAT is $\frac{-0.56\ a}{1.09\ K}$ = -0.51 a K^{-1} or -6.7 % K^{-1} (see below for the discussion of the response of GSAT).

Voulgarakis et al. (2013) assessed the sensitivity of the tropospheric CH_4 lifetime towards climate change in the ACCMIP model ensemble. In the corresponding sensitivity simulations the boundary conditions for SSTs, SICs and CO_2 were set to RCP8.5 condi-

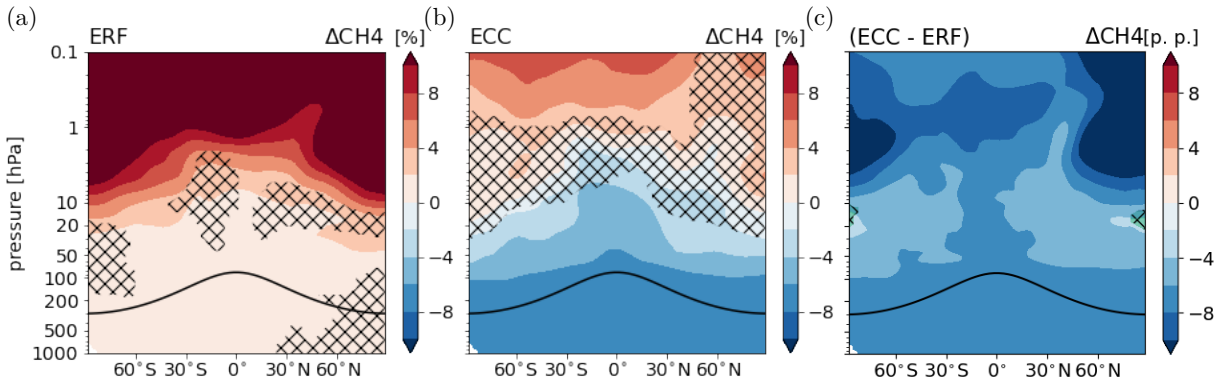

Figure 4.1: Relative differences between the annual zonal mean CH_4 mixing ratios of sensitivity simulations (a) ERF$CO_2{}^{SSTfix}{}_{chem}$ (fast response) and (b) ECC$CO_2{}^{SSTvar}{}_{chem}$ (full response) and their respective reference simulation in [%]. (c) Climate response as difference between the CH_4 responses in panels (a) and (b) in [percentage points (p.p.)]. Non-hatched areas are significant on the 95% confidence level according to a Welch's test based on annual mean values. The solid black line indicates the location of the climatological tropopause.

tions of the years 2030 or 2100, while all other boundary conditions were representative of the year 2000. They found sensitivities of the CH_4 lifetime of -0.31 ± 0.14 a K^{-1} (-3.2 ± 1.0 % K^{-1}) and -0.34 ± 0.12 a K^{-1} (-3.4 ± 0.8 % K^{-1}) for the year 2030 and the year 2100 experiments, respectively[1].

The CMIP6 AerChemMIP model ensemble as analysed by Thornhill et al. (2021b) suggests a sensitivity of the CH_4 lifetime towards climate change of -0.6 ± 4.5 % K^{-1} assessed from abrupt 4× pre-industrial CO_2 experiments. The large intermodel spread results from one model that shows an extension of CH_4 lifetime as a result to 4×CO_2. The three models showing a shortening of CH_4 lifetime suggest a sensitivity of -3.2 ± 0.8 % K^{-1} in close agreement with Voulgarakis et al. (2013). Thornhill et al. (2021a) analysed the response of the total whole-atmosphere CH_4 lifetime, whereby the lifetime with respect to OH was diagnosed from the models and the lifetime with respect to Cl and soil loss was assumed to be constant.

This study indicates a higher sensitivity of the CH_4 lifetime towards climate change compared to Voulgarakis et al. (2013) and Thornhill et al. (2021a). Possible reasons are the different magnitudes of the perturbations, differences in the simulation set-ups, a potential large sensitivity in the EMAC model, or the explicit treatment of the CH_4 feedback in

[1]Relative estimates were calculated from estimates given in Tables 1 and 4 of Voulgarakis et al. (2013)

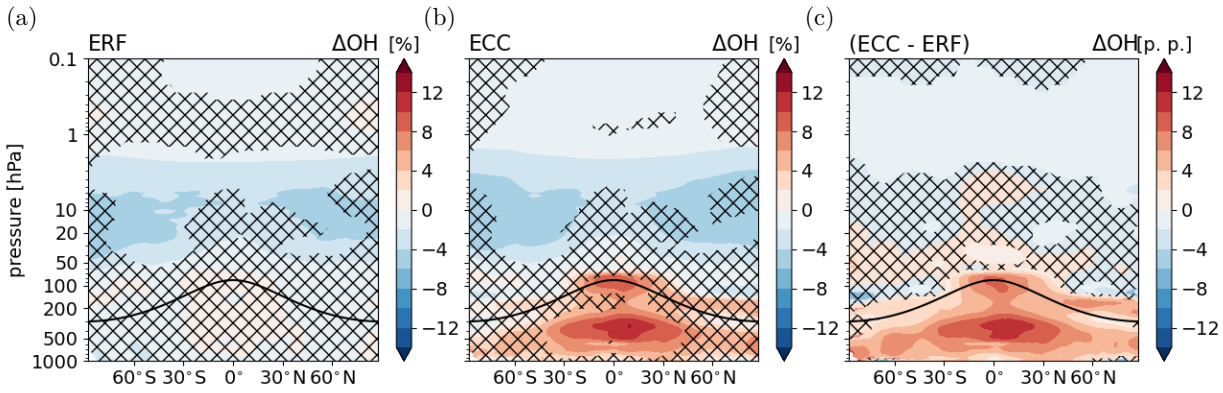

Figure 4.2: As Fig. 4.1 for OH.

this study. The similar estimates for the years 2030 and 2100 corresponding to 1.14 K and 4.76 K change of GSAT, respectively[2], by Voulgarakis et al. (2013) suggest that the sensitivity is not highly dependent on the magnitude of the perturbation. Furthermore, the set-ups of individual models in Voulgarakis et al. (2013) and Thornhill et al. (2021a) differ, e.g. in the level of complexity of the chemical mechanism, whether interactive aerosol is used, or through the different treatment of natural O_3 precursor emissions. Nevertheless, the present estimate is larger than the estimates of all individual models in Voulgarakis et al. (2013) and Thornhill et al. (2021a), except for two models which do not parameterize the effect of stratospheric O_3 on photolysis below which is taken into account by the present set-up.

In the simulation set-ups analysed by Voulgarakis et al. (2013) and Thornhill et al. (2021a) CH_4 mixing ratios are prescribed at the lower boundary so that CH_4 can not adapt to changes in its lifetime in all models except of the GISS-E2-R model analysed by Voulgarakis et al. (2013). The explicit treatment of the CH_4 feedback in the set-up of this study can lead to a subsequent feedback of OH and correspondingly a self-feedback on the CH_4 lifetime resulting in a larger sensitivity of the CH_4 lifetime towards climate change.

If the response of CH_4 mixing ratios is not explicitly simulated in the used set-up it can be estimated from the CH_4 lifetime response (e.g. Stevenson et al., 2020)

$$[CH_4]_{eq} = [CH_4]_{ref}(\frac{\tau_{exp}}{\tau_{ref}})^f, \tag{4.1}$$

[2]Multi-model mean changes of GSAT were calculated from the estimates given in Table 4 of Voulgarakis et al. (2013).

Table 4.1: Global mean values of tropospheric CH_4 lifetime with respect to the oxidation with OH, and CH_4 surface mixing ratios for the reference simulations and the CO_2 perturbation simulations. The corresponding interannual standard deviation based on 20 annual mean values is given to estimate the year to year variability.

	Trop. CH_4 lifetime [a]	CH_4 surface VMR [ppmv]
$REF^{SSTfix}{}_{chem}$	7.59 ± 0.03	1.82 ± 0.00
$REF^{SSTvar}{}_{chem}$	7.58 ± 0.03	1.82 ± 0.00
$ERFCO_2{}^{SSTfix}{}_{chem}$	7.59 ± 0.03	1.82 ± 0.00
$ECCCO_2{}^{SSTvar}{}_{chem}$	7.02 ± 0.05	1.69 ± 0.00

where f is the CH_4-OH feedback factor. Estimates of f are in the range of 1.2 to 1.4 (Fiore et al., 2009; Voulgarakis et al., 2013; Stevenson et al., 2013; Thornhill et al., 2021b; Stevenson et al., 2020). Eq. 4.1 predicts a global mean CH_4 equilibrium mixing ratio in the range of 1.63 to 1.66 ppmv when using $f = [1.2, 1.4]$ and the CH_4 lifetimes of the simulations $REF^{SSTvar}{}_{chem}$ and $ECCCO_2{}^{SSTvar}{}_{chem}$ from Tab. 4.1. Comparing with the CH_4 equilibrium mixing ratio the model adjusts to, 1.69 ppmv (see Tab. 4.1), Eq. 4.1 seems to overestimate the response of CH_4 mixing ratios towards the lifetime change. However, if the feedback factor is not applied (f=1), Eq. 4.1 gives 1.68 ppmv, which is in close agreement with the simulated response of CH_4 mixing ratios. This supports the assumption that the sensitivity of OH and the CH_4 lifetime towards climate change is larger if the feedback of CH_4 is explicitly simulated as thereby the CH_4-OH feedback is implicitly included in the simulated response. The climate response of CH_4 affects the climate response of O_3, which is presented in the next section.

4.1.2 Response of O_3

The fast response of O_3 shows increases of up to 8% in the middle and upper stratosphere (see Fig 4.3 (a)). In these regions, CO_2 induced stratospheric cooling causes slower chemical O_3 depletion (e.g. Rosenfield et al., 2002; Portmann and Solomon, 2007; Dietmüller et al., 2014; Chiodo et al., 2018) In the lowermost stratosphere, O_3 mixing ratios decrease slightly by up to 4%. This decrease can be explained by the so-called reversed self-healing (Rosenfield et al., 2002; Portmann and Solomon, 2007), which describes the effect that increases of O_3 above lead to a reduction of ultraviolet radiation that reaches the lower stratosphere and consequently to reduced photochemical production of O_3. The effect of transport from the troposphere into the stratosphere is expected to play a minor role in the fast response as the strength of tropical upwelling is coupled to the response of SSTs

(Garny et al., 2011; Butchart, 2014). The O_3 response in the SH lower polar stratosphere is not significant on the basis of annual means. However, it does show a significant decrease between 200 and 100 hPa for the season June, July, and August (JJA) shown in Appendix E.3 pointing towards enhanced O_3 depletion by the formation of PSCs. The fast response of tropospheric O_3 is smaller than 2%.

The climate response of O_3 is dominated by a decrease of up to 10% in the lowermost tropical stratosphere (see Fig 4.3 (c)). Enhanced tropical upwelling transports O_3 depleted air from the troposphere into the stratosphere more efficiently. This is a robust feature across CCMs (Dietmüller et al., 2014; Nowack et al., 2015; Marsh et al., 2016; Chiodo et al., 2018). In the troposphere, O_3 mixing ratios decrease by up to 6% in the tropics close to the surface and decrease slightly in the upper tropical troposphere.

The pattern of the full response of stratospheric O_3 is qualitatively consistent with previous studies of O_3 changes resulting from CO_2 perturbation (Dietmüller et al., 2014; Nowack et al., 2015; Marsh et al., 2016; Nowack et al., 2018; Chiodo et al., 2018; Thornhill et al., 2021a). However, the tropospheric response is different here. Most studies using different CCMs consistently show an increase of O_3 in the tropical upper troposphere as part of the full response (Dietmüller et al., 2014; Nowack et al., 2015; Marsh et al., 2016; Nowack et al., 2018; Chiodo et al., 2018), whereas two of the models (GFDL-ESM4 and UKESM1) analysed by Thornhill et al. (2021a) show a different pattern of tropospheric O_3 response (see their Fig. S12). In the studies by Dietmüller et al. (2014), Nowack et al. (2015, 2018), Thornhill et al. (2021a) and presumably also in the studies by Marsh et al. (2016) and Chiodo et al. (2018) CH_4 mixing ratios are prescribed at the lower boundary. Consequently, the negative CH_4 feedback as discussed in the section above can not evolve. This can lead to a potential overestimation of O_3 produced from products of the CH_4 oxidation and is consistent with the positive response of O_3 in the upper tropical troposphere. In particular the comparison with the study by Dietmüller et al. (2014) indicates an effect of the CH_4 feedback on O_3 because also the EMAC model was used. Different processes contribute to the tropospheric O_3 response and it is therefore analysed in more detail in the following section.

4.1.3 Contribution of individual processes to the tropospheric O_3 response

This section attributes the tropospheric O_3 response as presented in the previous section to individual categories representing different processes of O_3 production. The MESSy

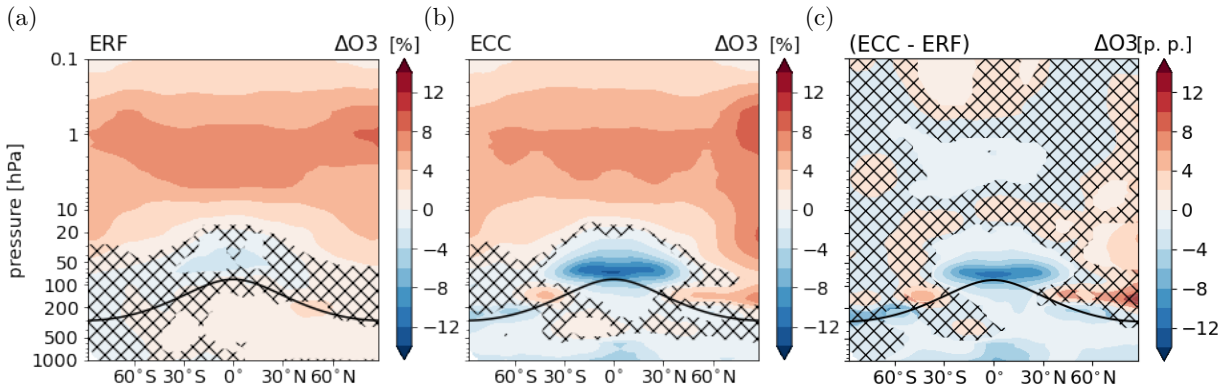

Figure 4.3: As Fig. 4.1 for O_3.

submodel TAGGING (Grewe et al. (2017); Rieger et al. (2018); see Sect. 3.1.6) gives the contribution of individual emission sectors or processes to the total O_3 mixing ratio. In this study O_3 production from the following categories is considered:

- through photolysis in the stratosphere (O_3 *stratosphere*),
- from emissions of lightning NO_x (O_3 *lightning*),
- from biogenic precursor emissions (O_3 *biogenic*),
- from products of the CH_4 decomposition (O_3 CH_4),
- from products of the N_2O decomposition (O_3 N_2O),
- from biomass burning precursor emissions (O_3 *biomass burning*)
- and from anthropogenic precursor emissions (O_3 *anthropogenic*).

The categories are the same as defined by Grewe et al. (2017), except for the category O_3 *anthropogenic* in this study, which combines O_3 production from emissions of the sectors industry, road traffic, shipping and aviation.

Fig. 4.4 shows the fast response of O_3 in the individual categories. Shown is the difference between $ERFCO_2{}^{SSTfix}{}_{chem}$ and $REF^{SSTfix}{}_{chem}$ in one category relative to the total reference O_3

$$\Delta O_{3_{cat}} = \frac{O_{3_{cat,ERF}} - O_{3_{cat,REF}}}{O_{3_{total,REF}}}.$$

This presentation allows to directly compare the response of the individual categories to the total relative O_3 response as shown in Fig. 4.3 (a) and Fig. 4.4 (a). The response of the category O_3 *stratosphere* as shown in Fig. 4.4 (b) confirms that less O_3 is produced via photolysis in the lower tropical stratosphere. Additionally, it indicates enhanced transport from the stratosphere into the troposphere in the Northern Hemisphere (NH). The categories with prescribed emissions, O_3 *biomass burning* and O_3 *anthropogenic*, show increasing O_3 mixing ratios as do the categories O_3 *lightning* and O_3 *biogenic*. The emissions of lightning NO_x and biogenic NO_x and C_5H_8 are calculated online (see Sect. 3.2.3). However, in the fast response, the emissions do not change significantly (see Appendix E.1). Consequently, for the latter four categories, the same emissions of O_3 precursors result in a slight increase of O_3 attributed to these categories. This points to a small increase of the O_3 production efficiency. On the contrary, the categories O_3 CH_4 and O_3 N_2O show a slight decrease of O_3 in the fast response. Overall, the fast response of tropospheric O_3 is small (below 0.5% of the total reference O_3 for all categories, except for O_3 *stratosphere*).

The climate response of individual categories is shown in Fig 4.5 as the difference between the fast and full response of each category in percentage points (p.p.)

$$\Delta O_{3_{\text{cat, climate response}}} = \left(\frac{O_{3_{\text{cat,ECC}}} - O_{3_{\text{cat,REF}}}}{O_{3_{\text{total,REF}}}}\right) - \left(\frac{O_{3_{\text{cat,ERF}}} - O_{3_{\text{cat,REF}}}}{O_{3_{\text{total,REF}}}}\right).$$

The climate response of the category O_3 *stratosphere* shows significantly enhanced transport of stratospheric O_3 into the troposphere in both hemispheres. In the extratropical middle troposphere, O_3 mixing ratios increase by up to 1.5% relative to the total reference O_3 in the full response, which is the highest positive contribution to the total tropospheric O_3 response. Enhanced entry of stratospheric O_3 under increasing GHG concentration is a robust feature in CCMs (Abalos et al., 2020). The category O_3 *stratosphere* contributes also most to the strong decrease in the lowermost stratosphere. The category O_3 *lightning* shows a significant increase of up to 1.25% relative to total reference O_3 in the middle tropical troposphere. This is consistent with an increase of lightning NO_x emissions of 0.32 Tg(N) a^{-1} globally. Lightning NO_x is emitted mainly in the upper tropical troposphere where convection is strongest (not shown). In addition, also biogenic emissions of NO_x and C_5H_8 increase in the full response. Biogenic C_5H_8 emissions increase strongest in the Amazon region and the Congo river basin, whereas biogenic NO_x emissions increase over land in the tropics and mid latitudes (see Appendix E.1). However, the climate response of O_3 *biogenic* is mostly not significant due to the competing effects of strengthened

precursor emissions and of enhanced chemical loss with H_2O. An enhanced sink of O_3 via the reaction of $O(^1D)$ with H_2O is expected in a warmer and moister troposphere (e.g. Stevenson et al., 2006). The spatial distribution of the tropospheric O_3 column shows mainly a decrease over the tropical ocean (see Appendix E.2), which is also reflected by the significant decrease between the equator and 30°N in the zonal mean (Fig. 4.5 (d)). Locally over regions with increasing precursor emissions, e.g. over the Amazon region and the Congo river basin, the tropospheric O_3 column increases in the category *O_3 biogenic* (see Appendix E.2). Anthropogenic and biomass burning emissions are prescribed and therefore do not change in the full response either. In these categories, decreasing O_3 from enhanced loss or reduced O_3 production efficiency is shown. The O_3 decrease of the anthropogenic category is most pronounced over the tropical ocean, where a decline of O_3 due to enhanced loss via H_2O is expected (Stevenson et al., 2006; Zanis et al., 2022). The decrease of the biomass burning category is small as also the contribution is small. In addition to the enhanced sink, reduced O_3 production per emitted NO_x could play a role in the latter two categories as O_3 precursor emissions from natural categories increase. The category *O_3 CH_4* shows a significant decrease throughout the troposphere. This is consistent with the reduction of CH_4 mixing ratios as in the new equilibrium less products of the CH_4 oxidation are available for O_3 production resulting in reduced O_3 production in this category (not shown). This effect is not present when CH_4 mixing ratios are prescribed at the lower boundary (e.g. Dietmüller et al., 2014) leading to a potential overestimation of the tropospheric O_3 response towards climate change. Further, enhanced chemical loss can contribute to the decrease of this category. In the upper tropical troposphere the increase of lightning NO_x emissions counteracts the effect of the CH_4 decrease by providing high levels of NO_x, which can react with the products of the CH_4 oxidation more efficiently. The climate response in the category *O_3 N_2O* shows significant decreases in the lower stratosphere and troposphere. In the stratosphere, N_2O mixing ratios increase (not shown) indicating less N_2O decomposition (Dietmüller et al., 2014). Thereby, less NO is produced to form O_3, which is consistent with the decrease of O_3 formed from N_2O decomposition.

4.1.4 Summary

This section presents the response of the chemically active species CH_4 and O_3 resulting from an increase of present-day CO_2 mixing ratios by a factor of 1.35. In the climate response, warming and associated moistening of the troposphere lead to an enhanced abundance of OH. This and the increase of the temperature, which increases the oxidation rate

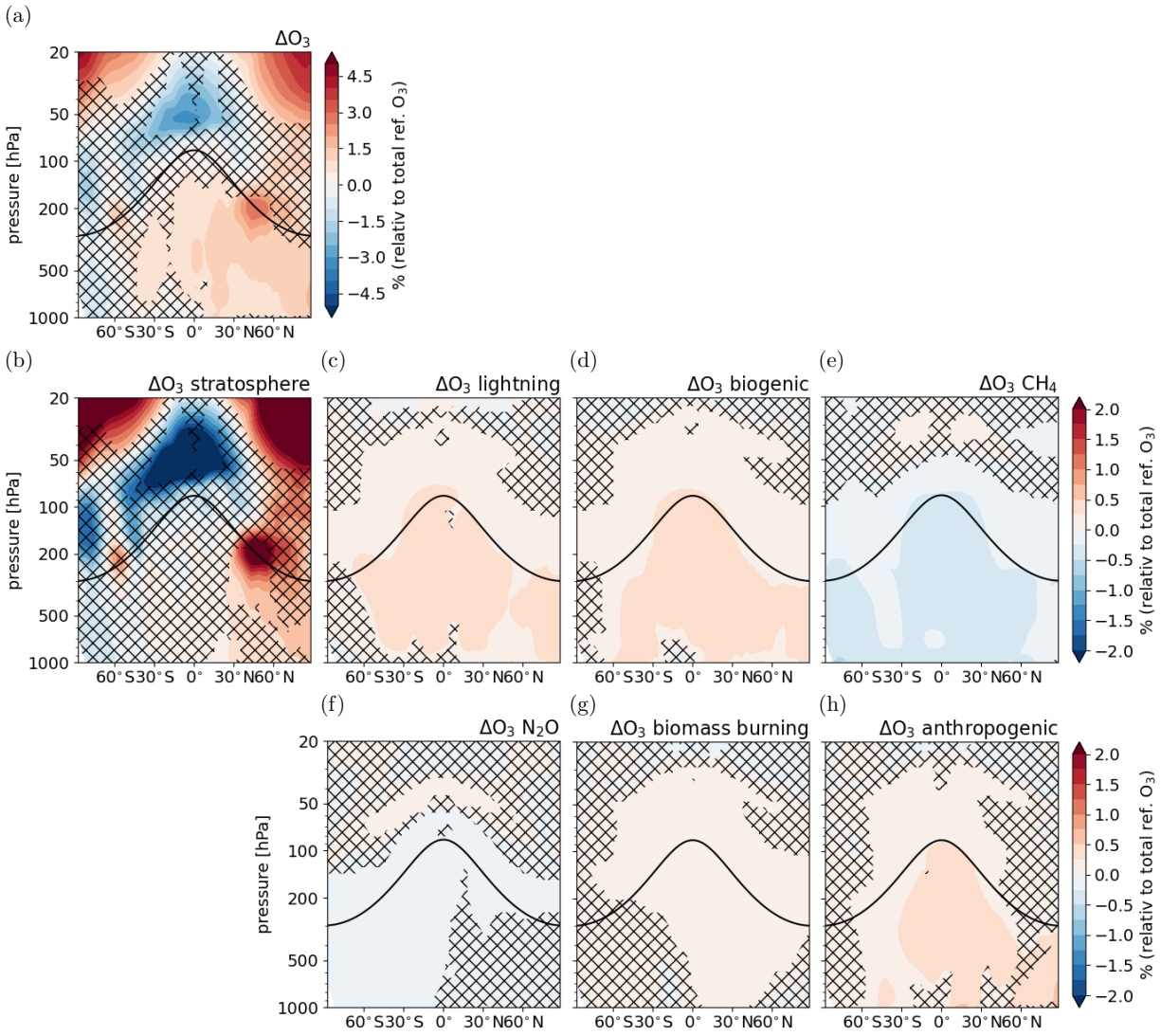

Figure 4.4: Fast response of tropospheric O_3 following the CO_2 perturbation: (a) response of total O_3 (same as Fig. 4.3 (a), but differently scaled colour levels to better compare with the response in the individual categories), (b) - (h) response of O_3 in individual categories relative to total reference O_3 ($\Delta O_{3_{\mathrm{cat}}} = \frac{O_{3_{\mathrm{cat,ERF}}} - O_{3_{\mathrm{cat,REF}}}}{O_{3_{\mathrm{total,REF}}}}$). Non-hatched areas are significant on the 95% confidence level according to a Welch's test based on annual mean values. The solid black line indicates the location of the climatological tropopause.

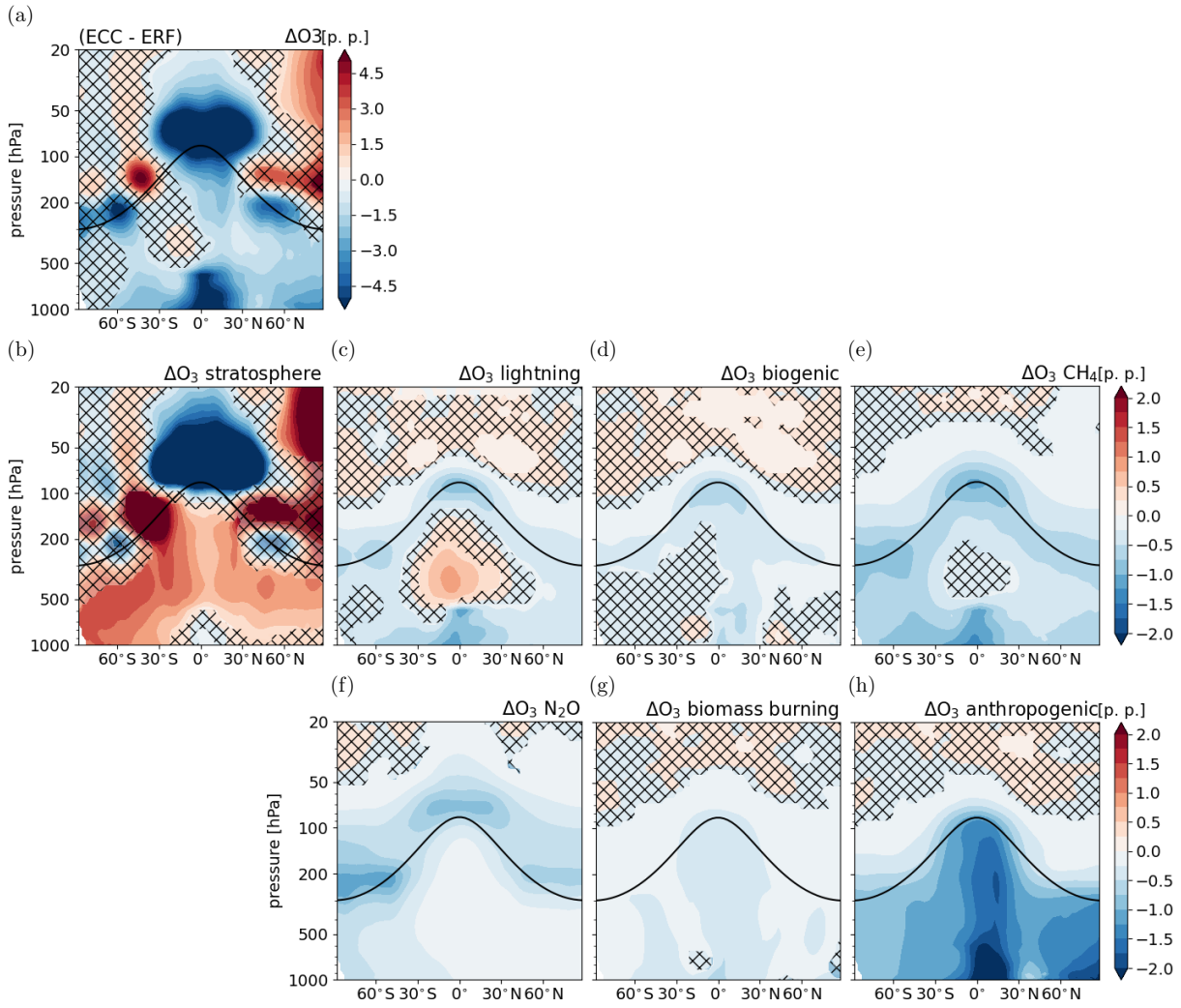

Figure 4.5: Climate response of tropospheric O_3 following the CO_2 perturbation: (a) response of total O_3 (same as Fig. 4.3 (c), but differently scaled colour levels to better compare with the response in the individual categories), (b) - (h) response of O_3 in individual categories relative to total reference O_3 ($\Delta O_{3_{\text{cat, climate response}}} = (\frac{O_{3_{\text{cat,ECC}}} - O_{3_{\text{cat,REF}}}}{O_{3_{\text{total,REF}}}}) - (\frac{O_{3_{\text{cat,ERF}}} - O_{3_{\text{cat,REF}}}}{O_{3_{\text{total,REF}}}})$). Non-hatched areas are significant on the 95% confidence level according to a Welch's test based on annual mean values. The solid black line indicates the location of the climatological tropopause.

of CH_4 due to its temperature dependent reaction rate coefficient, result in a shorter CH_4 lifetime. The corresponding decrease of CH_4 mixing ratios is explicitly simulated. The magnitude of the CH_4 lifetime change per change in GSAT indicates that the sensitivity of the CH_4 lifetime towards climate change is strengthened by the explicit treatment of the CH_4 feedback as thereby the CH_4-OH feedback is implicitly included.

The response of stratospheric O_3 is mainly a direct result of the stratospheric temperature response and thereby a rapid adjustment. An exception is the decrease of O_3 in the lowermost tropical stratosphere caused by tropical upwelling. The climate response of tropospheric O_3 can be attributed to different, partly counteracting, processes. Enhanced stratosphere – troposphere exchange leads to increased tropospheric O_3. Additionally, larger natural emissions of lightning NO_x, and biogenic NO_x and C_5H_8 result in local increases of O_3. On the contrary, enhanced chemical loss via the reaction of $O(^1D)$ with H_2O reduces O_3 mixing ratios, especially over the tropical ocean. The decrease of tropospheric CH_4 mixing ratios leads to a reduced formation of O_3. This effect is not included when CH_4 mixing ratios are prescribed at the surface and seems to lead to differences of the tropospheric O_3 response. The different processes that contribute to the tropospheric O_3 response resulting from climate change have been already suggested elsewhere (e.g. Stevenson et al., 2006; Dietmüller et al., 2014; Chiodo et al., 2018), but the quantitative attribution is a novelty of this study.

4.2 Atmospheric response of temperature and water vapour

4.2.1 Temperature response

The fast temperature response following the CO_2 perturbation is dominated by stratospheric cooling reaching up to 4 K in the upper stratosphere (see Fig. 4.6 (a)). Fig. 4.7 shows the stratospheric temperature adjustment induced directly by the CO_2 perturbation (panel (a)), and by the fast responses of stratospheric H_2O and O_3 (panels (b) and (c), respectively). The presented stratospheric temperature changes are derived from the additional atmosphere-only simulations with multiple perturbed radiation calls described in Sect. 3.3.2. The CO_2 perturbation induces a stratospheric cooling that increases with height with a maximum of 6 K in the upper stratosphere and mesosphere. The response of stratospheric O_3 dampens the cooling in the upper stratosphere and mesosphere, where it

induces local radiative heating up to 2 K. The effect on stratospheric temperatures induced by the fast response of stratospheric H_2O is small with a maximum cooling in the northern polar lower stratosphere up to 0.5 K. The induced stratospheric temperature adjustments from the fast response of tropospheric H_2O, tropospheric O_3 and CH_4 are all below 0.05 K and therefore not shown. As SSTs are prescribed in the simulation, the troposphere shows only a weak residual warming up to 0.7 K in the zonal mean.

In the full response, SSTs can adapt to the forcing and the troposphere warms significantly up to 1.9 K (see Fig. 4.6 (b) and (c)). The dipole pattern of the full temperature response consisting of stratospheric cooling and tropospheric warming is well known (e.g. Chap. 4 in IPCC, 2021; Lee et al., 2021). The corresponding response of GSAT is 1.09 ± 0.06 K (see Tab. 4.2). The climate response shows that the stratospheric cooling is mainly caused by the fast response. Fig. 4.8 shows the stratospheric temperature response induced by the full response of tropospheric and stratospheric H_2O and O_3. The decrease of O_3 in the lowermost tropical stratosphere in the climate response (see Fig. 4.3 (c)) leads to enhanced radiative cooling in the lowermost tropical stratosphere, which results in significant temperature differences between the fast and the full response (see Fig. 4.6 (c)). The climate response of stratospheric H_2O leads to cooling of up to 2 K in the polar lower stratosphere in both hemispheres. The climate response of tropospheric H_2O induces a cooling of up to 0.2 K in the lower stratosphere, whereas the climate response of tropospheric O_3 induces a weak stratospheric heating of up to 0.07 K. The effect of CH_4 is less than 0.04 K and is therefore not shown.

Panel (d) in Fig. 4.6 shows the temperature response that evolves in the simulation $ECCCO_2{}^{SSTvar}{}_{nochem}$ without interactive chemistry. Note that in this simulation monthly climatologies of CH_4, CO_2, O_3, N_2O and the CFCs from $ERFCO_2{}^{SSTfix}{}_{chem}$ are prescribed. The temperature response of $ECCCO_2{}^{SSTvar}{}_{nochem}$ is not significantly different from the temperature response of $ECCCO_2{}^{SSTvar}{}_{chem}$, except for the lowermost stratosphere where the climate response of O_3 leads to stronger cooling in $ECCCO_2{}^{SSTvar}{}_{chem}$ (see Fig. 4.6 (e)).

This seems to be in contradiction to the results by previous studies (Dietmüller et al., 2014; Nowack et al., 2015; Marsh et al., 2016; Chiodo and Polvani, 2019), who found a significantly reduced stratospheric cooling in their set-ups with interactive chemistry. However, an important difference between their set-ups and the present is that the fast response of chemical species is included in the simulation without interactive chemistry, i.e. $ECCCO_2{}^{SSTvar}{}_{nochem}$, as chemical species from the simulation $ERFCO_2{}^{SSTfix}{}_{chem}$ are prescribed. The local radiative heating that leads to reduced stratospheric cooling as reported

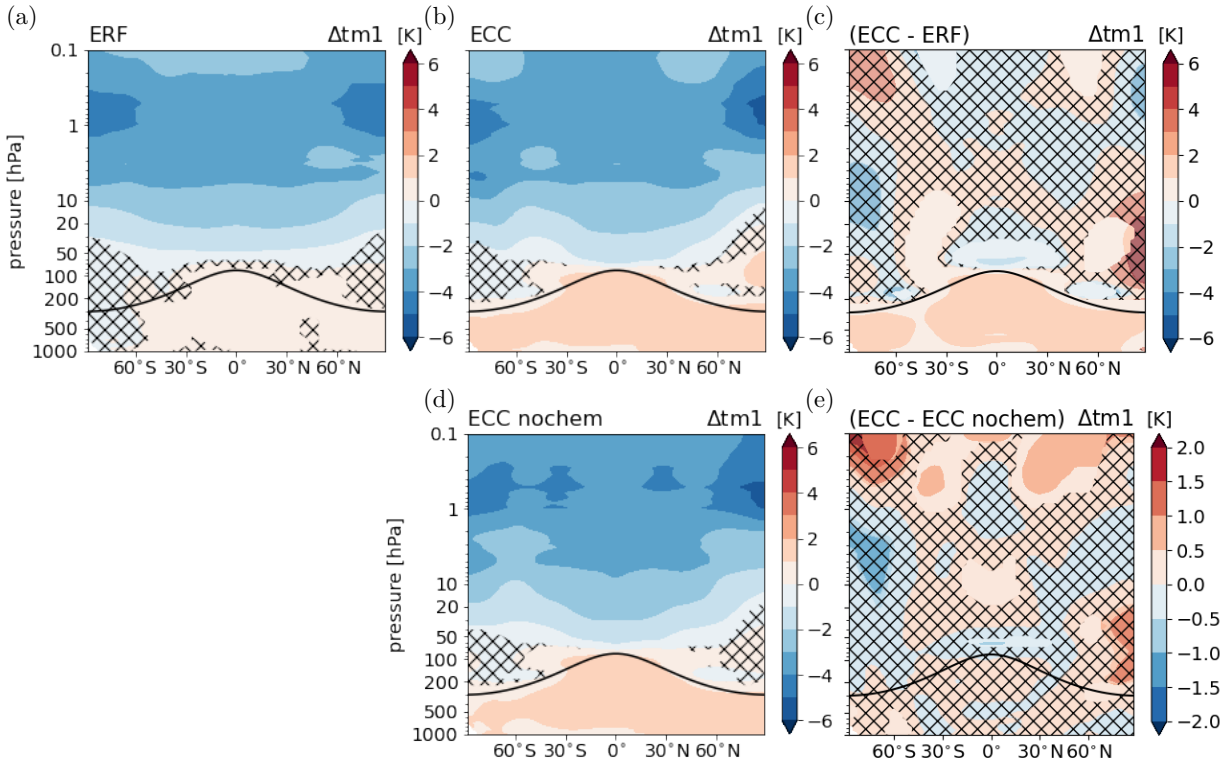

Figure 4.6: Absolute differences between the annual zonal mean temperature of sensitivity simulations (a) ERF$CO_2{}^{\mathrm{SSTfix}}{}_{\mathrm{chem}}$ (fast response) and (b) ECC$CO_2{}^{\mathrm{SSTvar}}{}_{\mathrm{chem}}$ (full response) and their respective reference simulation in [K]. (c) Climate response as difference between the temperature responses in panels (a) and (b) in [K]. (d) Absolute difference between the annual zonal mean temperature of the simulations without interactive chemistry ECC$CO_2{}^{\mathrm{SSTvar}}{}_{\mathrm{nochem}}$ and REF$^{\mathrm{SSTvar}}{}_{\mathrm{nochem}}$ in [K]. (e) Influence of chemical climate feedbacks presented as difference between the temperature responses in panels (b) and (d) in [K]. Non-hatched areas are significant on the 95% confidence level according to a Welch's test based on annual mean values. The solid black line indicates the location of the climatological tropopause.

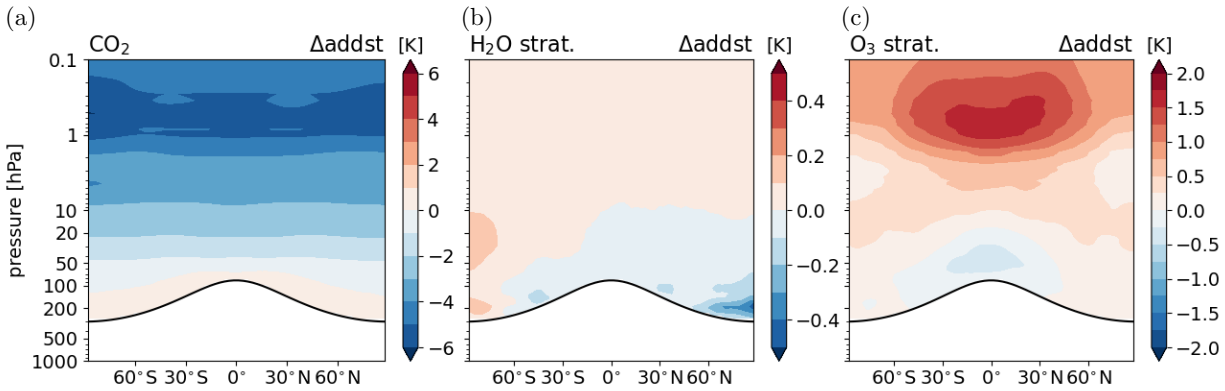

Figure 4.7: Stratospheric temperature adjustment radiatively induced by individual species changes in simulation $ERFCO_2{}^{SSTfix}{}_{chem}$ in comparison to $REF^{SSTfix}{}_{chem}$ in [K]: (a) CO_2, (b) stratospheric H_2O and (c) stratospheric O_3. No significance test is performed for the shown changes as only 2 years are available for the analysis. Note that the colour levels in the individual panel plots differ.

by previous studies (Dietmüller et al., 2014; Nowack et al., 2015; Marsh et al., 2016; Chiodo and Polvani, 2019) is caused by the O_3 increase in the middle and upper stratosphere, which is mainly a rapid adjustment (see Fig. 4.3). This can explain the difference to previous studies and also why there is no significant difference in the stratospheric temperature response between $ECCCO_2{}^{SSTvar}{}_{nochem}$ and $ECCCO_2{}^{SSTvar}{}_{chem}$.

Furthermore, also the temperature response in the troposphere is not significantly different between the simulations $ECCCO_2{}^{SSTvar}{}_{nochem}$ and $ECCCO_2{}^{SSTvar}{}_{chem}$. Accordingly, the response of GSAT without interactive chemistry is 1.07 ± 0.07 K, which is not significantly different from the response with interactive chemistry (1.09 ± 0.06 K, see Tab. 4.2). This indicates that chemical climate feedbacks do not significantly alter the response of GSAT, and thereby the climate sensitivity, in this set-up. This seems to contradict the results by Dietmüller et al. (2014) and Nowack et al. (2015), who found that interactive chemistry (mainly trough the response of stratospheric O_3 and related feedbacks of stratospheric H_2O) significantly dampens the climate sensitivity. A quantification of the radiative contributions of individual chemical and physical rapid adjustment and climate feedbacks and, thereby, resulting explanations will be presented in Sect. 4.3.

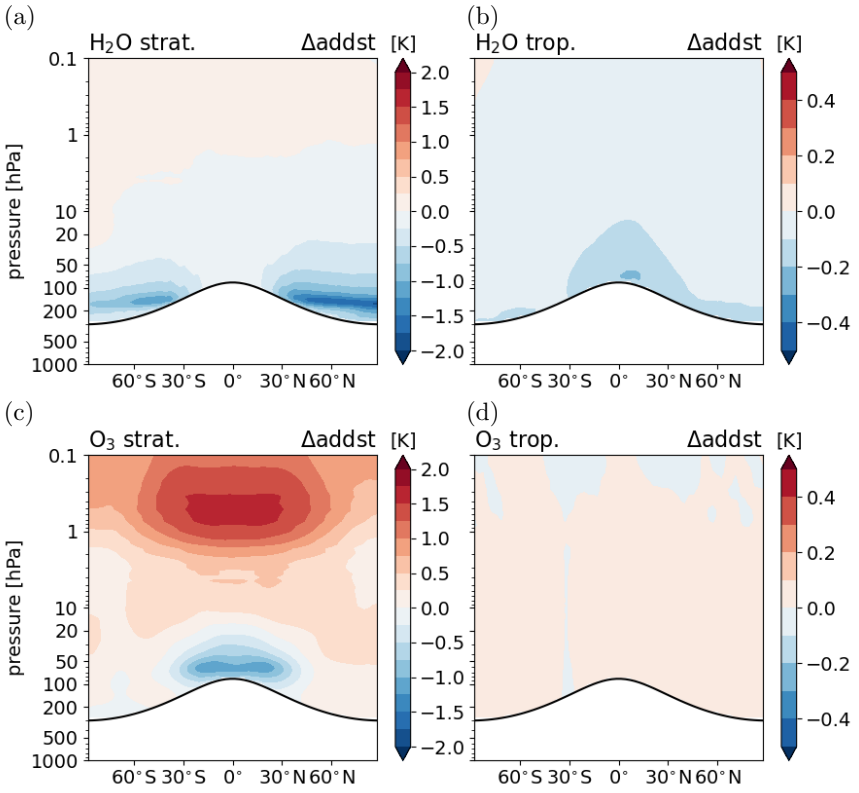

Figure 4.8: Stratospheric temperature adjustment radiatively induced by individual species changes in simulation $ECCCO_2{}^{SSTvar}{}_{chem}$ in comparison to $REF^{SSTvar}{}_{chem}$ in [K]: (a) stratospheric H_2O, (b) tropospheric H_2O, (c) stratospheric O_3 and (d) tropospheric O_3. No significance test is performed for the shown changes as only 2 years are available for the analysis. Note that the colour levels in the individual panel plots differ.

4.2.2 Water vapour response

Figure 4.9 (a) shows increasing tropospheric H_2O mixing ratios due to the residual warming in the fast response, but the effect is small (below 5%). H_2O mixing ratios increase slightly in the lowermost stratosphere as well. This is consistent with increases of the tropical cold point temperature by about 0.2 K (see Fig. 4.10) as the amount of H_2O entering the stratosphere is largely determined by the cold point temperatures (e.g. Randel and Park, 2019). In the upper stratosphere, H_2O mixing ratios decrease due to up to 8% reduced chemical production of H_2O (not shown) consistent with the slower CH_4 oxidation caused by stratospheric cooling (see previous section). In the southern polar stratosphere, decreasing H_2O mixing ratios, strongest in SH winter (see Appendix E.3), point towards enhanced formation of PSCs, consistent with the colder stratosphere and the response of

O_3.

In the full response, H_2O increases significantly throughout the troposphere with a maximum increase of up to 30% in the upper tropical troposphere (see Fig. 4.9 (b)). As tropospheric H_2O mixing ratios are strongly linked to tropospheric temperatures this can be expected. In addition, H_2O mixing ratios increase in the lower stratosphere. This is consistent with an increase of the tropical cold point temperature by about 0.45 K. The H_2O response in the upper stratosphere does not show a significant difference between the fast and the slow response (see Fig. 4.9 (c)). As stratospheric CH_4 mixing ratios are reduced in the full response (see Fig. 4.1 (b)), a weakened production of stratospheric H_2O from CH_4 oxidation can be expected. The diagnosed tendencies of the MESSy submodel MECCA of the chemical contribution to the specific humidity confirm that the chemical production of H_2O is reduced by up to 15% in the full response. However, the increase in the lower stratosphere and the insignificant difference above suggest that the effect of higher cold point temperatures dominates the response of stratospheric H_2O.

Figure 4.9 (e) shows the difference of the relative H_2O responses between the simulations with (ECCCO$_2$$^{\mathrm{SSTvar}}{}_{\mathrm{chem}}$) and without (ECCCO$_2$$^{\mathrm{SSTvar}}{}_{\mathrm{nochem}}$) interactive chemistry, which is not significant below approximately 10 hPa. In the lowermost tropical stratosphere, the increase of H_2O is (not significantly) more pronounced in ECCCO$_2$$^{\mathrm{SSTvar}}{}_{\mathrm{nochem}}$. The larger response is consistent with the response of the tropical cold point temperatures, which is about 0.2 K stronger in the simulation without interactive chemistry. The corresponding reduction of H_2O in the simulation with interactive chemistry is, however, not significant in the zonal mean.

Interactive chemistry leads to a significantly reduced climate response of stratospheric H_2O in the experiments of Dietmüller et al. (2014), Nowack et al. (2015) and Marsh et al. (2016). They attribute the difference of the H_2O response to the O_3 decrease in the lowermost stratosphere, which leads to local radiative cooling that counteracts the warming of the cold point and leads to stronger dehydration. This process seems to be also present in this study. However, the magnitude of the effect is weaker and the resulting differences are not significant. Possible explanations are that, firstly, the magnitude of the perturbation is not strong enough here to detect robust differences. As the relation between temperature and saturation H_2O pressure as given by the Clausius-Clapeyron equation is non-linear, also non-linear responses of stratospheric H_2O can be expected. For instance, Dietmüller et al. (2014) found a stronger feedback of stratospheric H_2O per unit change of GSAT for their 4xCO_2 than for their 2xCO_2 experiment. In addition, different reference conditions

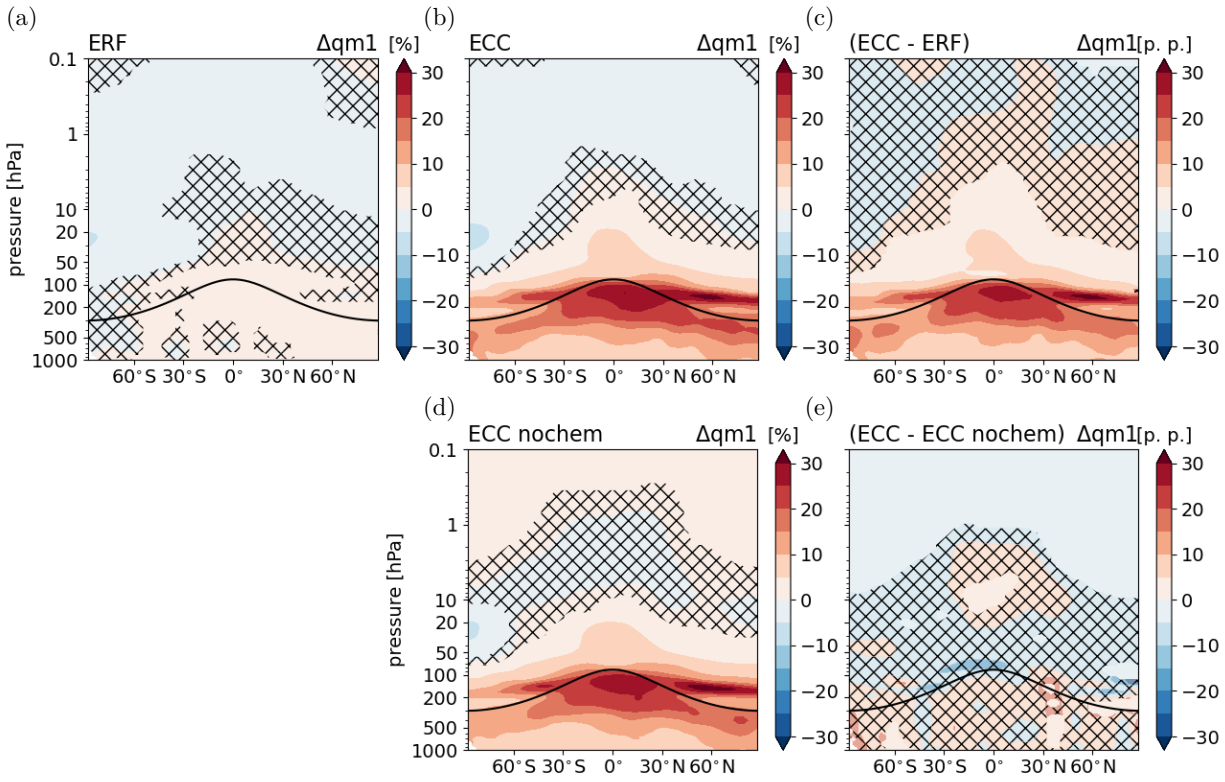

Figure 4.9: Relative differences between the annual zonal mean water vapour of sensitivity simulations (a) ERF$CO_2{}^{\mathrm{SSTfix}}{}_{\mathrm{chem}}$ (fast response) and (b) ECC$CO_2{}^{\mathrm{SSTvar}}{}_{\mathrm{chem}}$ (full response) and their respective reference simulation in [%]. (c) Climate response as difference between the water vapour responses in panels (a) and (b) in [percentage points (p.p.)]. (d) Relative difference between the annual zonal mean water vapour of the simulations without interactive chemistry ECC$CO_2{}^{\mathrm{SSTvar}}{}_{\mathrm{nochem}}$ and REF$^{\mathrm{SSTvar}}{}_{\mathrm{nochem}}$ in [%]. (e) Influence of chemical climate feedbacks presented as difference between the water vapour responses in panels (b) and (d) in [percentage points (p.p.)]. Non-hatched areas are significant on the 95% confidence level according to a Welch's test based on annual mean values. The solid black line indicates the location of the climatological tropopause.

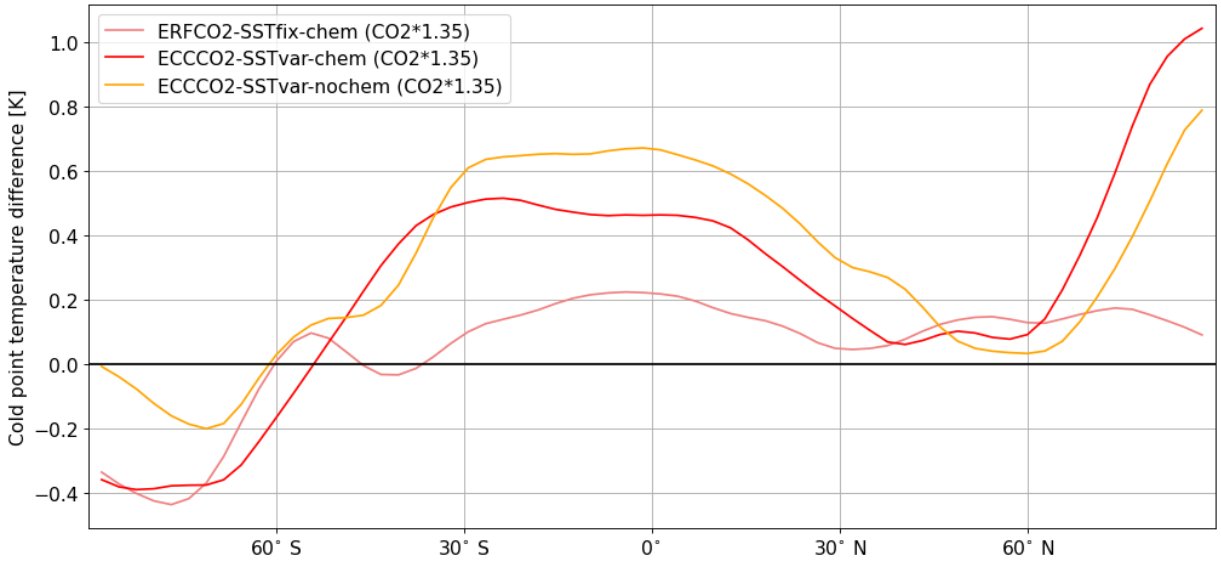

Figure 4.10: Zonal mean difference of cold point temperature between sensitivity simulations perturbed by 1.35× CO_2 increase and the respective references in [K].

of stratospheric H_2O mixing ratios might affect the corresponding climate response. The reference H_2O mixing ratios of the simulations $REF^{SSTvar}{}_{chem}$ and $REF^{SSTvar}{}_{nochem}$ differ by about 8% in the lower stratosphere (see Appendix C). Secondly, also the fast response of O_3 leads to cooling in the tropical tropopause region (see Fig. 4.7 (c)). As the fast response of O_3 is included in the simulation $ECCCO_2{}^{SSTvar}{}_{nochem}$, it can reduce the difference of the lower stratospheric H_2O response between $ECCCO_2{}^{SSTvar}{}_{nochem}$ and $ECCCO_2{}^{SSTvar}{}_{chem}$.

4.2.3 Summary

The fast temperature response is dominated by stratospheric cooling, mainly directly induced by the CO_2 perturbation, whereas the response of tropospheric temperatures is mostly suppressed. In the full response the troposphere warms significantly. The corresponding change of GSAT is 1.09 ± 0.06 K. The only significant difference between the stratospheric temperature response with and without interactive chemistry is enhanced stratospheric cooling in the lowermost stratosphere in the simulation with interactive chemistry. The cooling is radiatively induced by the decrease of O_3 mixing ratios in this region. Previous studies found that interactive chemistry significantly dampens stratospheric cooling in the middle and upper stratosphere (Dietmüller et al., 2014; Nowack et al., 2015; Marsh et al., 2016). However, the present results show that the reduced stratospheric

cooling is mainly induced by the fast response of stratospheric O_3, which is included by the chosen set-up of the simulation without interactive chemistry. Therefore, the temperature response in the middle and upper stratosphere is not significantly different in the simulations with and without interactive chemistry in this study. Additionally, also the temperature response in the troposphere is not significantly different in the simulations with and without interactive chemistry.

H_2O mixing ratios increase significantly in the troposphere and lower stratosphere in the full response. Higher tropical cold point temperatures lead to reduced dehydration and thereby to enhanced entry of H_2O into the stratosphere. The difference of the relative H_2O response between the simulations with and without interactive chemistry is not significant below approximately 10 hPa. Nevertheless, the results indicate that interactive chemistry dampens the increase of cold point temperatures, from which a weaker increase of lower stratospheric H_2O would be expected, which is qualitatively consistent with previous studies.

4.3 Adjustment and feedback analysis

This section presents the radiative effects corresponding to the responses discussed in the previous sections. First, estimates of different definitions of RF and resulting estimates of the climate sensitivity parameter are assessed in Sect. 4.3.1. Subsequently, the rapid radiative adjustments and slow climate feedbacks of individual processes that evolve in the simulations with interactive chemistry are presented in Sects. 4.3.2 and 4.3.3. For radiative estimates of trace gases (CO_2, H_2O, O_3 and CH_4) two different methods are used to derive the radiative effects, whose respective results are compared. In addition, also the potential effect of interactive chemistry on physical climate feedbacks is investigated in Sect. 4.3.4. Finally, Sect. 4.3.5 summarizes the effect of interactive chemistry on the ERF and on the climate sensitivity, and compares the estimates of chemical climate feedbacks of this study to available literature.

4.3.1 Radiative forcing and climate sensitivity

Table 4.2 shows estimates of different definitions of RF, namely RF_{inst}, RF_{adj} and ERF (see Sect. 2.2.1 for definitions) caused by the CO_2 perturbation. RF_{inst} is derived using two different methods, either by the PRP method with MBM RAD, or by additional EMAC atmosphere-only (AGCM) simulations using multiple diagnostic radiation

calls (see Sects. 3.3.1 and 3.3.2). Both methods derive RF_{inst} from a diagnostic radiation call perturbed by the CO_2 increase. The PRP method with input from the simulation $ERFCO_2{}^{SSTfix}{}_{chem}$ indicates a RF_{inst} of 1.081±0.001 W m^{-2}. Note that this is the centred estimate of a forward and a backward calculation (see Sect. 3.3.1). The respective estimates of RF_{inst} for the simulations $ECCCO_2{}^{SSTvar}{}_{chem}$ and $ECCCO_2{}^{SSTvar}{}_{nochem}$ are close to the one for $ERFCO_2{}^{SSTfix}{}_{chem}$, but not identical. The CO_2 perturbation is the same in all the simulations. Therefore, this suggests that the different climate backgrounds affect the radiative effect of the CO_2 perturbation moderately. The corresponding forward estimates differ by 0.004 W m^{-2}, whereas the backward estimates differ by 0.014 W m^{-2} or 0.017 W m^{-2}, if RF_{inst} from $ERFCO_2{}^{SSTfix}{}_{chem}$ is compared to the estimate of either $ECCCO_2{}^{SSTvar}{}_{chem}$ or $ECCCO_2{}^{SSTvar}{}_{nochem}$, respectively (see Tab. 4.2). This indicates that the differences between climate backgrounds of the equilibrium climate change simulations ($ECCCO_2{}^{SSTvar}{}_{chem}$ or $ECCCO_2{}^{SSTvar}{}_{nochem}$) compared to $ERFCO_2{}^{SSTfix}{}_{chem}$ affect the direct radiative effect of the CO_2 perturbation.

The estimates for RF_{inst} from the AGCM simulations are smaller than the ones derived with the PRP method. As already mentioned, the estimates from the PRP method are a combination of a forward and a backward calculation, whereas the AGCM method has the character of a forward calculation. Therefore, the AGCM estimates are closer to the corresponding forward estimates of the PRP method, but still about 0.01 W m^{-2} lower. The remaining difference can be caused by differences of the climate backgrounds between the reference simulations $REF^{SSTfix}{}_{chem}$, $REF^{SSTvar}{}_{chem}$ and $REF^{SSTvar}{}_{nochem}$, and the AGCM simulations, even though the set-up of the AGCM simulations is designed to reproduce the online simulations, e.g. corresponding climatologies for radiatively active trace gases and SSTs and SICs are used (see Sect. 3.1.5). The temporal variability of atmospheric CO_2 mixing ratios is small. Therefore, the use of a monthly mean climatology instead of instantaneous CO_2 mixing ratios is not expected to influence RF_{inst}. However, the use of a monthly climatology of H_2O mixing ratios might affect the estimate of RF_{inst} due to overlapping absorption bands of CO_2 and H_2O (e.g. Petty, 2006).

With the AGCM method RF_{adj} can be estimated as well if the option to calculate the corresponding adjustment of stratospheric temperatures is activated in the diagnostic radiation call (see Sect. 3.3.2). The differences between the respective estimates of RF_{inst} and RF_{adj} indicate a stratospheric temperature adjustment directly induced by the CO_2 perturbation of 0.662 W m^{-2} to 0.663 W m^{-2}. In addition, the estimate of ERF of 1.609±0.154 W m^{-2}, which is derived from the net radiative flux difference between the

simulations $ERFCO_2{}^{SSTfix}{}_{chem}$ and $REF^{SSTfix}{}_{chem}$, is shown in Tab. 4.2. The estimate of ERF is smaller than RF_{adj}, but not significantly different due to its large statistical uncertainty.

Furthermore, Table 4.2 shows estimates of the climate sensitivity parameter λ that are calculated by combining the estimates of RFs and of the corresponding responses of GSAT. For $\lambda_{RF_{inst}}$, RF_{inst} derived with the PRP method is used as it is considered to best represent the radiative effect of the CO_2 perturbation in the simulations. The climate sensitivity parameters of the simulation $ECCCO_2{}^{SSTvar}{}_{chem}$ are not statistically different from the ones of $ECCCO_2{}^{SSTvar}{}_{nochem}$, as neither are the respective responses of GSAT.

The estimate of $\lambda_{RF_{adj}}$ of 0.64±0.03 K / (W m^{-2}) corresponding to the simulation $ECCCO_2{}^{SSTvar}{}_{chem}$ is smaller than previous estimates for 2× and 4×CO_2 experiments with the EMAC model with interactive chemistry (Dietmüller et al., 2014), but in close agreement to $\lambda_{RF_{adj}}$ of $0.63^{+0.05}_{-0.06}$ K / (W m^{-2}) of the corresponding 1.2×CO_2 experiment (Dietmüller, 2011). On the contrary, $\lambda_{RF_{adj}}$ for the simulation $ECCCO_2{}^{SSTvar}{}_{nochem}$ is weaker than previous estimates derived from EMAC simulations without interactive chemistry (Dietmüller, 2011; Dietmüller et al., 2014), which range from $0.70^{+0.02}_{-0.01}$ K / (W m^{-2}) to $0.91^{+0.01}_{-0.01}$ K / (W m^{-2}). Rieger et al. (2017) provide the estimates of $\lambda_{RF_{inst}}$ for the latter simulations without interactive chemistry, which are calculated as the centred estimate of a forward and a backward simulation similarly to this study. These estimates range from 1.10±0.02 K / (W m^{-2}) to 1.37±0.02 K / (W m^{-2}), and are therefore also larger than the present estimate. In the previous simulations without interactive chemistry (Dietmüller, 2011; Dietmüller et al., 2014; Rieger et al., 2017), the chemical tracer distributions of radiatively active gases from the reference simulation are prescribed, whereas in the simulation $ECCCO_2{}^{SSTvar}{}_{nochem}$ climatologies from the simulation $ERFCO_2{}^{SSTfix}{}_{chem}$ are prescribed. Therefore, chemical rapid radiative adjustments are included in the simulation $ECCCO_2{}^{SSTvar}{}_{nochem}$. Thus, the comparison of the climate sensitivity of the simulation $ECCCO_2{}^{SSTvar}{}_{nochem}$ with previous estimates with the EMAC model suggests that chemical rapid radiative adjustments reduce the resulting response of GSAT. The estimates of RF_{inst} and RF_{adj} are not affected by the chemical rapid radiative adjustments, but their presence in the simulation $ECCCO_2{}^{SSTvar}{}_{nochem}$ can affect the resulting response of GSAT. However, different model versions with e.g. different vertical resolution, and different magnitudes of the CO_2 perturbation are used, which might also affect the climate sensitivity. In the following section, individual physical and chemical rapid radiative adjustments are assessed.

Table 4.2: Estimates of different definitions of radiative forcing (RF_{inst}, RF_{adj}, ERF) evaluated at TOA following the CO_2 perturbation in [W m^{-2}], the corresponding responses of global mean surface air temperature (ΔGSAT) in [K], and the corresponding estimates of the climate sensitivity parameter ($\lambda_{RF_{inst}}$, $\lambda_{RF_{adj}}$, λ_{ERF}) in [W m^{-2} K^{-1}].

		ERF chem	ECC chem	ECC nochem
RF_{inst} PRP	[W m^{-2}]	1.081±0.001	1.090±0.001	1.092±0.001
RF_{inst} $PRP^{forward}$	[W m^{-2}]	1.057±0.001	1.061±0.001	1.061±0.001
RF_{inst} $PRP^{backward}$	[W m^{-2}]	1.105±0.001	1.119±0.001	1.122±0.001
RF_{inst} AGCM	[W m^{-2}]	1.049	1.049	1.055
RF_{adj} AGCM	[W m^{-2}]	1.711	1.711	1.718
ERF	[W m^{-2}]	1.609±0.154	-	-
ΔGSAT	[K]	0.07±0.02	1.09±0.06	1.07±0.05
$\lambda_{RF_{inst}}$	[K/(W m^{-2})]	-	1.00±0.05	0.98±0.04
$\lambda_{RF_{adj}}$	[K/(W m^{-2})]	-	0.64±0.03	0.62±0.03
λ_{ERF}	[K/(W m^{-2})]	-	0.68±0.07	-

Values after the ± sign are 2× the standard error of the mean calculated on the basis of 20 annual mean values, which approximate the corresponding 95% confidence intervals. The standard errors for the climate sensitivity parameters are calculated from the standard error of the corresponding radiative forcing std_error_{RF} and the standard error ΔGSAT $std\_error_{\Delta GSAT}$, as $std\_error_{\lambda} = (\sqrt{\frac{std\_error_{RF}^2}{RF^2} + \frac{std\_error_{\Delta GSAT}^2}{\Delta GSAT^2}} \cdot \frac{\Delta GSAT}{RF})$. The AGCM method does not account for interannual variability, which is why no uncertainty estimates are provided for the corresponding radiative forcing estimates. The uncertainty estimates of $\lambda_{RF_{adj}}$ account for the interannual variability of ΔGSAT.

4.3.2 Rapid radiative adjustments

Panel (a) of Fig. 4.11 shows the rapid radiative adjustments that evolve in simulation $ERFCO_2{}^{SSTfix}{}_{chem}$ determined using the PRP method with MBM RAD (see Sect. 3.3.1). The largest contribution is the stratospheric temperature adjustment, which increases RF_{inst} by about 50%. The stratospheric temperature adjustment represents the radiative effect of the total ("bulk") response of temperatures in the stratosphere, either directly induced by the CO_2 perturbation, or indirectly through e.g. the response of O_3 (see Fig. 4.7). The other rapid radiative adjustments have a combined effect of -0.033 W m^{-2}. There are non-zero contributions from the Planck, lapse rate and tropospheric H_2O adjustments associated with the land surface temperature change. The cloud adjustment is positive, but not significantly different from zero. The forward and backward estimates of the cloud, lapse rate and tropospheric H_2O adjustments deviate strongly. This has been already pointed out by Rieger et al. (2017) and Bickel et al. (2020), and can be explained

by the fact that the impact of clouds is also indirectly included in the ambient profiles of the temperature and the humidity, which leads to correlations between these processes (Bickel, 2023). There are significant, but comparably small, rapid radiative adjustments of stratospheric H_2O and O_3. The sum of all rapid radiative adjustments plus RF_{inst} is 1.612 W m^{-2}, which reproduces the ERF derived from the radiative flux difference between the simulations $ERFCO_2{}^{SSTfix}{}_{chem}$ and $REF^{SSTfix}{}_{chem}$ (see Tab. 4.2) almost perfectly. Thus, the residuum is small (RES_{RA}, see Eq. 3.11), which suggests that the individual rapid radiative adjustments are separable if centred estimates are used.

Previous studies indicate as well that the adjustment of stratospheric temperatures is the most important rapid radiative adjustment for CO_2 perturbations (Smith et al., 2018; Bickel et al., 2020). In the multi-model comparison of Smith et al. (2018) it is about 40-45% of RF_{inst} (see their Fig. S3), whereas it is about 65% of RF_{inst} in the study of Bickel et al. (2020). Thus, the present estimate of about 50% of RF_{inst} is in between previous estimates. The positive albedo and tropospheric H_2O, as well as the negative Planck and lapse rate adjustments are qualitatively consistent with previous studies as well (Vial et al., 2013; Smith et al., 2018; Bickel et al., 2020) because these processes are coupled to the residual warming of land surfaces. Additionally, the positive cloud adjustment is consistent with results by Vial et al. (2013) and Smith et al. (2018). In the present study it is about 8% of RF_{inst}, but is strongly variable, whereas it is estimated at nearly 20% of RF_{inst} by Smith et al. (2018). In the studies of Smith et al. (2018) and Vial et al. (2013) the sum of tropospheric rapid radiative adjustments is close to zero for the multi-model mean. In this study, the sum of tropospheric physical rapid radiative adjustments of the surface albedo, clouds, Planck, the lapse rate and tropospheric H_2O is -0.082 W m^{-2}, and thus does not indicate a large effect of tropospheric physical rapid radiative adjustments either. Overall, the estimates of physical rapid radiative adjustments in the present study are in qualitative agreement with previous assessments of CO_2 perturbations.

The estimates shown in Fig. 4.11 do not include the effect of stratospheric temperature adjustment induced by the individual perturbations. Therefore, Tab. 4.3 additionally shows the instantaneous and stratospheric adjusted radiative perturbations for CO_2, H_2O, O_3 or CH_4, derived from the AGCM simulations using multiple diagnostic radiation calls, as described in Sect. 3.3.2. The AGCM method does not account for interannual variability of the radiative estimates because multi-year monthly mean climatologies of the trace gases are prescribed. Therefore, no uncertainty estimates are provided in Tab. 4.3. The uncertainty estimates of the respective perturbation derived with the PRP method can be

used as upper bounds for the interannual variability. The instantaneous estimates of the two methods, PRP and AGCM method, are supposed to be consistent. The rapid radiative adjustments of stratospheric H_2O and O_3 agree well between both methods suggesting robust results. A larger deviation occurs for the adjustment of tropospheric H_2O. As tropospheric humidity is temporally variable, the use of a monthly mean climatology for the perturbation might introduce errors. The AGCM estimate is also not close to the corresponding forward PRP calculation, which is 1.660±0.035 W m^{-2}, because the use of monthly mean instead of instantaneous fields for the perturbations removes part of the correlations between individual perturbations, which lead to large differences between the forward and the backward calculations of the PRP method (Colman and McAvaney, 1997). Combining the forward and the backward calculations of the PRP method reduces the correlations of individual perturbations (see above).

Accounting for the effect of stratospheric temperature adjustment doubles the rapid radiative adjustment of stratospheric H_2O resulting in 0.015 W m^{-2}. Furthermore, the rapid radiative adjustment of stratospheric O_3 changes sign from a positive instantaneous radiative effect of 0.033 W m^{-2} (0.036±0.007 W m^{-2} for the PRP method) to a negative radiative effect of -0.034 W m^{-2} with the stratospheric temperature adjustment included. The corresponding instantaneous radiative effect at TOA is dominated by enhanced absorption of SW radiation due the increased abundance of O_3 resulting in a positive radiative effect. However, if the stratospheric temperature adjustment is included, the associated radiative heating (see Fig. 4.7 (c)) leads to enhanced outgoing LW radiation and counteracts the positive SW effect (see Fig. E.13 in the Appendix). The importance of the stratospheric temperature adjustment for O_3 perturbations has already been noted elsewhere (e.g. Stuber et al., 2001; Dietmüller et al., 2016). Accounting for the effect of stratospheric temperature adjustment also enhances the rapid radiative adjustment of tropospheric O_3, which counteracts the negative adjustment of stratospheric O_3. The rapid radiative adjustment of CH_4 is small as tropospheric CH_4 does not change. The increase of stratospheric CH_4 (see Fig. 4.1 (a)) induces a small positive radiative perturbation with the stratospheric temperature adjustment included due to local radiative cooling. The combined effect of interactive chemistry, namely from O_3 and CH_4, on the ERF is -0.021 W m^{-2}. The adjustment of stratospheric H_2O is assumed to be mainly caused by the increase of cold point temperatures (see Sect. 4.2) and is therefore not considered as a chemical adjustment.

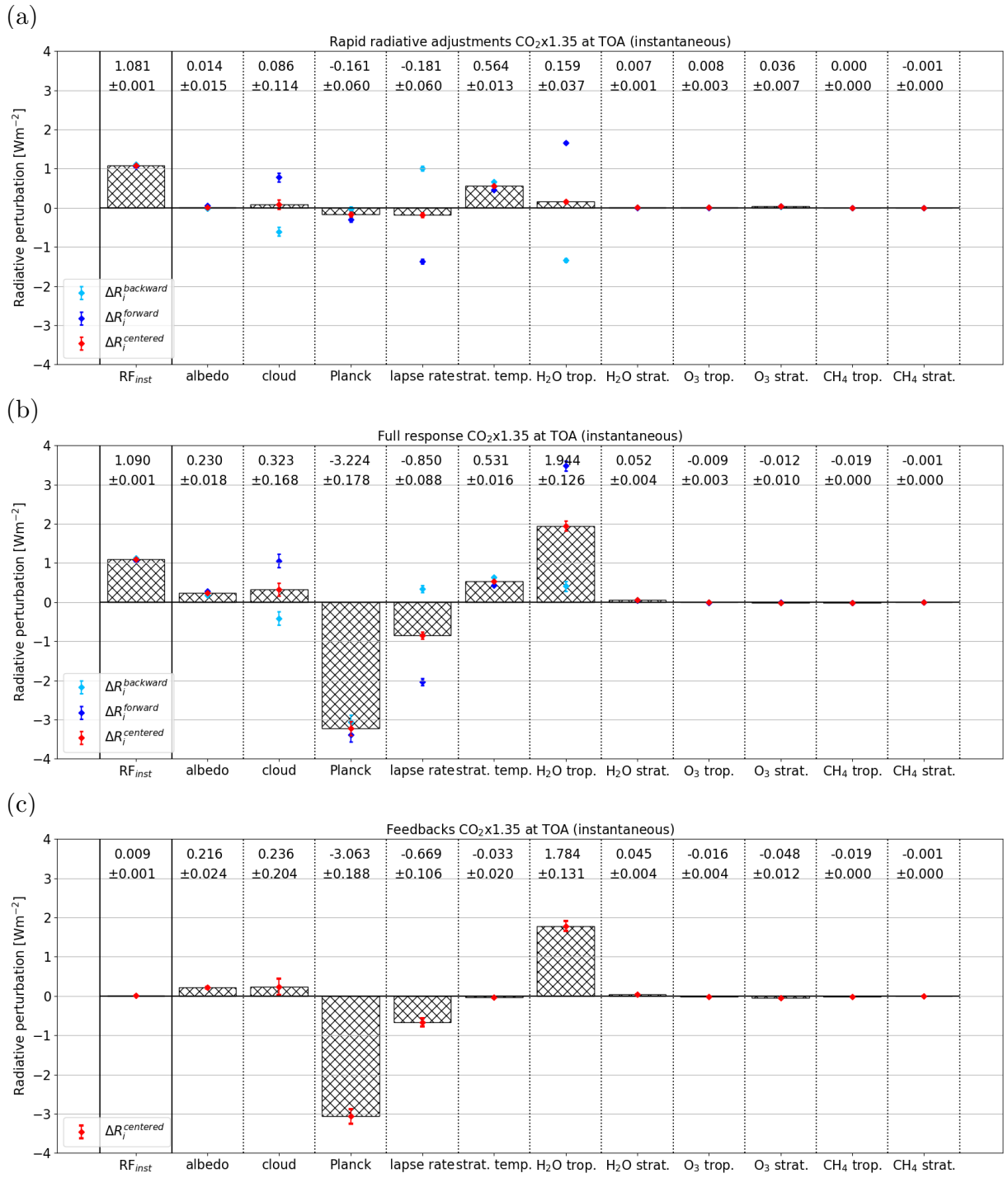

Figure 4.11: Radiative contributions in [W m^{-2}] of individual processes of (a) the fast response (interpreted as rapid radiative adjustments), (b) the full response, and (c) their difference (interpreted as slow climate feedbacks) for the CO_2 perturbation. Values after the ± sign are 2× the standard error of the mean approximating the corresponding 95% confidence interval calculated on the basis of 20 annual mean values.

Table 4.3: Individual radiative effects in [W m^{-2}] of composition changes of H_2O, O_3, and CH_4, split into the respective tropospheric and stratospheric contribution of the fast response in simulation $ERFCO_2{}^{SSTfix}{}_{chem}$ (interpreted as rapid radiative adjustments) and of the full response, either with interactive chemistry ($ECCCO_2{}^{SSTvar}{}_{chem}$), or without interactive chemistry $ECCCO_2{}^{SSTvar}{}_{nochem}$. The radiative estimates are calculated in separate simulations, either offline with MBM RAD, or in an AGCM set-up with EMAC. For the AGCM method both, instantaneous (inst.) and stratospheric adjusted (adj.) estimates, are provided. In addition, the feedback parameters α in [W m^{-2} K^{-1}], i.e. the radiative contributions of the full response minus the fast response normalized by the respective change of GSAT (see Tab. 4.2), are shown for the simulations with interactive chemistry.

	H_2O trop.	H_2O strat.	O_3 trop.	O_3 strat.	CH_4 trop.	CH_4 strat.
Fast [W m^{-2}]						
PRP (inst.)	0.159±0.037	0.007±0.001	0.008±0.003	0.036±0.007	0.0±0.0	-0.001±0.0
inst. AGCM	0.142	0.007	0.008	0.033	0.0	-0.001
adj. AGCM	0.144	0.015	0.012	-0.034	0.0	0.001
Full [W m^{-2}]						
PRP (inst.)	1.944±0.126	0.052±0.004	-0.009±0.003	-0.012±0.01	-0.019±0.0	-0.001±0.0
inst. AGCM	1.979	0.049	-0.008	-0.014	-0.023	-0.001
adj. AGCM	2.007	0.174	-0.013	-0.051	-0.024	-0.003
Full nochem [W m^{-2}]						
PRP (inst.)	1.846±0.109	0.044±0.003	-	-	-	-
inst. AGCM	1.866	0.045	-	-	-	-
adj. AGCM	1.892	0.162	-	-	-	-
α [W m^{-2} K^{-1}]						
PRP (inst.)	1.634±0.278	0.041±0.008	-0.015±0.008	-0.044±0.023	-0.018±0.002	-0.001±0.001
inst. AGCM	1.683	0.038	-0.015	-0.043	-0.021	-0.00
adj. AGCM	1.706	0.145	-0.023	-0.016	-0.022	-0.003

For the estimates with MBM RAD the respective standard error of the mean calculated on the basis of 20 annual mean values is provided, which approximate the corresponding 95% confidence intervals. The standard errors for the feedback parameters α are calculated from the standard error of the corresponding radiative perturbation std_error_{RF} and the standard error of the change of GSAT $std\_error_{\Delta GSAT}$, as $std\_error_{\alpha} = (\sqrt{\frac{std\_error^2_{RF}}{RF^2} + \frac{std\_error^2_{\Delta GSAT}}{\Delta GSAT^2}} \cdot \frac{RF}{\Delta GSAT})$. The AGCM method does not account for interannual variability, which is why no uncertainty estimates are provided for the respective estimates.
The tracer distributions of O_3 and CH_4 is prescribed in the simulation $ECCCO_2{}^{SSTvar}{}_{nochem}$. Therefore, no radiative effects are shown.

4.3.3 Slow climate feedbacks

The radiative effects of individual changes of the full response are shown in Fig. 4.11 (b). The sum of all radiative contributions of the full response plus the corresponding RF_{inst} is 0.054 W m^{-2}, which corresponds to about 5% of the RF_{inst}. This estimate is the residuum term of the PRP method (RES_α, see Eq. 3.12). For the forward and backward calculations the respective estimates are 0.884 W m^{-2} and -0.776 W m^{-2}. Thus, only if the centred estimates are used, the individual feedbacks are separable, which is consistent with the findings of Rieger et al. (2017).

Following the ERF framework, the differences between the radiative effects of full and fast response are interpreted as climate feedbacks, and are shown in Fig. 4.11 (c). The Planck feedback is quantitatively the largest feedback and is negative to balance the positive ERF. There are significant positive feedbacks from the surface albedo, clouds and tropospheric H_2O. The lapse rate feedback is negative. The climate response of stratospheric temperatures induces a small negative feedback of -0.033±0.020 W m^{-2}. The sum of the climate responses of individual stratospheric temperature adjustments of H_2O, O_3 and CH_4 is 0.157 W m^{-2} (calculated as the difference of the difference between instantaneous and stratospheric adjusted estimates from Tab. 4.3) and can therefore not explain the negative bulk stratospheric temperature feedback.

Stratospheric H_2O induces a significant positive climate feedback, which is estimated at 0.045±0.004 W m^{-2} with the PRP method. The corresponding estimate from the AGCM method is 0.042 W m^{-2}, which is calculated as the difference between the radiative effects of the full and the fast response in Tab. 4.3. It is smaller compared to the estimate with the PRP method, but inside the 95% confidence interval of the latter. Accounting for the induced stratospheric temperature adjustment enhances the radiative effect to 0.159 W m^{-2}. The feedback of tropospheric O_3 is estimated at -0.016±0.004 W m^{-2} if derived with the PRP method, which is consistent with the decrease of tropospheric O_3 in the climate response (see Fig. 4.3). Thus, it adds to the negative radiative effect of stratospheric O_3 of -0.048±0.012 W m^{-2}. The corresponding estimates derived with the AGCM method are -0.016 W m^{-2} for tropospheric O_3, and -0.047 W m^{-2} for stratospheric O_3. Including the stratospheric temperature adjustment results in -0.025 W m^{-2} for tropospheric O_3, and -0.017 W m^{-2} for stratospheric O_3. The climate response of tropospheric CH_4 induces a significant negative feedback, which is consistent with the decrease of CH_4. The corresponding estimate is -0.019 W m^{-2} if derived with the PRP method, and -0.023 W m^{-2} if derived with the ACGM method. Accounting for the effect of stratospheric temperature ad-

justment enhances the radiative effect to -0.024 W m^{-2}. Adding the stratospheric adjusted feedback of stratospheric CH_4, enhances the total CH_4 climate feedback to -0.027 W m^{-2}. In summary, the combined effect of O_3 and CH_4, including the associated stratospheric temperature adjustment, is -0.069 W m^{-2}. In addition, stratospheric H_2O can be affected by interactive chemistry as well. Therefore, the following section compares the radiative effects of the stratospheric H_2O response between the simulations with and without interactive chemistry.

4.3.4 Assessment of physical feedback processes

Figure 4.12 compares the individual physical feedbacks that evolve in the simulation with interactive chemistry (ECCCO$_2$$^{\mathrm{SSTvar}}{}_{\mathrm{chem}}$) to the simulation without interactive chemistry (ECCCO$_2$$^{\mathrm{SSTvar}}{}_{\mathrm{nochem}}$) to assess if physical feedbacks are altered by interactive chemistry. For each feedback process the feedback parameter, which is defined as the radiative perturbation normalized by the corresponding change in GSAT, is shown. Here, the radiative perturbation corresponds to the full response, without subtracting the fast response.

The individual feedback parameters do not deviate significantly between the simulations with and without interactive chemistry. The feedback parameters for the albedo, cloud, lapse rate and stratospheric temperature feedbacks are each about 0.03 W m^{-2} K^{-1} lower in the simulation with interactive chemistry. In contrast, the Planck, as well as the tropospheric and stratospheric H_2O feedbacks are larger. For the radiative effect of stratospheric H_2O, the stratospheric adjusted estimates are more meaningful. The AGCM method indicates a stratospheric adjusted climate feedback of stratospheric H_2O of 0.145 W m^{-2} K^{-1} for the simulation with interactive chemistry, or 0.159 W m^{-2} K^{-1} if the full response is considered (see Tab. 4.3). The corresponding radiative effect of the full response is estimated at 0.151 W m^{-2} K^{-1} for the simulation without interactive chemistry. Thus, the feedback is estimated to be about 0.008 W m^{-2} K^{-1} larger in the simulation with interactive chemistry. This is not consistent with the relative response of stratospheric H_2O, which is slightly, but not significantly, dampened by the O_3 response in the simulation with interactive chemistry (see Sect. 4.2). This result will be compared to available literature and discussed in more detail below.

The sum of all physical feedback parameters shown in Fig. 4.12, i.e. excluding O_3 and CH_4, is -0.958±0.407 W m^{-2} K^{-1} in the simulation with interactive chemistry, and -0.896±0.407 W m^{-2} K^{-1} in the simulation without interactive chemistry. These estimates do not suggest a significant influence of interactive chemistry on physical climate feedbacks.

Another aspect to note is that the residuum of the PRP method for the simulation without interactive chemistry, calculated as the sum of all radiative contributions of the full response plus RF_{inst} (RES_α, see Eq. 3.12), is 0.129 W m^{-2} (not shown). This corresponds to about 12% of the RF_{inst} and suggests that for the simulation without interactive chemistry the PRP analysis is not closed. The chemical rapid radiative adjustments of O_3 (and CH_4) are included in this simulation, but are not accounted for in the PRP analysis. The instantaneous effect of the O_3 rapid radiative adjustment is positive, but accounting for the corresponding stratospheric temperature adjustment makes it a negative rapid radiative adjustment, which might reduce the residuum.

Table 4.4 compares the feedback parameters of the simulation ECCCO$_2$$^{\text{SSTvar}}_{\text{chem}}$ to literature values. The feedback parameter of the surface albedo is in close agreement to the estimates of Rieger et al. (2017), but is at the lower end of the range of CMIP5 and CMIP6 models (Vial et al., 2013; Zelinka et al., 2020). The cloud feedback compares well to the literature values, which cover a wide range, however. The Planck feedback is comparably weak in this study. However, its 95% uncertainty range still covers the literature estimates. The lapse rate feedback is close to the estimate of Rieger et al. (2017), but more negative than the CMIP5 and CMIP6 multi-model mean estimates, while still staying in the comparably wide range of individual model estimates. The sum of tropospheric and stratospheric H_2O feedbacks reproduces the multi-model mean estimates reported by Zelinka et al. (2020) almost perfectly. The corresponding stratospheric adjusted estimate of the climate feedback of stratospheric H_2O of 0.159 W m^{-2} K^{-1} (see Tab. 4.3) agrees well with the CMIP5 multi-model mean estimate of 0.17±0.05 W m^{-2} K^{-1} provided by Banerjee et al. (2019). Overall, the physical climate feedbacks are in the range of previous estimates, while the largest deviations occur for the albedo and the Planck feedbacks.

4.3.5 Summary: Impact of interactive chemistry on ERF and climate sensitivity

This section summarizes the effect of interactive chemistry on the ERF and on the climate sensitivity, and compares the individual chemical rapid radiative adjustments and climate feedbacks to available literature. As accounting for the induced stratospheric temperature adjustment is crucial for perturbations of O_3 and stratospheric H_2O, and additionally modifies the radiative effect of CH_4, only stratospheric adjusted radiative estimates are repeated here. This is supported by the fact that both methods to derive instantaneous radiative effects of individual perturbations applied in this thesis, the PRP and the AGCM

Table 4.4: Feedback parameters of physical processes in [W m^{-2} K^{-1}] of this study (from Fig. 4.12) compared to literature values (Rieger et al., 2017; Vial et al., 2013; Zelinka et al., 2020). The estimates for 1.2× and 4×CO_2 of Rieger et al. (2017) are shown. The multi-model mean estimates of Vial et al. (2013) and Zelinka et al. (2020) are based on 4×CO_2 experiments from either CMIP5, or CMIP6. Values in brackets indicate the minimum and maximum feedback parameter of individual models.

	Results of this study (with interactive chemistry)	EMAC 1.2×CO_2 (Rieger et al., 2017)[1]	EMAC 4×CO_2 (Rieger et al., 2017)[1]	CMIP5 (Vial et al., 2013)[2]	CMIP5 (Zelinka et al., 2020)[3]	CMIP6 (Zelinka et al., 2020)[4]
albedo	0.211±0.025	0.25	0.20	0.28 [0.16;0.39]	0.45 [0.21;0.71]	0.45 [0.26;0.60]
clouds	0.296±0.156	0.25	0.50	0.27 [-0.36,1.21]	0.34 [-0.19;1.19]	0.42 [-0.36;1.71]
Planck	-2.952±0.301	-3.20	-3.20	-3.18 [-3.27;-3.10]	-3.27 [-3.38;-3.20]	-3.27 [-3.35;-3.20]
lapse rate	-0.778±0.105	-0.75	-0.85	-0.60 [-0.97;-0.23]	-0.48 [-0.96;-0.12]	-0.50 [-1.30;-0.09]
H_2O	1.828±0.191 (trop. + strat.)	1.75	2.20	1.68 [1.43;1.94]	1.81 [1.50;2.25]	1.83 [1.61;2.19]

[1] Combination of forward and backward PRP analysis, estimated from their Fig. 5.

[2] NCAR (National Center for Atmospheric Research) kernel results. The shown estimates have the character of feedbacks as the fast response is subtracted.

[3] Kernel results of their Tab. S2.

[4] Kernel results of their Tab. S1.

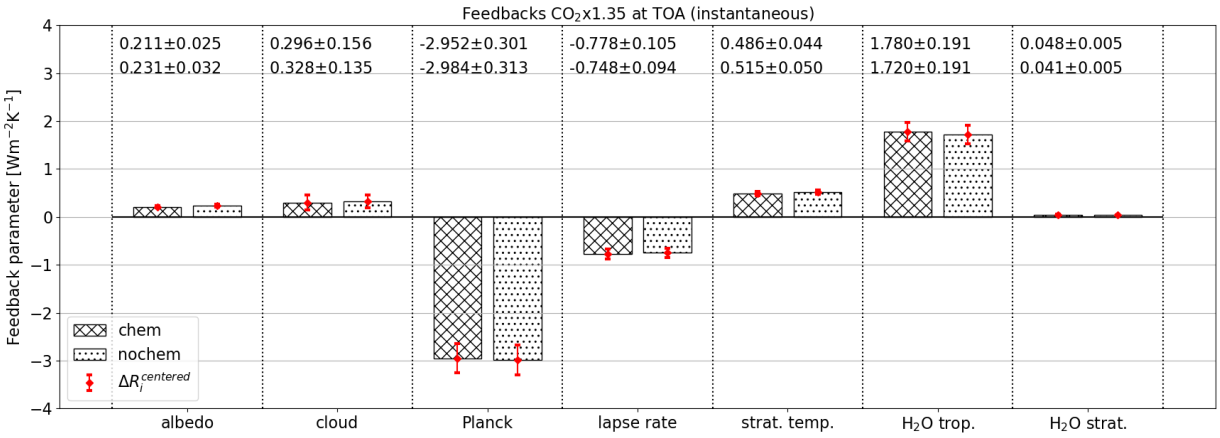

Figure 4.12: Feedback parameters in [W m^{-2} K^{-1}] of individual processes either derived from the simulation with interactive chemistry (ECCCO$_2$$^{\mathrm{SSTvar}}{}_{\mathrm{chem}}$; left bars) or without interactive chemistry (ECCCO$_2$$^{\mathrm{SSTvar}}{}_{\mathrm{nochem}}$; right bars). At the top of the figure, the corresponding mean values are listed. The upper estimates correspond to the simulation with interactive chemistry, and the lower estimates to the simulation without. Values after the ± sign are 2× the standard error of the mean approximating the corresponding 95% confidence interval calculated on the basis of 20 annual mean values.

method, yield consistent results for perturbations of O_3, stratospheric H_2O and CH_4.

Physical rapid radiative adjustments of the surface albedo, clouds, Planck, the lapse rate, and tropospheric H_2O are overall in qualitative agreement with previous studies for CO_2 perturbations. The fast response of stratospheric O_3 induces a negative rapid radiative adjustment of -0.034 W m^{-2}, whereas the fast response of tropospheric O_3 induces a positive rapid radiative adjustment of 0.012 W m^{-2}. The rapid radiative adjustment of tropospheric CH_4 is negligible, whereas stratospheric CH_4 induces a small positive rapid radiative adjustment of 0.001 W m^{-2} due to its increase in the stratosphere and associated local radiative cooling. The fast response of stratospheric H_2O is assumed to be mainly caused by the response of cold point temperatures (see Sect. 4.2) and is therefore not considered as a chemical adjustment. Thus, in the present simulations interactive chemistry influences the ERF mainly by the effect of O_3 with a small contribution of CH_4 resulting in a total chemical rapid radiative adjustment of -0.021 W m^{-2} or -1.3%.

The full response of tropospheric O_3 induces a negative radiative perturbation of -0.013 W m^{-2}, which corresponds to a feedback parameter of -0.012 W m^{-2} K^{-1}. This adds to the negative radiative perturbation of stratospheric O_3 of -0.051 W m^{-2}, which corresponds to a feedback parameter of -0.047 W m^{-2} K^{-1}. However, strictly follow-

ing the ERF concept, only the difference between the full and the fast response is interpreted as climate feedback. If the corresponding rapid radiative adjustments are subtracted, the climate feedback parameter of O_3 is -0.023 W m^{-2} K^{-1} for tropospheric, and -0.016 W m^{-2} K^{-1} for stratospheric O_3. Previous studies of the feedback parameter of total O_3 following a CO_2 perturbation have assessed the full response. The corresponding estimates range from -0.015 W m^{-2} K^{-1} and -0.022 W m^{-2} K^{-1} (Dietmüller et al., 2014), -0.018 W m^{-2} K^{-1} (Marsh et al., 2016), -0.046±0.018 W m^{-2} K^{-1} (Thornhill et al., 2021a), to -0.12 W m^{-2} K^{-1} (Nowack et al., 2015, if a corresponding GSAT response of 5.75 K is assumed). The feedback parameter of total O_3 in the full response of -0.059 W m^{-2} K^{-1} in the present study lies in the range of previous estimates, but is more pronounced than the estimates by Dietmüller et al. (2014), who also used the EMAC model. Part of the difference can be explained by the different sign of the feedback of tropospheric O_3. Dietmüller et al. (2014) found a positive feedback parameter of 0.008 W m^{-2} K^{-1} to 0.009 W m^{-2} K^{-1} for tropospheric O_3 compared to the negative feedback parameter of -0.012 W m^{-2} K^{-1} in this study. The decrease of tropospheric CH_4 mixing ratios leads to reduced O_3 production and thereby modifies the response of O_3 (see Sect. 4.2). However, also the negative feedback of stratospheric O_3 is more pronounced here, which might be explained by the different magnitude of the perturbations. Dietmüller et al. (2014) noted differences between their 2× and 4×CO_2 experiments. Therefore, deviations for the 1.35×CO_2 in this study can be expected. In addition, the different vertical resolution of the models might affect the response of stratospheric O_3.

The full response of tropospheric CH_4 induces a negative radiative perturbation of -0.024 W m^{-2} that is enhanced by -0.003 W m^{-2} by the response of stratospheric CH_4 resulting in -0.027 W m^{-2}, which corresponds to a feedback parameter of -0.024 W m^{-2} K^{-1}. Subtracting the small rapid radiative adjustment of stratospheric CH_4 results in a feedback parameter of -0.025 W m^{-2} K^{-1}. Previous estimates of the CH_4 feedback are derived from the change of atmospheric CH_4 lifetime, and range from -0.014±0.067 W m^{-2} K^{-1} (Thornhill et al., 2021a, if the estimates for biogenic volatile organic compounds, lightning NO_x and meteorology are combined[3]), -0.03±0.01 W m^{-2} K^{-1} (Heinze et al., 2019) to -0.036 W m^{-2} K^{-1} (Dietmüller et al., 2014). The present estimate is in the range of previous estimates. However, it is already known that the direct radiative effect of CH_4 is underestimated by the used ECHAM5 radiative transfer scheme (Winterstein et al., 2019;

[3]If the model CESM2-WACCM, which projects a prolongation of CH_4 lifetime with climate change, is excluded, the CH_4 feedback is estimated at -0.053±0.010 W m^{-2} K^{-1}. The given uncertainties are standard deviations across models.

Nützel et al., 2023). Applying the formula of Etminan et al. (2016) for the stratospheric adjusted radiative effect of CH_4 to the change of CH_4 mixing ratio results in -0.059 W m^{-2}, which corresponds to a feedback parameter of -0.054 W m^{-2} K^{-1}. Thus, this suggests a more pronounced negative radiative feedback if a different radiation scheme, that better represents the radiative effect of CH_4, would be used.

The feedback parameters of physical processes in the troposphere, i.e. the surface albedo, clouds, Planck, the tropospheric lapse rate, the stratospheric temperature and tropospheric H_2O are in general agreement with previous estimates. Moreover, the present analysis does not suggest that the latter feedbacks are altered by interactive chemistry as the estimates of individual feedbacks are not significantly different if interactive chemistry is used in the simulation setup. In the simulation with interactive chemistry, the radiative effect of the full response of stratospheric H_2O is estimated at 0.159 W m^{-2} K^{-1}, whereas in the simulation without interactive chemistry it is estimated at 0.151 W m^{-2} K^{-1}. Thus, the effect of interactive chemistry enhances the climate feedback parameter of stratospheric H_2O by 0.008 W m^{-2} K^{-1}, which counteracts the negative feedbacks of O_3 and CH_4. This finding contradicts previous studies, which indicate a reduced increase of stratospheric H_2O and an associated negative radiative effect of interactive chemistry, which ranges from -0.023 W m^{-2} K^{-1} (Marsh et al., 2016), -0.034 and -0.043 W m^{-2} K^{-1} (Dietmüller et al., 2014) to -0.14 W m^{-2} K^{-1} (Nowack et al., 2015, if a corresponding GSAT response of 5.75 K is assumed). In this study, the difference of the response of stratospheric H_2O mixing ratios between the simulation with and without interactive chemistry is not significant. Possible explanations for this disagreement with previous studies are discussed in more detail in Sect. 4.2. Firstly, the magnitude of the CO_2 perturbation might be too small to detect a robust result from the statistical variability. Secondly, part of the reduction of lower stratospheric O_3, that leads to the weakened response of stratospheric H_2O, is included in the response without interactive chemistry because a climatology of O_3 from the simulation $ERFCO_2{}^{SSTfix}{}_{chem}$ is prescribed, which includes the corresponding rapid radiative adjustments.

In summary, the combined climate feedback of O_3 and CH_4 corresponds to a feedback parameter of -0.063 W m^{-2} K^{-1}. Contrary to previous studies, interactive chemistry enhances the climate feedback parameter of stratospheric H_2O by 0.008 W m^{-2} K^{-1}, so that the total climate feedback parameter of interactive chemistry is estimated at -0.056 W m^{-2} K^{-1}. Therefore, a reduced climate sensitivity due to interactive chemistry would be expected from the analysis of individual feedbacks. However, in the present study

there is no significant difference regarding the response of GSAT, and of the corresponding climate sensitivity parameter, between the simulations with and without interactive chemistry.

Chapter 5

CH_4 perturbation

This chapter presents the response of chemically active species and physical parameters to the increase of present-day CH_4 emissions by a factor of 2.75. It is structured similarly as the previous chapter addressing the CO_2 perturbation. For each parameter the fast, the full and the slow climate response, calculated as their difference, are shown. First, the responses of the chemically active species CH_4 and O_3 are presented in Sect. 5.1, followed by the response of the temperature and the humidity in Sect. 5.2. Subsequently, individual radiative contributions to the ERF and the climate sensitivity are presented in Sect. 5.3.

5.1 Atmospheric response of chemically active species

5.1.1 Response of CH_4

Figure 5.1 shows the zonal mean distribution of CH_4 mixing ratios of the reference simulation $REF^{SSTfix}{}_{chem}$ and of the simulations perturbed by increased CH_4 emissions by a global factor of 2.75, namely $ERFCH_4{}^{SSTfix}{}_{chem}$ and $ECCCH_4{}^{SSTvar}{}_{chem}$. $ERFCH_4{}^{SSTfix}{}_{chem}$ represents the respective fast response (see Fig. 5.1 (b)). As expected, CH_4 mixing ratios increase everywhere. Hereby, the increase factor of CH_4 mixing ratios is even higher than the increase factor of the emissions. Tab. 5.1 shows that an increase of CH_4 emissions by a factor of 2.75 results in an increase of the global mean surface CH_4 mixing ratio by a factor of 4.76. This is caused by a large extension of the tropospheric CH_4 lifetime by 6.89 a to 14.48 a (see Tab. 5.1). The corresponding response of OH, as shown in Figure 5.2 (a), shows that tropospheric OH is reduced by up to 60%. The strong CH_4 perturbation decreases OH mixing ratios as OH is depleted by the CH_4 oxidation, thereby extending the

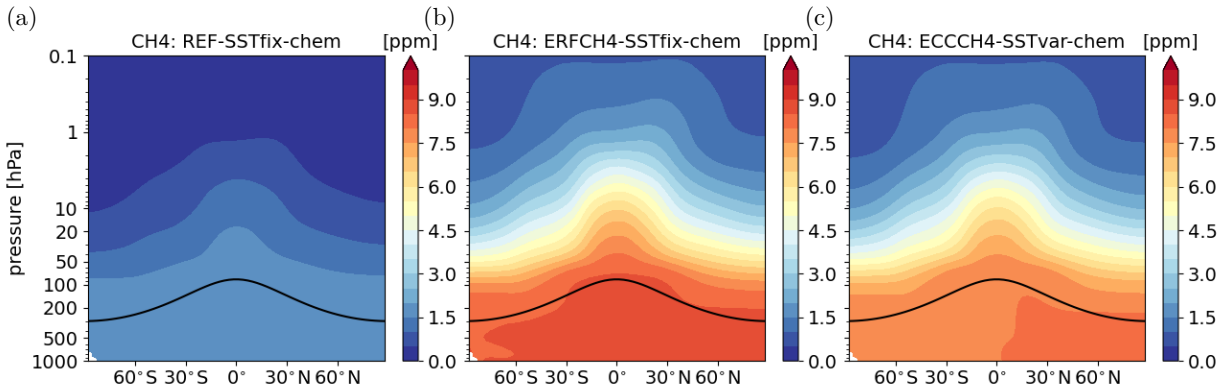

Figure 5.1: Annual zonal mean distribution of CH_4 mixing ratios in simulation (a) $REF^{SSTfix}{}_{chem}$, (b) $ERFCH_4{}^{SSTfix}{}_{chem}$ (fast response) and (c) $ECCCH_4{}^{SSTvar}{}_{chem}$ (full response) in [ppm].

CH_4 lifetime.

A similar effect was found by Winterstein et al. (2019) who analysed the fast response of 2× and 5×CH_4 surface mixing ratios in a set-up with prescribed CH_4 surface mixing ratios also using the CCM EMAC. The magnitude of the present CH_4 perturbation is comparable to their 5×CH_4 experiment. In particular, to reach the prescribed CH_4 surface mixing ratios an artificial surface emission flux is calculated in their set-up. The increase factor of the artificial flux that corresponds to an increase of 5×CH_4 is 2.75 (Stecher et al., 2021), exactly the increase factor of CH_4 surface emissions used in this study. In the present study the increase of emissions results in a close to fivefold increase of the CH_4 surface mixing ratio. The global mean reference CH_4 mixing ratio and the corresponding artificial flux are slightly lower in Winterstein et al. (2019), namely about 1.8 ppmv and 567.7 Tg(CH_4) a^{-1}. Additionally, the spatial distribution of the artificial flux is different and might be unrealistic. Therefore, it is not surprising that the increase factor of CH_4 mixing ratios is not exactly the same in this study. Winterstein et al. (2019) assessed an extension of the CH_4 lifetime by 7.54 a in their 5×CH_4 experiment. This is consistent with the CH_4 lifetime response of 6.89 a here considering the slightly weaker increase of CH_4 mixing ratios.

In the full response, as shown in Fig. 5.1 (c), CH_4 mixing ratios decrease in comparison to the fast response. Similar as in the climate response of the CO_2 perturbation (see previous chapter) higher tropospheric temperatures lead to increased production of OH. Additionally, the temperature dependent reaction rate coefficient leads to a faster CH_4

Table 5.1: Global mean values of tropospheric CH_4 lifetime with respect to the oxidation with OH and CH_4 surface mixing ratios for the reference simulations and CH_4 perturbation simulations. The corresponding interannual standard deviation based on 20 annual mean values is given to estimate the year to year variability.

	Trop. CH_4 lifetime [a]	CH_4 surface VMR [ppmv]
$REF^{SSTfix}{}_{chem}$	7.59 ± 0.03	1.82 ± 0.00
$REF^{SSTvar}{}_{chem}$	7.58 ± 0.03	1.82 ± 0.00
$ERFCH_4{}^{SSTfix}{}_{chem}$	14.48 ± 0.04	8.66 ± 0.01
$ECCCH_4{}^{SSTvar}{}_{chem}$	13.20 ± 0.08	8.05 ± 0.01

oxidation. The climate response of OH is shown in Fig. 5.2 (c) as difference between the full and the fast response. The full response of tropospheric OH weakens the decrease of the fast response by up to 8 p.p.. The tropospheric pattern of the OH climate response is similar to the one resulting from the CO_2 perturbation (see Fig. 4.3 (c)) with two maxima in the middle and upper tropical troposphere. Stecher et al. (2021) analysed the climate response of 2× and 5× CH_4 surface mixing ratios corresponding to Winterstein et al. (2019). Their response pattern of OH is qualitatively consistent with Fig. 5.2 (c) as well.

The sensitivity of the CH_4 lifetime per unit change of GSAT is $\frac{-1.27\ a}{1.17\ K}$ =-1.09 a K^{-1} or -7.6% K^{-1} (calculated with the CH_4 lifetimes in Tab. 5.1 and see below for the response of GSAT). Both, the absolute and the relative sensitivity, are larger compared to the CO_2 perturbation experiments, which is possibly due to the different CH_4 conditions in the respective fast response ($ERFCO_2{}^{SSTfix}{}_{chem}$ and $ERFCH_4{}^{SSTfix}{}_{chem}$).

In the study of Stecher et al. (2021) the sensitivity of CH_4 lifetime per unit change of GSAT is $\frac{-1.17\ a}{1.28\ K}$ =-0.91 a K^{-1}, and thereby weaker compared to the respective value of the present study. The major difference between the simulation set-ups is that CH_4 mixing ratios can not respond to the lifetime response in the set-up of Stecher et al. (2021). This suggests that in the present study the sensitivity of CH_4 lifetime towards climate change is stronger because the CH_4-OH feedback is included in the response of OH and of the CH_4 lifetime. The same is indicated by the results of the CO_2 perturbation.

5.1.2 Response of O_3

The response of O_3 is shown in Fig. 5.3. In the fast response (Fig. 5.3 (a)), tropospheric O_3 increases significantly by up to 60% in the upper tropical troposphere. The CH_4 perturbation leads to enhanced O_3 formation by enhanced production of NMHCs and CO through CH_4 oxidation (see Sect. 2.4 for details). Stratospheric cooling (see Fig. 5.6) leads

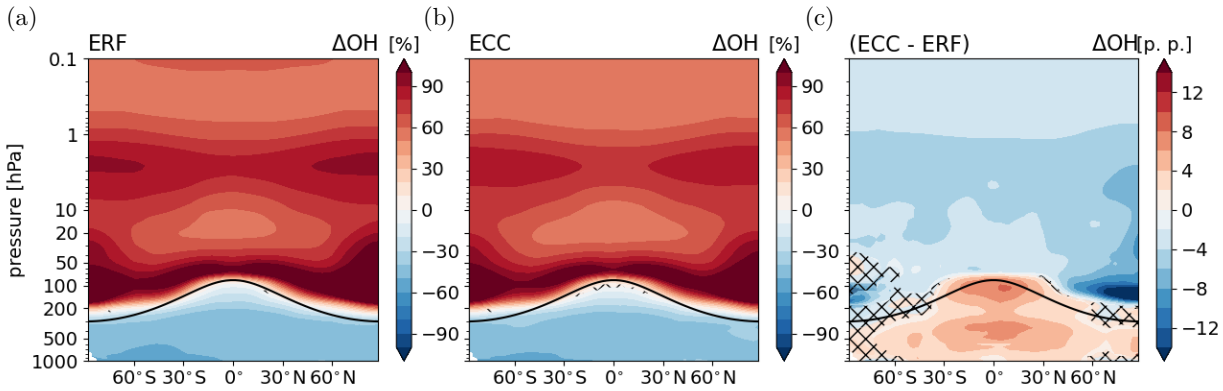

Figure 5.2: Relative differences between the annual zonal mean OH mixing ratios of sensitivity simulations (a) ERFCH$_4$$^{\mathrm{SSTfix}}_{\mathrm{chem}}$ (fast response) and (b) ECCCH$_4$$^{\mathrm{SSTvar}}_{\mathrm{chem}}$ (full response) and their respective reference simulation in [%]. (c) Climate response as difference between the OH responses in panels (a) and (b) in [percentage points (p.p.)]. Non-hatched areas are significant on the 95% confidence level. The solid black line indicates the climatological tropopause.

to O_3 increases in the middle stratosphere. In the upper stratosphere and mesosphere above 1 hPa, O_3 decreases due to enhanced catalytic depletion by HO_x. HO_x is increased by enhanced production of stratospheric H_2O due to CH_4 oxidation and also by enhanced formation via the sink reaction of CH_4 with $O(^1D)$ (see Sect. 2.4 for details). In the lower tropical stratosphere, O_3 decreases, which can be explained by reduced photochemical production caused by enhanced absorption of ultraviolet radiation above, where O_3 increases. This so-called reverse self-healing effect (Rosenfield et al., 2002; Portmann and Solomon, 2007) is also effective for the CO_2 perturbation (see previous chapter). The fast response of O_3 is consistent with the fast response evolving in the comparable $5\times CH_4$ surface mixing ratio experiment (Winterstein et al., 2019), as the same processes are effective, which are explained in more detail by Winterstein et al. (2019).

The climate response of O_3 shown as the difference between full and fast response (see Fig. 5.3 (c)) shows a strong decrease of O_3 mixing ratios in the lower stratosphere, which indicates enhanced tropical upwelling. In the polar region of the NH, O_3 mixing ratios are enhanced pointing towards strengthened poleward and downward transport. Apart from that, the full stratospheric O_3 response is mainly caused by the fast response. Tropospheric O_3 decreases as result of climate warming, except for the tropical middle troposphere, where the response shows a weak, not significant, increase in the zonal mean. The climate response of O_3 is qualitatively consistent with the climate response pattern resulting from

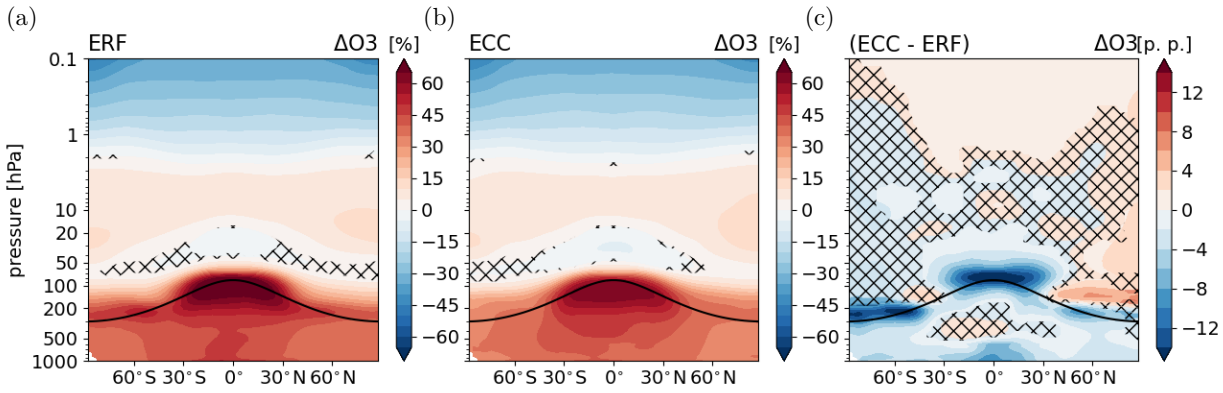

Figure 5.3: As Fig. 5.2 for O_3.

the CO_2 perturbation (see Fig. 4.3), even though the fast response is very different as CH_4 directly affects chemical interactions.

The similarity of the climate responses resulting from CO_2 and CH_4 perturbation has been also noted by Stecher et al. (2021). However, the O_3 climate response resulting from the CH_4 perturbation in their set-up shows a significant increase of O_3 in the tropical middle troposphere. As the main difference between their set-up and the present is the treatment of CH_4, this suggests an effect of the climate feedback of CH_4 on O_3. A similar effect was noted for the CO_2 perturbation (see previous chapter). To better understand the importance of individual processes that contribute to the fast and the climate response of O_3, the next section attributes the response of O_3 to separate processes.

5.1.3 Contribution of individual processes to the tropospheric O_3 response

This section attributes the tropospheric O_3 response as presented in the previous section to individual categories representing different processes of O_3 production using diagnostic output from the MESSy submodel TAGGING (Grewe et al. (2017); Rieger et al. (2018); see Sect. 3.1.6). The categories of O_3 production that are considered here are the same as for the CO_2 perturbation:

- through photolysis in the stratosphere (*O_3 stratosphere*),
- from emissions of lightning NO_x (*O_3 lightning*),
- from biogenic precursor emissions (*O_3 biogenic*),

- from products of the CH_4 decomposition (O_3 *CH*$_4$),
- from products of the N_2O decomposition (O_3 *N*$_2$*O*),
- from biomass burning precursor emissions (O_3 *biomass burning*)
- and from anthropogenic precursor emissions (O_3 *anthropogenic*).

Fig. 5.4 shows the fast response of individual O_3 categories. Shown is the difference between ERFCH$_4$$^{\text{SSTfix}}_{\text{chem}}$ and REF$^{\text{SSTfix}}_{\text{chem}}$ in one category divided by the total reference O_3

$$\Delta O_{3_{\text{cat}}} = \frac{O_{3_{\text{cat,ERF}}} - O_{3_{\text{cat,REF}}}}{O_{3_{\text{total,REF}}}}$$

allowing a direct comparison with the relative response of total O_3.

The O_3 mixing ratios increase in all categories except for the category O_3 *stratosphere* in the fast response. This category shows decreased O_3 production through photolysis of O_2 in the lower stratosphere consistent with the reverse self-healing effect. The increase is strongest in the category O_3 *CH*$_4$. The CH_4 perturbation leads to an enhanced abundance of NMHCs and CO produced by the CH_4 oxidation, which contribute to the formation of O_3. The increase of this category is most pronounced in the upper tropical troposphere and reaches up to 30% relative to the total reference O_3. The larger abundance of NMHCs and CO also affects O_3 production of the other categories as their reaction with precursors from other categories, in particular NO_x, leads to enhanced O_3 production in the category O_3 *CH*$_4$, but also in the other categories. In particular, the category O_3 *lightning* shows O_3 increases of up to 20% relative to the total reference O_3, even though emissions of lightning NO_x decrease by 0.32 Tg(N) a^{-1} globally in the simulation ERFCH$_4$$^{\text{SSTfix}}_{\text{chem}}$ compared to REF$^{\text{SSTfix}}_{\text{chem}}$ (see Appendix E.1). The CH_4 perturbation leads to upper tropospheric/lower stratospheric warming peaking at around 100 hPa in the tropics (see Fig. 5.6 for the temperature response). The higher static stability leads to less convection and thereby to decreasing lightning NO_x emissions. Upper troposphere/lower stratosphere warming following increased CH_4 has been already noted and is expected to be even more pronounced if SW absorption by CH_4 is accounted for in the simulation set-up (Modak et al., 2018; Allen et al., 2023). Nevertheless, the enhanced abundance of precursors from CH_4 oxidation lead to enhanced O_3 production in this category. The category showing the third most pronounced increase is O_3 *anthropogenic*. Here, the increase relative to the total reference O_3 is with up to 15% most pronounced in the lower NH.

Fig 5.5 shows the climate response of individual categories calculated as the difference between the fast and full response of each category

$$\Delta O_{3_{\text{cat, climate response}}} = \left(\frac{O_{3_{\text{cat,ECC}}} - O_{3_{\text{cat,REF}}}}{O_{3_{\text{total,REF}}}}\right) - \left(\frac{O_{3_{\text{cat,ERF}}} - O_{3_{\text{cat,REF}}}}{O_{3_{\text{total,REF}}}}\right).$$

The category *O_3 stratosphere* shows increasing tropospheric O_3 mixing ratios in the climate response. The increase is significant everywhere, except for the extratropical SH and the lower tropical troposphere. The increase indicates enhanced transport of stratospheric O_3 into the troposphere, consistently with the climate response following the CO_2 perturbation. In the lowermost tropical stratosphere, O_3 mixing ratios decrease strongest in this category. The mixing ratios of the category *O_3 lightning* increase in the tropical middle troposphere resulting from an increase of the lightning NO_x emissions by 0.20 Tg(N) a^{-1} in ECCCH$_4$$^{\text{SSTvar}}_{\text{chem}}$ compared to ERFCH$_4$$^{\text{SSTfix}}_{\text{chem}}$ (see Appendix E.1) and decrease in the lower stratosphere. The structure of the zonal mean climate response in this category is consistent with the respective response following the CO_2 perturbation. Biogenic NO_x emissions increase by 0.37 Tg(N) a^{-1} and biogenic C_5H_8 emissions increase by 49.2 Tg(C) a^{-1} as reaction to climate change (see Appendix E.1). However, the zonal mean climate response of O_3 in this category is mostly not significant and shows a decrease in the lower tropical and upper NH troposphere (see Fig. 5.5 (d)). The tropospheric O_3 columns in this category increase locally over the Amazon region and the Congo river basin, where biogenic emissions of C_5H_8 increase strongest, and decrease mostly over the tropical ocean (see Appendices E.1 and E.2). In a warmer and moister troposphere the sink of O_3 via the reaction of $O(^1D)$ with H_2O is expected to strengthen (Stevenson et al., 2006). Similar as for the CO_2 perturbation, the effects of increased precursor emissions and the enhanced chemical sink due to a larger abundance of tropospheric H_2O seem to compete in this category. The category *O_3 CH_4* decreases everywhere in the zonal mean, except for the tropical middle troposphere. The decrease is consistent with the reduction of CH_4 mixing ratios compared to the fast response, which leads to reduced formation of O_3 precursors. The increase in the tropical middle troposphere coincides with the increase of O_3 from lightning NO_x emissions indicating that enhanced NO_x from lightning reacts with products of the CH_4 oxidation resulting in an increased O_3 production in both categories. The corresponding response of the tropospheric O_3 columns is not significant in the tropics because of the counteracting responses in the lower and middle troposphere, but shows a significant decrease in the extra-tropics (see Appendix E.2). The categories with pre-

scribed O_3 precursor emissions, *O_3 biomass burning* and *O_3 anthropogenic*, show decreased O_3 mixing ratios throughout the troposphere (see Fig. 5.5 (g) and (h)), consistently with the climate response resulting from the CO_2 perturbation. Additionally, reduced O_3 production per emitted molecule NO_x could play a role as O_3 precursor emissions of natural categories increase.

5.1.4 Summary

This section presents the response of the chemically active species CH_4 and O_3 resulting from an increase of present-day CH_4 emissions by a factor of 2.75. CH_4 mixing ratios increase throughout the atmosphere as response to increased emissions. The increase factor of CH_4 mixing ratios, i.e. 4.76 for the global mean surface CH_4 mixing ratio, is even larger than the corresponding increase factor of the emissions. This is caused by a strong reduction of tropospheric OH leading to an extension of the tropospheric CH_4 lifetime. This makes the present experiment consistent with a previous study, for which - the other way around - the CH_4 surface mixing ratios were increased by a factor of 5 (Winterstein et al., 2019). Furthermore, the response patterns of OH and O_3 in the fast response are overall consistent with the results of Winterstein et al. (2019).

As a result to tropospheric warming, CH_4 mixing ratios decrease in the troposphere and in the stratosphere. Similarly as for the climate response following the CO_2 perturbation, a larger abundance of OH and the temperature dependent reaction rate coefficient lead to a shortening of the tropospheric CH_4 lifetime. The comparison with a previous study using the EMAC model (Stecher et al., 2021) indicates that the magnitude of the CH_4 lifetime change per change of GSAT is stronger when the CH_4 feedback is explicitly included, which is consistent with the results of the CO_2 perturbation. However, the CH_4 lifetime change per change of GSAT is more pronounced for the CH_4 perturbation compared to the CO_2 perturbation, which is possibly due to the different abundances of CH_4 in the respective fast responses.

The fast response of O_3 is different for the CH_4 compared to the CO_2 perturbation because the CH_4 increase directly affects chemical interactions. Nevertheless, the same processes play a role in the climate response. Enhanced stratosphere-troposphere exchange, as well as larger natural O_3 precursor emissions lead to increased tropospheric O_3. On the other hand, the decrease of CH_4 mixing ratios in the climate response compared to the fast response leads to reduced O_3 production. This effect is not included if CH_4 mixing ratios are prescribed at the lower boundary (Stecher et al., 2021), and might explain differences

of the total O_3 response. Additionally, an enhanced chemical sink due to the increase of H_2O leads to a further reduction of tropospheric O_3.

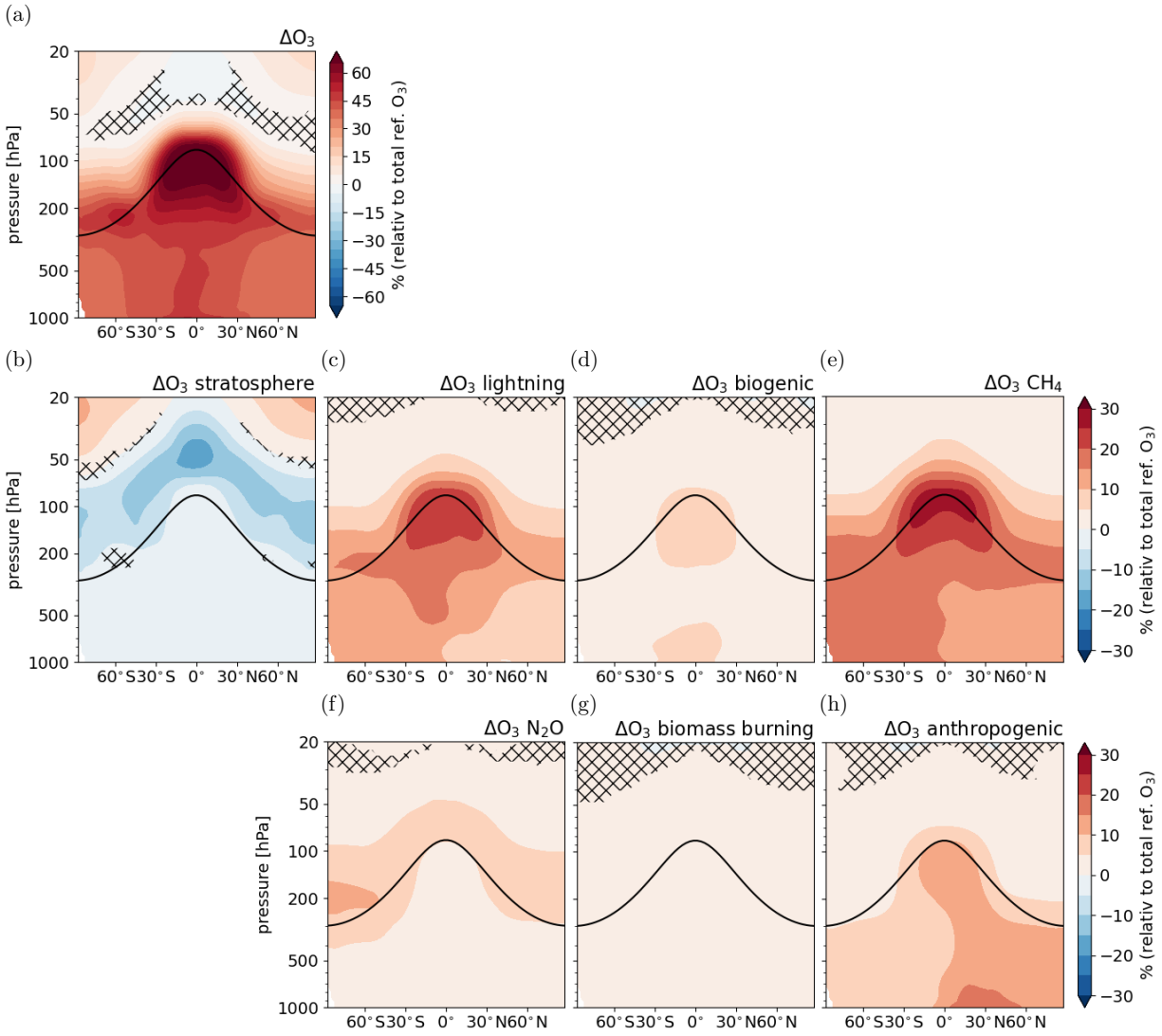

Figure 5.4: Fast response of tropospheric O_3 following CH_4 perturbation: (a) response of total O_3 (same as Fig. 5.3 (a), but differently scaled colour levels to better compare with response in categories), (b) - (h) response of O_3 in individual categories relative to total reference O_3 ($\Delta O_{3_{\mathrm{cat}}} = \frac{O_{3_{\mathrm{cat,ERF}}} - O_{3_{\mathrm{cat,REF}}}}{O_{3_{\mathrm{total,REF}}}}$). Non-hatched regions are significant on the 95% interval.

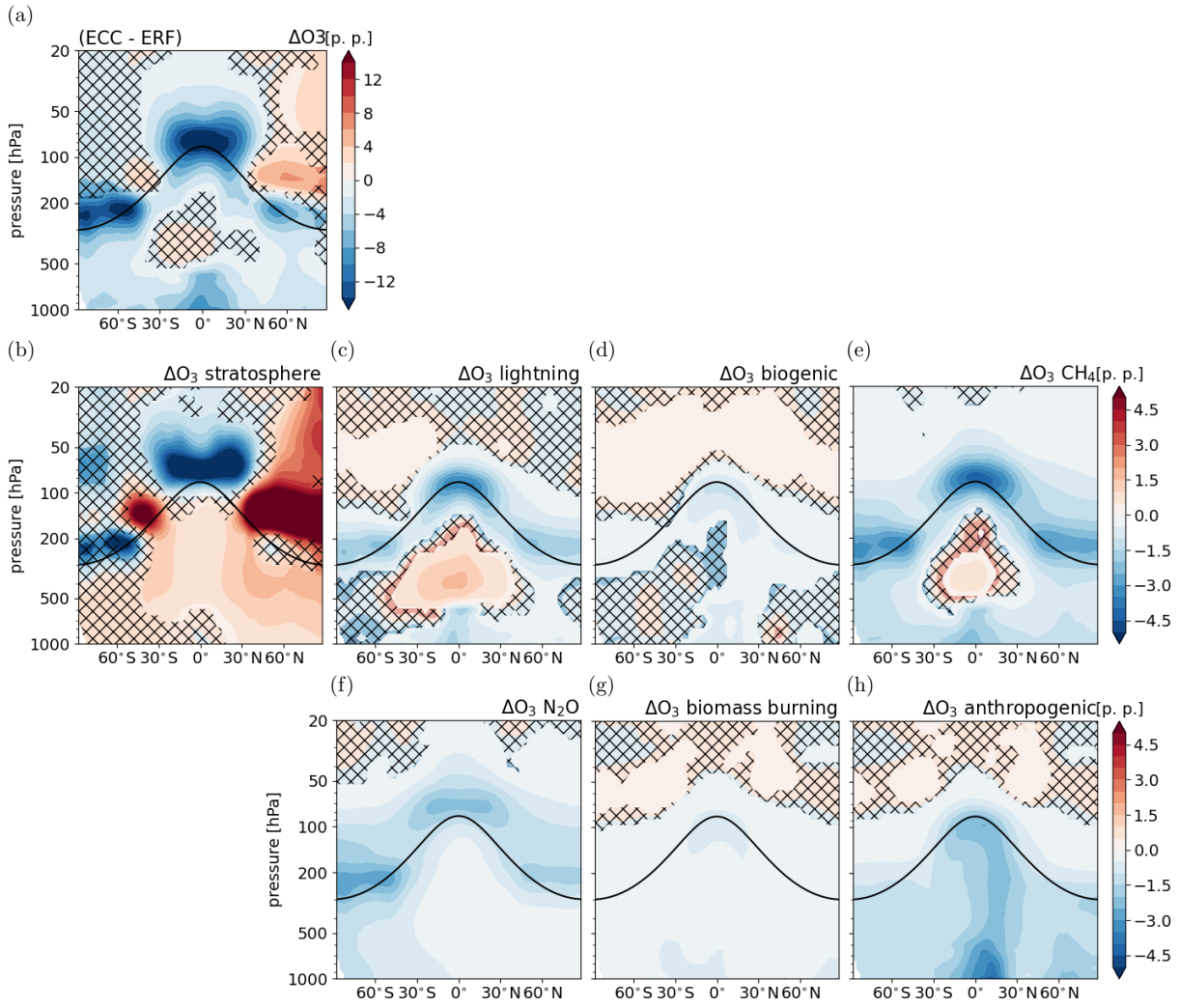

Figure 5.5: Climate response of tropospheric O_3 following CH_4 perturbation: (a) response of total O_3 (same as Fig. 5.3 (c), but differently scaled colour levels to better compare with response in categories), (b) - (h) response of O_3 in individual categories relative to total reference O_3 ($\Delta O_{3_{\text{cat, climate response}}} = (\frac{O_{3_{\text{cat,ECC}}} - O_{3_{\text{cat,REF}}}}{O_{3_{\text{total,REF}}}}) - (\frac{O_{3_{\text{cat,ERF}}} - O_{3_{\text{cat,REF}}}}{O_{3_{\text{total,REF}}}})$). Non-hatched regions indicate significant differences between the fast and the full response on the 95% interval.

5.2 Atmospheric response of temperature and water vapour

5.2.1 Temperature response

Figure 5.6 shows the temperature response resulting from the CH_4 perturbation. The fast response (Fig. 5.6 (a)) is dominated by stratospheric cooling, which is only partly directly caused by the CH_4 perturbation as also the changes of stratospheric H_2O and O_3 contribute significantly (see Fig. 5.7). The induced stratospheric temperature changes by individual composition changes are consistent with the results of Winterstein et al. (2019). The resulting structure of stratospheric cooling is different compared to the stratospheric temperature response resulting from the CO_2 perturbation. The upper troposphere/lower stratosphere region warms significantly by up to 2.3 K in the tropics, a pattern also shown by Winterstein et al. (2019), and the troposphere warms slightly. The corresponding response of GSAT is 0.07 K (see Tab. 5.2) because the tropospheric temperature response is largely suppressed by the prescribed SSTs.

The climate response is dominated by increasing temperatures in the troposphere, which can evolve in response to the perturbation. The corresponding response in GSAT is 1.17 ± 0.06 K (see Tab. 5.2). The maximum temperature response is in the upper tropical troposphere and reaches up to 2 K. Another significant pattern is enhanced cooling in the lowermost tropical stratosphere caused by radiative cooling, which results from the decrease of O_3 mixing ratios in this region (see Fig. 5.8).

The temperature response that evolves in the simulation without interactive chemistry ($ECCCH_4{}^{SSTvar}{}_{nochem}$) is shown in panel (d) of Fig. 5.6. It includes the effect of chemical rapid adjustments as monthly climatologies of CH_4, CO_2, O_3, N_2O and the CFCs from the simulation $ERFCH_4{}^{SSTfix}{}_{chem}$ are prescribed. Therefore, only chemical climate feedbacks lead to differences between $ECCCH_4{}^{SSTvar}{}_{nochem}$ and $ECCCH_4{}^{SSTvar}{}_{chem}$.

The temperature increase in the extratropical southern troposphere is up to 0.5 K lower in the simulation without interactive chemistry. In the NH, chemical climate feedbacks do not lead to significant temperature differences in the troposphere. The response of GSAT is 1.01 ± 0.07 K in the simulation $ECCCH_4{}^{SSTvar}{}_{nochem}$ and therefore lower than in $ECCCH_4{}^{SSTvar}{}_{chem}$, which is consistent with the zonal mean response. The interannual variability is, however, large. In the lowermost tropical stratosphere, O_3 induced radiative cooling leads to significantly stronger cooling in $ECCCH_4{}^{SSTvar}{}_{chem}$. This effect is consistent

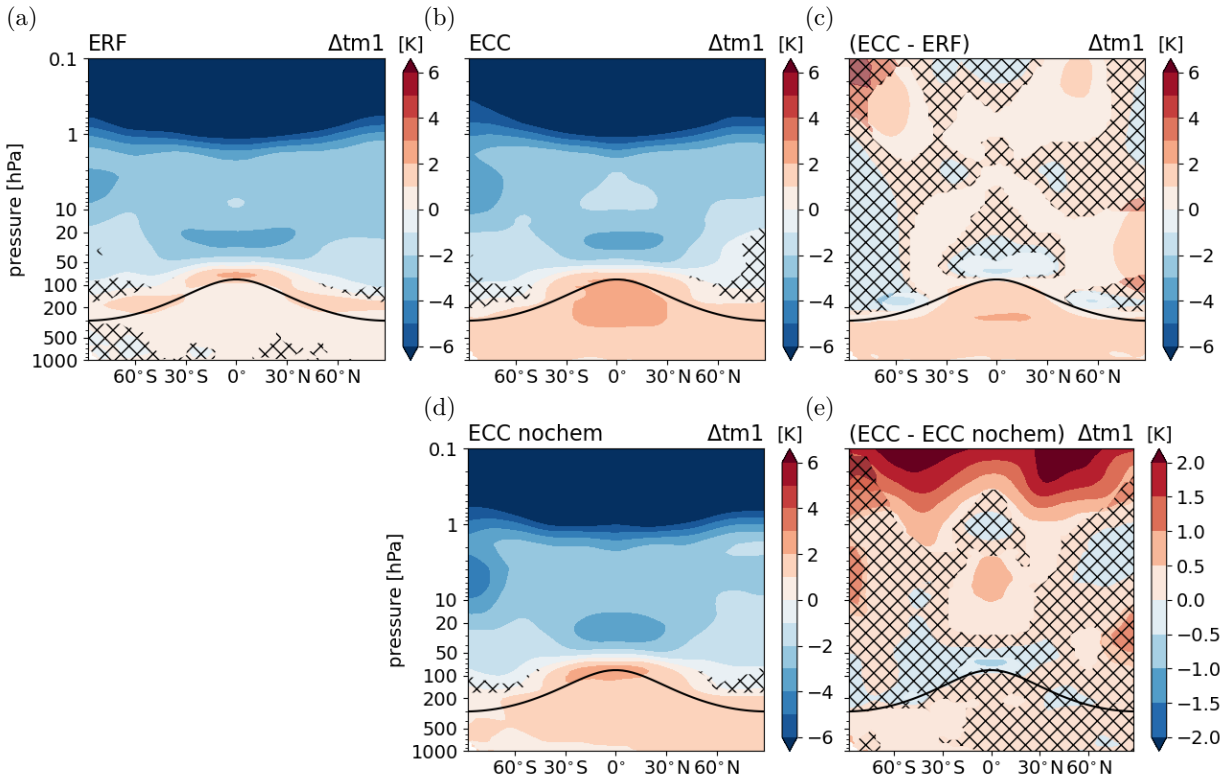

Figure 5.6: Absolute differences between the annual zonal mean temperature of sensitivity simulations (a) ERF$CH_4{}^{\mathrm{SSTfix}}{}_{\mathrm{chem}}$ (fast response) and (b) ECC$CH_4{}^{\mathrm{SSTvar}}{}_{\mathrm{chem}}$ (full response) and their respective reference simulation in [K]. (c) Climate response as difference between the temperature responses in panels (a) and (b) in [K]. (d) Absolute difference between the annual zonal mean temperature of the simulations without interactive chemistry ECC$CH_4{}^{\mathrm{SSTvar}}{}_{\mathrm{nochem}}$ and REF$^{\mathrm{SSTvar}}{}_{\mathrm{nochem}}$ in [K]. (e) Influence of chemical climate feedbacks presented as difference between the temperature responses in panels (b) and (d) in [K]. Non-hatched areas are significant on the 95% confidence level. The solid black line indicates the climatological tropopause.

with the CO_2 perturbation (see previous chapter). In the tropical middle stratosphere, the cooling is reduced in the simulation ECCCH$_4$$^{\mathrm{SSTvar}}_{\mathrm{chem}}$, which can be explained by the decrease of H_2O mixing ratios and associated reduced radiative cooling (see Figs. 5.7 and 5.8).

5.2.2 Water vapour response

Figure 5.9 shows the response of H_2O. In the fast response the change of tropospheric H_2O is mostly suppressed, but shows increases of up to about 10% consistently with the residual warming of land surfaces. Stratospheric H_2O increases strongly by up to 250% in the upper stratosphere and mesosphere because the increased abundance of CH_4 leads to enhanced production of H_2O by the CH_4 oxidation. Additionally, warming of the tropical cold point leads to reduced dehydration of upwelling air parcels, and thus to an increased abundance of H_2O in the lower stratosphere. The zonal mean warming of the tropical cold point is 1.5 K and thereby more pronounced than in the respective CO_2 experiment (see Fig. 5.10). The CH_4 perturbation induces a direct radiative heating in the tropical upper stratosphere of up to 1 K (see Fig. 5.7 (a)), and the response of stratospheric O_3 leads to additional radiative heating of up to 2 K in this region (see Fig. 5.7 (d)).

Tropospheric H_2O mixing ratios increase significantly as a result of tropospheric warming (see Fig. 5.9 (b) and (c)). The maximum increase of up to 40% is located in the tropical upper troposphere. H_2O mixing ratios increase also in the lower stratosphere because tropical cold point temperatures increase further by about 0.5 K in comparison to the fast response (see Fig. 5.10). In contrast, H_2O mixing ratios above approximately 50 hPa in the extra-tropics, and above 20 hPa in the tropics, decrease by up to 20%. The diagnosed tendencies of the MESSy submodel MECCA of the chemical contribution to the specific humidity confirm that the chemical production of stratospheric H_2O is reduced in ECCCH$_4$$^{\mathrm{SSTvar}}_{\mathrm{chem}}$ compared to ERFCH$_4$$^{\mathrm{SSTfix}}_{\mathrm{chem}}$. An explanation for this reduction could be the decrease of CH_4 in the simulation ECCCH$_4$$^{\mathrm{SSTvar}}_{\mathrm{chem}}$ in comparison to ERFCH$_4$$^{\mathrm{SSTfix}}_{\mathrm{chem}}$ resulting in a reduced production of stratospheric H_2O from CH_4 oxidation. However, a similar reduction of stratospheric H_2O was effective in the climate response of the 5×CH_4 experiments with prescribed CH_4 surface mixing ratios (Stecher et al., 2021). In the respective experiment simulation more CH_4 reached the stratosphere due to enhanced tropical upwelling. From this it was concluded that CH_4 cannot be the limiting factor (Stecher et al., 2021). This suggests that the production of H_2O from CH_4 oxidation is limited by the decreased abundance of OH also in the present experiment

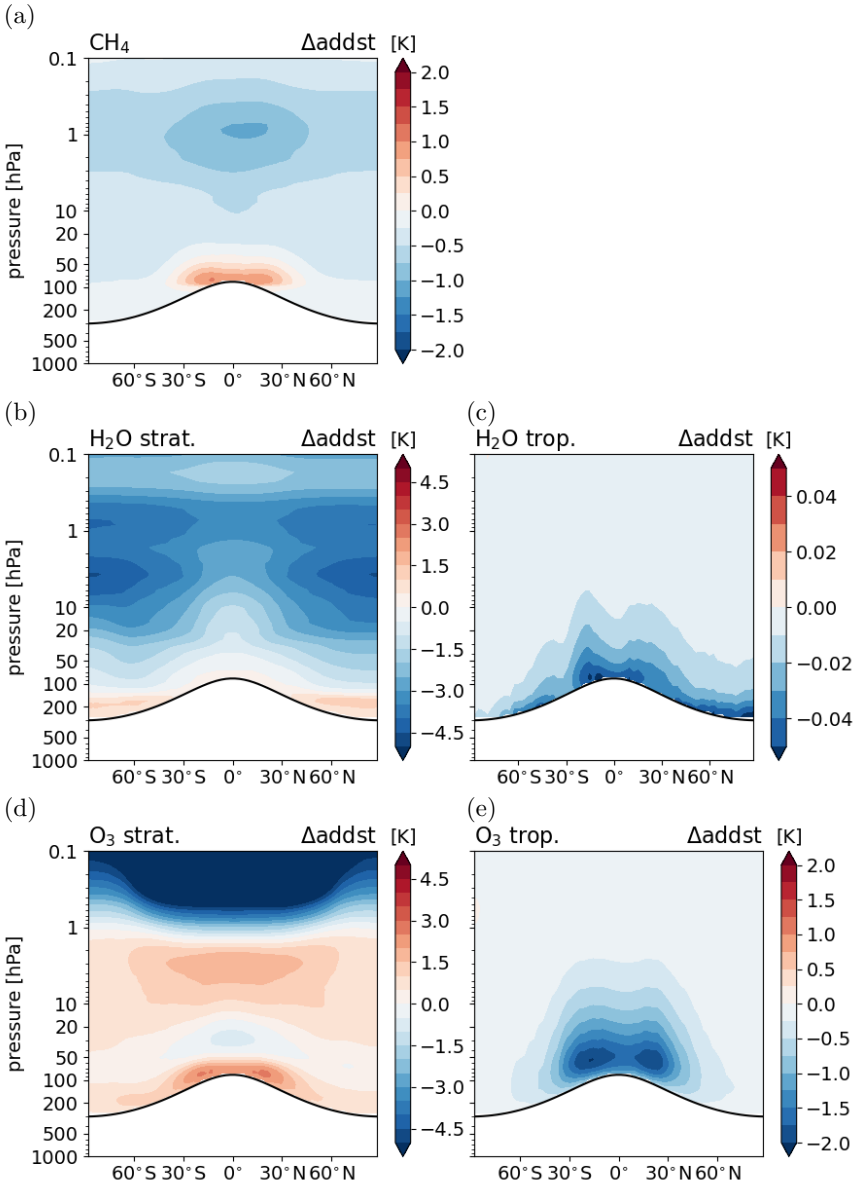

Figure 5.7: Stratospheric temperature adjustment radiatively induced by individual species changes in simulation ERFCH$_4{}^{\mathrm{SSTfix}}{}_{\mathrm{chem}}$ in comparison to REF$^{\mathrm{SSTfix}}{}_{\mathrm{chem}}$ in [K]: (a) CH_4, (b) stratospheric H_2O, (c) tropospheric H_2O, (d) stratospheric O_3, and (e) tropospheric O_3. No significance test is performed for the shown changes as only 2 years are available for the analysis. Note that the colour levels in the individual panel plots differ.

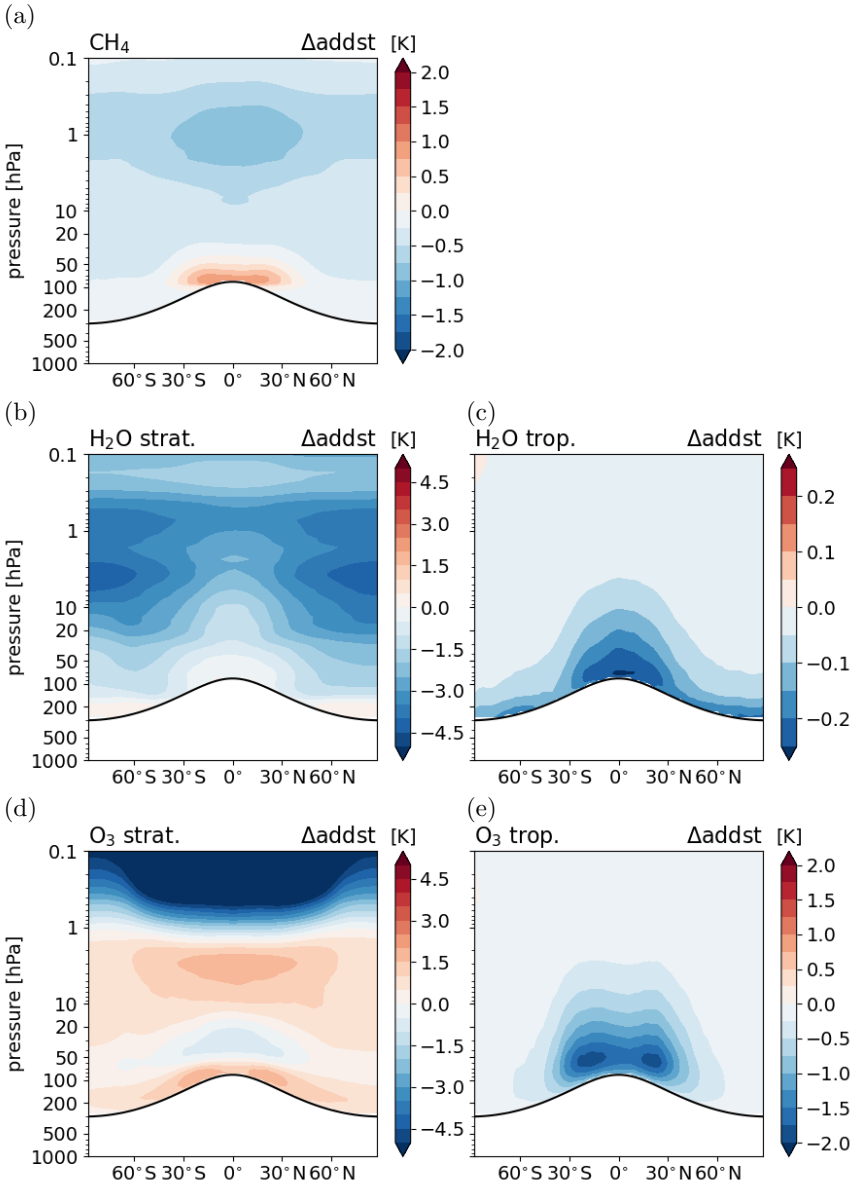

Figure 5.8: Stratospheric temperature adjustment radiatively induced by individual species changes in simulation ECCCH$_4$$^{\mathrm{SSTvar}}{}_{\mathrm{chem}}$ in comparison to REF$^{\mathrm{SSTvar}}{}_{\mathrm{chem}}$ in [K]: (a) CH_4, (b) stratospheric H_2O, (c) tropospheric H_2O, (d) stratospheric O_3, and (e) tropospheric O_3. No significance test is performed for the shown changes as only 2 years are available for the analysis. Note that the colour levels in the individual panel plots differ.

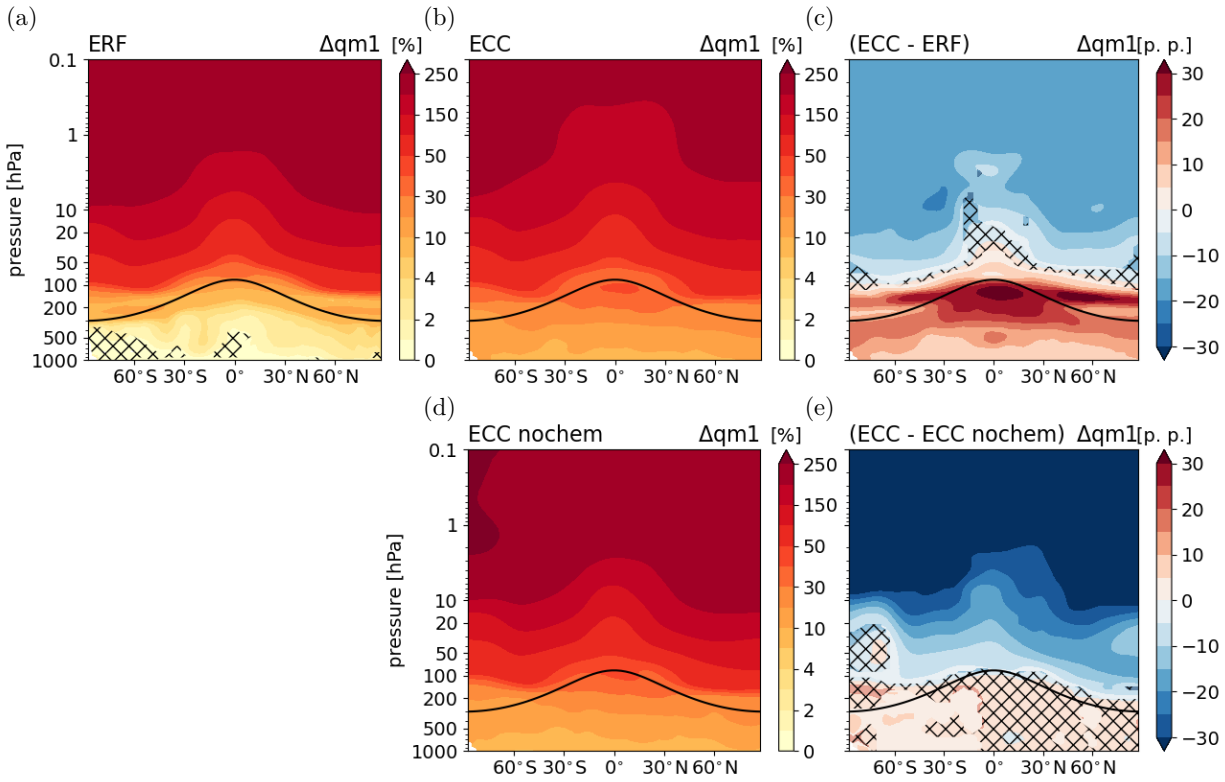

Figure 5.9: Relative differences between the annual zonal mean water vapour of sensitivity simulations (a) ERFCH$_4$$^{\mathrm{SSTfix}}{}_{\mathrm{chem}}$ (fast response) and (b) ECCCH$_4$$^{\mathrm{SSTvar}}{}_{\mathrm{chem}}$ (full response) and their respective reference simulation in [%]. (c) Climate response as difference between the water vapour responses in panels (a) and (b) in [%]. (d) Relative difference between the annual zonal mean water vapour of the simulations without interactive chemistry ECCCH$_4$$^{\mathrm{SSTvar}}{}_{\mathrm{nochem}}$ and REF$^{\mathrm{SSTvar}}{}_{\mathrm{nochem}}$ in [%]. (e) Influence of chemical climate feedbacks presented as difference between the water vapour responses in panels (b) and (d) in [percentage points (p.p.)]. Non-hatched areas are significant on the 95% confidence level. The solid black line indicates the climatological tropopause.

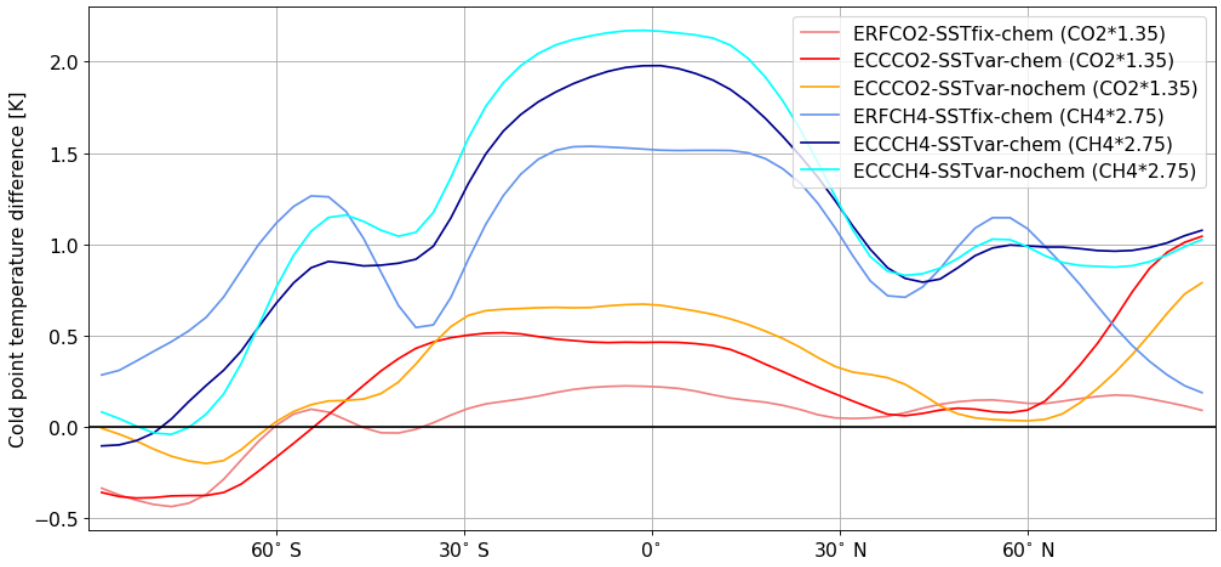

Figure 5.10: Zonal mean difference of cold point temperature between sensitivity simulations perturbed by 1.35×CO_2 mixing ratio (reddish colours) and 2.75×CH_4 emission increase (bluish colours) and the respective references in [K].

simulation.

Panel (d) of Fig. 5.9 shows the response of H_2O in the simulation without interactive chemistry (ECCCH$_4$$^{\mathrm{SSTvar}}_{\mathrm{nochem}}$). In this simulation, the chemical decomposition of CH_4 is calculated using prescribed climatologies of CH_4, OH, Cl and O(^{1}D) from simulation ERFCH$_4$$^{\mathrm{SSTfix}}_{\mathrm{chem}}$. A constant yield of two H_2O molecules per oxidised CH_4 molecule is assumed for the corresponding stratospheric H_2O production (Winterstein and Jöckel, 2021). The difference between the climate responses of ECCCH$_4$$^{\mathrm{SSTvar}}_{\mathrm{nochem}}$ and ECCCH$_4$$^{\mathrm{SSTvar}}_{\mathrm{chem}}$ is shown in Fig. 5.9 (e). The response of stratospheric H_2O is significantly less pronounced in the simulation with interactive chemistry. In the middle and upper stratosphere, this can be explained by the chemically-driven reduction as described in the previous paragraph. Additionally, the increase of tropical cold point temperatures is more pronounced in the simulation without interactive chemistry (see Fig. 5.10) resulting in more strongly increased H_2O mixing ratios in the lower stratosphere as well. In the troposphere, the difference between the response with and without chemical climate feedbacks shows a more pronounced H_2O response in the SH, which is consistent with the temperature response.

5.2.3 Summary

The fast temperature response following the CH_4 perturbation is dominated by stratospheric cooling, which is partly directly induced by CH_4, but there are also important contributions from stratospheric H_2O and O_3, which is consistent with a previous study of $5\times CH_4$ surface mixing ratios (Winterstein et al., 2019). The increase of cold point temperatures is more pronounced for the CH_4 compared to the CO_2 perturbation, which is a consequence of radiative heating induced by composition changes of CH_4 and O_3 in the tropopause region. Stratospheric H_2O mixing ratios increase strongly due to enhanced chemical production by the CH_4 oxidation, and reduced dehydration of upwelling airmasses in the tropical cold point region. The response of H_2O is also consistent with the results of Winterstein et al. (2019).

The troposphere warms significantly in the full response. The corresponding response of GSAT is 1.17 $\pm$ 0.06 K in the simulation with interactive chemistry. The response of GSAT is 1.01 $\pm$ 0.07 K in the simulation without interactive chemistry, which points towards an enhanced climate sensitivity if interactive chemistry is included. The interannual variability of the GSAT responses is, however, large. The zonal mean difference of the temperature response between the simulations with and without interactive chemistry suggests that tropospheric warming is more pronounced in the simulation with interactive chemistry as well, in particular in the SH.

In the climate response of the simulation with interactive chemistry, stratospheric H_2O mixing ratios increase in the lowermost stratosphere as a result of enhanced transport from the troposphere, and decrease above as a result of reduced chemical production compared to the fast response. In the simulation without interactive chemistry, the production of H_2O by CH_4 oxidation represents conditions as in the fast response. Therefore, the corresponding response of stratospheric H_2O is significantly more pronounced in comparison to the simulation with interactive chemistry. In addition, the climate response of O_3 leads to more pronounced radiative cooling in the lowermost tropical stratosphere. Therefore, the increase of tropical cold point temperatures is larger in the simulation without interactive chemistry, which leads to a more pronounced increase of lower stratospheric H_2O in this simulation.

5.3 Adjustment and feedback analysis

This section presents the radiative effects corresponding to the responses discussed in the previous sections. The outline follows Sect. 4.3, which presents the radiative effects corresponding to the CO_2 perturbation experiments. Firstly, estimates of different definitions of RF and associated estimates of the climate sensitivity parameter are assessed in Sect. 5.3.1. Secondly, Sects. 5.3.2 and 5.3.3 present the rapid radiative adjustments and slow climate feedbacks of individual processes that evolve in the simulations with interactive chemistry. For radiative estimates of trace gases (CH_4, H_2O, and O_3) two different methods are used to derive the radiative effects, whose respective results are compared. In addition, also the potential effect of interactive chemistry on physical climate feedbacks is investigated in Sect. 5.3.4. Finally, Sect. 5.3.5 summarizes the effect of interactive chemistry on the ERF and the climate sensitivity and compares the results of this study to available literature.

5.3.1 Radiative forcing and climate sensitivity

Tab. 5.2 summarizes the estimates for different definitions of RF, namely RF_{inst}, RF_{adj} and ERF (see Sect. 2.2.1 for definitions) caused by the CH_4 perturbation. For RF_{inst}, the estimates derived using two different methods are shown. The first is the PRP method with MBM RAD (see Sect. 3.3.1). It indicates a RF_{inst} of 0.356±0.001 W m^{-2}. The second methods derives RF_{inst} from additional EMAC atmosphere-only (AGCM) simulations with diagnostic radiation calls (see Sect. 3.3.2), and suggests a RF_{inst} of 0.405 W m^{-2}. The absorption band that contributes most to the GHG effect of CH_4 overlaps with a strong H_2O absorption band (e.g. Petty, 2006). Therefore, large abundances of H_2O partly saturate the absorption in this band and reduce the radiative effect of CH_4. For instance, Feldman et al. (2018) found a significant dependence of the radiative effect of CH_4 on the H_2O abundance. As the PRP method uses the instantaneous H_2O mixing ratios for the radiation calculation, whereas the AGCM method uses a monthly varying climatology, this can explain part of the difference of about 0.05 W m^{-2} between the estimates of RF_{inst} from the two methods. Both methods rely on the same radiative transfer scheme, i.e. the default scheme of ECHAM5, which underestimates the radiative effect of CH_4 (Winterstein et al., 2019; Nützel et al., 2023, see also Sect. 3.1.5). For example, using the PSrad radiation scheme (Pincus et al., 2003) for a perturbation of 5×CH_4 mixing ratios also representing present-day conditions results in a RF_{inst} of 1.75 W m^{-2} (Nützel et al., 2023).

With the AGCM method also RF_{adj} is estimated, which accounts for the stratospheric

temperature adjustment directly induced by the CH_4 perturbation, and is about 0.1 W m^{-2}, or 26%, larger compared to RF_{inst} in this study (see Tab. 5.2). The used radiative transfer scheme does not account for SW absorption by CH_4. If SW absorption by CH_4 was accounted for, the induced stratospheric temperature adjustment would be expected to reduce RF_{adj} in comparison to RF_{inst} as the SW absorption leads to stratospheric heating rather than cooling (Smith et al., 2018; Byrom and Shine, 2022; Nützel et al., 2023). The estimate of RF_{adj} of 0.510 W m^{-2} reproduces the respective estimate of a 5×CH_4 mixing ratios experiment with the EMAC model (Winterstein et al., 2019), which is not surprising as the increase of CH_4 emissions by a factor of 2.75 results in an increase of CH_4 mixing ratios by about a factor of 5 (see Sect. 5.1). However, just as the estimate of RF_{inst}, also the estimate of RF_{adj} is expected to be underestimated by the used radiative transfer scheme (Winterstein et al., 2019; Nützel et al., 2023). Using the formula by Etminan et al. (2016)[1] for the present CH_4 perturbation indicates a RF_{adj} of about 1.7 W m^{-2}. Similarly, using the PSrad radiation scheme for a perturbation of 5×CH_4 mixing ratios also representing present-day conditions results in a RF_{adj} of 1.70 W m^{-2} (Nützel et al., 2023).

The ERF is calculated as the difference of global mean net radiative flux at TOA between the simulations $ERFCH_4{}^{SSTfix}{}_{chem}$ and $REF^{SSTfix}{}_{chem}$. It is 1.722±0.173 W m^{-2}, and thus close to the 1.79 W m^{-2} of the comparable experiment of the study described by Winterstein et al. (2019). Chemical rapid radiative adjustments enhance the ERF, which is shown in the next section. Therefore, the ERF is significantly larger than RF_{adj} in contrast to studies, which assess only physical rapid radiative adjustments (e.g. Smith et al., 2018).

Table 5.2 also shows estimates of the climate sensitivity parameters $\lambda_{RF_{inst}}$, $\lambda_{RF_{adj}}$ and λ_{ERF}, corresponding to the different definitions of RF. The climate sensitivity parameter $\lambda_{RF_{inst}}$ is calculated using the centred estimate from the PRP method for RF_{inst} because it is expected to best represent RF_{inst} in the simulation $ERFCH_4{}^{SSTfix}{}_{chem}$. λ_{ERF} is significantly smaller compared to $\lambda_{RF_{inst}}$ and $\lambda_{RF_{adj}}$, which is due to the difference between ERF and the other RF definitions. The estimate of λ_{ERF} of 0.68±0.08 K / (W m^{-2}) for the CH_4 perturbation is the same as λ_{ERF} for the CO_2 perturbation (see Tab. 4.2). In contrast, the feedback parameters $\lambda_{RF_{inst}}$ and $\lambda_{RF_{adj}}$ differ significantly between the CH_4 and the CO_2 perturbation. This finding confirms the results of previous studies that the climate sensitivity is in general less dependent on the type of perturbation using ERF (e.g. Richardson et al., 2019). The use of λ_{ERF} as sensitivity parameter to obtain an efficacy

[1]The CH_4 mixing ratios of simulation $ERFCH_4{}^{SSTfix}{}_{chem}$ are outside of the range tested to derive the formula of Etminan et al. (2016), but the formula can still provide a rough estimate for the CH_4 radiative effect.

close to unity for the CH_4 perturbation is even more important in this study compared to Richardson et al. (2019) because of the effect of interactive chemistry, which leads to larger differences between RF_{adj} and ERF.

The estimate of λ_{ERF} is smaller than the estimate of 0.72±0.07 K / (W m^{-2}) corresponding to the 5×CH_4 mixing ratios experiment by Stecher et al. (2021). This suggests a smaller climate sensitivity caused by the explicit simulation of the CH_4 climate feedback (see Sect. 5.1). The difference between the two estimates is, however, not statistically significant.

Th estimates of $\lambda_{RF_{inst}}$ and $\lambda_{RF_{adj}}$ are more pronounced for the simulation with interactive chemistry, i.e. ECCC$CH_4$$^{SSTvar}_{chem}$, in comparison to the simulation ECCC$CH_4$$^{SSTvar}_{nochem}$. The estimates of RF_{inst} and RF_{adj} are comparable, but the temperature response is significantly more pronounced for the simulation with interactive chemistry. Reasons for this are discussed below.

5.3.2 Rapid radiative adjustments

Panel (a) of Fig. 5.11 shows the rapid radiative adjustments that evolve in simulation ERFC$H_4$$^{SSTfix}_{chem}$ derived using the PRP method with MBM RAD (see Sect. 3.3.1). The rapid radiative adjustments of the surface albedo and of clouds are close to zero. The Planck and the tropospheric lapse rate rapid radiative adjustments are negative, and result from the land surface temperature change in the simulation with prescribed SSTs. They are in qualitative agreement with the respective estimates of the CO_2 perturbation experiment (see Fig. 4.11 (a)). The forward and backward estimates of the cloud, lapse rate and tropospheric H_2O rapid radiative adjustments differ strongly due to dependencies between these processes, similarly as noted for the CO_2 perturbation experiment (see Sect. 4.3).

The rapid radiative adjustment of tropospheric H_2O is about twice as large as the respective estimate of the CO_2 perturbation. Tropospheric H_2O mixing ratios are largely driven by the temperature, whose response is similar in ERFC$H_4$$^{SSTfix}_{chem}$ compared to ERFC$O_2$$^{SSTfix}_{chem}$. Nevertheless, the increase of H_2O in the upper troposphere/lower stratosphere region is stronger for the CH_4 perturbation experiment. The CH_4 perturbation leads to strong increases of stratospheric H_2O via chemical production from the oxidation of CH_4 (see Sect. 5.2), which seems to also influence the transition region between troposphere and stratosphere. In addition, a constant tropopause definition is used for the separation into troposphere and stratosphere (see Sect. 3.3.1). Therefore, part of the H_2O increase in this region contributes to the radiative estimate of tropospheric H_2O.

Table 5.2: Estimates of different definitions of radiative forcing (RF_{inst}, RF_{adj}, ERF) evaluated at TOA following the CH_4 perturbation in [W m^{-2}], the corresponding responses of global mean surface air temperature (ΔGSAT) in [K], and the corresponding estimates of the climate sensitivity parameter ($\lambda_{RF_{inst}}$, $\lambda_{RF_{adj}}$, λ_{ERF}) in [K/(W m^{-2})]. For the simulation ECCCH$_4$$^{SSTvar}_{chem}$, the radiative perturbations of CH_4 are not interpreted as radiative forcings because of the decrease of the CH_4 mixing ratios in comparison to the simulation ERFCH$_4$$^{SSTfix}_{chem}$.

		ERF chem	ECC chem	ECC nochem
RF_{inst} PRP	[W m^{-2}]	0.356±0.001	-	0.362±0.001
RF_{inst} $PRP^{forward}$	[W m^{-2}]	0.344±0.001	-	0.333±0.001
RF_{inst} $PRP^{backward}$	[W m^{-2}]	0.368±0.001	-	0.392±0.002
RF_{inst} AGCM	[W m^{-2}]	0.405	-	0.400
RF_{adj} AGCM	[W m^{-2}]	0.510	-	0.505
ERF	[W m^{-2}]	1.722±0.173	-	-
ΔGSAT	[K]	0.07±0.02	1.17±0.06	1.01±0.07
$\lambda_{RF_{inst}}$	[K/(W m^{-2})]	-	3.30±0.16	2.78±0.18
$\lambda_{RF_{adj}}$	[K/(W m^{-2})]	-	2.30±0.11	1.99±0.13
λ_{ERF}	[K/(W m^{-2})]	-	0.68±0.08	-

Values after the ± sign are 2× the standard error of the mean calculated on the basis of 20 annual mean values, which approximate the corresponding 95% confidence intervals. The standard errors for the climate sensitivity parameters are calculated from the standard error of the corresponding radiative forcing std_error_{RF} and the standard error of ΔGSAT $std\_error_{\Delta GSAT}$, as $std\_error_{\lambda} = (\sqrt{\frac{std\_error^2_{RF}}{RF^2} + \frac{std\_error^2_{\Delta GSAT}}{\Delta GSAT^2}} \cdot \frac{\Delta GSAT}{RF})$. The AGCM method does not account for interannual variability, which is why no uncertainty estimates are provided for the corresponding radiative forcing estimates. The uncertainty estimates of $\lambda_{RF_{adj}}$ account for the interannual variability of ΔGSAT.

The stratospheric temperature adjustment is the quantitative largest rapid radiative adjustment. Its estimate, normalized by the corresponding ERF, is close to the respective estimate of the CO_2 perturbation, even though the structure of the temperature change is different, and even though it is induced by composition changes of different species. The CO_2 perturbation induces a strong direct stratospheric temperature adjustment (see previous chapter), whereas for the CH_4 perturbation also the response of stratospheric H_2O, and tropospheric and stratospheric O_3 contribute significantly, which is illustrated by Fig. 5.7 and is quantified in the following.

The sum of all rapid radiative adjustments plus RF_{inst} is 1.694 W m^{-2}, which is close to the estimate of ERF derived from the radiative flux difference between the simulations ERFCH$_4$$^{SSTfix}_{chem}$ and REF$^{SSTfix}_{chem}$ of 1.722±0.173 W m^{-2} (see Tab. 5.2). Thus, the

residuum (RES_{RA}, see Eq. 3.11) is about 0.03 W m^{-2} or 1.7% relative to the ERF, which suggests that the individual rapid radiative adjustments are separable if centred estimates are used.

The estimates shown in Fig. 5.11 do not account for the effect of stratospheric temperature adjustment induced by the individual perturbations. Therefore, Tab. 5.3 shows the estimates derived from additional EMAC atmosphere-only (AGCM) simulations using diagnostic radiation calls (see Sect. 3.3.2). Both, instantaneous and stratospheric adjusted, estimates are shown for this method. The instantaneous estimates derived with the AGCM method are supposed to be consistent with the ones derived using the PRP method, which is the case for the perturbations of tropospheric and stratospheric O_3. For these perturbations, the difference of the mean values between the methods is smaller than the corresponding 95% intervals of the PRP estimates. The estimates associated with the tropospheric H_2O change deviate strongest, by about 0.05 W m^{-2}, as was already noted for the CO_2 perturbation (see Sect. 4.3). The estimates corresponding to the stratospheric H_2O changes deviate by about 0.01 W m^{-2}.

Accounting for the induced stratospheric cooling leads to a change of the sign of the TOA radiative effect induced by the response of stratospheric H_2O. The stratospheric adjusted radiative effect is estimated at 0.507 W m^{-2}. The effect of the induced stratospheric temperature adjustment enhances the rapid radiative adjustment of tropospheric O_3 resulting in 0.642 W m^{-2}, whereas it dampens the rapid radiative adjustment of stratospheric O_3 resulting in 0.163 W m^{-2}.

Physical rapid radiative adjustments following a $3\times CH_4$ perturbation have been assessed in the multi-model comparison by Smith et al. (2018). The negative Planck and tropospheric temperature rapid radiative adjustments, and the positive rapid radiative adjustment of tropospheric H_2O are in qualitative agreement with this study. However, the results of Smith et al. (2018) indicate that the multi-model mean stratospheric temperature adjustment is negligible, which is explained by the counteracting results of models that include SW absorption by CH_4 in the radiation parameterization and models, which do not. As already mentioned in the previous section, the used radiation scheme does not account for SW absorption by CH_4, which results in a positive stratospheric temperature adjustment directly induced by the CH_4 perturbation. However, the increase of stratospheric H_2O driven by enhanced CH_4 oxidation (see Sect. 5.2) induces an even larger positive stratospheric temperature adjustment, which is not included in the estimates by Smith et al. (2018). Furthermore, the results of Smith et al. (2018) and Allen et al. (2021)

suggest a strong dependence on the cloud rapid radiative adjustment on SW absorption by CH_4 so that it is expected to be positive if CH_4 absorption is not accounted for, and to be negative if it is. In this study, it is not significantly different from zero.

The stratospheric adjusted estimates in Tab. 5.3 agree closely with the radiative effects of composition changes resulting from a $5\times CH_4$ mixing ratios experiment using the EMAC model (Winterstein et al., 2019, see Tab. 3 by Stecher et al. (2021) for the corresponding estimates split into tropospheric and stratospheric composition changes). The total radiative effect of O_3 is about 0.05 W m^{-2} larger in the present study. In the study of Winterstein et al. (2019) the sum of the stratospheric adjusted radiative effects corresponding to composition changes of CH_4, stratospheric H_2O, and tropospheric and stratospheric O_3 deviate by -0.03 W m^{-2} from the total ERF suggesting a minor influence of physical rapid radiative adjustments. In the present study, the respective deviation is -0.10 W m^{-2}, which is smaller than the 95% confidence interval of the ERF. Additionally, the sum of the physical rapid radiative adjustments of the surface albedo, clouds, lapse rate, Planck and tropospheric H_2O as shown in Fig. 5.11 is -0.020±0.153 W m^{-2}. Therefore, the results of the present study do not indicate a significant effect of physical rapid radiative adjustments for the CH_4 perturbation either. However, part of the H_2O response in the upper troposphere might be chemically induced (see above), which would suggest a more pronounced negative effect of physical rapid radiative adjustments. For a clear separation, an additional simulation without interactive chemistry and prescribed SSTs and SICs would be necessary.

5.3.3 Slow climate feedbacks

The radiative perturbations corresponding to the full response of individual processes are shown in Fig. 5.11 (b). The sum of all radiative contributions of the full response plus the corresponding RF_{inst} is 0.029 W m^{-2}, which corresponds to about 8% of RF_{inst}. This estimate is the residuum of the PRP method (RES_α, see Eq. 3.12) The deviations of the forward and the backward calculations are 0.748 W m^{-2} and -0.806 W m^{-2}, respectively. Thus, similarly as for the CO_2 perturbation, only the centred estimates fulfil the requirement of separability of individual feedbacks.

Following the ERF framework, the difference between the full and the fast radiative response of an individual process represents the corresponding climate feedback, which is shown in Fig. 5.11 (c). The climate feedbacks corresponding to physical processes of the surface albedo, clouds, Planck, lapse rate and tropospheric H_2O are in qualitative agreement

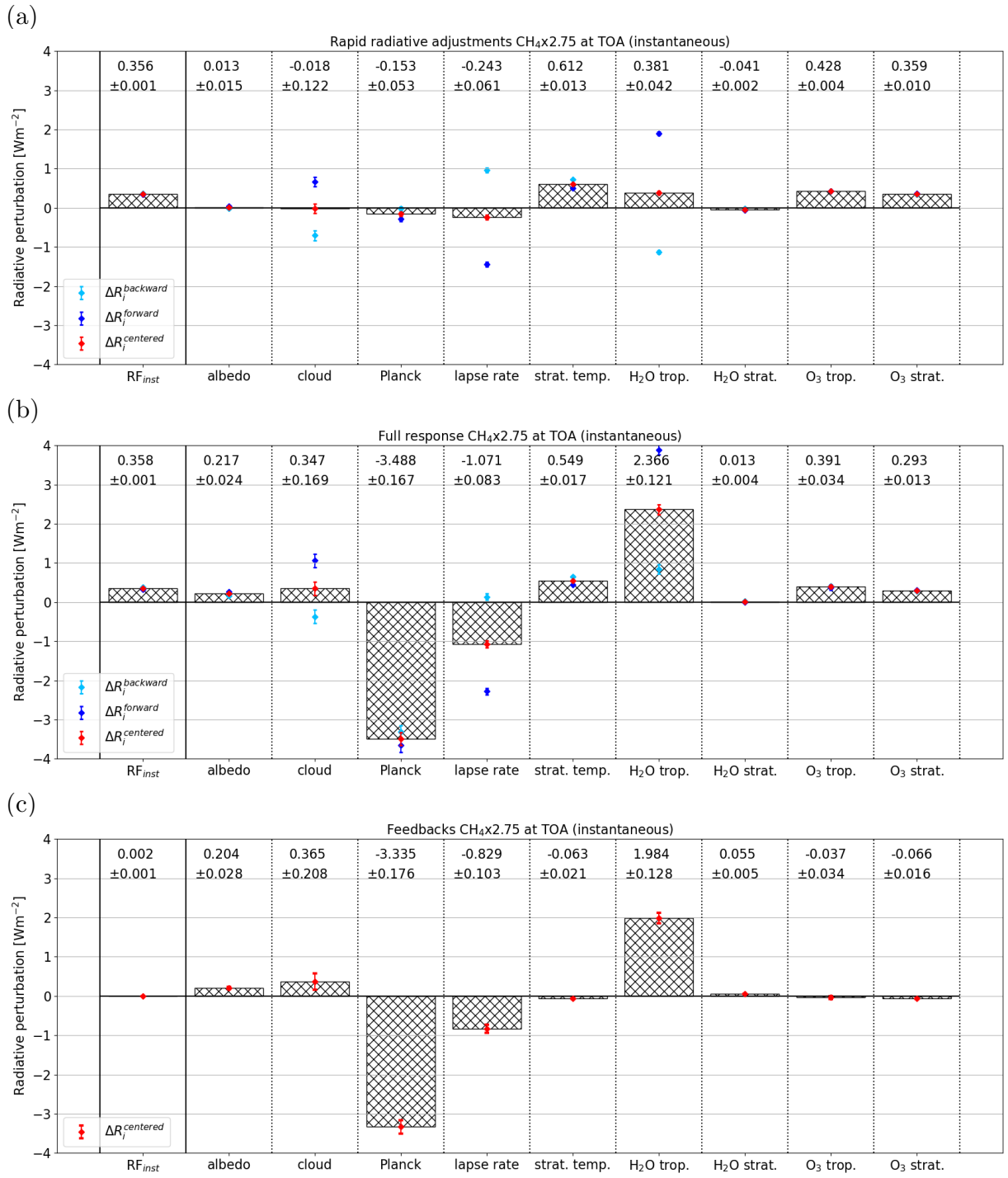

Figure 5.11: Radiative contributions in [W m^{-2}] of individual processes of (a) the fast response (interpreted as rapid radiative adjustments), (b) the full response, and (c) their difference (interpreted as slow climate feedbacks) for the CH_4 perturbation. Values after the ± sign are 2× the standard error of the mean approximating the corresponding 95% confidence interval calculated on the basis of 20 annual mean values.

Table 5.3: Individual radiative effects in [W m^{-2}] of composition changes of CH_4, tropospheric and stratospheric H_2O, and tropospheric and stratospheric O_3 of the fast response in simulation ERFCH$_4$$^{\text{SSTfix}}_{\text{chem}}$ (interpreted as rapid radiative adjustments) and of the full response, either with interactive chemistry (ECCCH$_4$$^{\text{SSTvar}}_{\text{chem}}$), or without interactive chemistry ECCCH$_4$$^{\text{SSTvar}}_{\text{nochem}}$. The radiative estimates are calculated in separate simulations, either offline with MBM RAD, or in an AGCM set-up with EMAC. For the AGCM method both, instantaneous (inst.) and stratospheric adjusted (adj.) estimates, are provided. In addition, the feedback parameters α in [W m^{-2} K^{-1}], i.e. the radiative contributions of the full response minus the fast response normalized by the respective change of GSAT (see Tab. 5.2), are shown for the simulations with interactive chemistry.

	CH_4	H_2O trop.	H_2O strat.	O_3 trop.	O_3 strat.
Fast [W m^{-2}]					
PRP (inst.)	0.356±0.001	0.381±0.044	-0.041±0.002	0.428±0.004	0.359±0.010
inst. AGCM	0.405	0.327	-0.053	0.425	0.359
adj. AGCM	0.510	0.333	0.507	0.642	0.163
Full [W m^{-2}]					
PRP (inst.)	0.358±0.001	2.366±0.121	0.013±0.004	0.391±0.034	0.293±0.013
inst. AGCM	0.386	2.350	-0.000	0.402	0.291
adj. AGCM	0.487	2.385	0.640	0.607	0.134
Full nochem [W m^{-2}]					
PRP (inst.)	0.362±0.001	2.138±0.143	-0.006±0.004	-	-
inst. AGCM	0.400	2.103	-0.017	-	-
adj. AGCM	0.505	2.133	0.660	-	-
α [W m^{-2} K^{-1}]					
PRP (inst.)	0.001±0.002	1.689±0.261	0.046±0.009	-0.031±0.058	-0.056±0.028
inst. AGCM	-0.016	1.722	0.045	-0.019	-0.058
adj. AGCM	-0.019	1.746	0.114	-0.029	-0.025

For the estimates with MBM RAD the respective standard error of the mean calculated on the basis of 20 annual mean values is provided, which approximate the corresponding 95% confidence intervals. The standard errors for the feedback parameters α are calculated from the standard error of the corresponding radiative perturbation std_error_{RF} and the standard error of the change of GSAT $std\_error_{\Delta GSAT}$, as $std\_error_{\alpha} = (\sqrt{\frac{std\_error^2_{RF}}{RF^2} + \frac{std\_error^2_{\Delta GSAT}}{\Delta GSAT^2}} \cdot \frac{RF}{\Delta GSAT})$. The AGCM method does not account for interannual variability, which is why no uncertainty estimates are provided for the respective estimates.
The tracer distributions of O_3 and CH_4 are prescribed in the simulation ECCCH$_4$$^{\text{SSTvar}}_{\text{nochem}}$. Therefore, no radiative effects are shown.

with the estimates for the CO_2 perturbation. This is confirmed by the more quantitative comparison of the associated feedback parameters (see Fig. E.15 in the Appendix).

The radiative effect directly induced by CH_4 is slightly more pronounced in the full response compared to the fast response. This is surprising as CH_4 mixing ratios are lower in the full response compared to the fast response (see Sect. 5.1), which is why a negative climate feedback would be expected. The forward calculations, which represent the radiative effects of adding the respective CH_4 perturbation of the simulation ERFCH$_4$$^{\mathrm{SSTfix}}_{\mathrm{chem}}$ or ECCCH$_4$$^{\mathrm{SSTvar}}_{\mathrm{chem}}$ to the climate background of the simulation REF$^{\mathrm{SSTfix}}_{\mathrm{chem}}$ or REF$^{\mathrm{SSTvar}}_{\mathrm{chem}}$, result in 0.344±0.001 W m^{-2} or 0.328±0.001 W m^{-2}, respectively (see Tab. 5.2). Thus, the forward calculations suggest a negative climate feedback of CH_4 of about -0.016 W m^{-2}. However, the backward calculations, which represent the radiative effect of removing the respective CH_4 perturbation from the climate background of ERFCH$_4$$^{\mathrm{SSTfix}}_{\mathrm{chem}}$ or ECCCH$_4$$^{\mathrm{SSTvar}}_{\mathrm{chem}}$, respectively, result in 0.368±0.001 W m^{-2} and 0.388±0.002 W m^{-2}, respectively. Thus, the backward calculations suggest a positive climate feedback of about 0.02 W m^{-2}. The climate feedback of CH_4 derived using the AGCM method indicates a negative feedback of -0.019 W m^{-2} (see Tab. 5.3). The AGCM method has the character of a forward calculation because the background climate represents conditions of the reference simulations (see Sect. 3.3.2). Accounting for the induced stratospheric temperature adjustment enhances the climate feedback to -0.023 W m^{-2} (see Tab. 5.3).

The radiative effect of the perturbation of stratospheric H_2O is strongly influenced by its induced stratospheric temperature adjustment. Accounting for the latter results in a climate feedback of 0.133 W m^{-2} (see Tab. 5.3). This means that the radiative effect is dominated by the increase of lower stratospheric H_2O mixing ratios because middle and upper stratospheric H_2O mixing ratios decrease in the climate response (see Fig. 4.9).

The radiative effects of both, tropospheric and stratospheric O_3, are less pronounced in the full response compared to the fast response. The climate feedback of tropospheric O_3 is -0.034 W m^{-2} with the effect of stratospheric temperature adjustment included. The respective climate feedback of stratospheric O_3 is -0.029 W m^{-2} (see Tab. 5.3).

5.3.4 Assessment of physical feedback processes

Figure 5.12 compares the individual feedbacks of the simulation with interactive chemistry (ECCCH$_4$$^{\mathrm{SSTvar}}_{\mathrm{chem}}$) to the simulation without interactive chemistry (ECCCH$_4$$^{\mathrm{SSTvar}}_{\mathrm{nochem}}$) to assess if physical feedbacks are altered by interactive chemistry. For each feedback pro-

cess the feedback parameter, which is defined as the radiative perturbation normalized by the corresponding change in GSAT, is shown. Here, the radiative perturbations correspond to the full response, without subtracting the fast response. The individual feedbacks of the surface albedo, Planck, the lapse rate, tropospheric H_2O are not significantly different between the simulations with and without interactive chemistry.

The simulation with interactive chemistry suggests a positive climate feedback of clouds, which is consistent with the response of the CO_2 perturbation. In contrast, the cloud feedback of the simulation without interactive chemistry is not significantly different from zero. The interannual variability of the cloud feedback is comparably large so that the difference between the two estimates is not significant. Nevertheless, this result indicates that different processes affect the cloud response in the simulation without interactive chemistry.

In contrast, the radiative effect of the response of stratospheric temperatures is larger in the simulation without interactive chemistry. This can be explained by the more pronounced response of stratospheric H_2O mixing ratios in the full response, which lead to stronger radiative cooling (see Sect. 5.2). It is important to note that the response of stratospheric H_2O is largely caused by chemical production, which is included in simulation ECCCH$_4$$^{\mathrm{SSTvar}}_{\mathrm{nochem}}$ because the chemical tracer distributions from ERFCH$_4$$^{\mathrm{SSTfix}}_{\mathrm{chem}}$ are prescribed. In accordance, the stratospheric adjusted radiative effect of stratospheric H_2O is more pronounced in the simulation without interactive chemistry (see Tab. 5.3). In addition, the decrease of CH_4 mixing ratios in simulation ECCCH$_4$$^{\mathrm{SSTvar}}_{\mathrm{chem}}$ in comparison to the fast response, dampens the stratospheric cooling (see Figs. 5.7 and 5.8).

5.3.5 Summary: Impact of interactive chemistry on ERF and climate sensitivity

This section summarizes the effect of interactive chemistry on the ERF and the climate sensitivity for the CH_4 perturbation simulations. For the radiative effects associated with composition changes of CH_4, O_3 and H_2O only the stratospheric adjusted estimates of the previous sections are repeated.

For the CH_4 perturbation, chemical rapid radiative adjustments of tropospheric and stratospheric O_3, and stratospheric H_2O are important contributions to the ERF. The rapid radiative adjustments associated with the fast response of tropospheric O_3 is 0.642 W m^{-2}, and for stratospheric O_3 it is 0.163 W m^{-2}. The rapid radiative adjustment of the total O_3 response is in close agreement with the radiative effects of O_3 changes resulting from

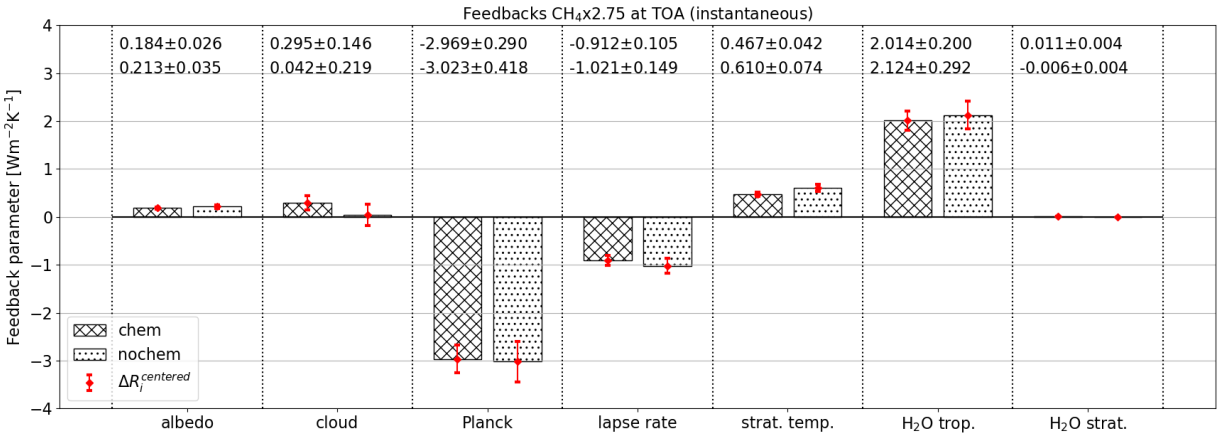

Figure 5.12: Feedback parameters in [W m^{-2} K^{-1}] of individual physical processes either derived from the simulation with interactive chemistry (ECCCH$_4$$^{\mathrm{SSTvar}}$$_{\mathrm{chem}}$; left bars) or without interactive chemistry (ECCCH$_4$$^{\mathrm{SSTvar}}$$_{\mathrm{nochem}}$; right bars). At the top of the figure, the corresponding mean values are listed. The upper estimates correspond to the simulation with interactive chemistry, and the lower estimates to the simulation without. Values after the ± sign are 2× the standard error of the mean approximating the corresponding 95% confidence interval calculated on the basis of 20 annual mean values.

a 5×CH_4 mixing ratios experiment with the EMAC model (Winterstein et al., 2019). In addition, enhanced chemical production from the oxidation of CH_4 leads to a rapid radiative adjustment of stratospheric H_2O of 0.507 W m^{-2}, which is in close agreement with the results of Winterstein et al. (2019) as well. Enhanced chemical production of H_2O influences also the transition region between troposphere and stratosphere. Therefore, the estimate of the rapid radiative adjustment of tropospheric H_2O is larger than the corresponding estimate of the CO_2 perturbation. The separation of the chemically and the temperature driven contributions would, however, require an additional simulation without interactive chemistry and prescribed SSTs and SICs. In summary, the rapid radiative adjustments of O_3 and stratospheric H_2O increase the ERF by about 1.31 W m^{-2}.

The importance of chemical rapid radiative adjustments for CH_4 perturbations has already been mentioned elsewhere (Winterstein et al., 2019; Thornhill et al., 2021b; O'Connor et al., 2022). The contribution of the rapid radiative adjustment of O_3 to the total ERF is about 47% in this study, whereas Thornhill et al. (2021b) estimate the O_3 contribution at about 25% of RF_{adj} and O'Connor et al. (2022) at about 20% of the ERF. Further, the results of the multi-model comparison by Thornhill et al. (2021b) suggest only a minor influence of the stratospheric H_2O response on the ERF. O'Connor et al. (2022) suggest

a rapid radiative adjustment of stratospheric H_2O of about 7% of the total ERF, whereas in this study it is almost 30% of the ERF. The relative larger importance of the rapid radiative adjustments of O_3 and stratospheric H_2O in this study can be explained, on the one hand side, by the underestimation of the direct radiative effect of CH_4. On the other hand side, in the study of O'Connor et al. (2022) also aerosol-cloud interactions contribute significantly to the ERF, so that the relative contributions of O_3 and stratospheric H_2O are smaller.

Furthermore, the change of CH_4 lifetime caused by the reduction of OH affects the direct radiative effect of CH_4. If the chemical sink of CH_4 did not change, a smaller increase of CH_4 mixing ratios would be expected from an increase of the emissions by a factor of 2.75 (see Sect. 5.1). The corresponding difference could be interpreted as an additional chemical rapid radiative adjustment. However, the direct radiative effect of CH_4 is underestimated by the used ECHAM5 radiation scheme, which leads to an underestimation of the associated RF_{inst}, RF_{adj} and ERF.

The results of this study do not indicate a significant effect of physical rapid radiative adjustments for the CH_4 perturbation, which is in agreement with the study of Winterstein et al. (2019). However, accounting for the absorption by CH_4 in the SW spectrum could influence this finding (Smith et al., 2018; Allen et al., 2023).

The climate feedback associated with the reduction of CH_4 mixing ratios in the full response in comparison to the fast response (see Sect. 5.1) does not translate into a clear radiative effect for the centred estimate of the PRP method. The CH_4 absorption bands of the used radiative transfer scheme might be already saturated for such large perturbations of CH_4 so that the comparably small decrease of CH_4 does not result in a clear radiative effect. Nevertheless, the AGCM method indicates a negative climate feedback of -0.023 W m^{-2} with the associated stratospheric temperature adjustment included, which corresponds to a feedback parameter of -0.019 W m^{-2} K^{-1}. The climate feedbacks of both, tropospheric and stratospheric O_3, are negative. The estimate for tropospheric O_3 is -0.034 W m^{-2}, which corresponds to a feedback parameter of -0.029 W m^{-2} K^{-1}. For stratospheric O_3 it is -0.029 W m^{-2}, which corresponds to -0.025 W m^{-2} K^{-1}. The results of the 5×CH_4 mixing ratio experiment by Stecher et al. (2021) do not indicate a significant climate feedback of O_3, neither in the troposphere, nor in the stratosphere. This suggests that the decrease of CH_4 mixing ratios in the full response drives the negative O_3 climate feedback. A similar effect is also present for the CO_2 perturbation (see previous chapter). This conclusion is also supported by the fact that the climate sensitivity parameter of this

study is smaller compared to the corresponding estimate based on the $5\times CH_4$ experiment of Stecher et al. (2021). However, the difference of the two estimates is not statistically significant.

The climate response of stratospheric H_2O induces a radiative effect of 0.133 W m^{-2}, which corresponds to a feedback parameter of 0.114 W m^{-2} K^{-1}. The positive radiative effect is dominated by increasing H_2O mixing ratios in the lowermost stratosphere, which is in agreement with the findings by Stecher et al. (2021). The radiative effect associated with the full response of stratospheric H_2O is 0.020 W m^{-2} stronger in the simulation without interactive chemistry, because the increase of stratospheric H_2O is less pronounced in the simulation with interactive chemistry as a result of reduced chemical production and less strongly increased cold point temperatures (see Sect. 5.2). Thus, the combined effect of O_3 and stratospheric H_2O suggests a negative climate feedback of about -0.084 W m^{-2} caused by interactive chemistry. In addition, the decrease of CH_4 mixing ratios is expected to contribute to the negative climate feedback, but the used radiative transfer scheme might not capture the radiative effect well. In contrast, the results suggest that the climate feedback parameter associated with clouds is about 0.25 W m^{-2} K^{-1} larger in the simulation with interactive chemistry, which would more than offset the dampening effect of interactive chemistry. The difference between the cloud feedbacks is, however, not statistically significant because the corresponding interannual variability is large. The response of GSAT is less pronounced for the simulation without interactive chemistry, which suggests that the negative climate feedbacks induced by composition changes of O_3, stratospheric H_2O and CH_4 are indeed offset by another climate feedback.

Finally, the results of this thesis suggest that the efficacy of the CH_4 perturbation is close to unity if the climate sensitivity parameters based on ERF are compared. The estimates of RF_{inst} and RF_{adj} underestimate the response of GSAT because they do not include the effects of chemical rapid radiative adjustments.

Chapter 6

Discussion

This chapter discusses the results presented in the previous two chapters. A comparison of individual results with literature is already provided in the respective sections of Chapters 4 and 5. This chapter aims at placing the findings in a larger perspective, and at discussing limitations of the used methodology. Firstly, the two methods for the quantification of individual radiative effects are assessed. Secondly, the question, whether the attribution of the O_3 response into individual processes is also representative for other CCMs, is considered. Subsequently, the influence of interactive chemistry on the response of GSAT is discussed. Finally, the influence of the used radiation scheme on the results is assessed.

6.1 Methods for quantification of individual radiative effects

In this thesis two methods are used to derive the radiative effects of individual processes (see Sect. 3.3). Both methods rely on the same radiation scheme, which is also used for the online EMAC simulations. Therefore, the derived radiative estimates can be assumed to be representative for the radiative effects acting in the online simulations, which is an advantage in comparison to the kernel method, for which the radiative kernels are sometimes based on differing radiation schemes (e.g. Soden et al., 2008; Smith et al., 2018). However, this means that shortcomings of the used radiation scheme affect the estimates of individual radiative effects as well (see Sect. 6.4).

The first method, the PRP method (Colman and McAvaney, 1997; Rieger et al., 2017, see Sect. 3.3.1), derives the radiative perturbations of individual processes by re-calculating

a subset of the radiation calls of the online simulations with the respective perturbation substituted. The background state, e.g. the temperature and the cloud field, of the individual radiation calls is thereby fully consistent with the respective time step of the online simulation. This allows the application of the method to temporally variable processes such as clouds. Moreover, the radiative estimates are fully representative of the effect of the perturbation in the online simulation at the re-calculated time step. A sampling error for the time average could occur as not every radiation time step of the online simulation is repeated, but it is expected to be small for the used frequency of a radiation calculation every 10 hours over 20 years. However, the comparably long time in between radiation calculations seems to prohibit the inclusion of the stratospheric temperature adjustment induced by the perturbation (see Sect. 3.3.1). It is known from previous studies (e.g. Stuber et al., 2001; Dietmüller et al., 2016; Banerjee et al., 2019) and confirmed by this thesis that the induced stratospheric temperature adjustment is an important contribution to the radiative effect of perturbations of O_3 stratospheric H_2O, and also to a lesser degree of CH_4. Therefore, an additional method is used to estimate the stratospheric adjusted radiative effects.

This second method derives the radiative perturbations from additional atmosphere-only simulations with the EMAC model, in which the perturbations are substituted using the MESSy option of multiple diagnostic radiation calls (see Sect. 3.3.2 Dietmüller et al., 2016; Nützel et al., 2023), which has already been applied in previous studies (e.g. Winterstein et al., 2019; Stecher et al., 2021). The perturbations are multi-year monthly mean climatologies. With this method both, instantaneous and stratospheric adjusted, radiative perturbations are estimated. The comparison of the instantaneous radiative estimates from both methods indicates that the use of monthly averaged fields influences the radiative effect of tropospheric H_2O. As tropospheric H_2O is temporally highly variable, the interannual variability is comparably large for this process. Interestingly, also the radiative effect of the CH_4 perturbation differs between the two methods. This is somewhat surprising as the spatial distribution of CH_4 in the atmosphere is not particularly variable. However, the most important absorption band of CH_4 overlaps with absorption bands of H_2O, so that the temporal variability of H_2O seems to influence the radiative effect of CH_4 as well. An improvement of the method to be tested in future studies might be therefore to use the prognostic specific humidity instead of the climatology as background for all perturbations except for the perturbations of the specific humidity itself. The estimates of the direct radiative effect of the CO_2 perturbation of both methods deviate by about 3%.

The estimate of the second method is closer to the forward calculation of the PRP method, which is excepted as it also has the character of a forward calculation (see Sect. 3.3.2). The radiative estimates of both methods corresponding to changes of stratospheric H_2O are in close agreement for the CO_2 perturbation, but larger differences occur in case of the CH_4 perturbation, for which the stratospheric H_2O changes are more pronounced. For perturbations of O_3, both methods give consistent results so that the stratospheric adjusted estimates can be considered to represent the radiative effect of the online simulations well.

In summary, it would be desirable to apply the stratospheric temperature adjustment also with the PRP method. Modifications of the method to allow for this should be tested in the future. However, both methods are in sufficiently good agreement, so that the estimates including the stratospheric temperature adjustment can be regarded as representative for the individual radiative effects of the perturbations in the online simulations.

6.2 Assessment of attribution of O_3 response

The contributions of individual processes to the climate response of tropospheric O_3 following the CO_2 or the CH_4 perturbation are quantified in this study (see Sect. 4.1.3 and 5.1.3) using the TAGGING method (Grewe et al. (2017); Rieger et al. (2018); see Sect. 3.1.6). The response of tropospheric O_3 is influenced by different, partly counteracting processes. Enhanced stratosphere-troposphere exchange, as well as larger natural O_3 precursor emissions lead to increased tropospheric O_3 mixing ratios. On the other hand, the decrease of CH_4 mixing ratios and an enhanced chemical sink reduce O_3 mixing ratios. The importance of these processes has been already suggested by other studies (e.g. Stevenson et al., 2006; Dietmüller et al., 2014; Chiodo et al., 2018), but the quantitative attribution in form of the TAGGING approach is a novelty of the present study. The results suggest that the same processes contribute to the climate responses following both perturbations, the CO_2 and the CH_4 increase. However, it remains to be seen whether the attribution is also representative for the tropospheric O_3 response simulated by other CCMs. In particular, the climate response of natural precursor emissions depends on the used representation in the respective model (e.g. Voulgarakis et al., 2013; Stevenson et al., 2020; Zanis et al., 2022).

The climate response of lightning NO_x emissions is uncertain so that even the sign of the projected change depends on the used parameterization (Finney et al., 2016, 2018;

Zanis et al., 2022). This has implications for the climate response of tropospheric O_3, for which changed lightning NO_x emissions are found to be an important contribution. Most schemes used in CCMs to date project increasing lightning NO_x emissions in response to tropospheric warming (Voulgarakis et al., 2013; Finney et al., 2016), which is in accordance with the results of this study. More precisely, the increase of the global lightning NO_x emissions normalized by the response of GSAT is 0.23 Tg(N) a^{-1}/K for the CO_2 perturbation and 0.16 Tg(N) a^{-1}/K for the CH_4 perturbation of the present study. A previous estimate of the EMAC model using the same parameterization for lightning NO_x emissions (Grewe et al., 2001) suggests a smaller sensitivity of 0.14 Tg(N) a^{-1}/K, while the multi-model mean of CCMs based on a different parameterization suggests a larger sensitivity of 0.44±0.05 Tg(N) a^{-1}/K (Finney et al., 2016). However, a more sophisticated lightning NO_x parameterization indicates a decrease of lightning NO_x emissions (Finney et al., 2018).

The increases of biogenic C_5H_8 emissions over the Amazonian region and the Congo river basin (see Appendix E.1) are in qualitative agreement with the climate response of biogenic emissions simulated by other CCMs (Zanis et al., 2022, see their Fig. S6). However, biogenic emissions of C_5H_8 depend on the underlying vegetation, which is expected to interact with changes in e.g. climate, atmospheric CO_2 abundance, tropospheric O_3 or land use change (e.g. Zhou et al., 2018; Vella et al., 2023), but such interactions are not included in the used set-up. Moreover, the contribution of biogenic C_5H_8 emissions is underestimated by the applied version of the TAGGING method because an error was identified after the simulations were performed (M. Mertens, personal communication). The NMHC emissions are scaled by the number of C-atoms in the molecule, i.e. 5 for C_5H_8, before they are added to the NMHC family tracer, which was not done in the case of the online calculated biogenic C_5H_8 emissions. This error affects the diagnostic TAGGING results only, but not the total O_3 response. Therefore, and due to the computational costs of the simulations, it was decided to not repeat the simulations.

To summarize, the climate response of natural precursors of O_3 is partly uncertain, and its representation in a CCM depends on the complexity of the used parameterizations. In this thesis, the contributions of individual processes that contribute to the climate response of tropospheric O_3 caused by either CO_2 or CH_4 increase in the EMAC model are identified for the first time.

6.3 Influence of interactive chemistry on the temperature response

In this thesis, simulations with prescribed chemical tracer distributions, ECCCO$_2$$^{\mathrm{SSTvar}}{}_{\mathrm{nochem}}$ and ECCCH$_4$$^{\mathrm{SSTvar}}{}_{\mathrm{nochem}}$, are performed in addition to the simulation with interactive chemistry to assess the influence of chemical climate feedbacks on the response of GSAT. It turns out that the respective responses of GSAT are not significantly different for the CO_2 perturbation simulations, even though individual chemical climate feedbacks suggest a dampening of the climate sensitivity. In contrast to that, the results of the CH_4 perturbation simulations indicate that a more pronounced positive cloud feedback in the simulation with interactive chemistry offsets the negative climate feedback of chemically active trace gases. Previous studies report a significant reduction of the GSAT response by interactive chemistry for CO_2 perturbations (Dietmüller et al., 2014; Nowack et al., 2015). The simulation set-up of these studies differs, however, in two aspects.

Firstly, previous studies assessed the influence of interactive chemistry on the climate sensitivity for larger perturbations of CO_2 (Dietmüller et al., 2014; Nowack et al., 2015; Marsh et al., 2016). In this thesis the strength of the CO_2 perturbation is chosen to result in a comparable ERF to the one of the CH_4 perturbation, so that the resulting estimates of the climate sensitivity can be compared as the latter can depend on the magnitude of the perturbation (Dietmüller et al., 2014). For the CH_4 perturbation a not too unrealistically large scaling is desired. However, the ERFs of around 1.5 W m^{-2} result in a large interannual variability of the GSAT response, and might therefore be too small to detect robust differences between the GSAT response with and without interactive chemistry. The effect of interactive chemistry on the climate sensitivity parameter was found to be close to the limit of statistical significance for a CO_2 perturbation corresponding to a RF_{adj} of about 1 W m^{-2} (Dietmüller, 2011). Moreover, the influence of interactive chemistry on the GSAT response was found to increase for an increasing magnitude of the CO_2 perturbation (Dietmüller, 2011).

Secondly, the simulations without interactive chemistry in this thesis intrinsically include the effect of chemical rapid radiative adjustment, as the prescribed chemical tracer distributions, in particular O_3 and CH_4, stem from the interactive chemistry simulations representing the fast response to the perturbations of either CO_2 or CH_4 (ERFCO$_2$$^{\mathrm{SSTfix}}{}_{\mathrm{chem}}$ and ERFCH$_4$$^{\mathrm{SSTfix}}{}_{\mathrm{chem}}$, see Sect. 3.2). This set-up is chosen as an attempt to isolate the effect of chemical climate feedbacks. For the CO_2 perturbation, the chemical rapid radiative

adjustment, mainly caused by stratospheric O_3, is negative. This suggests that part of the difference of the GSAT response between simulations with and without interactive chemistry reported by previous studies is caused by the fast response of interactive chemistry. In addition, the climate sensitivity parameter corresponding to the CO_2 perturbed simulation without interactive chemistry is smaller than previous estimates with the EMAC model (Dietmüller, 2011; Dietmüller et al., 2014; Rieger et al., 2017, see Sect. 4.3) which indicates a dampening effect of chemical rapid radiative adjustments as well.

Furthermore, the difference of the GSAT response between the simulations with and without interactive chemistry of this thesis does not reflect the total effect of interactive chemistry on the temperature response. For instance, chemical rapid radiative adjustments significantly enhance the ERF of the CH_4 perturbation, and thereby presumably also the associated response of GSAT (see Sect. 5.3). In addition, as land surface temperatures respond to the perturbation in the fast response, the rapid radiative adjustments and the climate feedbacks are not separated at zero GSAT response, which would be conceptually desirable (e.g. Sherwood et al., 2015; Forster et al., 2016). In particular, for larger perturbations the response of land surface temperatures is not negligible (e.g. Andrews et al., 2021), and might therefore influence chemical interactions and online calculated O_3 precursor emissions. It is therefore debatable whether the complete effect of interactive chemistry on the GSAT response is more meaningful, especially with regard to communication to policy makers. However, from a scientific point of view the attribution into the fast and the full response is desirable as it helps to understand the underlying processes better. Based on the experience of this study, a set-up with two simulations with prescribed reference chemical tracer distributions, one with fixed SSTs and the other coupled to an ocean model, is suggested for future assessments. The comparison of the results of these simulations with the respective simulations with interactive chemistry allows to estimate the effect of interactive chemistry on the ERF and on the total response of GSAT. Combining the estimates of ERF and the GSAT response, the climate sensitivity parameter without interactive chemistry can be determined, which represents the effect of climate feedbacks isolated from rapid radiative adjustments as it is based on ERF. The effect of chemical climate feedbacks on the climate sensitivity is then assessed by comparing the climate sensitivity parameters derived from the simulations with and without interactive chemistry.

Another aspect to note is that the used radiation scheme underestimates the direct radiative effect of CH_4 (Winterstein et al., 2019; Nützel et al., 2023). Therefore, the

effect of the decrease of CH_4 mixing ratios on the climate sensitivity is expected to be underestimated as well, which is discussed in more detail in the following section. However, this can not explain the differing results in comparison to previous studies (Dietmüller et al., 2014; Nowack et al., 2015; Marsh et al., 2016) because in their set-ups CH_4 mixing ratios are prescribed so that the CH_4 climate feedback does not come into effect at all. Therefore, actually a more pronounced negative climate feedback of interactive chemistry would be expected in the present set-up due to the additional dampening by the CH_4 feedback. In this study, however, the points mentioned above seem to mask this effect.

6.4 Dependence on the radiation scheme

The EMAC simulations, as well as the offline radiation calculations with MBM RAD, use the default radiation scheme of the ECHAM5 model, which is known to underestimate the direct radiative effect of CH_4 (Winterstein et al., 2019; Nützel et al., 2023). This is mainly due to the representation of CH_4 absorption in the LW range. Additionally, the radiation scheme does not account for CH_4 absorption in the SW range, which is known to increase the direct radiative effect of CH_4 (Etminan et al., 2016; Byrom and Shine, 2022). The underestimation of the radiative effect of CH_4 has implications for the results of this thesis, which are discussed in the following.

Firstly, the climate feedback associated with the decrease of CH_4 mixing ratios (see Sect. 4.1 and 5.1) is expected to be underestimated, which has consequences for the corresponding climate sensitivity. For the CO_2 perturbation, the radiative effect of the CH_4 decrease calculated with the formula by Etminan et al. (2016) suggests a climate feedback parameter of -0.054 W m^{-2} K^{-1}, whereas the feedback analysis that relies on the ECHAM5 scheme suggests -0.025 W m^{-2} K^{-1} (see Sect. 4.3). Following the CH_4 emission perturbation, CH_4 mixing ratios increase by about a factor of 5 in the fast response. In the full response, CH_4 mixing ratios decrease by about 7% relative to the fast response (see Sect. 5.1). The centred estimate of the PRP method does not suggest a significant radiative effect associated with this CH_4 reduction, whereas the forward radiation calculations indicate a climate feedback parameter of about -0.019 W m^{-2} K^{-1} (see Sect. 5.3). An explanation for the missing radiative effect with the PRP method might be that the CH_4 absorption bands are already saturated for such strong perturbations of CH_4, and that the comparably small decrease of CH_4 shows therefore no noticeable change in the radiative effect. It remains an open question at this point whether a different radiation

scheme would be more sensitive to small differences between such strong perturbations of CH_4.

Secondly, the radiative forcing of the CH_4 perturbation experiments is underestimated. The corresponding ERF is estimated at 1.722 ± 0.173 W m^{-2}, whereby about 0.51 W m^{-2} are attributed to the direct radiative effect of CH_4 (see Sect. 5.3). However, other studies indicate that a radiative effect of about 1.7 W m^{-2} would be more representative for the respective CH_4 perturbation (Etminan et al., 2016; Nützel et al., 2023). Under the assumption that all other rapid radiative adjustments remain the same, only the direct contribution of CH_4 is exchanged, which results in an ERF of about 2.9 W m^{-2}. This considerably larger ERF suggests a correspondingly larger response of GSAT as well.

Thirdly, recent studies indicate that accounting for the absorption of radiation in the (near-infrared) SW spectrum by CH_4 affects the ERF and the climate sensitivity of CH_4 perturbations (Modak et al., 2018; Allen et al., 2023). The SW absorption by CH_4 affects the response of the vertical temperature profile, which in turn influences the response of clouds. The associated rapid radiative adjustment of clouds is expected to be negative if CH_4 SW absorption is accounted for (Smith et al., 2018; Modak et al., 2018; Allen et al., 2023), while in the present study it was not found to be significantly different from zero. In addition, enhanced SW absorption by CH_4 counteracts the LW induced stratospheric cooling. This process has a dampening effect on the radiative forcing (Smith et al., 2018; Byrom and Shine, 2022; Allen et al., 2023).

Chapter 7

Conclusions and Outlook

CH_4, the second most important GHG directly emitted by human activity, is removed from the atmosphere via chemical decomposition. The chemical sink of CH_4 depends on the temperature and on the abundance of its reaction partners, of which OH is the most important. Therefore, the atmospheric lifetime of CH_4 is not constant, which influences its atmospheric abundance, and thereby its potential as a GHG. In addition, products of the chemical sink of CH_4 influence the atmospheric composition, and thereby its climate impact. This thesis investigates the role of CH_4 for chemistry-climate feedbacks to understand these processes better and to quantify their individual importance for the radiation budget.

Therefore, simulations with the CCM EMAC in a configuration with prescribed CH_4 surface emissions are performed to explicitly simulate the response of CH_4 mixing ratios to either increased CO_2 mixing ratios, or increased CH_4 emissions. Hereby, the so called fast response and the climate response are assessed separately. The fast response represents the direct effect of the perturbation excluding the response of SSTs, and thereby most of the tropospheric temperature response, whereas the climate response is driven by the tropospheric temperature change. This chapter first summarizes some technical developments related to this thesis. Subsequently, it brings together the results of this thesis by answering the research questions, which are introduced in Sect. 1.2. At the end a short outlook concludes this thesis.

7.1 Summary and Conclusions

7.1.1 Technical Developments

In the framework of this thesis, I contributed to the implementation of the PSrad radiation scheme (Pincus et al., 2003) into MESSy, as well as to the tuning and the evaluation of EMAC with PSrad as driving radiation scheme (Nützel et al., 2023). Repeating the sensitivity simulations with PSrad as driving radiation scheme and analysing the isolated effect of the changed radiation scheme is beyond the scope of this thesis. Nevertheless, estimates of the CH_4 radiative effect using PSrad (Nützel et al., 2023) serve as comparison values for the results of this thesis.

In addition, the MESSy base model RAD (MBM RAD) was further developed so that it can be used for offline radiative transfer calculations for the Partial Radiative Perturbation (PRP) method. MBM RAD has the advantage that it uses the same routines for the radiation calculations as the EMAC model. Therefore, it is fully consistent with the radiative transfer calculation of the online simulation, and developments regarding the routines of the radiation calculation can be made easily available for MBM RAD, e.g. the implementation of the additional radiation scheme PSrad.

Furthermore, this thesis is one of the first applications of the EMAC model in the configuration with CH_4 emissions instead of prescribed CH_4 mixing ratios (Frank, 2018). The used simulation set-up can be applied to other perturbation experiments, for which influences on the chemical sink of CH_4 are expected, e.g. the climate impact of the usage of hydrogen as widely-used energy source (e.g. Ocko and Hamburg, 2022) or reductions of anthropogenic O_3 precursor emissions.

7.1.2 Research Questions

The section summarizes the results presented in detail in the Chapters 4 and 5 by answering the detailed research questions, which are introduced in Sect. 1.2.

RQ 1: ***How does the chemical sink of atmospheric CH_4 respond in the fast and in the climate response if perturbed by either increased CO_2 mixing ratios or increased CH_4 emissions? How do these changes of the chemical sink feed back on atmospheric CH_4 mixing ratios?***

In fast response of the CO_2 perturbation, the tropospheric lifetime of CH_4, and therefore also the tropospheric CH_4 mixing ratios, remain unchanged. In the upper stratosphere and mesosphere, radiatively induced cooling leads to the prolongation of the CH_4 lifetime and to increasing CH_4 mixing ratios.

The CH_4 emissions are increased by a globally constant factor of 2.75 in the CH_4 perturbation experiments. This increase of the emissions results in an increase of the global mean surface mixing ratio by a factor of about 5, more precisely 4.76. This simulation is therefore consistent with a corresponding experiment simulation, in which CH_4 mixing ratios are increased by a factor of 5 (Winterstein et al., 2019). To reach the targeted surface mixing ratios of CH_4 in the latter set-up, an artificial surface emission flux is diagnosed in the model, which increases by a factor of 2.75 (Stecher et al., 2021). The increase factor of the CH_4 mixing ratios is larger than the increase factor of the surface emissions due to a large reduction of OH mixing ratios in the troposphere, which leads to the extension of the tropospheric CH_4 lifetime.

The climate response of the tropospheric CH_4 lifetime and the corresponding response of the mixing ratios is in qualitative agreement for both perturbations, the CO_2 and the CH_4 increase. Tropospheric warming and associated moistening result in increases of the OH mixing ratios. In addition, the oxidation rate of CH_4 increases due to its temperature dependent reaction rate coefficient. As a consequence, the tropospheric mean lifetime of CH_4 shortens, and the CH_4 mixing ratios decrease throughout the troposphere. While a shortening of the CH_4 lifetime as a consequence of tropospheric warming has been already reported by previous studies (Voulgarakis et al., 2013; Dietmüller et al., 2014; Frank, 2018; Stecher et al., 2021; Thornhill et al., 2021a), the novelty of this thesis is that the corresponding response of the CH_4 mixing ratios evolves explicitly, which has been investigated by only a few studies so far (Heimann et al., 2020). A simulation set-up with CH_4 emissions, instead of prescribed mixing ratios at the lower boundary, is necessary so that the

CH_4 feedback can be explicitly taken into account. The results suggest that the sensitivity of the CH_4 lifetime to the response of GSAT is larger in this study compared to previous work (Voulgarakis et al., 2013; Thornhill et al., 2021a; Stecher et al., 2021) because the CH_4-OH feedback is implicitly included in the lifetime response since CH_4 mixing ratios are not prescribed. This finding is consistent for the climate responses following the CO_2 and the CH_4 perturbation.

RQ 2: ***Which processes play a role in the fast and in the climate response of O_3 if perturbed by either CO_2 or CH_4 increase? Is the climate response of O_3 affected by the explicit accounting for of the CH_4 feedback?***

O_3 mixing ratios respond differently to the CO_2 and to the CH_4 perturbation in the fast response. The CO_2 perturbation affects O_3 mainly indirectly through the temperature response. Radiatively induced cooling in the stratosphere causes slower chemical O_3 depletion and leads therefore to increasing O_3 mixing ratios. The increase of O_3 above reduces lower stratospheric O_3 formation because less ultraviolet radiation is available for photochemical production in this region. This effect is known as reversed self-healing (Rosenfield et al., 2002; Portmann and Solomon, 2007).

In contrast, the CH_4 perturbation affects the chemical composition directly by its oxidation products, which lead to increases of tropospheric O_3 mixing ratios by up to 60%. The O_3 response in the stratosphere is driven by temperature changes and enhanced levels of HO_x. Stratospheric cooling results in increased O_3 mixing ratios in the middle stratosphere, whereas enhanced catalytic depletion via the HO_x cycle leads to reduced O_3 mixing ratios in the upper stratosphere and mesosphere.

Unlike the fast response, the climate response of O_3 is in qualitative agreement for the CO_2 and for the CH_4 perturbation. O_3 mixing ratios decrease in the lower tropical stratosphere, which indicates enhanced tropical upwelling as thereby more O_3 depleted air is transported into the stratosphere, which is a robust response pattern across CCMs (Dietmüller et al., 2014; Nowack et al., 2015; Marsh et al., 2016; Chiodo et al., 2018; Stecher et al., 2021). Different, partly counteracting, processes are involved in the climate response of tropospheric O_3, whose contributions to the total response are quantified using an attribution method. Stronger stratosphere – troposphere exchange and larger natural emissions of O_3 precursors lead to increases of tropospheric O_3, whereas enhanced chemical loss caused by the increased tropospheric humidity and the decrease of CH_4 mixing ratios lead to decreases. The reduced production of O_3 caused by the decrease of CH_4 mixing

ratios leads to differences of the climate response of tropospheric O_3 between this study and previous work with prescribed CH_4 mixing ratios, instead of prescribed CH_4 emissions, at the lower boundary (Dietmüller et al., 2014; Nowack et al., 2015; Marsh et al., 2016; Nowack et al., 2018; Chiodo et al., 2018; Stecher et al., 2021). The latter studies consistently show an increase of O_3 mixing ratios in the tropical upper troposphere, whereas in this study the response is either not significant or indicates a reduction of O_3 mixing ratios in this region.

RQ3: ***What is the effect of interactive chemistry on the temperature response and on the response of H_2O mixing ratios?***

A diagnostic from additional perturbed radiation calls allows to assess the effect of composition changes of individual species on the stratospheric temperature. This so called stratospheric temperature adjustment indicates that the fast response of stratospheric O_3, which follows the CO_2 perturbation, reduces the CO_2 induced cooling by up to 25% in the upper stratosphere and mesosphere. The decrease of O_3 mixing ratios in the lower tropical stratosphere in the climate response leads to enhanced cooling in this region and reduces the temperature increase at the tropical cold point. This effect leads to a significant reduction of the climate response of stratospheric H_2O in previous studies (Dietmüller et al., 2014; Nowack et al., 2015; Marsh et al., 2016), whereas the effect is not significant in this study. Explanations for this disagreement with previous studies are, firstly, the smaller magnitude of the CO_2 perturbation in this study, which might be too low to detect a robust result from the statistical variability, and secondly, the different simulation set-ups. With the used set-up only the effect of chemical climate feedbacks is considered, but part of the reduction of the stratospheric H_2O increase might be caused by the fast response of O_3, which was not identified as a separate entity by the previous studies.

The CH_4 perturbation leads to a large increase of stratospheric H_2O in the fast response with a maximum relative increase up to 250% in the upper stratosphere and mesosphere. On the one hand, the oxidation of CH_4 leads to local production of H_2O, and on the other hand, a temperature increase at the tropical cold point reduces the dehydration of upwelling airmasses in this region. The radiative cooling associated with the H_2O increase is an important contribution to the stratospheric temperature response. In addition, also the response of O_3 contributes significantly to the stratospheric temperature change. The structure of the radiatively induced temperature tendencies are consistent with a previous CH_4 perturbation experiment with the EMAC model (Winterstein et al., 2019).

In the corresponding climate response, stratospheric H_2O mixing ratios increase in the lowermost stratosphere and decrease above. The increase in the lowermost stratosphere is caused by reduced dehydration at the cold point. However, the temperature increase at the cold point is dampened by the decrease of O_3 mixing ratios at this altitudes, which dampens the increase of H_2O accordingly. In addition, the chemical production of H_2O is reduced compared to the fast response. In summary, chemical climate feedbacks reduce the increase of stratospheric H_2O in the climate response. Nevertheless, the H_2O mixing ratios are still larger compared to the reference throughout the stratosphere.

The response of GSAT is not significantly altered by chemical climate feedbacks in the present CO_2 perturbation experiments. The results regarding the CH_4 perturbation indicate that the response of GSAT is more pronounced if chemical climate feedbacks are free to evolve.

RQ 4: ***How large are the contributions of chemical rapid radiative adjustments and slow climate feedbacks on the ERF and on the climate sensitivity?***

The stratospheric temperature adjustments induced by composition changes of stratospheric H_2O, O_3, and to a lesser degree also of CH_4, are important contributions to the associated radiative effects, which has been already noted by previous studies (e.g. Stuber et al., 2001; Dietmüller et al., 2016; Banerjee et al., 2019) and is confirmed by the present study. Therefore, not the instantaneous, but the stratospheric adjusted rapid radiative adjustments and slow climate feedbacks are summarized here. The corresponding radiative effects excluding the associated stratospheric temperature adjustment are listed in the chapters addressing the respective results.

The fast response of stratospheric O_3 that follows the CO_2 perturbation induces a negative rapid radiative adjustment of -0.034 W m^{-2}, whereas the radiative effect of the corresponding response of tropospheric O_3 is estimated at 0.012 W m^{-2}. In addition, the increase of stratospheric CH_4 induces a small positive rapid radiative adjustment of 0.001 W m^{-2}, so that the total effect of interactive chemistry on the ERF is estimated at -0.021 W m^{-2} for the CO_2 perturbation in this study, which corresponds to -1.3% of the total ERF.

In comparison to the CO_2 perturbation, chemical rapid radiative adjustments represent a larger part of the ERF for the CH_4 perturbation. The rapid radiative adjustment corresponding to the fast response of stratospheric O_3 is estimated at 0.163 W m^{-2}. In addition, the rapid radiative adjustment of tropospheric O_3 is 0.642 W m^{-2}. Enhanced

chemical production leads to large increases of stratospheric H_2O. Therefore, the corresponding rapid radiative adjustment, which is estimated at 0.507 W m^{-2}, is considered to be mainly chemically induced. In summary, the rapid radiative adjustments of O_3 and stratospheric H_2O make up for about 1.31 W m^{-2} of the total ERF of 1.722 W m^{-2}. The relative importance of the contributions of O_3 and H_2O are expected to be overestimated due to the underestimation of the direct radiative effect of CH_4 by the used radiation scheme. However, this is not expected to influence the absolute contributions.

The climate responses of O_3 mixing ratios reduce the climate sensitivity for both, the CO_2 and the CH_4 perturbation. The climate response of tropospheric O_3 corresponds to a climate feedback parameter of -0.023 W m^{-2} K^{-1} for the CO_2 perturbation, and of -0.029 W m^{-2} K^{-1} for the CH_4 perturbation. The climate feedback parameters associated with the climate responses of stratospheric O_3 are estimated at -0.016 W m^{-2} K^{-1} and -0.025 W m^{-2} K^{-1} for the CO_2 and the CH_4 perturbation, respectively. The decrease of CH_4 mixing ratios in the climate response which follows the CO_2 perturbation results in a climate feedback parameter of -0.025 W m^{-2} K^{-1}. For the CH_4 perturbation, CH_4 mixing ratios decrease in the climate response compared to the fast response as well. The corresponding climate feedback parameter is estimated at -0.019 W m^{-2} K^{-1}. However, the radiative effects of the climate feedback of CH_4 are expected to be underestimated by the used radiation scheme. The climate feedback parameters of O_3 and CH_4 are in agreement with previous estimates, which cover a comparably wide range (Dietmüller et al., 2014; Nowack et al., 2015; Marsh et al., 2016; Thornhill et al., 2021a; Heinze et al., 2019). The comparison with results derived using the same CCM (Dietmüller et al., 2014; Stecher et al., 2021) indicates that the tropospheric O_3 feedback is more strongly negative and becomes comparable in magnitude to the stratospheric O_3 feedback in this study because of the explicit treatment of the CH_4 feedback, which leads to reduced O_3 formation.

For the CH_4 perturbation, chemical climate feedbacks reduce the climate response of stratospheric H_2O (see previous research question). The corresponding reduction of the radiative effect is estimated at -0.020 W m^{-2}. In contrast, the radiative effect of stratospheric H_2O is estimated to be 0.008 W m^{-2} larger if chemical climate feedbacks are included for the CO_2 perturbation. This finding is not consistent with previous studies, which suggest a significant negative effect of interactive chemistry on the stratospheric H_2O climate feedback (Dietmüller et al., 2014; Nowack et al., 2015; Marsh et al., 2016, see also previous research question).

In summary, the climate feedbacks corresponding to composition changes of O_3 and

CH_4 are negative so that they are expected to reduce the climate sensitivity. In addition, interactive chemistry influences the climate feedback of stratospheric H_2O by O_3 induced radiative cooling in the lower tropical stratosphere. However, this effect does not translate into a dampening effect on the response of GSAT for the CO_2 perturbation in this study.

Furthermore, the results of this thesis do not indicate an effect of interactive chemistry on physical climate feedbacks for the CO_2 perturbation. In contrast, for the CH_4 perturbation, the climate feedback of clouds is larger in the simulation with interactive chemistry, which seems to offset the negative chemical climate feedbacks of O_3, CH_4 and stratospheric H_2O.

As mentioned in the answer to the previous research question, accounting for chemical climate feedbacks does not result in a significantly different response of GSAT for the CO_2 perturbation simulations of the present study, even though individual climate feedbacks indicate a reduction. A detailed discussion can be found in the previous chapter. For the CH_4 perturbation, the results of this thesis suggest that the positive cloud feedback offsets the negative climate feedbacks induced by composition changes of O_3, CH_4 and stratospheric H_2O. However, the statistical uncertainty of the cloud feedback is large, so that this finding must be confirmed by other studies.

RQ5: ***Is the climate sensitivity parameter different for the CH_4-perturbation compared to the CO_2-perturbation if chemical feedbacks are accounted for in the simulation set-up?***

Conceptually, the comparison of the RF of different perturbation types is meaningful if the RF is representative of the associated response of GSAT, or in other words, if the corresponding climate sensitivity parameters are the same. The efficacy of a perturbation is the corresponding climate sensitivity parameter normalized by the climate sensitivity parameter of the CO_2 perturbation, so that an efficacy of unity means that the climate sensitivity parameters of the considered perturbation is the same as for the CO_2 perturbation.

The scaling of the CO_2 and the CH_4 perturbations in this study are chosen so that the resulting ERFs are of similar magnitude. This allows an optimal comparison of the climate sensitivity parameters as these can depend on the magnitude of the perturbation (Hansen et al., 2005; Dietmüller et al., 2014). The results of this thesis suggest an efficacy of unity for the CH_4 perturbation if the climate sensitivity parameters are based on ERF. The climate sensitivity parameters based on RF_{inst} and RF_{adj} deviate strongly between

the CO_2 and the CH_4 perturbation because of the large effect of chemical rapid radiative adjustments for the CH_4 perturbation.

7.2 Outlook

The PSrad radiation scheme (Pincus et al., 2003) is now available in the MESSy framework (Nützel et al., 2023). This provides the opportunity to investigate climate feedbacks of CH_4 using the EMAC model in a configuration with an improved representation of the radiative effect of CH_4 in future studies. With PSrad not only an improved quantification of the radiative effect of CH_4 is achieved, but the accounting for SW absorption by CH_4 in this scheme might also influence adjustment and feedback processes of, e.g. clouds (Smith et al., 2018; Allen et al., 2023).

This thesis focuses on the role of CH_4 for interactions between the gas-phase chemistry and climate change. The applied simulation set-up uses surface emission fluxes for CH_4 so that the CH_4 mixing ratios can explicitly respond to changes of the chemical sink, which allows for secondary feedbacks of, e.g. O_3. However, further processes can also play a role, which are not accounted for by the used simulation set-up. For instance, chemistry-aerosol-cloud coupling was identified to contribute to the ERF of CH_4 perturbations (Kurtén et al., 2011; O'Connor et al., 2022) and might therefore also influence the corresponding climate response. In addition, natural emission sources of CH_4, e.g. from wetlands or permafrost, have the potential to increase in a warming climate (e.g. O'Connor et al., 2010; Dean et al., 2018). For instance, the results of Thornhill et al. (2021b) suggest that the negative radiative effect corresponding to the shortening of the CH_4 lifetime is offset by the positive radiative effect of CH_4 emission increases from wetlands as response to a $4\times CO_2$ perturbation. The net effect of feedbacks of the gas-phase chemistry and of natural emissions influences the effect of associated secondary feedbacks, e.g. regarding the formation of O_3.

In summary, the atmospheric abundance of CH_4 is linked to a number of complex interactions. The novelty of this study is that the response of CH_4 mixing ratios to changes of its chemical sink, and thereby also associated secondary feedbacks, are accounted for explicitly. However, further studies that integrate even more processes are necessary to robustly project the change of CH_4, and secondary feedbacks, in a changing climate, and to assess climate mitigation options.

Acronyms

AOGCM	Atmosphere Ocean General Circulation model
BMIL	Base Model Interface Layer
BML	Base Model Layer
C_2H_2	ethyne
C_5H_8	isoprene
CCM	chemistry-climate model
CFC	chlorofluorocarbon
CH_3	methyl
CH_3CCl_3	methylchloroform
CH_3O	methoxy radical
CH_3O_2	methyldioxide
CH_3OH	methanol
CH_3OOH	methylhydroperoxide
CH_4	methane
Cl	chlorine
CO	carbon monoxide
CO_2	carbon dioxide
DMS	dimethyl sulfide
$ECCCH_4{}^{SSTvar}{}_{chem}$	CH_4 perturbation simulation with MLO and interactive chemistry

$ECCCH_4^{SSTvar}{}_{nochem}$	CH_4 perturbation simulation with MLO and prescribed chemical tracer distributions
$ECCCO_2^{SSTvar}{}_{chem}$	CO_2 perturbation simulation with MLO and interactive chemistry
$ECCCO_2^{SSTvar}{}_{nochem}$	CO_2 perturbation simulation with MLO and prescribed chemical tracer distributions
ECHAM5	5th generation European Centre Hamburg General Circulation model
EMAC	ECHAM/MESSy Atmospheric Chemistry
ERF	effective radiative forcing
$ERFCH_4^{SSTfix}{}_{chem}$	CH_4 perturbation simulation with prescribed SSTs and SICs and interactive chemistry
$ERFCO_2^{SSTfix}{}_{chem}$	CO_2 perturbation simulation with prescribed SSTs and SICs and interactive chemistry
ESM	Earth System model
GCM	General Circulation model
GHG	greenhouse gas
GSAT	global surface air temperature
H_2O	water vapour
HCFC	hydrochlorofluorocarbon
HCHO	formaldehyde
HCl	hydrogen chloride
HO_2	hydroperoxyl
HO_x	odd hydrogen
IPCC	Intergovernmental Panel on Climate Change
JJA	June, July, and August
KPP	kinetic preprocessor
K / (W m^{-2})	K per Watt per square meter

LW	longwave
McICA	Monte Carlo Independent Column Approximation
MECCA	MECCA (Module Efficiently Calculating the Chemistry of the Atmosphere)
MESSy	Modular Earth Submodel System
MLO	mixed layer ocean
N_2O	nitrous oxide
NH	Northern Hemisphere
NMHC	non-methane hydrocarbon
NO	nitrogen oxide
NO_2	nitrogen dioxide
NO_x	nitrogen oxides NO and NO_2
NO_y	reactive nitrogen compounds
O_2	molecular oxygen
O_3	ozone
$O(^1D)$	excited oxygen
OH	the hydroxyl radical
p.p.	percentage points
PAN	peroxyacyl nitrate
ppmv	parts per million volume
PSC	polar stratospheric cloud
$REF^{SSTfix}{}_{chem}$	reference simulation with prescribed SSTs and SICs and interactive chemistry
$REF^{SSTvar}{}_{chem}$	reference simulation with MLO and interactive chemistry

$\mathrm{REF^{SSTvar}}_{\mathrm{nochem}}$	reference simulation with MLO and prescribed chemical tracer distributions
RF	radiative forcing
$\mathrm{RF_{adj}}$	stratospheric adjusted radiative forcing
$\mathrm{RF_{inst}}$	instantaneous radiative forcing
SH	Southern Hemisphere
SIC	sea ice concentration
SMCL	Submodel Core Layer
SMIL	Submodel Interface Layer
SST	sea surface temperature
SW	shortwave
$\mathrm{Tg(CH_4)\ a^{-1}}$	$\times\ 10^{12}$ g $\mathrm{CH_4}$ per year
TOA	top of the atmosphere
$\mathrm{W\ m^{-2}}$	Watt per square meter
$\mathrm{W\ m^{-2}\ K^{-1}}$	Watt per square meter per K

Appendix A

Additional information on the MESSy basemodel RAD (MBM RAD)

A.1 MBM RAD input

Table A.1 summarizes the input variables that are in general needed for simulations with MBM RAD. Depending on the set-up, not all input variables might be required. For instance, if the surface albedo is directly imported, the variables *vlt* (leaf area index), *cvs* (snow cover), *cvsc* (snow covered canopy), *seaice* (ice cover) and *sni* (water equivalent of snow on ice) are not needed, and the ALBEDO submodel can be SWITCHed off. Similarly, if the cloud optical properties are directly imported the variables *acdnc* (cloud droplet number concentration), *xim*1 (cloud ice), *xlm*1 (cloud water), *radlp* (effective radius of liquid droplets) and *radip* (effective radius of ice particles) are not needed, and the CLOUDOPT submodel can be turned of via the SWITCH namelist (see, e.g. Jöckel et al., 2005).

The variables *tslm*1 (surface temperature of land), *tsi* (surface temperature of ice) and *sni* are required from the default EMAC output of the time step before to reproduce the radiation calculation of the EMAC simulation. The variables *tsw* (surface temperature of water), *cvs* and the surface pressure that are required for the radiation calculation are not identical to the default EMAC output. If the radiative fluxes calculated by MBM RAD should be consistent with a previous EMAC simulation, snapshots of these variables as they are used in the radiation call have to be provided as special output.

Table A.1: List of all variables that are required as input for MBM RAD. For each variable the name used in EMAC and its usual output channel are listed.

Name	**Output channel**	**notes**
Always required:		
slm	*constant*	
glac	*constant*	
geosp	*constant*	
tslm1	ECHAM5	time step before
tsw	as used in rad_radiation	
tsi	ECHAM5	time step before
tslnew	ECHAM5	
icecov	ECHAM5	
seacov	ECHAM5	
surface pressure	as used in rad_radiation	
tm1	ECHAM5	
qm1	ECHAM5	
CH4	depends on set-up (RAD01, TRACER_GP,..)	
O3	—”—	
N2O	—”—	
CFC11	—”—	
CFC12	—”—	
CO2	—”—	
sum_cov	CLOUDOPT	
Required for online calculation of surface albedo:		
alb	*constant*	
forest	*constant*	
vlt	ECHAM5	
cvs	as used in rad_radiation	
cvsc	ECHAM5	
seaice	ECHAM5	
sni	ECHAM5	time step before

Table A.1 – *Continued from previous page*

Required if surface albedo is imported instead:		
albedo	ALBEDO	
alsol	ALBEDO	
alsow	ALBEDO	
alsoi	ALBEDO	
Required for calculation of cloud optical properties:		
acdnc	ECHAM5	Only used for re-calculation of radlp and radip
xim1	ECHAM5	
xlm1	ECHAM5	
radlp	CLOUDOPT	
radip	CLOUDOPT	
Required if cloud optical properties are imported instead:		
tau_cld_lw	CLOUDOPT	
tau_cld_sw	CLOUDOPT	
gamma_cld_sw	CLOUDOPT	
omega_cld_sw	CLOUDOPT	
Required if aerosol optical properties are imported:		
aot_lw	AEROPT	
aot_sw	AEROPT	
gamma_sw	AEROPT	
omega_sw	AEROPT	

A.2 MBM RAD namelist

For simulations with MBM RAD the MBM RAD coupling namelist (`CPL_MBM`) is required as additional entry in the `rad.nml` file. The parameters `LV_ECHAM`, `LZONAL_MEAN`, `NN`, and `NLEV` control the grid definition. The logical `LADD_TTE` controls whether the radiative temperature tendency should be added to the temperature $tm1$. This is not related to the stratospheric temperature adjustment as explained in Sect. 3.1.5.

The following `CPL_MBM` defines the three-dimensional native grid of ECHAM5 at a resolution of T42L90MA for MBM RAD. In this simulation the calculated temperature tendency

is not added to the temperature:

```
&CPL_MBM
! with LADD_TTE = T the temperature tendency is added
! to the actual temperature every time step
!
LADD_TTE = F,
LV_ECHAM = T,
LZONAL_MEAN = F,
NN   = 42,
NLEV = 90
/
```

A.3 Assessment of sampling error

Table A.2 shows the TOA radiation fluxes of 1-year simulations with EMAC and MBM RAD, conducted with the default ECHAM5 radiation scheme E5rad or PSrad. For the EMAC results, annual averages of instantaneous fluxes at the output time step (inst) or averaged over the 5-hour output interval (ave) are shown. As the latter include all time steps in the average, they are more representative of the annual mean. The radiation was called every 5 or 10 hours for MBM RAD. For the calculation of feedbacks of a multi-year EMAC simulation, it is not feasible to re-calculate every EMAC radiation time step with MBM RAD as this would require to store large amounts of input data. Normally, twice daily data is used (Rieger et al., 2017). Therefore, the presented test simulations assess the potential sampling error of the annual mean net radiation budget at TOA caused by a frequency corresponding to a radiation call every 5 or 10 hours. As mentioned in Sect. 3.1.5 a single radiation time step is bit-identically reproduced by MBM RAD if the required output is provided in double precision.

The global mean LW fluxes differ by up to 0.007 W m^{-2}, regardless of the radiation scheme. The deviation is more pronounced in the SW. With E5rad, the SW all-sky fluxes differ by up to 0.017 W m^{-2} and the SW clear-sky fluxes by up to 0.111 W m^{-2}. The SW clear-sky fluxes are negatively biased with MBM RAD if the MBM RAD radiation calculation does not coincide with an EMAC radiation time step. The probable reason for that is, that the time offset for orbital parameters does not lay in the middle of the interval for which the transmissivities are calculated, but is shifted to later times (Nützel et al.,

2023). During the implementation of PSrad, an option to use the time offset corresponding to the middle of the interval was implemented (Nützel et al., 2023). This option was active for the MBM RAD tests with PSrad. The mean error of the SW clear-sky fluxes is up to 0.029 W m^{-2} with PSrad and thereby smaller than with E5rad.

However, in PSrad the implementation of the cloud sampling with the Monte Carlo Independent Column Approximation (McICA) (Pincus et al., 2003) method leads to higher deviations of the all-sky SW flux. McICA draws independent samples of the cloud state for each g-point (see Sect. 3.1.5). The used Monte Carlo random seeds are calculated from the surface pressure. Therefore, one single radiation call can only be bit-identically reproduced if the surface pressure of a previous EMAC simulation is provided in double precision to guarantee identical Monte Carlo random seeds and thereby identical cloud samples. However, the cloud samples are still representative for the present cloud state, even with differing Monte Carlo random seeds. Therefore, the error should average out for a longer simulation.

For both radiation schemes, the deviations are comparable if MBM RAD calls the radiation every 5 or 10 hours.

Table A.2: Comparison of TOA global mean radiation fluxes [W m^{-2}] of 1-year simulations with EMAC and MBM RAD using, either E5rad, or PSrad. For MBM RAD the results when calling the radiation with a frequency corresponding to a radiation call every 5 or 10 hours are shown. Shown are LW (all-sky), clear-sky LW, SW (all-sky), clear-sky SW and net (all-sky) fluxes. For EMAC, both the instantaneous fluxes (inst) and the fluxes averaged over the 5-hour output interval (ave) are shown.

	LW	**Clear-sky LW**	**SW**	**Clear-sky SW**	**Net**
E5rad:					
EMAC inst	-233.457	-260.769	238.450	287.835	4.997
EMAC ave	-233.462	-260.770	238.454	287.835	4.988
MBM (5 hrs)	-233.455	-260.768	238.445	287.724	4.990
MBM (10 hrs)	-233.460	-260.769	238.437	287.725	4.977
PSrad:					
EMAC inst	-234.048	-261.002	239.289	289.253	5.241
EMAC ave	-234.054	-261.003	239.303	289.252	5.255
MBM (5 hrs)	-234.047	-261.001	239.385	289.230	5.338
MBM (10 hrs)	-234.050	-261.002	239.374	289.223	5.324

Appendix B

Table of used submodels

Table B.1: Alphabetic list and short description of used MESSy submodels.

Submodel	**Description**	**Reference**
AEROPT	aerosol optical properties	Dietmüller et al. (2016); Nützel et al. (2023)
AIRSEA	air-sea exchange of chemical species	Pozzer et al. (2006)
ALBEDO	surface albedo	Nützel et al. (2023)
CH4	simplified CH_4 chemistry	Winterstein and Jöckel (2021)
CLOUD	ECHAM5 cloud microphysics and cloud cover	Roeckner et al. (2006); Jöckel et al. (2005)
CLOUDOPT	cloud optical properties	Dietmüller et al. (2016); Nützel et al. (2023)
CONVECT	convection parameterization	Tost (2019a)
CVTRANS	transport of tracers due to convection	Tost (2019b)
DDEP	dry deposition of gases and aerosols	Kerkweg et al. (2006a)
E5VDIFF	ECHAM5 routines for vertical diffusion and land-atmosphere exchange	MESSy Consortium (2023)

Table B.1 – *Continued from previous page*

GWAVE	non-orographic gravity waves	MESSy Consortium (2023)
H2OISO	hydrological cycle for water isotopologues	Eichinger et al. (2015)
JVAL	photolysis rate coefficients	Sander et al. (2014)
LNOX	lightning NO_x emissions	Tost et al. (2007)
MECCA	tropospheric and stratospheric chemistry	Sander et al. (2019)
MLOCEAN	mixed layer ocean	Roeckner et al. (1995, 2003); Kunze et al. (2014)
MSBM	heterogeneous chemistry on polar stratospheric cloud particles and on stratospheric aerosol	Jöckel et al. (2010)
O3ORIG	tracing of ozone origin	Grewe (2006)
OFFEMIS	offline emissions	Kerkweg et al. (2006b)
ONEMIS	online emissions	Kerkweg et al. (2006b)
ORBIT	parameters associated with the Earth's orbit around the Sun	Dietmüller et al. (2016)
OROGW	orographic gravity waves	Roeckner et al. (2003); Eichinger et al. (2023)
PTRAC	additional user-defined tracers	Jöckel et al. (2008)
QBO	assimilation of the quasi-biennial oscillation	MESSy Consortium (2023)
RAD	radiative transfer	Dietmüller et al. (2016); Nützel et al. (2023)
SCALC	simple algebraic calculations	Jöckel et al. (2016)
SCAV	aqueous phase chemistry and wet deposition	Tost et al. (2006)
SEDI	aerosol particle sedimentation	Kerkweg et al. (2006a)
SURFACE	surface processes	MESSy Consortium (2023)
TAGGING	attribution of mixing ratios of O_3, HO_x and additional species to individual source categories	Grewe et al. (2017); Rieger et al. (2018)

Table B.1 – *Continued from previous page*

TNUDGE	pseudo emissions of tracers calculated by Newtonian relaxation to prescribed mixing ratios	Kerkweg et al. (2006b)
TREXP	decay and release of tracers	Jöckel et al. (2010)
TROPOP	tropopause diagnostics	MESSy Consortium (2023)
TRSYNC	synchronisation of HDO tracer between chemistry and H2OISO	Winterstein and Jöckel (2021)
VISO	iso-surfaces and mapping of 3D fields on surfaces	Jöckel et al. (2010)

Appendix C

Evaluation of reference simulations

This chapter compares the three reference simulations $REF^{SSTfix}{}_{chem}$, $REF^{SSTvar}{}_{chem}$ and $REF^{SSTvar}{}_{nochem}$, which aim at representing the same climatic conditions. A detailed evaluation of the EMAC model is discussed by Jöckel et al. (2016).

Panel (a) of Fig. C.1 shows the zonal mean air temperature in simulation $REF^{SSTfix}{}_{chem}$ and panel (b) its difference to ERA5 reanalysis data (Hersbach et al., 2020) averaged over the years 2000 to 2019. The cold bias in the tropopause region and the warm bias in the SH above 100 hPa are known patterns also in previous free-running EMAC simulations (Jöckel et al., 2016; Nützel et al., 2023). Panels (c) and (d) of Fig. C.1 show the temperature difference in the simulations $REF^{SSTvar}{}_{chem}$ and $REF^{SSTvar}{}_{nochem}$, respectively, compared to $REF^{SSTfix}{}_{chem}$. The difference between the simulations with interactive chemistry is mostly not significant, but shows significant higher temperatures in the SH troposphere and in the lowermost tropical stratosphere. The latter coincidences with higher O_3 mixing ratios in $REF^{SSTvar}{}_{chem}$ (see Fig. C.4 (b)), and is therefore likely due to corresponding stronger local radiative heating. Tropical lower stratospheric H_2O mixing ratios are up to 4% higher in the simulation with MLO (see Fig. C.3 (a)). The temperature differences in the SH troposphere are caused by differences of the sea ice cover between $REF^{SSTfix}{}_{chem}$ and $REF^{SSTvar}{}_{chem}$, which lead to locally up to 3 K higher near surface air temperatures in the SH (see Fig. C.2) and 0.19 K in the global mean (see Tab. 3.4 in Chap. 3.2). The tendency of the MLO to underestimate SH sea ice area was also found in a previous EMAC simulation with MLO (Stecher et al., 2021).

Tropospheric temperatures in the reference simulation without interactive chemistry, $REF^{SSTvar}{}_{nochem}$, are significantly lower compared to $REF^{SSTfix}{}_{chem}$ even though climatologies of radiatively active trace gases (CH_4, CO_2, O_3, N_2O and CFCs) are prescribed from

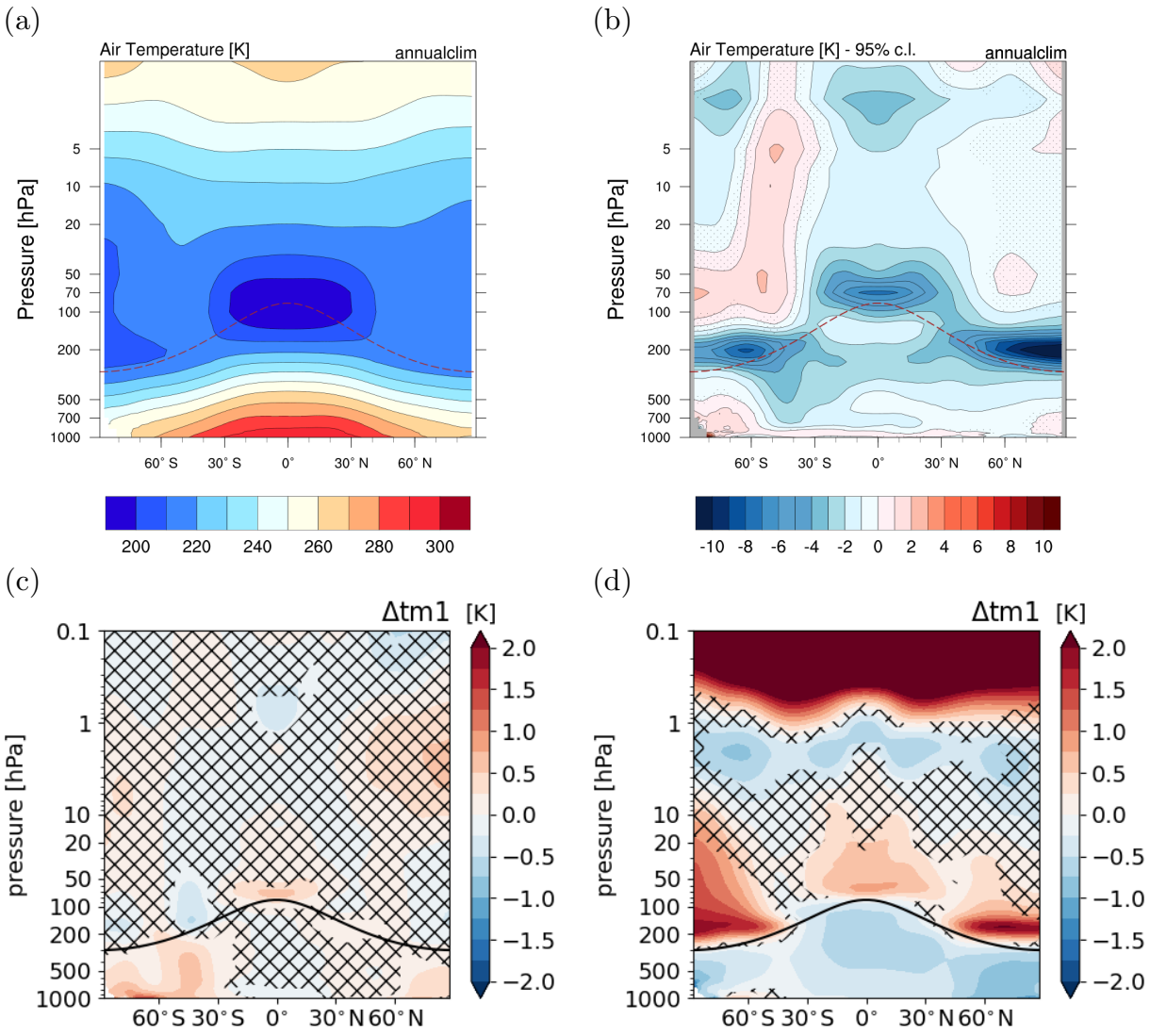

Figure C.1: (a) Annual zonal mean temperature in simulation $\mathrm{REF^{SSTfix}}_{\mathrm{chem}}$ [K]. (b) Annual zonal mean temperature difference of $\mathrm{REF^{SSTfix}}_{\mathrm{chem}}$ compared to ERA5 reanalysis of the years 2000 to 2019 [K]. The plots of panel (a) and (b) were created using the ESMValTool (version 2.9.0) (Righi et al., 2020; Schlund et al., 2023). (c) and (d) Annual zonal mean temperature difference of (c) $\mathrm{REF^{SSTvar}}_{\mathrm{chem}}$ and (d) $\mathrm{REF^{SSTvar}}_{\mathrm{nochem}}$ compared to $\mathrm{REF^{SSTfix}}_{\mathrm{chem}}$ [K]. Non-hatched areas are significant on the 95% confidence level. The solid black line indicates the climatological tropopause.

the latter simulation. The corresponding difference of GSAT is 0.39 K (see Tab. 3.4 in Sect. 3.2). The temperatures in the tropical and polar lower stratosphere are higher in the simulation without interactive chemistry. Fig. C.3 (b) shows that stratospheric H_2O

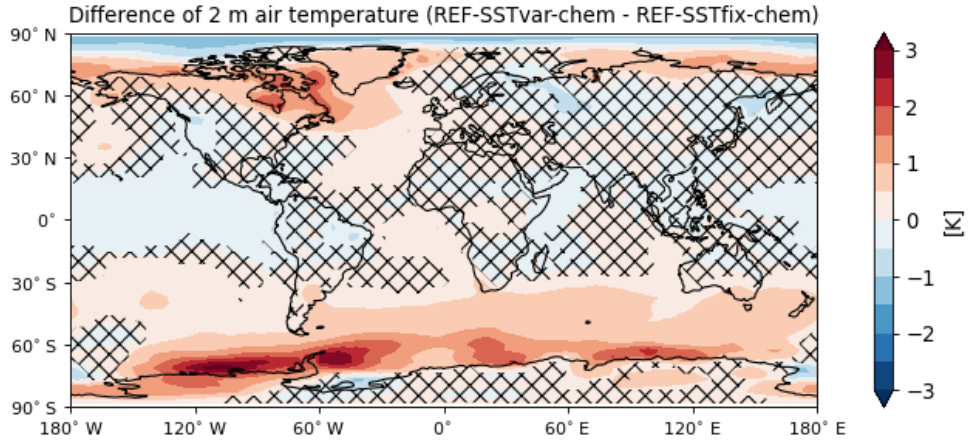

Figure C.2: Difference of 2m air temperature between simulations REF^{SSTvar}_{chem} and REF^{SSTfix}_{chem} [K]. Non-hatched areas are significant on the 95% confidence level.

Table C.1: Tropical (10°S - 10°N) mean H_2O mixing ratio [ppm] at different pressure levels. The corresponding interannual standard deviation based on 20 annual mean values is given to estimate the year to year variability.

	100 hPa	70 hPa	50 hPa
REF^{SSTfix}_{chem}	1.82 ± 0.03	1.78 ± 0.05	1.98 ± 0.04
REF^{SSTvar}_{chem}	1.84 ± 0.05	1.84 ± 0.06	2.04 ± 0.06
REF^{SSTvar}_{nochem}	1.67 ± 0.03	1.59 ± 0.05	1.79 ± 0.05

is in general lower in the simulation without interactive chemistry. The difference is up to -20% and -25% in the southern and northern polar lower stratosphere, respectively, which can result in reduced radiative cooling in REF^{SSTvar}_{nochem} and thereby leads to higher temperatures. Table C.1 shows tropical stratospheric H_2O mixing ratios for the three reference simulations at different pressure levels. Simulation REF^{SSTvar}_{chem} shows the largest tropical lower stratospheric H_2O mixing ratios. The difference compared to REF^{SSTfix}_{chem} is between 0.02 and 0.06 ppmv for the three pressure levels. In contrast, tropical lower stratospheric H_2O is between 0.15 and 0.19 ppmv lower in REF^{SSTvar}_{nochem} compared to REF^{SSTfix}_{chem}.

The zonal mean difference of CH_4 mixing ratios between REF^{SSTfix}_{chem} and REF^{SSTvar}_{chem} is below 0.5% in the troposphere. In the upper stratosphere and mesosphere the difference reaches up to 5% in the zonal mean, which is, however, not significant. The difference of O_3 mixing ratios is shown in Fig. C.4 (b). O_3 mixing ratios are up to 5% higher in the tropical tropopause region in REF^{SSTvar}_{chem}, which is linked to a slightly higher (less

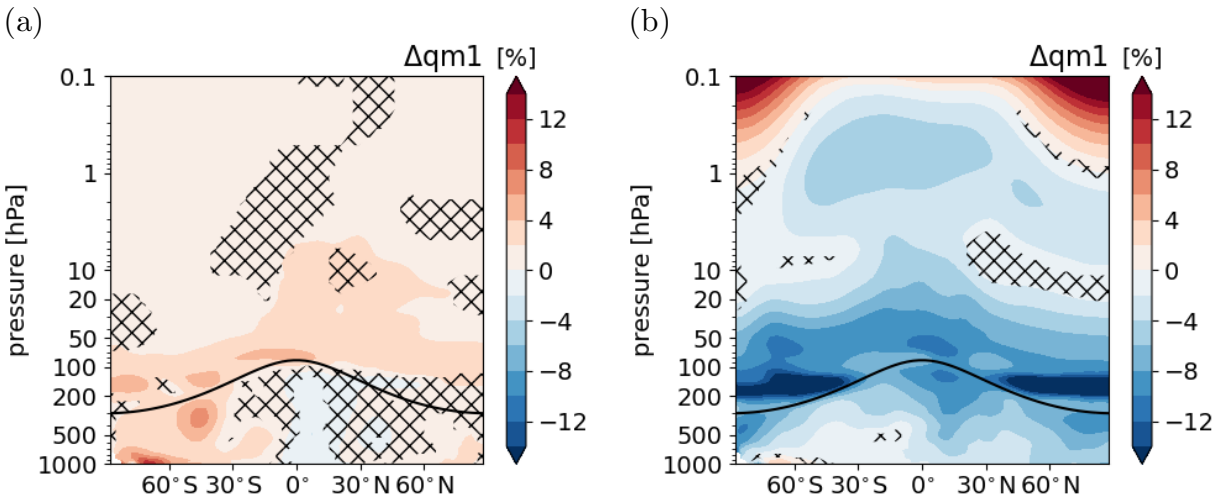

Figure C.3: Relative differences between the annual zonal mean water vapour of simulation (a) $REF^{SSTvar}{}_{chem}$ and (b) $REF^{SSTvar}{}_{nochem}$ compared to $REF^{SSTfix}{}_{chem}$ [%]. Non-hatched areas are significant on the 95% confidence level. The solid black line indicates the climatological tropopause.

than 1 hPa) tropopause pressure in $REF^{SSTvar}{}_{chem}$. Further, O_3 mixing ratios are up to 2% lower in the lower southern troposphere, which can be linked to a higher abundance of H_2O and thereby a stronger chemical sink. Overall, the difference of CH_4 and O_3 between the simulations $REF^{SSTvar}{}_{chem}$ and $REF^{SSTvar}{}_{chem}$ is small.

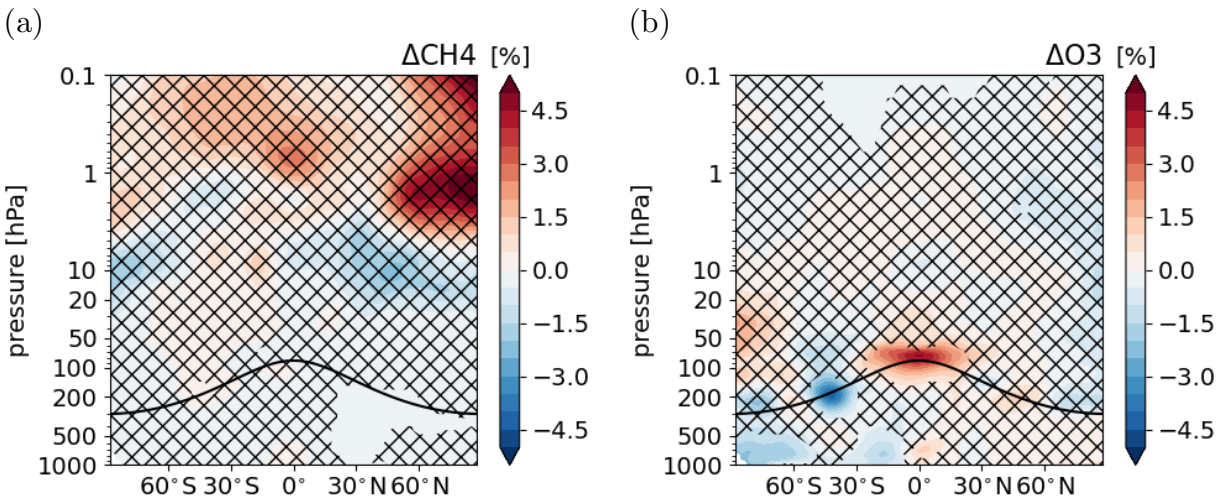

Figure C.4: Relative differences between the annual zonal mean (a) CH_4 and (b) O_3 $REF^{SSTvar}{}_{chem}$ compared to $REF^{SSTfix}{}_{chem}$ [%]. Non-hatched areas are significant on the 95% confidence level. The solid black line indicates the climatological tropopause.

Appendix D

Spin-up of CH_4 emission increase experiment

In this Appendix, the evolution of the mass of CH_4 during the spin-up period in the CH_4 emissions increase simulation, $ERFCH_4^{SSTfix}{}_{chem}$, is analysed in more detail. More precisely, it discusses the questions (1) if the evolution of mass can be described by theoretical formulation, and (2) if the new equilibrium is reached after the spin-up with sufficient accuracy.

First, I start with the derivation of a formulation of the time evolution of the mass of CH_4 during the spin-up period until a new equilibrium is reached. The mass balance equation of the mass of CH_4 m (Eq. (2) deduced by Holmes (2018)) states that the temporal change of m is determined by its emissions E and its sinks $k \cdot m$, whereby k is the loss rate:

$$\frac{dm}{dt} = E - k \cdot m. \tag{D.1}$$

Before increasing the emissions, i.e. in the reference set-up $REF^{SSTfix}{}_{chem}$, it holds (with constant E_0, k_0 and m_0)

$$\begin{aligned} &\frac{dm_0}{dt} = E_0 - k_0 \cdot m_0 = 0 \\ &\Rightarrow E_0 = k_0 \cdot m_0. \end{aligned} \tag{D.2}$$

Now the emissions are increased by a constant global factor α ($E_1 = \alpha \cdot E_0$) and it holds

$$\frac{dm}{dt} = E_1 - k \cdot m \neq 0. \tag{D.3}$$

I apply the linearisation to (D.1) as is done by Holmes (2018): $m' = m - m_0$ and $k = k_0 + m' \cdot \frac{dk}{dm}$. This gives the following differential equation

$$\frac{d(m' + m_0)}{dt} = E_1 - (k_0 + m' \cdot \frac{dk}{dm}) \cdot (m' + m_0). \tag{D.4}$$

Under the assumption that m' is small, all terms on the order of $(m')^2$ are neglected. As m_0 is a constant, this reduces the equation to

$$\begin{aligned} \frac{dm'}{dt} &= E_1 - k_0 \cdot m_0 - k_0 \cdot m' - m' \cdot \frac{dk}{dm} \cdot m_0 \\ &= E_1 - k_0 \cdot m_0 - k_0 \cdot (1 + \frac{\frac{dk}{k_0}}{\frac{dm}{m_0}}) \cdot m' \\ &= E_1 - E_0 - k_0 \cdot (1 + R) \cdot m' \\ &= \Delta E - \frac{m'}{\tau_p} \end{aligned} \tag{D.5}$$

$$\text{with } R \equiv \frac{\frac{dk}{k_0}}{\frac{dm}{m_0}} \ , \ \tau_p \equiv \frac{1}{k_0 \cdot (1 + R)} = f \cdot \tau_0 \text{ and } f \equiv \frac{1}{1 + R}$$

Note that Eq. D.5 is different to Eq. (3) of Holmes (2018) as the emissions changed here. τ_p is generally called the perturbation time scale and f the feedback factor. A solution for D.5 is given by

$$m'(t) = \Delta E \cdot \tau_p + m_0 - \Delta E \cdot \tau_p \cdot e^{-\frac{t}{\tau_p}} \tag{D.6}$$

with

$$\begin{aligned} m'(t = 0) &= m_0 \\ \lim_{t \to \infty} m'(t) &= \Delta E \cdot \tau_p + m_0. \end{aligned} \tag{D.7}$$

$m'(t)$ describes the evolution of the mass of CH_4 after the emission increase.

However, the spin-up of the CH_4 increase simulation, $ERFCH_4{}^{SSTfix}{}_{chem}$, is not initialized with $m(t = 0) = m_0$, but $m(t = 0) = \alpha \cdot m_0$ to save computing time. Accounting for this, results in the slightly different solution

$$m'(t) = \Delta E \cdot \tau_p + m_0 - (\Delta E \cdot \tau_p + (1 - \alpha) \cdot m_0) \cdot e^{-\frac{t}{\tau_p}} \tag{D.8}$$

with

$$\begin{aligned} m'(t=0) &= \alpha \cdot m_0 \\ \lim_{t\to\infty} m'(t) &= \Delta E \cdot \tau_p + m_0. \end{aligned} \tag{D.9}$$

Now, the theoretical formulation is applied to the spin-up period of the simulation ERFCH$_4$$^{\mathrm{SSTfix}}_{\mathrm{chem}}$. Figure D.1 shows the evolution of the total mass of CH_4 from the latter simulation as yearly means, as well as three functions of the form $a_1 - a_2 \cdot e^{-\frac{t}{a3}}$. One used a curve fit to determine the parameters a_1, a_2, a_3, one used the simulation results, and one applied the curve fit only to determine τ_p whereas ΔE, m_0 and α stem from the simulation. For the CH_4 lifetime the mean tropospheric lifetime with respect to the oxidation with OH is used as approximation. The values for a_1, a_2, a_3, and their respective formulas are summarized in Tab. D.1.

The curve with all parameters from the fit follows the time evolution of the simulation closely. It gives a_1 = 23886.71 Tg, which represents the new equilibrium of the mass of CH_4 (see Eq. D.9). The last year of the spin-up of ERFCH$_4$$^{\mathrm{SSTfix}}_{\mathrm{chem}}$ has a total mass of 23759.88 Tg, which corresponds to a 0.5 % relative difference to the fitted equilibrium value. The other two curves end up with an equilibrium mass of CH_4 that is too low. There are multiple possible explanations for this. Firstly, the assumptions for the derivation of Eq. D.5 might not hold. The linearisation might not hold for a CH_4 perturbation as strong as the one applied here, and the feedback factor f might not be constant. Secondly, the analysis here is based on annual mean values to remove the seasonal cycle. However, $m(t=0) = \alpha \cdot m_0$ is not exactly true as m increased already by about 1.6 % in the first simulation year. Thirdly, the mean tropospheric lifetime with respect to the oxidation with OH does not account for the total loss of CH_4, which affects the calculation of f and τ_p. Nevertheless, an important finding is that the mass of CH_4 in the last year of the spin-up is only 0.5 % lower than the expected equilibrium value, which means that the mass of CH_4 can be assumed to be spun-up sufficiently well.

Table D.1: Results of parameters a_1, a_2 and a_3, either derived from a curve fit (first column, see Fig. D.1 red dashed line), from Eq D.8 and simulation results (second column), or a combination for which only a_3 is fitted (third column, see Fig. D.1 black dashed line).

Parameter	formula	all fitted	all from $ERFCH_4{}^{SSTfix}{}_{chem}$	a_3 (τ_p) fitted
a_1	$\Delta E \cdot \tau_p + m_0$	23886.71 Tg	19131.35 Tg	23425.31Tg
a_2	$\Delta E \cdot \tau_p + (1-\alpha) \cdot m_0$	9892.93 Tg	5431.24 Tg	9725.19 Tg
a_3	τ_p	21.63 a	12.93 a	16.86 a

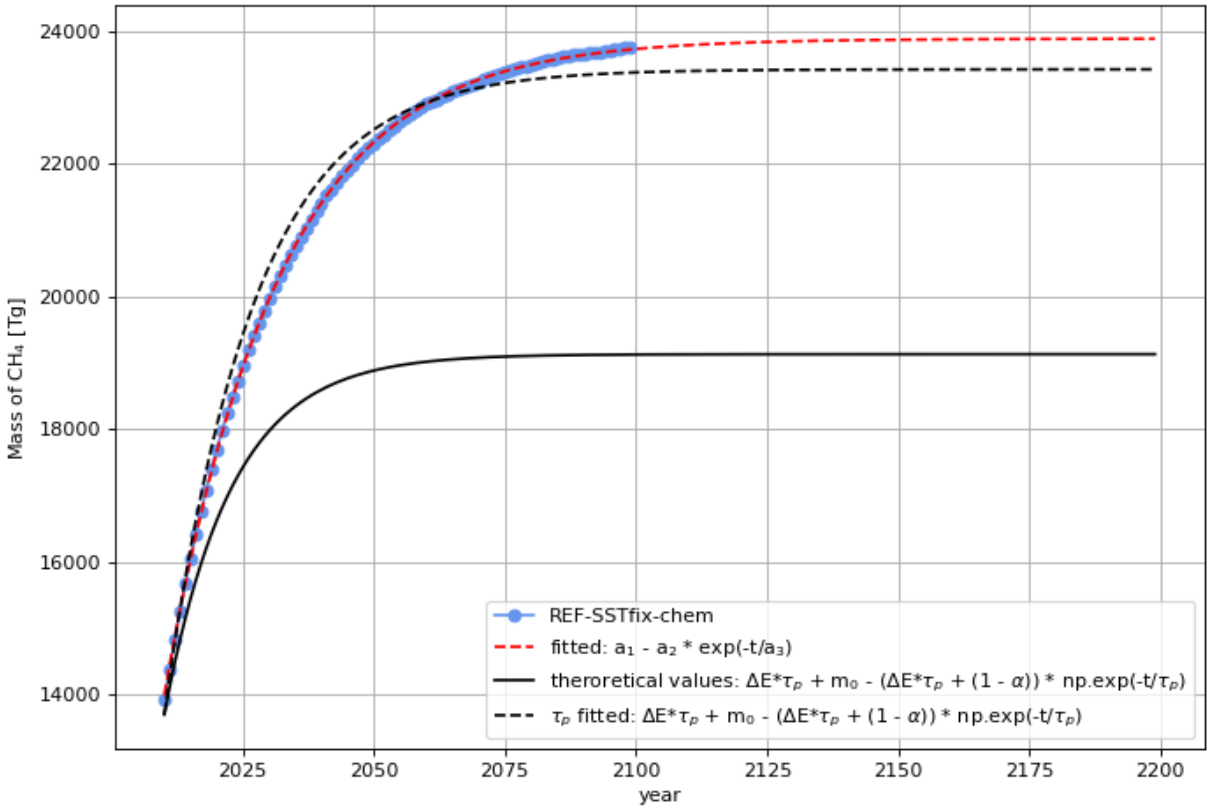

Figure D.1: Spin-up of the total mass of CH_4. Blue dots: values of the the total mass of CH_4 in [Tg] from the simulation $ERFCH_4{}^{SSTfix}{}_{chem}$. Other curves are functions of the form $a_1 - a_2 \cdot e^{-\frac{t}{a3}}$. The red dashed line shows the results of a curve fit to derive the parameters a_1, a_2 and a_3. The black solid line uses the derived formula (Eq. D.8) and simulation results from $ERFCH_4{}^{SSTfix}{}_{chem}$ to calculate the parameters. For the black dashed line only parameter a_3 is derived with the curve fit and a_1 and a_2 are calculated from the simulation results.

Appendix E

Supplementary Figures

E.1 Natural O_3 precursor emissions

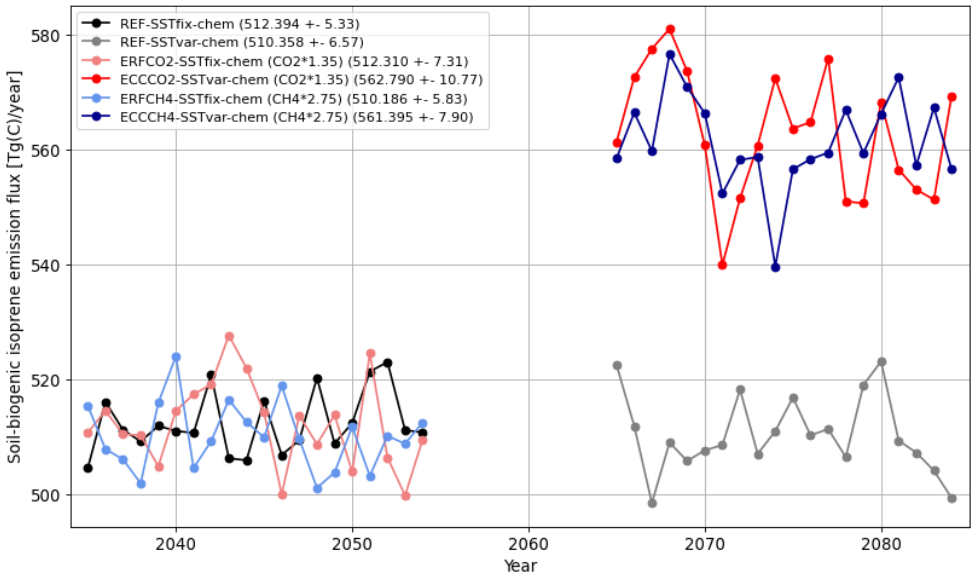

Figure E.1: Timeline of annual mean global biogenic C_5H_8 emissions in [Tg(C) year^{-1}]. Values in brackets in the legend indicate the multi-year mean ± the interannual standard deviation for each simulation.

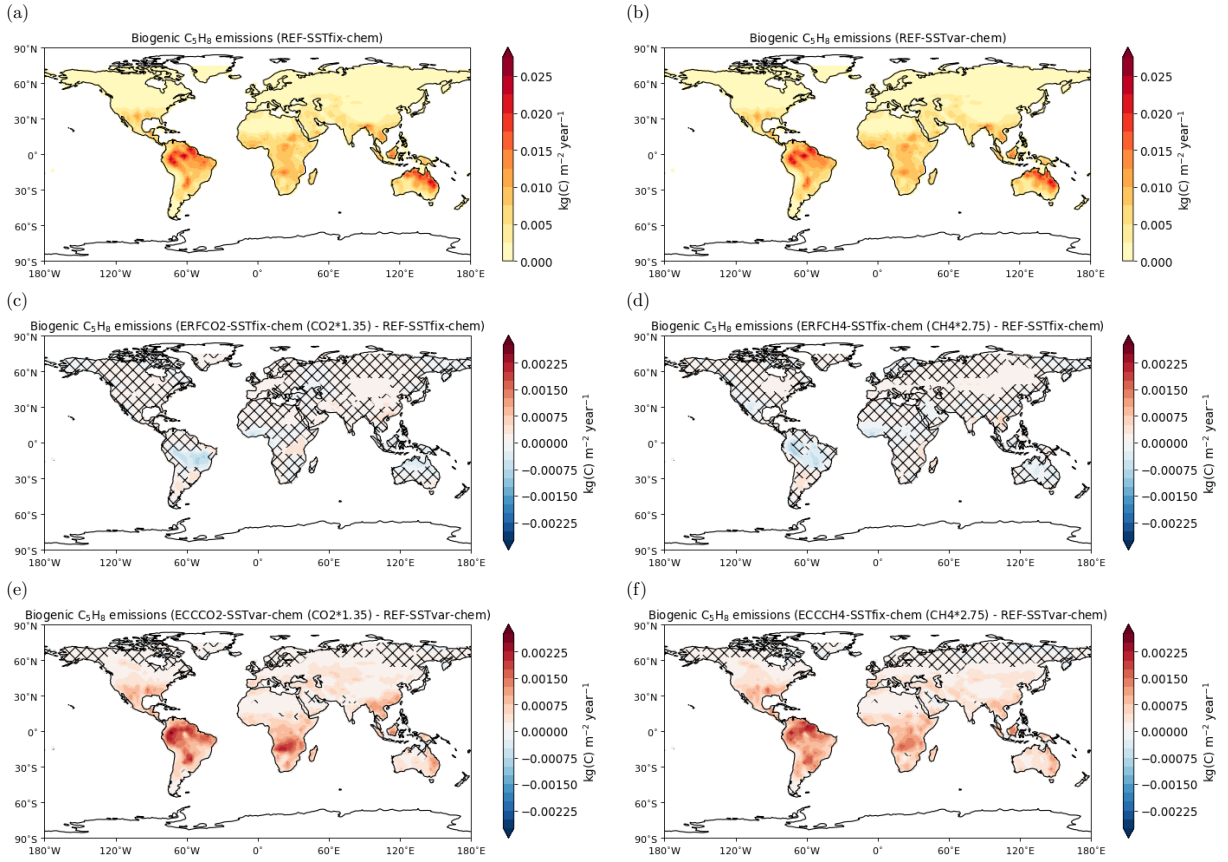

Figure E.2: Panels (a) and (b): Spatial distribution of biogenic C_5H_8 emissions in the reference simulations (a) $REF^{SSTfix}{}_{chem}$ and (b) $REF^{SSTvar}{}_{chem}$ in [kg(C) m^{-2} $year^{-1}$]. Panels (c)-(f): Difference of biogenic C_5H_8 emissions between (c) $ERFCO_2{}^{SSTfix}{}_{chem}$, (d) $ERFCH_4{}^{SSTfix}{}_{chem}$, (e) $ECCCO_2{}^{SSTvar}{}_{chem}$, and (f) $ECCCH_4{}^{SSTvar}{}_{chem}$, and their respective reference in [kg(C) m^{-2} $year^{-1}$]. Non-hatched areas are significant on the 95% confidence level according to a Welch's test based on annual mean values.

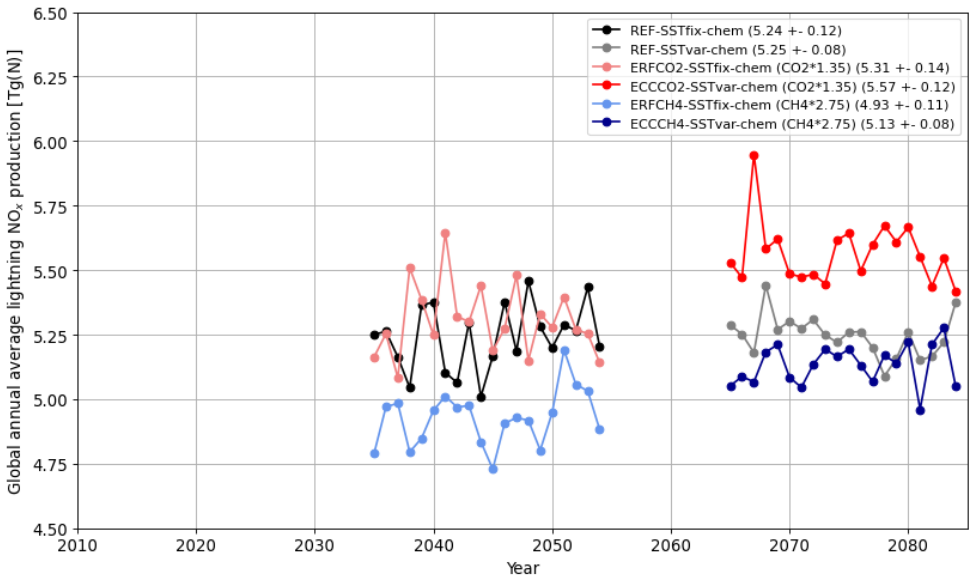

Figure E.3: Timeline of annual mean global lightning NO_x emissions in [Tg(N) year^{-1}]. Values in brackets in the legend indicate the multi-year mean ± the interannual standard deviation for each simulation.

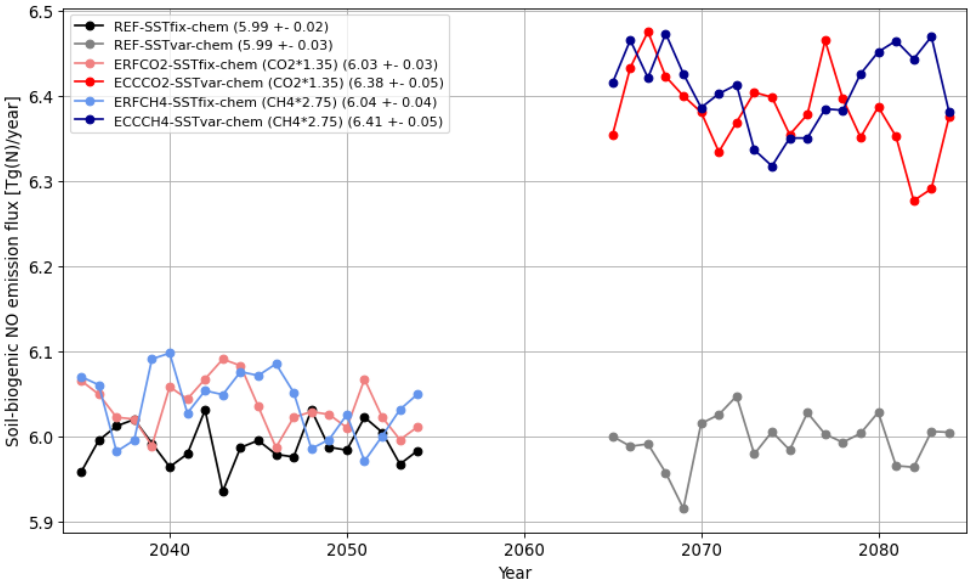

Figure E.4: Timeline of annual mean global biogenic NO emissions in [Tg(N) year^{-1}]. Values in brackets in the legend indicate the multi-year mean ± the interannual standard deviation for each simulation.

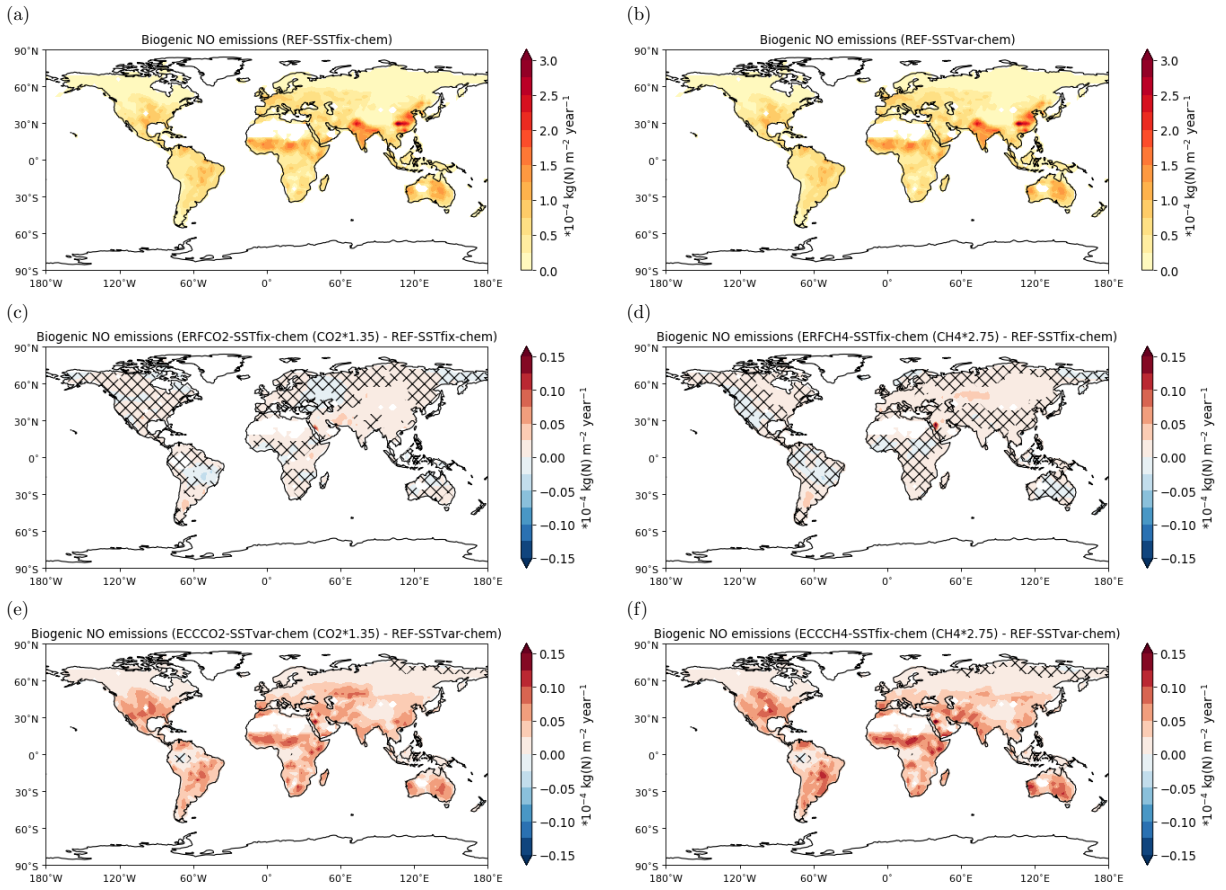

Figure E.5: Panels (a) and (b): Spatial distribution of biogenic NO emissions in the reference simulations (a) $\mathrm{REF}^{\mathrm{SSTfix}}{}_{\mathrm{chem}}$ and (b) $\mathrm{REF}^{\mathrm{SSTvar}}{}_{\mathrm{chem}}$ in [10^{-4} kg(N) m^{-2} year^{-1}]. Panels (c)-(f): Difference of biogenic NO emissions between (c) $\mathrm{ERFCO_2}^{\mathrm{SSTfix}}{}_{\mathrm{chem}}$, (d) $\mathrm{ERFCH_4}^{\mathrm{SSTfix}}{}_{\mathrm{chem}}$, (e) $\mathrm{ECCCO_2}^{\mathrm{SSTvar}}{}_{\mathrm{chem}}$, and (f) $\mathrm{ECCCH_4}^{\mathrm{SSTvar}}{}_{\mathrm{chem}}$, and their respective reference in [10^{-4} kg(N) m^{-2} year^{-1}]. Non-hatched areas are significant on the 95% confidence level according to a Welch's test based on annual mean values.

E.2 Tropospheric O_3 columns of TAGGING categories

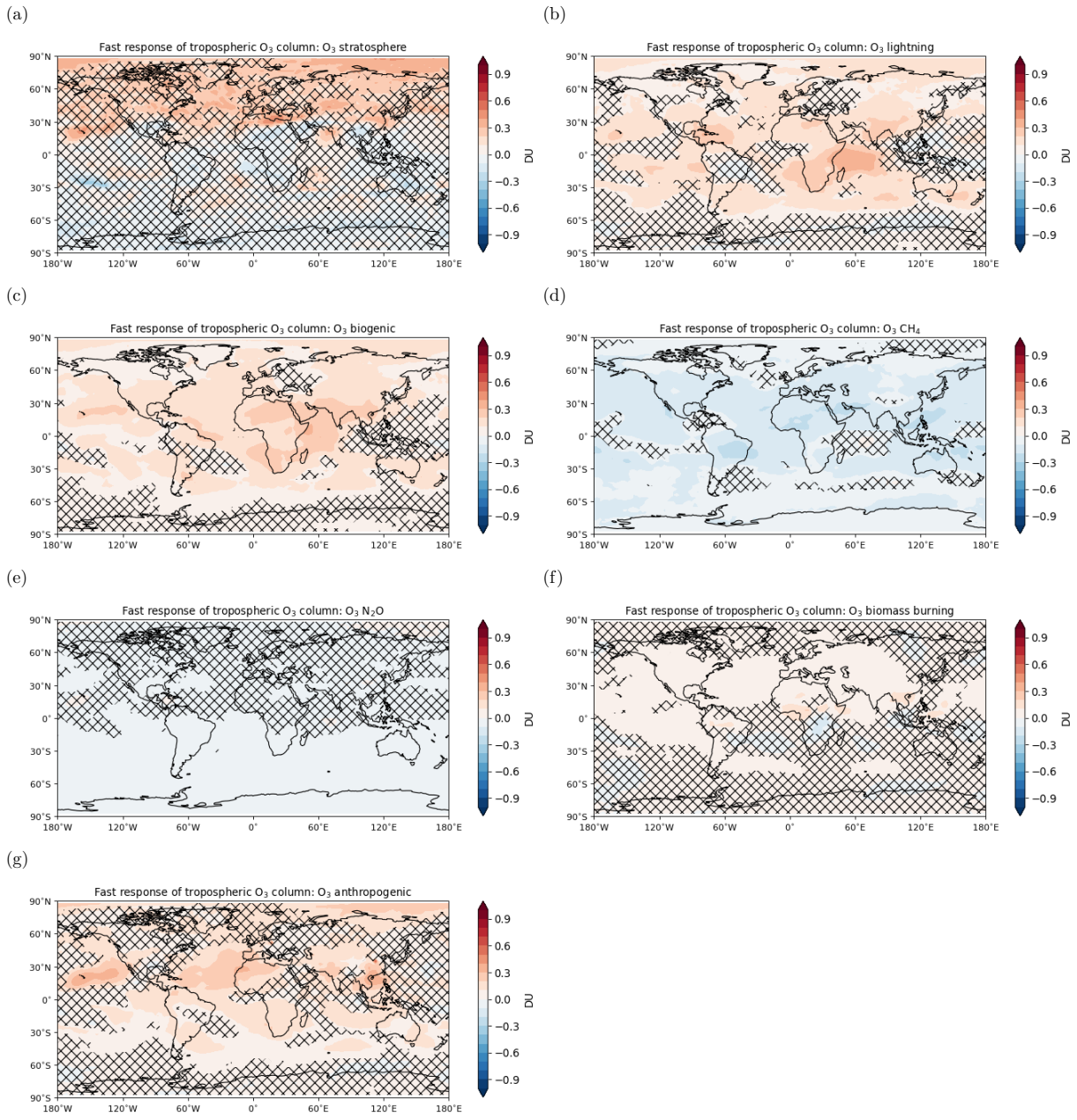

Figure E.6: Fast response of tropospheric O_3 column following CO_2 perturbation for individual categories in DU. Non-hatched regions indicate significant differences between the simulation $ERFCO_2{}^{SSTfix}{}_{chem}$ and $REF^{SSTfix}{}_{chem}$ on the 95% interval.

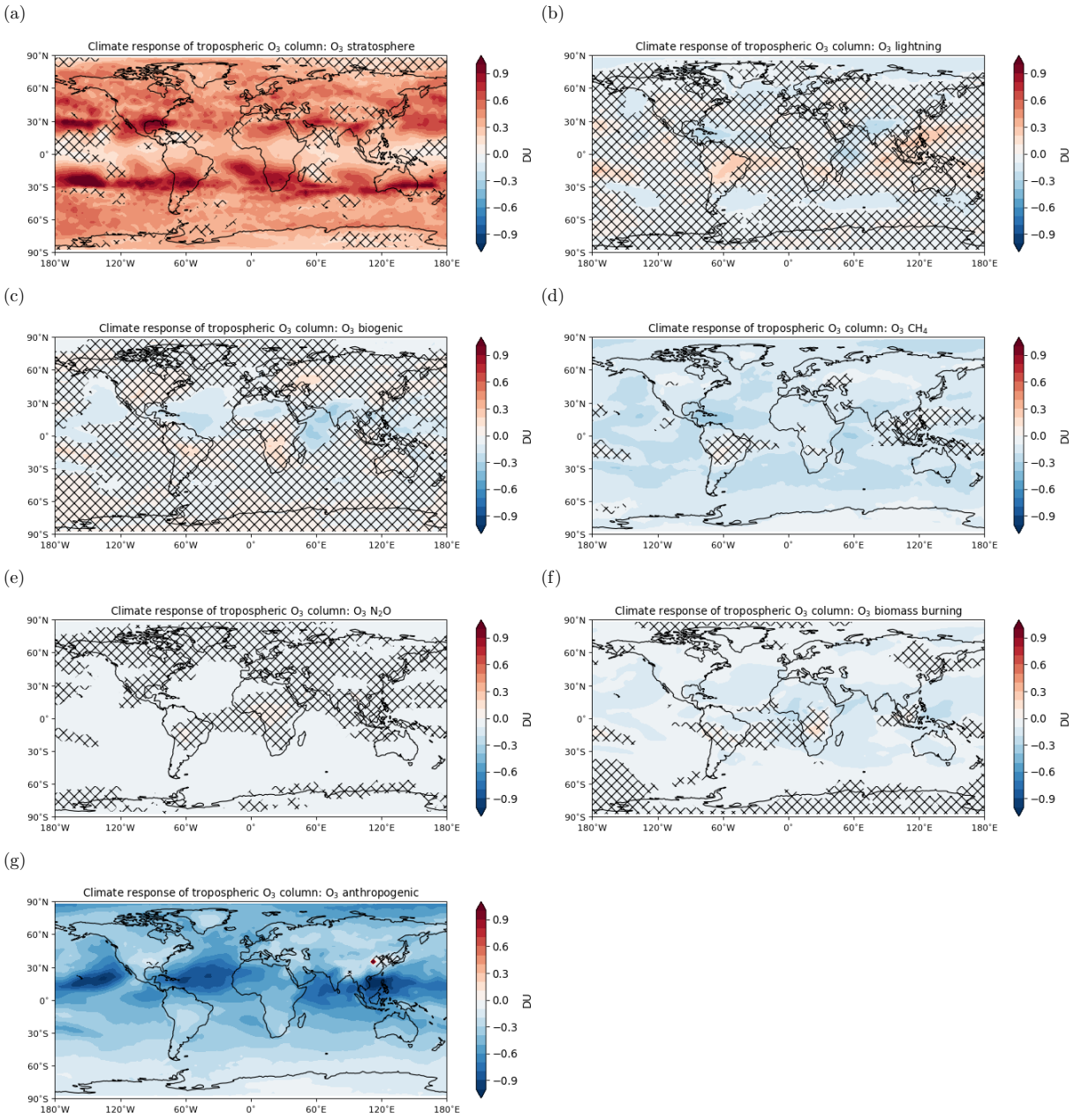

Figure E.7: Climate response of tropospheric O_3 column following CO_2 perturbation for individual categories in DU. Non-hatched regions indicate significant differences between the fast and the full response on the 95% interval.

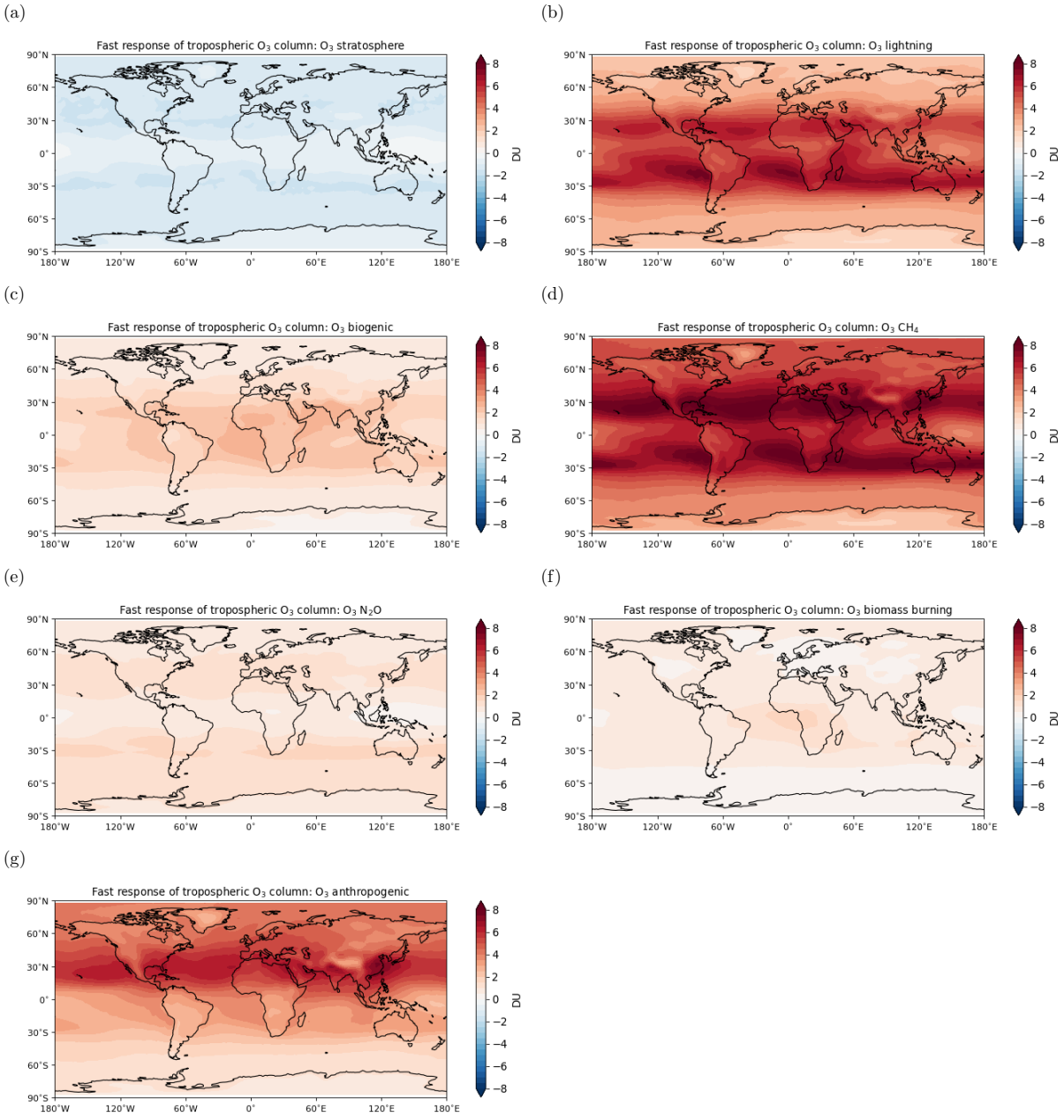

Figure E.8: Fast response of tropospheric O_3 column following CH_4 perturbation for individual categories in DU. Non-hatched regions indicate significant differences between the simulation $ERFCH_4{}^{SSTfix}{}_{chem}$ and $REF^{SSTfix}{}_{chem}$ on the 95% interval.

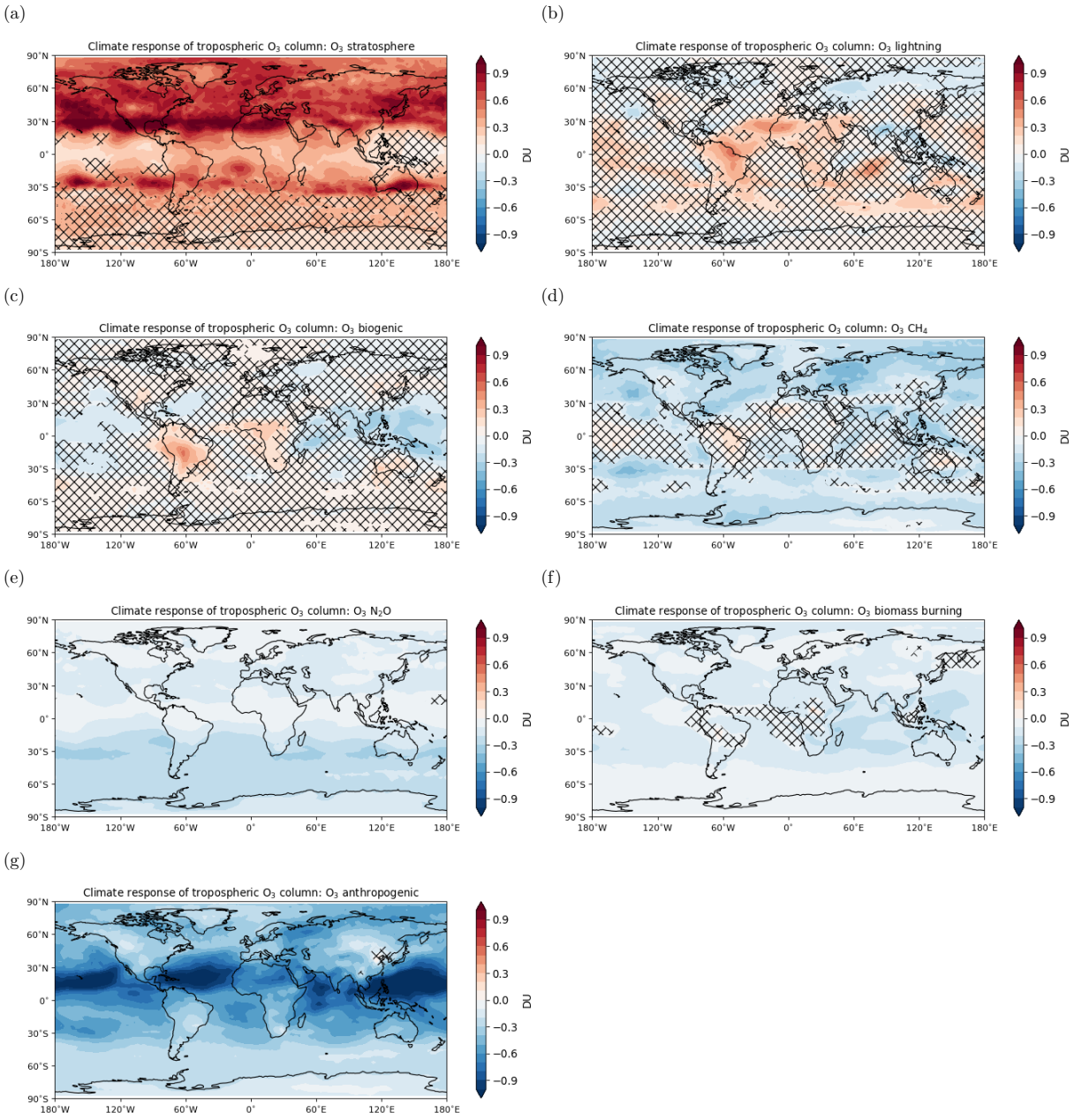

Figure E.9: Climate response of tropospheric O_3 column following CH_4 perturbation for individual categories in DU. Non-hatched regions indicate significant differences between the fast and the full response on the 95% interval.

E.3 Seasonal plots

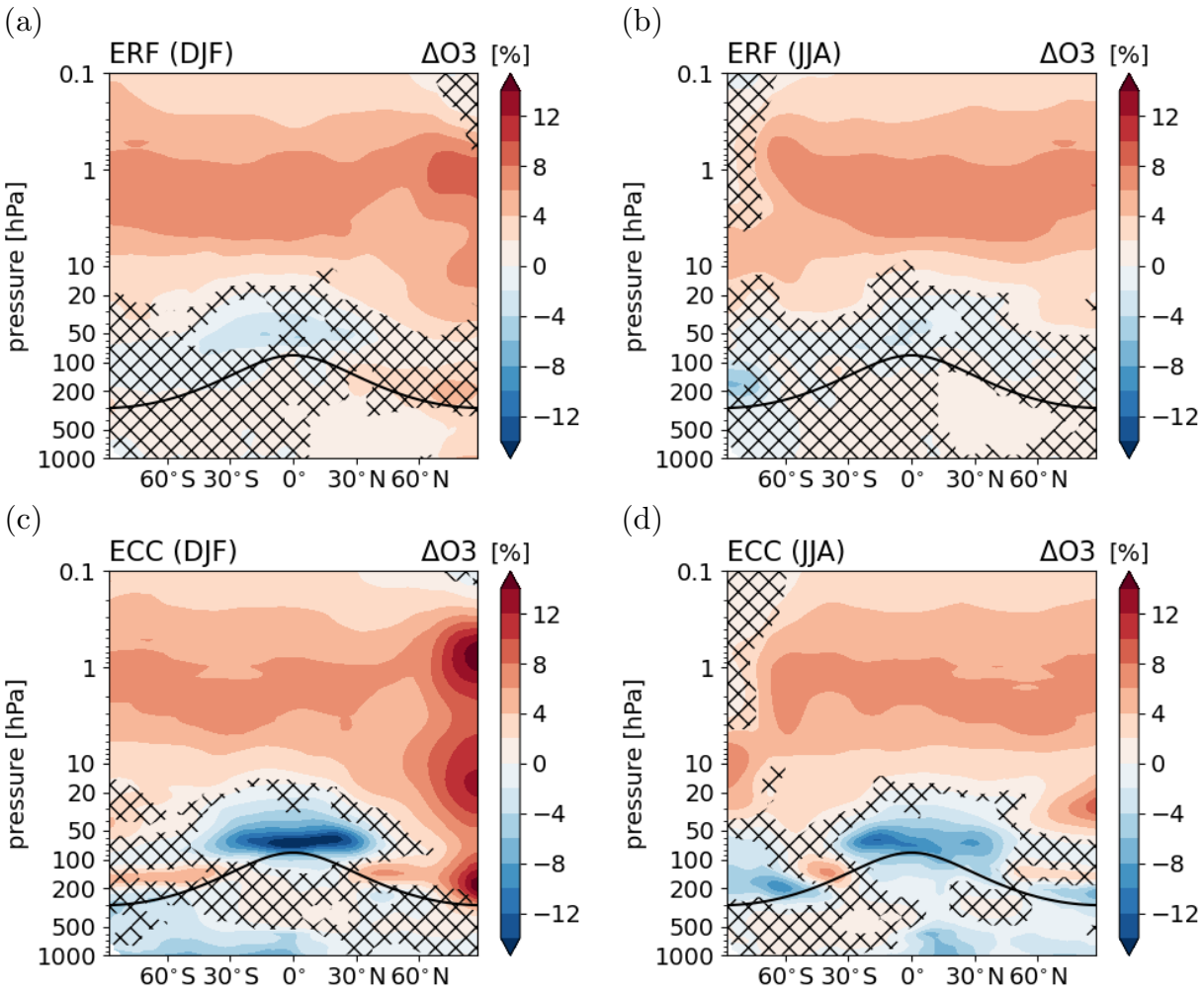

Figure E.10: Relative differences of the zonal mean O_3 mixing ratios split into the seasons December, January and February (DJF) or June, July, August (JJA) between the sensitivity simulations (a) and (b) $ERFCO_2{}^{SSTfix}{}_{chem}$, and (c) and (d) $ECCCO_2{}^{SSTvar}{}_{chem}$ and their respective reference simulation in [%]. Non-hatched areas are significant on the 95% confidence level according to a Welch's test based on annual mean values. The solid black line indicates the location of the climatological tropopause.

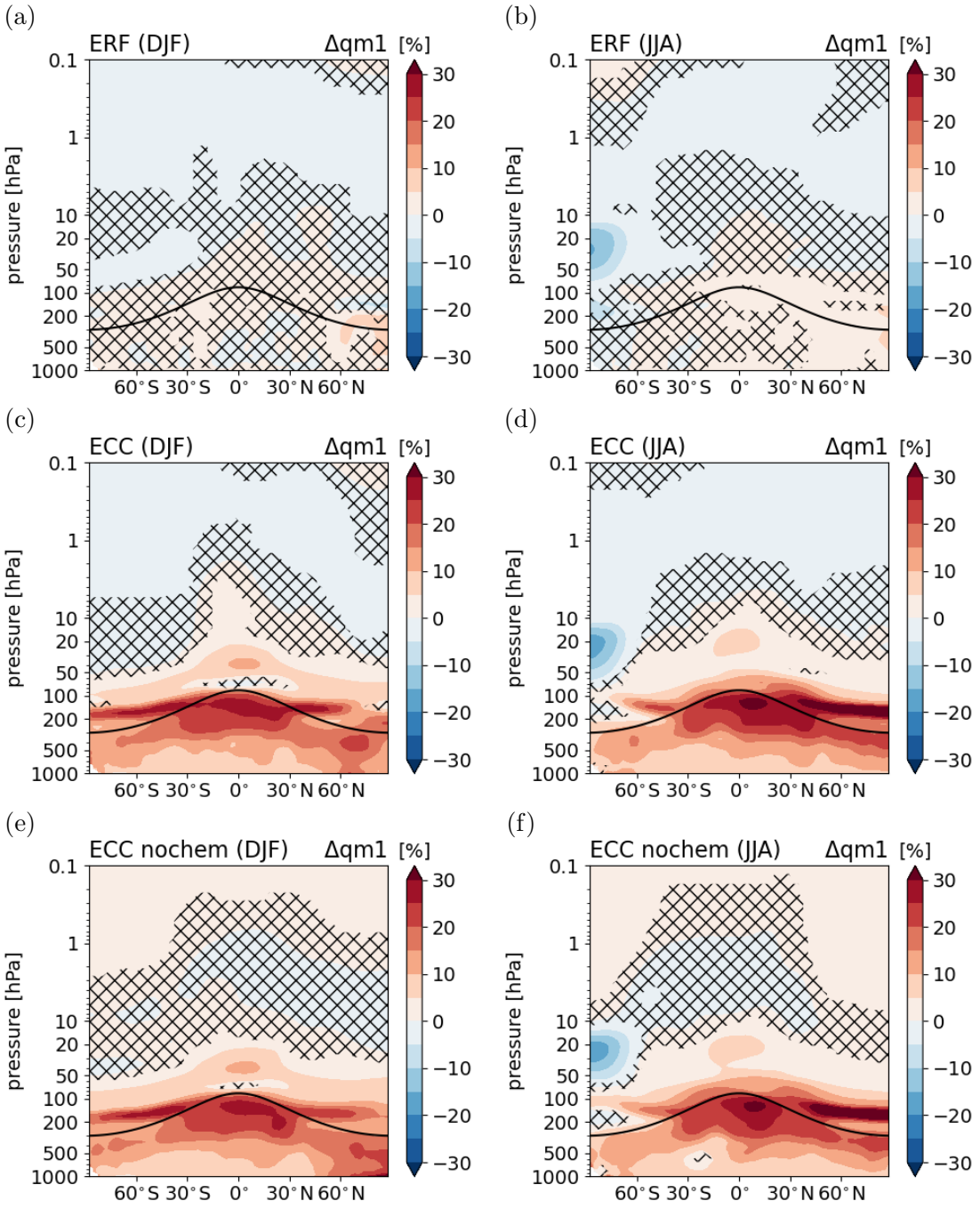

Figure E.11: Relative differences of the zonal mean H_2O mixing ratios split into the seasons December, January and February (DJF) or June, July, August (JJA) between the sensitivity simulations (a) and (b) ERF$CO_2{}^{\mathrm{SSTfix}}{}_{\mathrm{chem}}$, (c) and (d) ECC$CO_2{}^{\mathrm{SSTvar}}{}_{\mathrm{chem}}$, and (e) and (f) ECC$CO_2{}^{\mathrm{SSTvar}}{}_{\mathrm{nochem}}$ and their respective reference simulation in [%]. Non-hatched areas are significant on the 95% confidence level according to a Welch's test based on annual mean values. The solid black line indicates the location of the climatological tropopause.

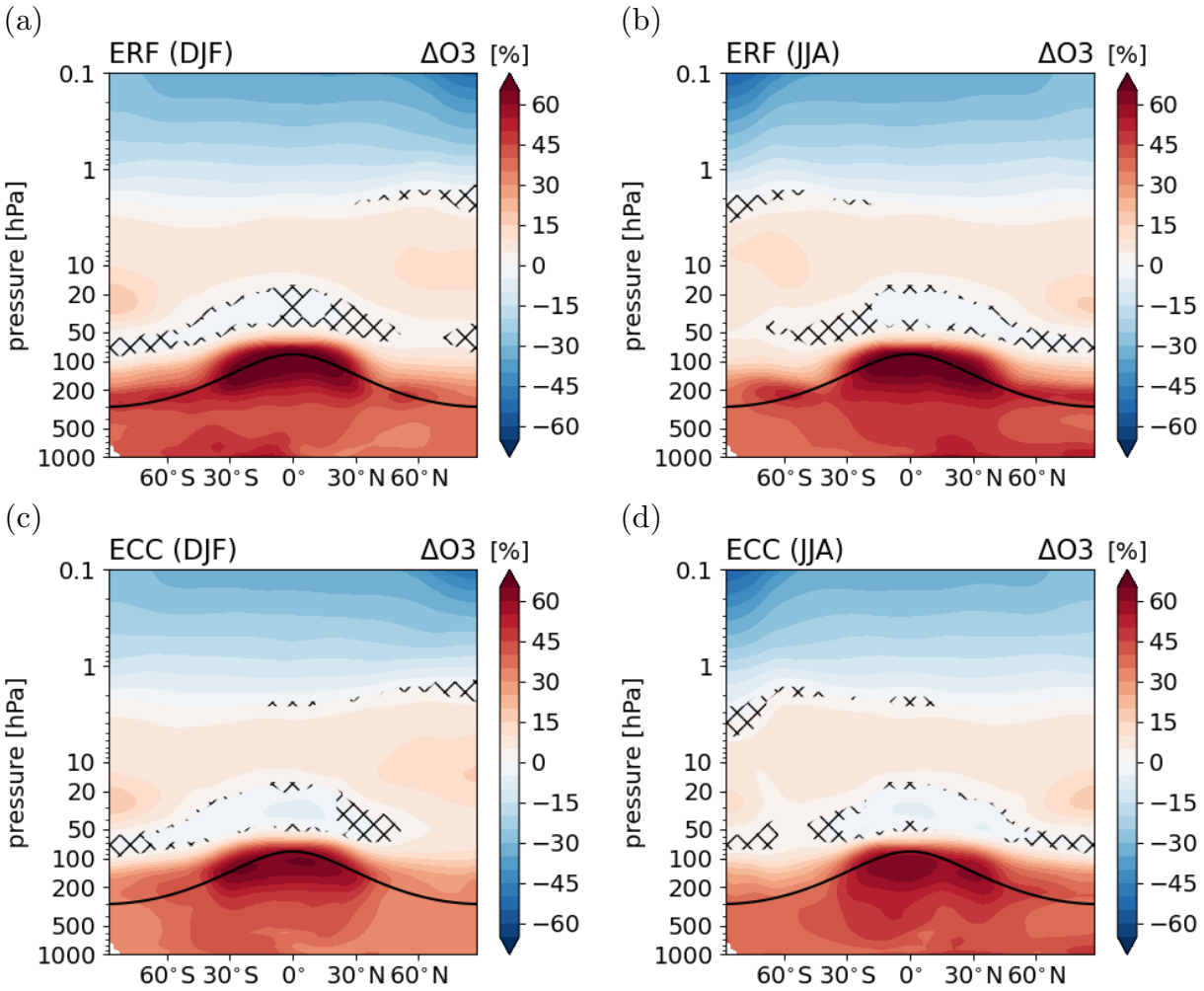

Figure E.12: Relative differences of the zonal mean O_3 mixing ratios split into the seasons December, January and February (DJF) or June, July, August (JJA) between the sensitivity simulations (a) and (b) ERFCH$_4$$^{\text{SSTfix}}_{\text{chem}}$, and (c) and (d) ECCCH$_4$$^{\text{SSTvar}}_{\text{chem}}$ and their respective reference simulation in [%]. Non-hatched areas are significant on the 95% confidence level according to a Welch's test based on annual mean values. The solid black line indicates the location of the climatological tropopause.

E.4 Radiative perturbations

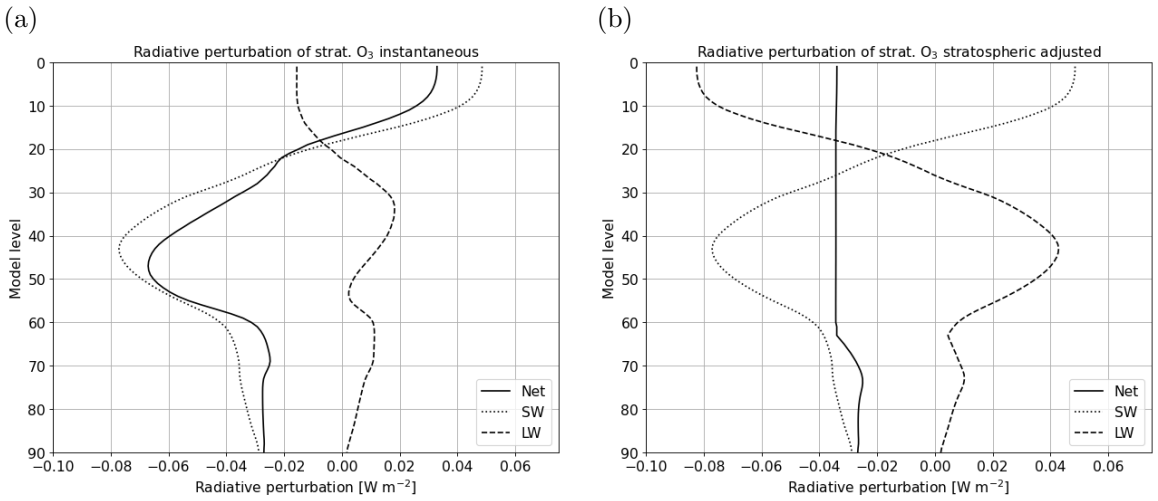

Figure E.13: Vertical profile of the radiative perturbation of the response of stratospheric O_3 in the simulation $ERFCO_2{}^{SSTfix}{}_{chem}$ in [W m^{-2}]: (a) instantaneous radiative flux change. (b) radiative flux change including the induced stratospheric temperature adjustment. The shortwave (SW) radiative flux changes of panel (a) and (b) are identical.

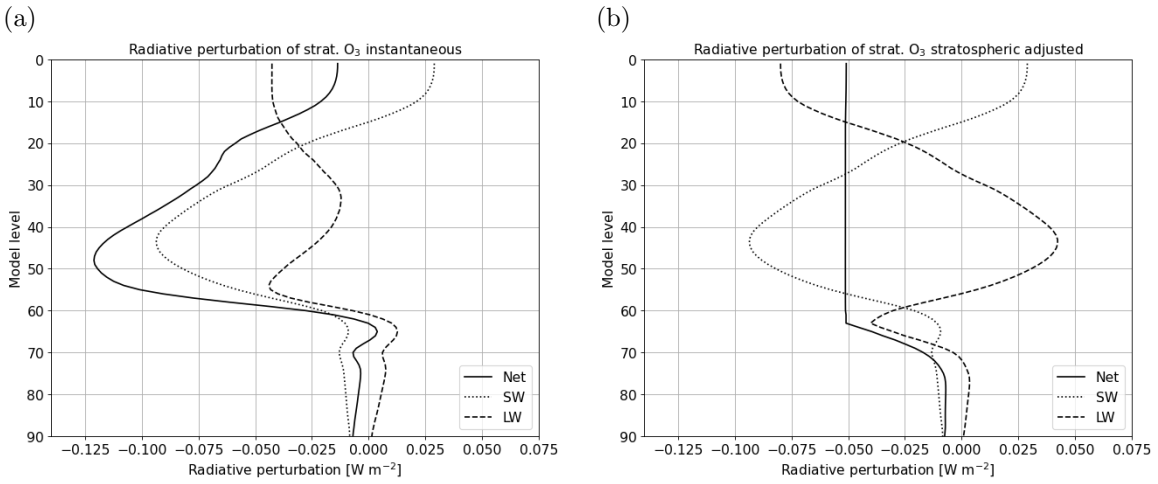

Figure E.14: Vertical profile of the radiative perturbation of the response of stratospheric O_3 in the simulation $ECCCO_2{}^{SSTvar}{}_{chem}$ in [W m^{-2}]: (a) instantaneous radiative flux change. (b) radiative flux change including the induced stratospheric temperature adjustment. The shortwave (SW) radiative flux changes of panel (a) and (b) are identical.

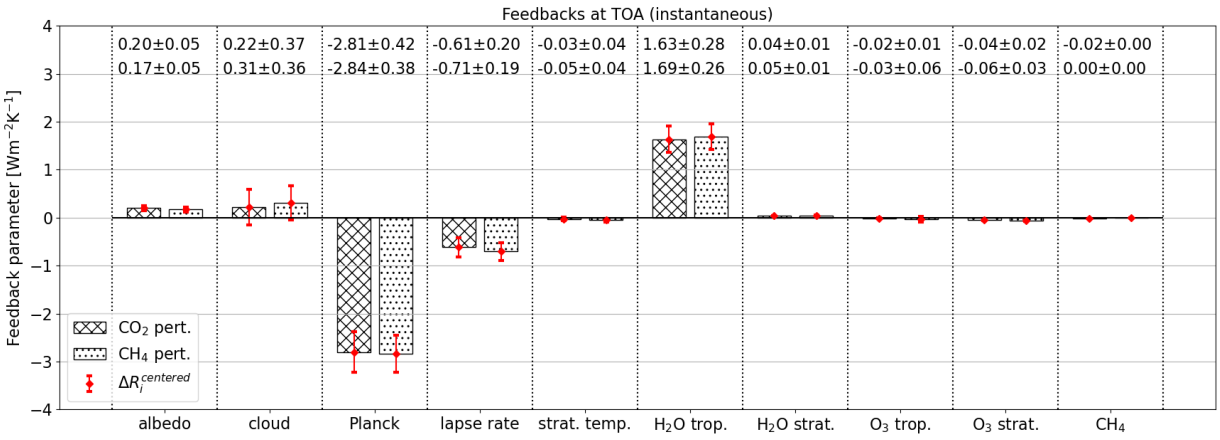

Figure E.15: Feedback parameters in [W m^{-2} K^{-1}] of individual processes for either the CO_2 perturbation (left bars), or the CH_4 perturbation (right bars). The feedback parameters represent the radiative effect of the climate response. i.e. the full response minus the rapid radiative adjustments. At the top of the figure, the corresponding mean values are listed. The upper estimates correspond to the CO_2 perturbation, and the lower estimates to the CH_4 perturbation. Values after the ± sign are 2× the standard error of the mean approximating the corresponding 95% confidence interval calculated on the basis of 20 annual mean values.

References

Abalos, M., Orbe, C., Kinnison, D. E., et al.: Future trends in stratosphere-to-troposphere transport in CCMI models, Atmos. Chem. Phys., 20, 6883–6901, https://doi.org/10.5194/acp-20-6883-2020, 2020.

Acquah, C.: Impact of different emission inventories on the tropospheric ozone budget, Master's thesis, Universität zu Köln, 2023.

Allen, R. J., Horowitz, L. W., Naik, V., et al.: Significant climate benefits from near-term climate forcer mitigation in spite of aerosol reductions, Environ. Res. Lett., https://doi.org/10.1088/1748-9326/abe06b, 2021.

Allen, R. J., Zhao, X., Randles, C. A., et al.: Surface warming and wetting due to methane's long-wave radiative effects muted by short-wave absorption, Nat. Geosci., https://doi.org/10.1038/s41561-023-01144-z, 2023.

Andrews, T., Smith, C. J., Myhre, G., et al.: Effective Radiative Forcing in a GCM With Fixed Surface Temperatures, J. Geophys. Res. Atmos., 126, e2020JD033 880, https://doi.org/10.1029/2020JD033880, 2021.

Ashmore, M. R.: Assessing the future global impacts of ozone on vegetation, Plant, Cell & Environment, 28, 949–964, https://doi.org/10.1111/j.1365-3040.2005.01341.x, 2005.

Atkinson, R.: Kinetics of the gas-phase reactions of OH radicals with alkanes and cycloalkanes, Atmos. Chem. Phys., 3, 2233–2307, https://doi.org/10.5194/acp-3-2233-2003, 2003.

Banerjee, A., Chiodo, G., Previdi, M., et al.: Stratospheric water vapor: an important climate feedback, Clim. Dyn, 53, 1697–1710, https://doi.org/10.1007/s00382-019-04721-4, 2019.

Bickel, M.: Climate Impact of Contrail Cirrus, Ph.D. thesis, Ludwig-Maximilians-Universität München, https://doi.org/10.5282/edoc.32411, 2023.

Bickel, M., Ponater, M., Bock, L., Burkhardt, U., and Reineke, S.: Estimating the Effective Radiative Forcing of Contrail Cirrus, Journal of Climate, 33, 1991–2005, https://doi.org/10.1175/JCLI-D-19-0467.1, 2020.

Bony, S., Colman, R., Kattsov, V. M., et al.: How Well Do We Understand and Evaluate Climate Change Feedback Processes?, Journal of Climate, 19, 3445–3482, https://doi.org/10.1175/JCLI3819.1, 2006.

Brewer, A. W.: Evidence for a world circulation provided by the measurements of helium and water vapour distribution in the stratosphere, Q.J.R. Meteorol. Soc., 75, 351–363, https://doi.org/10.1002/qj.49707532603, 1949.

Butchart, N.: The Brewer-Dobson circulation, Reviews of Geophysics, 52, 157–184, https://doi.org/10.1002/2013RG000448, 2014.

Byrom, R. E. and Shine, K. P.: Methane's Solar Radiative Forcing, Geophys. Res. Lett., 49, e2022GL098 270, https://doi.org/10.1029/2022GL098270, 2022.

CCMI: The Chemistry Climate Model Initiative (CCMI), `https://blogs.reading.ac.uk/ccmi/`, 2023.

Chapman, S.: XXXV. On ozone and atomic oxygen in the upper atmosphere, The London, Edinburgh, and Dublin Philosophical Magazine and Journal of Science, 10, 369–383, https://doi.org/10.1080/14786443009461588, 1930.

Chiodo, G. and Polvani, L. M.: The Response of the Ozone Layer to Quadrupled CO_2 Concentrations: Implications for Climate, J. Climate, 32, 7629–7642, https://doi.org/10.1175/JCLI-D-19-0086.1, 2019.

Chiodo, G., Polvani, L. M., Marsh, D. R., et al.: The Response of the Ozone Layer to Quadrupled CO_2 Concentrations, J. Climate, 31, 3893–3907, https://doi.org/10.1175/JCLI-D-17-0492.1, 2018.

Collins, W. J., Webber, C. P., Cox, P. M., et al.: Increased importance of methane reduction for a 1.5 degree target, Environ. Res. Lett., 13, 054 003, https://doi.org/10.1088/1748-9326/aab89c, 2018.

Colman, R. and Soden, B. J.: Water vapor and lapse rate feedbacks in the climate system, Rev. Mod. Phys., 93, 045 002, https://doi.org/10.1103/RevModPhys.93.045002, 2021.

Colman, R. A. and McAvaney, B. J.: A study of general circulation model climate feedbacks determined from perturbed sea surface temperature experiments, J. Geophys. Res. Atmos, 102, 19 383–19 402, https://doi.org/10.1029/97JD00206, 1997.

Curry, C. L.: Modeling the soil consumption of atmospheric methane at the global scale, Global Biogeochem. Cy., 21, https://doi.org/10.1029/2006GB002818, 2007.

Dean, J. F., Middelburg, J. J., Röckmann, T., et al.: Methane Feedbacks to the Global Climate System in a Warmer World, Rev. Geophys., 56, 207–250, https://doi.org/10.1002/2017RG000559, 2018.

Diehl, T., Heil, A., Chin, M., et al.: Anthropogenic, biomass burning, and volcanic emissions of black carbon, organic carbon, and SO_2 from 1980 to 2010 for hindcast model experiments, Atmos. Chem. Phys. Discuss., 12, 24 895–24 954, https://doi.org/10.5194/acpd-12-24895-2012, 2012.

Dietmüller, S.: Relative Bedeutung chemischer und physikalischer Rückkopplungen in Klimasensitivitätsstudien mit dem Klima-Chemie-Modellsystem EMAC/MLO, Ph.D. thesis, Ludwig-Maximilians-Universität München, https://doi.org/10.5282/edoc.13680, 2011.

Dietmüller, S., Ponater, M., and Sausen, R.: Interactive ozone induces a negative feedback in CO_2-driven climate change simulations, J. Geophys. Res. Atmos., 119, 1796–1805, https://doi.org/10.1002/2013JD020575, 2014.

Dietmüller, S., Jöckel, P., Tost, H., et al.: A new radiation infrastructure for the Modular Earth Submodel System (MESSy, based on version 2.51), Geosci. Model Dev., 9, 2209–2222, https://doi.org/10.5194/gmd-9-2209-2016, 2016.

Dobson, G. M. B., Harrison, D., and Lawrence, J.: Measurements of the amount of ozone in the Earth's atmosphere and its relation to other geophysical conditions, Proceedings of the Royal Society of London. Series A, Containing Papers of a Mathematical and Physical Character, 122, 456–486, https://doi.org/10.1098/rspa.1926.0040, 1929.

Eichinger, R., Jöckel, P., Brinkop, S., Werner, M., and Lossow, S.: Simulation of the isotopic composition of stratospheric water vapour – Part 1: Description and evaluation

of the EMAC model, Atmos. Chem. Phys., 15, 5537–5555, https://doi.org/10.5194/acp-15-5537-2015, 2015.

Eichinger, R., Rhode, S., Garny, H., et al.: Emulating lateral gravity wave propagation in a global chemistry–climate model (EMAC v2.55.2) through horizontal flux redistribution, Geosci. Model Dev., 16, 5561–5583, https://doi.org/10.5194/gmd-16-5561-2023, 2023.

Etminan, M., Myhre, G., Highwood, E. J., and Shine, K. P.: Radiative forcing of carbon dioxide, methane, and nitrous oxide: A significant revision of the methane radiative forcing, Geophys. Res. Lett., 43, 12,614–12,623, https://doi.org/10.1002/2016GL071930, 2016.

Eyring, V., Gillett, N., Rao, K. A., et al.: Human Influence on the Climate System. Climate Change 2021: The Physical Science Basis. Contribution of Working Group I to the Sixth Assessment Report of the Intergovernmental Panel on Climate Change [Masson-Delmotte, V., P. Zhai, A. Pirani, S.L. Connors, C. Péan, S. Berger, N. Caud, Y. Chen, L. Goldfarb, M.I. Gomis, M. Huang, K. Leitzell, E. Lonnoy, J.B.R. Matthews, T.K. Maycock, T. Waterfield, O. Yelekçi, R. Yu, and B. Zhou (eds.)], pp. 423–552, Cambridge University Press, Cambridge, United Kingdom and New York, NY, USA, https://doi.org/10.1017/9781009157896.005, 2021.

Feldman, D. R., Collins, W. D., Biraud, S. C., et al.: Observationally derived rise in methane surface forcing mediated by water vapour trends, Nature Geosci., 11, 238–243, https://doi.org/10.1038/s41561-018-0085-9, 2018.

Fels, S. B., Mahlman, J. D., Schwarzkopf, M. D., and Sinclair, R. W.: Stratospheric Sensitivity to Perturbations in Ozone and Carbon Dioxide: Radiative and Dynamical Response, Journal of Atmospheric Sciences, 37, 2265–2297, https://doi.org/10.1175/1520-0469(1980)037⟨2265:SSTPIO⟩2.0.CO;2, 1980.

Finney, D. L., Doherty, R. M., Wild, O., Young, P. J., and Butler, A.: Response of lightning NO_x emissions and ozone production to climate change: Insights from the Atmospheric Chemistry and Climate Model Intercomparison Project, Geophys. Res. Lett., 43, 5492–5500, https://doi.org/10.1002/2016GL068825, 2016.

Finney, D. L., Doherty, R. M., Wild, O., et al.: A projected decrease in lightning under climate change, Nature Climate Change, 8, 210–213, https://doi.org/10.1038/s41558-018-0072-6, 2018.

Fiore, A. M., Dentener, F. J., Wild, O., et al.: Multimodel estimates of intercontinental source-receptor relationships for ozone pollution, J. Geophys. Res. Atmos., 114, https://doi.org/10.1029/2008JD010816, 2009.

Forster, P., Storelvmo, T., Armour, K., et al.: The Earth's Energy Budget, Climate Feedbacks, and Climate Sensitivity. Climate Change 2021: The Physical Science Basis. Contribution of Working Group I to the Sixth Assessment Report of the Intergovernmental Panel on Climate Change [Masson-Delmotte, V., P. Zhai, A. Pirani, S.L. Connors, C. Péan, S. Berger, N. Caud, Y. Chen, L. Goldfarb, M.I. Gomis, M. Huang, K. Leitzell, E. Lonnoy, J.B.R. Matthews, T.K. Maycock, T. Waterfield, O. Yelekçi, R. Yu, and B. Zhou (eds.)], pp. 423–552, Cambridge University Press, Cambridge, United Kingdom and New York, NY, USA, https://doi.org/10.1017/9781009157896.009, 2021.

Forster, P. M., Richardson, T., Maycock, A. C., et al.: Recommendations for diagnosing effective radiative forcing from climate models for CMIP6, J. Geophys. Res. Atmos, 121, 12,460–12,475, https://doi.org/10.1002/2016JD025320, 2016.

Fouquart, Y. and Bonnel, B.: Computations of solar heating of the Earth's atmosphere: A new parameterization, Beitr. Phys. Atmos., 53, 35–62, 1980.

Frank, F.: Atmospheric methane and its isotopic composition in a changing climate: A modeling study, Ph.D. thesis, Ludwig-Maximilians-Universität München, https://doi.org/10.5282/edoc.22578, 2018.

Frank, F., Jöckel, P., Gromov, S., and Dameris, M.: Investigating the yield of H_2O and H_2 from methane oxidation in the stratosphere, Atmos. Chem. Phys., 18, 9955–9973, https://doi.org/10.5194/acp-18-9955-2018, 2018.

Garny, H., Dameris, M., Randel, W., Bodeker, G. E., and Deckert, R.: Dynamically Forced Increase of Tropical Upwelling in the Lower Stratosphere, Journal of the Atmospheric Sciences, 68, 1214–1233, https://doi.org/10.1175/2011JAS3701.1, 2011.

Gaubert, B., Worden, H. M., Arellano, A. F. J., et al.: Chemical Feedback From Decreasing Carbon Monoxide Emissions, Geophys. Res. Lett., 44, 9985–9995, https://doi.org/10.1002/2017GL074987, 2017.

Giorgetta, M. A. and Bengtsson, L.: Potential role of the quasi-biennial oscillation in the stratosphere-troposphere exchange as found in water vapor in general circulation

model experiments, J. Geophys. Res. Atmos., 104, 6003–6019, https://doi.org/10.1029/1998JD200112, 1999.

Granier, C., Bessagnet, B., Bond, T., et al.: Evolution of anthropogenic and biomass burning emissions of air pollutants at global and regional scales during the 1980–2010 period, Climatic Change, 109, https://doi.org/10.1007/s10584-011-0154-1, 2011.

Gregory, J. M., Ingram, W. J., Palmer, M. A., et al.: A new method for diagnosing radiative forcing and climate sensitivity, Geophys. Res. Lett., 31, https://doi.org/10.1029/2003GL018747, 2004.

Grewe, V.: The origin of ozone, Atmos. Chem. Phys., 6, 1495–1511, https://doi.org/10.5194/acp-6-1495-2006, 2006.

Grewe, V., Brunner, D., Dameris, M., et al.: Origin and variability of upper tropospheric nitrogen oxides and ozone at northern mid-latitudes, Atmospheric Environment, 35, 3421–3433, https://doi.org/10.1016/S1352-2310(01)00134-0, 2001.

Grewe, V., Tsati, E., Mertens, M., Frömming, C., and Jöckel, P.: Contribution of emissions to concentrations: the TAGGING 1.0 submodel based on the Modular Earth Submodel System (MESSy 2.52), Geosci. Model Dev., 10, 2615–2633, https://doi.org/10.5194/gmd-10-2615-2017, 2017.

Griffiths, P. T., Murray, L. T., Zeng, G., et al.: Tropospheric ozone in CMIP6 simulations, Atmos. Chem. Phys., 21, 4187–4218, https://doi.org/10.5194/acp-21-4187-2021, 2021.

Gromov, S., Brenninkmeijer, C. A. M., and Jöckel, P.: A very limited role of tropospheric chlorine as a sink of the greenhouse gas methane, Atmos. Chem. Phys., 18, 9831–9843, https://doi.org/10.5194/acp-18-9831-2018, 2018.

Hansen, J., Sato, M., Ruedy, R., et al.: Efficacy of climate forcings, J. Geophys. Res. Atmos., 110, https://doi.org/10.1029/2005JD005776, 2005.

Heimann, I., Griffiths, P. T., Warwick, N. J., et al.: Methane Emissions in a Chemistry-Climate Model: Feedbacks and Climate Response, J. Adv. Model. Earth Syst., 12, e2019MS002 019, https://doi.org/10.1029/2019MS002019, 2020.

Heinze, C., Eyring, V., Friedlingstein, P., et al.: ESD Reviews: Climate feedbacks in the Earth system and prospects for their evaluation, Earth Syst. Dynam., 10, 379–452, https://doi.org/10.5194/esd-10-379-2019, 2019.

Hersbach, H., Bell, B., Berrisford, P., et al.: The ERA5 global reanalysis, Quarterly Journal of the Royal Meteorological Society, 146, 1999–2049, https://doi.org/10.1002/qj.3803, 2020.

Holmes, C. D.: Methane Feedback on Atmospheric Chemistry: Methods, Models, and Mechanisms, J. Adv. Model. Earth Syst., 10, 1087–1099, https://doi.org/10.1002/2017MS001196, 2018.

Hossaini, R., Chipperfield, M. P., Saiz-Lopez, A., et al.: A global model of tropospheric chlorine chemistry: Organic versus inorganic sources and impact on methane oxidation, J. of Geophys. Res. Atmos., 121, 14,271–14,297, https://doi.org/10.1002/2016JD025756, 2016.

Iacono, M. J., Delamere, J. S., Mlawer, E. J., et al.: Radiative forcing by long-lived greenhouse gases: Calculations with the AER radiative transfer models, J. Geophys. Res. Atmos., 113, https://doi.org/10.1029/2008JD009944, 2008.

Jenkin, M. E., Saunders, S. M., and Pilling, M. J.: The tropospheric degradation of volatile organic compounds: a protocol for mechanism development, Atmospheric Environment, 31, 81–104, https://doi.org/10.1016/S1352-2310(96)00105-7, 1997.

Jöckel, P., Sander, R., Kerkweg, A., Tost, H., and Lelieveld, J.: Technical Note: The Modular Earth Submodel System (MESSy) - a new approach towards Earth System Modeling, Atmos. Chem. Phys., 5, 433–444, https://doi.org/10.5194/acp-5-433-2005, 2005.

Jöckel, P., Kerkweg, A., Buchholz-Dietsch, J., et al.: Technical Note: Coupling of chemical processes with the Modular Earth Submodel System (MESSy) submodel TRACER, Atmos. Chem. Phys., 8, 1677–1687, https://doi.org/10.5194/acp-8-1677-2008, 2008.

Jöckel, P., Kerkweg, A., Pozzer, A., et al.: Development cycle 2 of the Modular Earth Submodel System (MESSy2), Geosci. Model Dev., 3, 717–752, https://doi.org/10.5194/gmd-3-717-2010, 2010.

Jöckel, P., Tost, H., Pozzer, A., et al.: Earth System Chemistry integrated Modelling (ESCiMo) with the Modular Earth Submodel System (MESSy) version 2.51, Geosci. Model Dev., 9, 1153–1200, https://doi.org/10.5194/gmd-9-1153-2016, 2016.

Kerkweg, A., Buchholz, J., Ganzeveld, L., et al.: Technical Note: An implementation of the dry removal processes DRY DEPosition and SEDImentation in the Modular Earth Submodel System (MESSy), Atmos. Chem. Phys., 6, 4617–4632, https://doi.org/10.5194/acp-6-4617-2006, 2006a.

Kerkweg, A., Sander, R., Tost, H., and Jöckel, P.: Technical note: Implementation of prescribed (OFFLEM), calculated (ONLEM), and pseudo-emissions (TNUDGE) of chemical species in the Modular Earth Submodel System (MESSy), Atmos. Chem. Phys., 6, 3603–3609, https://doi.org/10.5194/acp-6-3603-2006, 2006b.

Kirner, O., Ruhnke, R., Buchholz-Dietsch, J., et al.: Simulation of polar stratospheric clouds in the chemistry-climate-model EMAC via the submodel PSC, Geosci. Model Dev., 4, 169–182, https://doi.org/10.5194/gmd-4-169-2011, 2011.

Klocke, D., Quaas, J., and Stevens, B.: Assessment of different metrics for physical climate feedbacks, Clim. Dyn., 41, 1173–1185, https://doi.org/10.1007/s00382-013-1757-1, 2013.

Kunze, M., Godolt, M., Langematz, U., et al.: Investigating the early Earth faint young Sun problem with a general circulation model, Planet. Space Sci., 98, 77–92, https://doi.org/10.1016/j.pss.2013.09.011, planetary evolution and life, 2014.

Kurtén, T., Zhou, L., Makkonen, R., et al.: Large methane releases lead to strong aerosol forcing and reduced cloudiness, Atmos. Chem. and Phys., 11, 6961–6969, https://doi.org/10.5194/acp-11-6961-2011, 2011.

Lamarque, J.-F., Bond, T. C., Eyring, V., et al.: Historical (1850–2000) gridded anthropogenic and biomass burning emissions of reactive gases and aerosols: methodology and application, Atmos. Chem. Phys., 10, 7017–7039, https://doi.org/10.5194/acp-10-7017-2010, 2010.

Lan, X., Thoning, K., and Dlugokencky, E.: Trends in globally-averaged CH_4, N_2O, and SF_6 determined from NOAA Global Monitoring Laboratory measurements, https://doi.org/10.15138/P8XG-AA10, 2023.

Lee, J.-Y., Marotzke, J., Bala, G., et al.: Future Global Climate: Scenario-Based Projections and Near- Term Information. Climate Change 2021: The Physical Science Basis. Contribution of Working Group I to the Sixth Assessment Report of the Intergovernmental Panel on Climate Change [Masson-Delmotte, V., P. Zhai, A. Pirani, S.L. Connors,

C. Péan, S. Berger, N. Caud, Y. Chen, L. Goldfarb, M.I. Gomis, M. Huang, K. Leitzell, E. Lonnoy, J.B.R. Matthews, T.K. Maycock, T. Waterfield, O. Yelekçi, R. Yu, and B. Zhou (eds.)], pp. 553–672, Cambridge University Press, Cambridge, United Kingdom and New York, NY, USA, https://doi.org/110.1017/9781009157896.006, 2021.

Li, F. and Newman, P.: Prescribing stratospheric chemistry overestimates southern hemisphere climate change during austral spring in response to quadrupled CO_2, Clim. Dyn., 61, 1105—-1122, https://doi.org/10.1007/s00382-022-06588-4, 2023.

Marsh, D. R., Lamarque, J.-F., Conley, A. J., and Polvani, L. M.: Stratospheric ozone chemistry feedbacks are not critical for the determination of climate sensitivity in CESM1(WACCM), Geophys. Res. Lett., 43, 3928–3934, https://doi.org/10.1002/2016GL068344, 2016.

Masson-Delmotte, V., Zhai, P., Pörtner, H.-O., et al., eds.: Global Warming of 1.5°C. An IPCC Special Report on the impacts of global warming of 1.5°C above pre-industrial levels and related global greenhouse gas emission pathways, in the context of strengthening the global response to the threat of climate change, sustainable development, and efforts to eradicate poverty, Cambridge University Press, Cambridge, United Kingdom and New York, NY, USA, https://doi.org/10.1017/9781009157940, 2018.

Masson-Delmotte, V., P. Zhai, A. P., Connor, S., et al., eds.: Climate Change 2021: The Physical Science Basis. Contribution of Working Group I to the Sixth Assessment Report of the Intergovernmental Panel on Climate Change, Cambridge University Press, Cambridge, United Kingdom and New York, NY, USA, https://doi.org/10.1017/9781009157896, 2021.

Matthes, K., Funke, B., Andersson, M. E., et al.: Solar forcing for CMIP6 (v3.2), Geosci. Model Dev., 10, 2247–2302, https://doi.org/10.5194/gmd-10-2247-2017, 2017.

Meinshausen, M., Vogel, E., Nauels, A., et al.: Historical greenhouse gas concentrations for climate modelling (CMIP6), Geosci. Model Dev., 10, 2057–2116, https://doi.org/10.5194/gmd-10-2057-2017, 2017.

MESSy Consortium: Modular Earth Submodel System (MESSy), `https://messy-interface.org/`, last access: 2023-02-13, 2023.

Mlawer, E. J., Taubman, S. J., Brown, P. D., Iacono, M. J., and Clough, S. A.: Radiative transfer for inhomogeneous atmospheres: RRTM, a validated correlated-k model for

the longwave, J. Geophys. Res. Atmos., 102, 16 663–16 682, https://doi.org/10.1029/97JD00237, 1997.

Modak, A., Bala, G., Caldeira, K., and Cao, L.: Does shortwave absorption by methane influence its effectiveness?, Climate Dyn., 51, 3653–3672, https://doi.org/10.1007/s00382-018-4102-x, 2018.

Nissen, K. M., Matthes, K., Langematz, U., and Mayer, B.: Towards a better representation of the solar cycle in general circulation models, Atmos. Chem. Phys., 7, 5391–5400, https://doi.org/10.5194/acp-7-5391-2007, 2007.

Nowack, P. J., Luke Abraham, N., Maycock, A. C., et al.: A large ozone-circulation feedback and its implications for global warming assessments, Nature Climate Change, 5, 41–45, https://doi.org/10.1038/nclimate2451, 2015.

Nowack, P. J., Abraham, N. L., Braesicke, P., and Pyle, J. A.: The Impact of Stratospheric Ozone Feedbacks on Climate Sensitivity Estimates, J. Geophys. Res. Atmos., 123, 4630–4641, https://doi.org/10.1002/2017JD027943, 2018.

Nützel, M., Stecher, L., Jöckel, P., et al.: Updating the radiation infrastructure in MESSy (based on MESSy version 2.55), EGUsphere, 2023, 1–44, https://doi.org/10.5194/egusphere-2023-2140, 2023.

Nuvolone, D., Petri, D., and Voller, F.: The effects of ozone on human health, Environ. Sci. Pollut. Res., 25, 8074–8088, https://doi.org/10.1007/s11356-017-9239-3, 2018.

Ocko, I. B. and Hamburg, S. P.: Climate consequences of hydrogen emissions, Atmos. Chem. Phys., 22, 9349–9368, https://doi.org/10.5194/acp-22-9349-2022, 2022.

Ocko, I. B., Sun, T., Shindell, D., et al.: Acting rapidly to deploy readily available methane mitigation measures by sector can immediately slow global warming, Environ. Res. Lett., 16, 054 042, https://doi.org/10.1088/1748-9326/abf9c8, 2021.

O'Connor, F. M., Boucher, O., Gedney, N., et al.: Possible role of wetlands, permafrost, and methane hydrates in the methane cycle under future climate change: A review, Rev. Geophys., 48, https://doi.org/10.1029/2010RG000326, 2010.

O'Connor, F. M., Johnson, B. T., Jamil, O., et al.: Apportionment of the Pre-Industrial to Present-Day Climate Forcing by Methane Using UKESM1: The Role of the Cloud

Radiative Effect, J. Adv. Model. Earth Syst., 14, e2022MS002 991, https://doi.org/10.1029/2022MS002991, 2022.

Petty, G. W.: A First Course in Atmospheric Radiation, Sundog Publishing, 2nd edn., 2006.

Pincus, R. and Stevens, B.: Paths to accuracy for radiation parameterizations in atmospheric models, J. Adv. Model. Earth Syst., 5, 225–233, https://doi.org/10.1002/jame.20027, 2013.

Pincus, R., Barker, H. W., and Morcrette, J.-J.: A fast, flexible, approximate technique for computing radiative transfer in inhomogeneous cloud fields, J. Geophys. Res. Atmos., 108, https://doi.org/10.1029/2002JD003322, 2003.

Portmann, R. W. and Solomon, S.: Indirect radiative forcing of the ozone layer during the 21st century, Geophys. Res. Lett., 34, https://doi.org/10.1029/2006GL028252, 2007.

Pozzer, A., Jöckel, P., Sander, R., et al.: Technical Note: The MESSy-submodel AIRSEA calculating the air-sea exchange of chemical species, Atmos. Chem. Phys., 6, 5435–5444, https://doi.org/10.5194/acp-6-5435-2006, 2006.

Prather, M. J., Holmes, C. D., and Hsu, J.: Reactive greenhouse gas scenarios: Systematic exploration of uncertainties and the role of atmospheric chemistry, Geophys. Res. Lett., 39, https://doi.org/10.1029/2012GL051440, 2012.

Prinn, R. G., Huang, J., Weiss, R. F., et al.: Evidence for variability of atmospheric hydroxyl radicals over the past quarter century, Geophys. Res. Lett., 32, https://doi.org/10.1029/2004GL022228, 2005.

Ramanathan, V.: Greenhouse Effect Due to Chlorofluorocarbons: Climatic Implications, Science, 190, 50–52, https://doi.org/10.1126/science.190.4209.50, 1975.

Ramanathan, V. and Dickinson, R. E.: The Role of Stratospheric Ozone in the Zonal and Seasonal Radiative Energy Balance of the Earth-Troposphere System, Journal of Atmospheric Sciences, 36, 1084–1104, https://doi.org/10.1175/1520-0469(1979)036⟨1084:TROSOI⟩2.0.CO;2, 1979.

Ramaswamy, V., Collins, W., Haywood, J., et al.: Radiative Forcing of Climate: The Historical Evolution of the Radiative Forcing Concept, the Forcing Agents and

their Quantification, and Applications, Meteorological Monographs, 59, 14.1 – 14.101, https://doi.org/10.1175/AMSMONOGRAPHS-D-19-0001.1, 2018.

Randel, W. and Park, M.: Diagnosing Observed Stratospheric Water Vapor Relationships to the Cold Point Tropical Tropopause, J. Geophys. Res. Atmos., 124, 7018–7033, https://doi.org/10.1029/2019JD030648, 2019.

Rayner, N. A., Parker, D. E., Horton, E. B., et al.: Global analyses of sea surface temperature, sea ice, and night marine air temperature since the late nineteenth century, J. Geophys. Res. Atmos., 108, 4407, https://doi.org/10.1029/2002JD002670, 2003.

Richardson, T. B., Forster, P. M., Smith, C. J., et al.: Efficacy of Climate Forcings in PDRMIP Models, J. Geophys. Res. Atmos., 124, 12 824–12 844, https://doi.org/10.1029/2019JD030581, 2019.

Rieger, V. S., Dietmüller, S., and Ponater, M.: Can feedback analysis be used to uncover the physical origin of climate sensitivity and efficacy differences?, Climate Dyn., 49, 2831–2844, https://doi.org/10.1007/s00382-016-3476-x, 2017.

Rieger, V. S., Mertens, M., and Grewe, V.: An advanced method of contributing emissions to short-lived chemical species (OH and HO_2): the TAGGING 1.1 submodel based on the Modular Earth Submodel System (MESSy 2.53), Geosci. Model Dev., 11, 2049–2066, https://doi.org/10.5194/gmd-11-2049-2018, 2018.

Righi, M., Andela, B., Eyring, V., et al.: Earth System Model Evaluation Tool (ESMValTool) v2.0 – technical overview, Geosci. Model Dev., 13, 1179–1199, https://doi.org/10.5194/gmd-13-1179-2020, 2020.

Roeckner, E., Siebert, T., and Feichter, J.: Climatic response to anthropogenic sulfate forcing simulated with a general circulation model, Aerosol Forcing of Climate, pp. 349–362, 1995.

Roeckner, E., Bäuml, G., Bonaventura, L., et al.: The atmospheric general circulation model ECHAM5. PART I: Model description, Report / Max-Planck-Institut für Meteorologie, 349, `https://hdl.handle.net/11858/00-001M-0000-0012-0144-5`, 2003.

Roeckner, E., Brokopf, R., Esch, M., et al.: Sensitivity of Simulated Climate to Horizontal and Vertical Resolution in the ECHAM5 Atmosphere Model, Journal of Climate, 19, 3771–3791, https://doi.org/10.1175/JCLI3824.1, 2006.

Rosenfield, J. E., Douglass, A. R., and Considine, D. B.: The impact of increasing carbon dioxide on ozone recovery, J. Geophys. Res. Atmos., 107, ACH 7–1–ACH 7–9, https://doi.org/10.1029/2001JD000824, 2002.

RRTMG: RRTMG description on the Atmospheric and Environmental Research (AER) Radiative Transfer Working Group Website, `http://rtweb.aer.com/rrtm_frame.html`, last access: 2023-10-24, 2023.

Sander, R., Jöckel, P., Kirner, O., et al.: The photolysis module JVAL-14, compatible with the MESSy standard, and the JVal PreProcessor (JVPP), Geosci. Model Dev., 7, 2653–2662, https://doi.org/10.5194/gmd-7-2653-2014, 2014.

Sander, R., Baumgaertner, A., Cabrera-Perez, D., et al.: The community atmospheric chemistry box model CAABA/MECCA-4.0, Geosci. Model Dev., 12, 1365–1385, https://doi.org/10.5194/gmd-12-1365-2019, 2019.

Sandu, A. and Sander, R.: Technical note: Simulating chemical systems in Fortran90 and Matlab with the Kinetic PreProcessor KPP-2.1, Atmos. Chem. Phys., 6, 187–195, https://doi.org/10.5194/acp-6-187-2006, 2006.

Saunois, M., Jackson, R. B., Bousquet, P., Poulter, B., and Canadell, J. G.: The growing role of methane in anthropogenic climate change, Environ. Res. Lett., 11, 120 207, https://doi.org/10.1088/1748-9326/11/12/120207, 2016.

Saunois, M., Stavert, A. R., Poulter, B., et al.: The Global Methane Budget 2000–2017, Earth Syst. Sci. Data, 12, 1561–1623, https://doi.org/10.5194/essd-12-1561-2020, 2020.

Schlund, M., Hassler, B., Lauer, A., et al.: Evaluation of native Earth system model output with ESMValTool v2.6.0, Geosci. Model Dev., 16, 315–333, https://doi.org/10.5194/gmd-16-315-2023, 2023.

Seinfeld, J. H. and Pandis, S. N.: Atmospheric chemistry and physics: from air pollution to climate change, John Wiley & Sons, Inc., 3rd edn., 2016.

Sherwood, S. C., Bony, S., Boucher, O., et al.: Adjustments in the Forcing-Feedback Framework for Understanding Climate Change, B. Am. Meteorol. Soc., 96, 217–228, https://doi.org/10.1175/BAMS-D-13-00167.1, 2015.

Shindell, D., Kuylenstierna, J. C. I., Vignati, E., et al.: Simultaneously Mitigating Near-Term Climate Change and Improving Human Health and Food Security, Science, 335, 183–189, https://doi.org/10.1126/science.1210026, 2012.

Shindell, D. T., Faluvegi, G., Koch, D. M., et al.: Improved Attribution of Climate Forcing to Emissions, Science, 326, 716–718, https://doi.org/10.1126/science.1174760, 2009.

Shine, K. P., Cook, J., Highwood, E. J., and Joshi, M. M.: An alternative to radiative forcing for estimating the relative importance of climate change mechanisms, Geophys. Res. Lett., 30, https://doi.org/10.1029/2003GL018141, 2003.

Sitch, S., Cox, P. M., Collins, W. J., and Huntingford, C.: Indirect radiative forcing of climate change through ozone effects on the land-carbon sink, Nature, 448, 791–794, https://doi.org/10.1038/nature06059, 2007.

Skeie, R. B., Hodnebrog, Ø., and Myhre, G.: Trends in atmospheric methane concentrations since 1990 were driven and modified by anthropogenic emissions, Commun. Earth Environ., https://doi.org/10.1038/s43247-023-00969-1, 2023.

Smalley, K. M., Dessler, A. E., Bekki, S., et al.: Contribution of different processes to changes in tropical lower-stratospheric water vapor in chemistry–climate models, Atmos. Chem. Phys., 17, 8031–8044, https://doi.org/10.5194/acp-17-8031-2017, 2017.

Smith, C. J., Kramer, R. J., Myhre, G., et al.: Understanding Rapid Adjustments to Diverse Forcing Agents, Geophys. Res. Lett., 45, 12,023–12,031, https://doi.org/10.1029/2018GL079826, 2018.

Soden, B. J., Held, I. M., Colman, R., et al.: Quantifying Climate Feedbacks Using Radiative Kernels, Journal of Climate, 21, 3504–3520, https://doi.org/10.1175/2007JCLI2110.1, 2008.

Spahni, R., Wania, R., Neef, L., et al.: Constraining global methane emissions and uptake by ecosystems, Biogeosciences, 8, 1643–1665, https://doi.org/10.5194/bg-8-1643-2011, 2011.

Staniaszek, Z., Griffiths, P. T., Folberth, G. A., et al.: The role of future anthropogenic methane emissions in air quality and climate, npj Clim Atmos Sci, 5, https://doi.org/10.1038/s41612-022-00247-5, 2022.

Stecher, L., Winterstein, F., Dameris, M., et al.: Slow feedbacks resulting from strongly enhanced atmospheric methane mixing ratios in a chemistry–climate model with mixed–layer ocean, Atmos. Chem. Phys., 21, 731–754, https://doi.org/10.5194/acp-21-731-2021, 2021.

Stevenson, D. S., Dentener, F. J., Schultz, M. G., et al.: Multimodel ensemble simulations of present-day and near-future tropospheric ozone, J. Geophys. Res. Atmos., 111, https://doi.org/10.1029/2005JD006338, 2006.

Stevenson, D. S., Young, P. J., Naik, V., et al.: Tropospheric ozone changes, radiative forcing and attribution to emissions in the Atmospheric Chemistry and Climate Model Intercomparison Project (ACCMIP), Atmos. Chem. Phys., 13, 3063–3085, https://doi.org/10.5194/acp-13-3063-2013, 2013.

Stevenson, D. S., Zhao, A., Naik, V., et al.: Trends in global tropospheric hydroxyl radical and methane lifetime since 1850 from AerChemMIP, Atmos. Chem. Phys, 20, 12 905–12 920, https://doi.org/10.5194/acp-20-12905-2020, 2020.

Stevenson, D. S., Derwent, R. G., Wild, O., and Collins, W. J.: COVID-19 lockdown emission reductions have the potential to explain over half of the coincident increase in global atmospheric methane, Atmos. Chem. and Phys., 22, 14 243–14 252, https://doi.org/10.5194/acp-22-14243-2022, 2022.

Stocker, T., Qin, D., Plattner, G.-K., et al., eds.: Climate Change 2013: The Physical Science Basis. Contribution of Working Group I to the Fifth Assessment Report of the Intergovernmental Panel on Climate Change, Cambridge University Press, Cambridge, United Kingdom and New York, NY, USA, https://doi.org/10.1017/CBO9781107415324, 2013.

Stohl, A., Aamaas, B., Amann, M., et al.: Evaluating the climate and air quality impacts of short-lived pollutants, Atmos. Chem. Phys., 15, 10 529–10 566, https://doi.org/10.5194/acp-15-10529-2015, 2015.

Stuber, N., Sausen, R., and Ponater, M.: Stratosphere adjusted radiative forcing calculations in a comprehensive climate model, Theor. Appl. Climatol., 68, 125–135, https://doi.org/10.1007/s007040170041, 2001.

Tang, T., Shindell, D., Faluvegi, G., et al.: Comparison of Effective Radiative Forcing Calculations Using Multiple Methods, Drivers, and Models, J. Geophys. Res. Atmos., 124, 4382–4394, https://doi.org/10.1029/2018JD030188, 2019.

Tanre, D., Geleyn, J., and Slingo, J.: First results of an advanced aerosol-radiation interaction in ECMWF low resolution global model, in: Aerosols and Their Climatic Effects, edited by Gerber, H. and Deepak, A., 133–177, 1984.

Thornhill, G., Collins, W., Olivié, D., et al.: Climate-driven chemistry and aerosol feedbacks in CMIP6 Earth system models, Atmos. Chem. Phys., 21, 1105–1126, https://doi.org/10.5194/acp-21-1105-2021, 2021a.

Thornhill, G. D., Collins, W. J., Kramer, R. J., et al.: Effective radiative forcing from emissions of reactive gases and aerosols – a multi-model comparison, Atmos. Chem. Phys., 21, 853–874, https://doi.org/10.5194/acp-21-853-2021, 2021b.

Tost, H.: The CONVECTion Submodel CONVECT, `https://envmodel.ipa.uni-mainz.de/submodels-convect/`, last access: 2023-10-26, 2019a.

Tost, H.: The Convective Tracer Transport submodel CVTRANS, `https://envmodel.ipa.uni-mainz.de/submodels-cvtrans/`, last access: 2023-10-26, 2019b.

Tost, H., Jöckel, P., Kerkweg, A., Sander, R., and Lelieveld, J.: Technical note: A new comprehensive SCAVenging submodel for global atmospheric chemistry modelling, Atmos. Chem. Phys., 6, 565–574, https://doi.org/10.5194/acp-6-565-2006, 2006.

Tost, H., Jöckel, P., and Lelieveld, J.: Lightning and convection parameterisations - uncertainties in global modelling, Atmos. Chem. Phys., 7, 4553–4568, https://doi.org/10.5194/acp-7-4553-2007, 2007.

UNEP-CCAC: Global Methane Assessment: Benefits and Costs of Mitigating Methane Emissions, United Nations Environment Programme and Climate and Clean Air Coalition. Nairobi: United Nations Environment Programme, `https://www.unep.org/resources/report/global-methane-assessment-benefits-and-costs-mitigating-methane-emissions`, 2021.

Vella, R., Forrest, M., Lelieveld, J., and Tost, H.: Isoprene and monoterpene simulations using the chemistry–climate model EMAC (v2.55) with interactive vegetation from LPJ-GUESS (v4.0), Geosci. Model Dev., 16, 885–906, https://doi.org/10.5194/gmd-16-885-2023, 2023.

Vial, J., Dufresne, J.-L., and Bony, S.: On the interpretation of inter-model spread in CMIP5 climate sensitivity estimates, Clim. Dyn., 41, 3339–3362, https://doi.org/10.1007/s00382-013-1725-9, 2013.

Voulgarakis, A., Naik, V., Lamarque, J.-F., et al.: Analysis of present day and future OH and methane lifetime in the ACCMIP simulations, Atmos. Chem. Phys., 13, 2563–2587, https://doi.org/10.5194/acp-13-2563-2013, 2013.

Wild, M., Folini, D., Hakuba, M. Z., et al.: The energy balance over land and oceans: an assessment based on direct observations and CMIP5 climate models, Clim. Dyn., 44, 3393–3429, https://doi.org/10.1007/s00382-014-2430-z, 2015.

Wild, M., Hakuba, M. Z., Folini, D., et al.: The cloud-free global energy balance and inferred cloud radiative effects: an assessment based on direct observations and climate models, Clim. Dyn., 52, 4787–4812, https://doi.org/10.1007/s00382-018-4413-y, 2019.

Winterstein, F. and Jöckel, P.: Methane chemistry in a nutshell – the new submodels CH4 (v1.0) and TRSYNC (v1.0) in MESSy (v2.54.0), Geosci. Model Dev., 14, 661–674, https://doi.org/10.5194/gmd-14-661-2021, 2021.

Winterstein, F., Tanalski, F., Jöckel, P., Dameris, M., and Ponater, M.: Implication of strongly increased atmospheric methane concentrations for chemistry–climate connections, Atmos. Chem. Phys., 19, 7151–7163, https://doi.org/10.5194/acp-19-7151-2019, 2019.

WMO: WMO Greenhouse Gas Bulletin (GHG Bulletin) - No.18: The State of Greenhouse Gases in the Atmosphere Based on Global Observations through 2021, `https://library.wmo.int/idurl/4/58743`, 2022.

Yoshimori, M. and Broccoli, A. J.: Equilibrium Response of an Atmosphere–Mixed Layer Ocean Model to Different Radiative Forcing Agents: Global and Zonal Mean Response, Journal of Climate, 21, 4399–4423, https://doi.org/10.1175/2008JCLI2172.1, 2008.

Zanis, P., Akritidis, D., Turnock, S., et al.: Climate change penalty and benefit on surface ozone: a global perspective based on CMIP6 earth system models, Environ. Res. Lett., 17, 024 014, https://doi.org/10.1088/1748-9326/ac4a34, 2022.

Zelinka, M. D., Myers, T. A., McCoy, D. T., et al.: Causes of Higher Climate Sensitivity in CMIP6 Models, Geophys. Res. Lett., 47, e2019GL085 782, https://doi.org/10.1029/2019GL085782, 2020.

Zhou, S. S., Tai, A. P. K., Sun, S., et al.: Coupling between surface ozone and leaf area index in a chemical transport model: strength of feedback and implications for ozone air quality and vegetation health, Atmos. Chem. Phys., 18, 14 133–14 148, https://doi.org/10.5194/acp-18-14133-2018, 2018.

Danksagung

An dieser Stelle möchte ich mich ganz herzlich bei Professor Martin Dameris für seine Unterstützung bei dieser Doktorarbeit bedanken. Er hat immer ein offenes Ohr für meine Fragen, ob inhaltlich oder administrativ. Außerdem möchte ich mich für seinen großen Einsatz bei den Verlängerungen meiner Stelle bedanken, und nicht zuletzt auch für seinen kölschen Humor.

Mein Dank gilt zudem Professor Bernhard Mayer, der sich bereit erklärte, das Zweitgutachten dieser Arbeit zu übernehmen. Er verfolgte meine Arbeit über die 4 Jahre Hinweg mit Interesse und unterstützte mich bei verschienen Fragen rund um Strahlungstransfer und die Strahlungswirkung von Methan.

Ein herzliches Dankeschön geht an meine Betreuerin Dr. Franziska Winterstein. Ohne ihren bewilligten Projektantrag wäre dieses Projekt nicht möglich gewesen. Außerdem stand sie mir immer mit Rat zur Seite und unterstütze mich bei technischen und inhaltlichen Fragen.

Außerdem möchte ich mich ganz herzlich bei Dr. Patrick Jöckel bedanken, dass er sich immer Zeit nahm, alle meine Fragen rund um das Modellsystem geduldig zu beantworten und Franziska während ihrer Elternzeit auch formal als Betreuer vertrat.

Ebenso gilt mein Dank Dr. Michael Ponater, der trotz seines Ruhestandes meine Doktorarbeit aktiv mitverfolgte. Sein Wissen zu Radiative Forcing, Rapid Radiative Adjustments und Feedbacks lieferte einen wertvollen Beitrag zu dieser Arbeit. Außerdem möchte ich mich für seine Reisetipps für Reading und Wien bedanken.

Bedanken möchte ich mich zudem bei unserer Abteilungsleiterin Professor Anja Schmidt, vor allem für ihre Befürwortung meines Aufenthalts in Reading, aber auch für die generelle Förderung und Wertschätzung meiner Arbeit.

I would like to especially thank Professor Keith Shine for agreeing to host me during a 3 months research stay at the University of Reading. Thanks to him and his group, this stay was very enjoyable and I benefited greatly from it.

Ganz besonders bedanken möchte ich mich auch bei Dr. Matthias Nützel für die gute Zusammenarbeit rund um die Implementierung des neuen Strahlungschemas. An dieser Stelle möchte ich mich auch bei Dr. Markus Kunze bedanken, der geduldig unsere dabei entstehenden Fragen beantwortete und extra für diese Arbeit eine 3-D Version von MBM RAD vorbereitete. Zudem gilt mein Dank Dr. Astrid Kerkweg, die mit der Implementierung einiger Spezialfälle für MBM RAD unterstützte. Außerdem möchte ich mich bei Dr. Marius Bickel für die vielen Diskussionen über das Feedbacktool und die Interpretation der Ergebnisse bedanken.

Ebenso danke ich Dr. Mariano Mertens für seinen Vorschlag, TAGGING in den Simulationen für meine Arbeit zu aktivieren. Noch viel wichtiger als es vorzuschlagen, nahm er sich auch viel Zeit, um mir die TAGGING-Methode zu erklären und die Ergebnisse zu interpretieren.

Außerdem möchte ich die Bereitstellung der Rechenressourcen durch das BMBF am DKRZ anerkennen, mit denen ich die Simulationen meiner Arbeit durchführen konnte. Bedanken möchte ich mich auch bei den Mitarbeitenden des DKRZ User Support, die Anfragen immer sehr freundlich und hilfreich beantworteten. Anerkennen möchte ich auch die Finanzierung meiner Stelle durch das DFG Projekt IRFAM-ClimS, sowie die finanzielle Unterstützung durch das Reisestipendium der Rheinhard-Süring Stiftung für den Aufenthalt in Reading.

Ein großes Dankeschön geht an alle Kolleginnen und Kollegen der Abteilung ESM. Unser Arbeitsumfeld habe ich immer als sehr angenehm empfunden und die gemeinsamen Mittagessen, Kaffeerunden, Brettspielabende, Weihnachtsmarktbesuche und Fahrten zum EMAC Symposium haben mir viel Freude bereitet.

Ebenso gilt mein Dank meiner Familie und Freunden für die emotionale Unterstützung. Ganz besonders bedanken möchte ich mich bei meinem Partner Julian, der zudem über große Teile dieser Doktorarbeit mein Home Office Kollege war.